U.PORTO

PROGRAMA DOUTORAL EM ENGENHARIA BIOMÉDICA

CHARACTERIZATION OF A NANO-HYDROXYAPATITE/ CHITOSAN SCAFFOLD FOR BONE REGENERATION

Mariana do Souto Fontes Antunes Lopes

D

2024

Characterization of a Nano-Hydroxyapatite/Chitosan Scaffold for Bone Regeneration

Mariana do Souto Fontes Antunes Lopes

Porto
2024

U.PORTO
FEUP FACULDADE DE ENGENHARIA
UNIVERSIDADE DO PORTO

Thesis presented to the

Faculty of Engineering of the University of Porto

to obtain the Doctoral Degree in Biomedical Engineering

Supervision

Professor Christiane Laranjo Salgado

Assistant Researcher

INEB – Instituto de Engenharia Biomédica, Universidade do Porto

i3S – Instituto de Investigação e Inovação em Saúde da Universidade do Porto

Co-Supervision

Professor Maria Helena Fernandes

Full Professor

Faculty of Dental Medicine of the University of Porto (FMDUP)

Laboratory for Bone Metabolism and Regeneration (FMDUP)

LAQV/REQUIMTE – Laboratório Associado para a Química Verde/Rede de Química e Tecnologia

Advisors

Professor Fernando Jorge Monteiro

Full Professor

Faculty of Engineering of the University of Porto (FEUP)

INEB – Instituto de Engenharia Biomédica, Universidade do Porto

i3S – Instituto de Investigação e Inovação em Saúde da Universidade do Porto

Porto Comprehensive Cancer Center (P.CCC)

Professor Madalena Maria Dias

Associate Professor

Faculty of Engineering of the University of Porto (FEUP)

LSRE-LCM – Laboratory of Separation and Reaction Engineering – Laboratory of Catalysis and Materials (FEUP)

ALiCE – Associate Laboratory in Chemical Engineering (FEUP)

The work described in this thesis was performed at:

FEUP – Faculty of Engineering of the University of Porto, Portugal;

INEB – Instituto de Engenharia Biomédica, University of Porto, Portugal;

i3S – Instituto de Investigação e Inovação em Saúde, University of Porto, Portugal;

FMDUP – Laboratory for Bone Metabolism and Regeneration, Faculty of Dental Medicine of the University of Porto, Portugal

FINANCIAL SUPPORT

This work was performed at i3S – Institute for Research and Innovation in Health that is supported by Portuguese funds through FCT/MCTES (Fundação para a Ciência e a Tecnologia) – UIDB/04293/2020. This project was also supported by of LA/P/0045/2020 (ALiCE), UIDB/50020/2020 and UIDP/50020/2020 (LSRE-LCM), funded by national funds through FCT/MCTES (PIDDAC). The supervisor, CLS, is financed by FCT (CEECINST/00091/2018/CP1500/CT0019). The microCT and CLSM used in this project are from the i3S Scientific Platform Bioimaging, which is financed by PPBI-POCI-01-0145-FEDER-022122.

to my husband Pedro

and to my son Rodrigo

to my parents Paula and Alexandre,

to my sister Sara,

to my dog Tim

“If I have seen further it is by standing on ye sholders of Giants.”

Sir Issac Newton, 1676

ACKNOWLEDGEMENTS

Acknowledgements

If I have successfully reached the end of this journey, it was, to a great extent, due to the lessons and support I have received from several people.

Firstly, I would like to thank to my supervisor, Professor Christiane Laranjo Salgado, for the most dedicated guidance of this research, for teaching me several techniques and for sharing with me the difficulties and the joys of this journey. Her encouragement and patience were fundamental for the successful conclusion of this thesis.

I would also like to thank to my co-supervisor, Professor Maria Helena Fernandes, for the experienced guidance of this research, for all the patience and comprehension. Her knowledge and wise advices were essential and inspired me not to give up, even at the most challenging moments.

I am very grateful to Professor Fernando Jorge Monteiro, who, as the director of the Doctoral Program in Biomedical Engineering and group leader of the Biocomposites research group, kindly accepted me as a doctorate student. His leadership, experience and knowledge were essential for the conclusion of this research project.

I am also thankful to Professor Madalena Maria Dias, who was responsible for the initial project that developed the nano-hydroxyapatite/chitosan scaffold, and for giving me the opportunity to participate in its characterization for my thesis research.

I would like to thank to the Laboratory of Separation and Reaction Engineering – Laboratory of Catalysis and Materials (LSRE-LCM – Faculty of Engineering of the University of Porto (FEUP)), where the nano-hydroxyapatite/chitosan scaffold was developed. In particular, I would like to thank to Professor Gabriela Ruphuy, who started this research during her doctorate project, and to Professor Yaidelin Manrique, who gave continuation to the project, for their friendship, for helping me when I needed and for sharing with me the difficulties and the victories of this research.

I am very grateful to the Laboratory for Bone Metabolism and Regeneration (Faculty of Dental Medicine of the University of Porto (FMDUP)), where many experiments of this research were conducted. In particular, I would like to thank Professor Liliana Grenho for her friendship, for her patience to teach me several techniques and for her very helpful support at all times. I would also like to thank to Professor Pedro Sousa Gomes for his wise advices, as well as to my fellow colleagues at the laboratory: Víctor Martin, Carla Baptista, Laura Pinho, Maria Guerra Gomes, Thais Francini Garbieri, José Carlos Silva, Lorena Mariano and Sanjana Vig.

I would like to thank to Instituto de Investigação e Inovação em Saúde, Universidade do Porto (i3S) and to Instituto de Engenharia Biomédica, Universidade do Porto (INEB), where many

experiments of this research were conducted as well. In particular, I would like to thank to everyone in the Biocomposites group, who welcomed and helped me, and especially to my fellow colleagues at the laboratory: Joana Barros, Ângela Carvalho, Catarina Coelho, Tiago Ribeiro and Professor Marta Laranjeira.

I would also like to thank to the Biointerfaces and Nanotechnology (BN) Scientific Platform at i3S, especially to Ricardo Vidal and Dalila Pedro for all their help and support that enabled me to use the BN resources during my experiments. I am also very grateful to the Bioimaging Scientific Platform at i3S, in particular to María Lázaro for all of her support and encouragement when using the microCT and the confocal laser scanning microscope. I would also like to thank to the Animal Facility at i3S, and especially to Sofia Lamas, for all the support to perform the *in vivo* experiments.

PUBLICATIONS

Publications

The work performed within the scope of this thesis resulted in the following publications (in the chronological order in which they were published):

Souto-Lopes, M., Grenho, L., Manrique, Y., Dias, M. M., Fernandes, M. H., Monteiro, F. J., Salgado, C. L. Full physicochemical and biocompatibility characterization of a supercritical CO_2 sterilized nano-hydroxyapatite/chitosan biodegradable scaffold for periodontal bone regeneration. Biomater Adv, 2023, 146:213280. doi: 10.1016/j.bioadv.2023.213280
(Impact factor: 7.9)

Souto-Lopes, M., Fernandes, M. H., Monteiro, F. J., Salgado, C. L. Bioengineering Composite Aerogel-Based Scaffolds That Influence Porous Microstructure, Mechanical Properties and *In Vivo* Regeneration for Bone Tissue Application. Materials, 2023, 16: 4483. doi: 10.3390/ma16124483
(Impact factor: 3.4)

Souto-Lopes, M., Grenho, L., Manrique, Y., Dias, M. M., Lopes, J. C., Fernandes, M. H., Monteiro, F. J., Salgado, C. L. Bone Regeneration driven by a Nano-Hydroxyapatite/Chitosan Composite Bioaerogel for Periodontal Regeneration. Front Bioeng Biotechnol, 2024, 12:1355950. doi: 10.3389/fbioe.2024.1355950
(Impact factor: 4.3)

ABSTRACTS

Characterization of a nano-hydroxyapatite/chitosan scaffold for bone regeneration

Tissue engineering is a rapidly evolving field in biomedical sciences, due to the global need of human population for tissue regeneration, particularly of bone tissue. Bone regeneration biomaterials play a crucial role in addressing periodontal/peri-implant clinical cases, standing out as one of its primary applications. The commercially available treatments nowadays rely on autogenous grafts or on biomaterials that not always show predictable results in the long-term application. New biomimetic porous biodegradable composite biomaterials have been developed, namely in the aerogel form, by combining a polymeric matrix with dispersed nano-ceramic, from either natural or synthetic origins.

This research project aimed at characterizing the physicochemical features and the biological response of a nano-hydroxyapatite/chitosan (nHAp/CS 70/30) composite aerogel scaffold, which could be applied in periodontal/peri-implant bone regenerative surgery. This ready-to-use nHAp/CS scaffold, which is prepared by a sustainable and green three-step method (dispersion, freeze drying and supercritical CO_2 solvent extraction/sterilization), was compared with a plain CS scaffold.

Microcomputed tomography (microCT) analysis showed that the nHAp/CS scaffold has a highly interconnected open porous structure, with a porosity of 78 % and a mean pore size of 200 µm. The *in vitro* biodegradation and biomechanical properties of the scaffolds were evaluated simultaneously over time until the 4th week. When compared to the CS control scaffold, the nHAp/CS biomaterials exhibited a significantly lower degradation rate after 4 weeks in PBS (8.65 %), even in the presence of lysozyme (9.82 %). Dynamic mechanical analysis showed that the nHAp/CS scaffolds were viscoelastic and their storage modulus (40 – 50 kPa after 4 weeks in a wet environment) was significantly higher when compared to the CS control. Moreover, the deposition of an apatite layer on the nHAp/CS scaffold's surface was observed by scanning electron microscopy (SEM) after 21 days of immersion in simulated body fluid (SBF).

Both scaffold types showed a significant antimicrobial effect (measured by the metabolic activity and colony formation) against *S. aureus* and *E. coli* in a planktonic state. Furthermore, none of the extracts prepared from both nHAp/CS and CS scaffolds showed cytotoxic effects on indirect culture of human pre-osteoblasts (MG63 cell line). When MG63 cells were seeded for 21 days on the scaffolds, they showed a significantly higher metabolic activity (Alamar blue® assay), cell morphology (observed at SEM and confocal laser scanning microscopy (CLSM)) and proliferation (DNA quantification) on the nHAp/CS scaffold when compared to the control material. The MG63 cells seeded on the nHAp/CS scaffolds also showed a higher expression of osteogenic genes (RUNX2, collagen A1 and Sp7) at the 21st day. The nHAp/CS scaffolds also showed favorable conditions for primary human dental follicle mesenchymal stem cells (hDFMSCs)

adhesion, cell morphology (CLSM) and proliferation (DNA quantification). Moreover, after 21 days of culture, the presence of nHAp promoted an increased alkaline phosphatase (ALP) activity, expression of osteogenic genes (Sp7 and OPN), as well as osteopontin deposition (CLSM) by the hDFMSCs, which demonstrated the cells' response towards the osteogenic differentiation.

The *in vivo* subcutaneous implantation of both scaffold types in mice confirmed their biocompatibility, as well as their structural stability after 5 weeks. The nHAp/CS scaffold promoted a higher vascularization and collagen fiber deposition, assessed by histological analysis after 3 and 5 weeks. Finally, in calvaria critical size bone defects in rats after 3 months, microCT analysis showed that the nHAp/CS scaffold enhanced significantly the new bone formation, when compared to the CS scaffold. The histological analysis revealed that, on the contrary to the CS biomaterial, the nHAp/CS scaffold promoted the formation of new bone tissue within its structure.

The promising *in vitro* and *in vivo* results found in this research project showed that the nHAp/CS aerogel scaffold has potential to become an alternative graft biomaterial for bone regeneration, with application in the Periodontology field.

Caracterização de um biomaterial de enxerto de nano-hidroxiapatite/quitosano para regeneração óssea

A engenharia de tecidos é uma área das ciências biomédicas em rápida evolução, devido à necessidade global que a população humana tem de regeneração de tecidos, em particular de tecido ósseo. Os biomateriais para regeneração óssea desempenham um papel crucial na abordagem terapêutica de casos clínicos periodontais/peri-implantares, destacando-se como uma das suas principais aplicações. Atualmente, os produtos comerciais que estão disponíveis para tratamento destes defeitos ósseos baseiam-se em enxertos autógenos ou em biomateriais que nem sempre demonstram resultados previsíveis na sua aplicação a longo prazo. Assim, têm-se vindo a desenvolver novos biomateriais compósitos, que são biomiméticos, porosos e biodegradáveis, nomeadamente sob a forma de aerogéis, combinando uma matriz polimérica com uma fase dispersa nano-cerâmica, e que podem ser de origem natural ou sintética.

Este projeto de investigação teve como objetivo a caracterização físico-química e das respostas biológicas de um aerogel compósito tridimensional de nano-hidroxiapatite/quitosano (nHAp/CS 70/30), que poderá ser implantado para promover a regeneração óssea periodontal/peri-implantar. Este biomaterial de enxerto à base de nHAp/CS, preparado através de um método sustentável, ecológico e pronto para usar, com apenas três passos (dispersão, liofilização e extração de solvente/esterilização através de CO_2 supercrítico), foi comparado com um biomaterial constituído apenas por CS.

A análise do biomaterial de nHAp/CS através da técnica de microtomografia computadorizada (microCT) demonstrou que a sua estrutura de poros abertos é altamente interconectada, com uma porosidade de 78 % e um tamanho médio dos poros de 200 µm. As propriedades *in vitro* de biodegradação e biomecânica dos biomateriais foram avaliadas simultaneamente ao longo do tempo até à 4ª semana. Comparativamente com o biomaterial de CS de controlo, os biomateriais de nHAp/CS demonstraram uma taxa de degradação significativamente mais baixa após 4 semanas em PBS (8.65 %), sendo semelhante na presença de lisozima (9.82 %). A análise dinâmico-mecânica mostrou que os biomateriais de nHAp/CS eram viscoelásticos e o seu módulo de armazenamento (40 – 50 kPa após 4 semanas em ambiente húmido) era significativamente mais elevado quando comparado com o controlo de CS. Além disso, foi observada, através de microscopia eletrónica de varrimento (SEM), a deposição de uma camada de apatite sobre a superfície do biomaterial de nHAp/CS após 21 dias de imersão em fluido corporal simulado (SBF).

Ambos os tipos de biomateriais demonstraram um efeito antimicrobiano significativo (quantificado através da atividade metabólica e formação de colónias) em cultura de *S. aureus* e *E. coli* na sua forma planctónica. Além disso, nenhum dos extratos que foram preparados a partir dos biomateriais de nHAp/CS e CS demonstraram ter efeitos citotóxicos na cultura indireta de

uma linha celular de pré-osteoblastos humanos (MG63). Quando as células MG63 foram semeadas sobre os biomateriais durante 21 dias, demonstraram ter uma atividade metabólica (teste Alamar blue®), morfologia celular (observada através de SEM e microscopia confocal de varrimento a laser (CLSM)) e proliferação (quantificação de DNA) significativamente mais elevada nos biomateriais de nHAp/CS do que nos materiais de controlo. As células MG63 semeadas sobre os biomateriais de nHAp/CS mostraram ainda uma expressão mais elevada de genes osteogénicos (RUNX2, colagénio A1 e Sp7) ao 21º dia. Os biomateriais de nHAp/CS demonstraram também terem condições mais favoráveis para a adesão, morfologia celular (CLSM) e proliferação (quantificação de DNA) de células estaminais mesenquimais primárias humanas derivadas do folículo dentário (hDFMSCs). Além disso, após 21 dias de cultura, a presença de nHAp promoveu um aumento da atividade da fosfatase alcalina (ALP), a expressão de genes osteogénicos (Sp7 e OPN), assim como a deposição de osteopontina (CLSM) por parte das hDFMSCs, demonstrando uma resposta celular no sentido da diferenciação osteogénica.

Os dois tipos de biomateriais foram cirurgicamente implantados por via subcutânea *in vivo* em ratinhos, confirmando-se a sua biocompatibilidade, assim como a sua estabilidade estrutural após 5 semanas. A análise histológica após 3 e 5 semanas demonstrou que o biomaterial de nHAp/CS promoveu uma maior vascularização e deposição de fibras de colagénio. Finalmente, 3 meses após o enxerto dos biomateriais em defeitos ósseos de tamanho crítico na calvaria de ratos, a análise de microCT indicou que o biomaterial de nHAp/CS aumentou significativamente a neo-formação óssea, quando comparado com o biomaterial de CS. A análise histológica revelou que, ao contrário do que aconteceu com o biomaterial de CS, o material de enxerto de nHAp/CS promoveu a formação de novo tecido ósseo no interior da sua estrutura.

Os resultados promissores obtidos *in vitro* e *in vivo* neste projeto de investigação demonstraram que o aerogel de nHAp/CS tem o potencial de se tornar um biomaterial para enxerto ósseo, e a sua aplicação na área da Periodontologia.

CONTENTS

Contents

Chapter III

Chapter IV

2D – two-dimensional
3D – three-dimensional
3T3 – mouse fibroblast cell line
Aa – acetic acid
ACTB – beta-actin gene
ADSCs – human adipose-derived stem cells
Alg – alginate
ALP – alkaline phosphatase
BCP – biphasic calcium phosphate
BET – Brunauer-Emmett-Teller
BJH – Barrett-Joyner-Halenda method
BMD – bone mineral density
BMP – bone morphogenetic protein
BMU – basic multicellular unit
BrCa – metastatic breast cancer cells
BSA – bovine serum albumin
BSP – bone sialoprotein
BS/TS – bone surface/tissue surface
BV – bone volume
BV/TV – bone volume/tissue volume
B_x % – biodegradation rate
CAD – computer-aided design
CaP – calcium phosphate
CC BY – Creative Commons Attribution Licence
CFU – colony forming unit
CLSM – confocal laser scanning microscopy
Col A1 – collagen A1 gene
CPC – calcium phosphate cement
CPD – critical point dryer
CPH – chitosan/poly (γ-glutamic acid)/hydroxyapatite
CS – chitosan
Cw – swelling capacity
DD – deacetylation degree
DF – dental follicle
DFDBA – demineralized freeze-dried bone allografts
DGAV – Direção-Geral da Alimentação e Veterinária
DMA – Dynamic mechanical analysis
DMSO – dimethyl sulfoxide
E' – Storage modulus
ECM – Extracellular matrix
EDC/NHS – ethyl(dimethylaminopropyl)carbodiimide/N-hydroxysuccinimide
EDS – Energy dispersive X-ray spectroscopy
EDTA – Ethylenediaminetetraacetic acid
EGF – endothelial growth factor
EMD – enamel matrix-derived proteins
FBR – fraction of bone regeneration
FBS – fetal bovine serum
FC – fold change
FDBA – freeze-dried bone allografts
FELASA – Federation of European Laboratory Animal Science Associations
FEUP – Faculty of Engineering of the University of Porto
FFB – fresh frozen bone
FGF – fibroblast growth factor
FMDUP – Faculty of Dental Medicine of the University of Porto
GAPDH – glyceraldehyde 3-phosphate dehydrogenase gene
GBR – guided bone regeneration
Gel – gelatin
GF – growth factor
GMSCs – gingival mesenchymal stem cells
GPTMS – glycidoxypropyltrimethoxysilane
GTR – guided tissue regeneration

H&E – hematoxylin and eosin
HAp – hydroxyapatite
hDFMSCs – primary human dental follicle mesenchymal stem cells
hDPMSCs – human dental pulp mesenchymal stem cells
HIV – human immunodeficiency virus
HOBs – primary human osteoblasts
HTSD – high-temperature supercritical drying
HUVECs – human umbilical vein endothelial cells
IGF – insulin-like growth factor
Ihh – Indian hedgehog gene
IL – interleukin
INEB – Institute of Biomedical Engineering
ISO – International Organization for Standardization
LSRE – Laboratory of Separation and Reaction Engineering
LTSD – low-temperature supercritical drying
lys – lysozyme
MC3T3-E1 – mouse calvaria pre-osteoblasts cell line
MG63 – human osteoblastic cell line
microCT – microcomputed tomography
MSCs – mesenchymal stem cells
MTT – 3-(4,5-dimethylthiazol-2-yl)-2,5-diphenyl-2H-tetrazolium bromide
nHAp – nano-hydroxyapatite
nHAp/CS – nano-hydroxyapatite/chitosan
NPCs – non-collagenous proteins
OCN – osteocalcin
Oct3/4 – Octamer-binding transcription factor 4
OD – optical density
OPG – osteoprotegerin
OPN – osteopontin
PAA – peracetic acid
PBS – phosphate buffer saline
Pc – critical pressure
PCL – poly-e-caprolactone
PDGF – platelet-derived growth factor
PDL – periodontal ligament
PDLSCs – periodontal ligament stem cells
PEG – polyethylene glycol
PGLA – co-polymer poly *d*, *l*-lactic-co-glycolic acid
PLA – poly (lactic acid)
PRF – platelet-rich fibrin
QCS – quaterinized chitosan
RT – room temperature
RT-qPCR – real-time quantitative polymerase chain reaction
RUNX2 – Runt-related transcription factor 2 gene
RZ – resazurin
SAL – sterility assurance level
Saos-2 – human osteoblastic cell line
SBF – simulated body fluid
SCAPs – stem cells from apical papilla
$scCO_2$ – supercritical CO_2
SEM – scanning electron microscope
SF – silk fibroin
SHEDs – stem cells from human exfoliated deciduous teeth
Sp7 – Sp7 transcription factor (osterix)
Tb.N – trabecular number
Tb.Sp – trabecular separation
Tb.Th – trabecular thickness
Tc – critical temperature
TGF-β – transforming growth factor beta
TNF-α – tumor necrosis factor alpha
TSB – tryptic soy broth
VEGF – vascular endothelial growth factor
wt. – weight
XAN – xanthan gum
α-MEM – modified Eagle medium alfa modification

β-TCP – beta-tricalcium phosphate

ΔΔCt – delta-delta cycle threshold method

λem – emission wavelength

λex – excitation wavelength

CHAPTER I

Introduction and Objectives

INTRODUCTION AND OBJECTIVES

A tissue can be defined as an “organization of cells and/or extra-cellular constituents” [1]. Tissue engineering is a recent field that combines “materials science, cell biology, engineering technology, and transplantation” to develop biomaterials capable of promoting tissue regeneration [2-5]. In particular, bone regeneration has been one of the most studied subjects of tissue engineering, yet, due to the complexity of this hard tissue, many challenges are still unresolved [6]. Furthermore, there is a growing need for bone regeneration biomaterials owing to the exponential increase of the world human population, its longevity and expectations of quality of life, which implies a higher number of bone treatments due to trauma, infections, congenital abnormalities, oncologic and age-related diseases [7-11]. Specifically, periodontal and peri-implant diseases are highly prevalent infectious and inflammatory conditions, in which teeth and dental implants may be lost due to the irreversible destruction of their supporting tissues, namely bone [12-14]. Consequently, if left untreated, periodontal diseases may have dramatic functional and esthetic effects on an individual’s health and quality of life [13, 15, 16]. According to Gill *et al.* (2022) bone graft biomaterials for dentistry represented a global market of $663.2 million in 2020, with an estimated growth rate of 11.4 % annually until 2028 [8, 11]. However, most bone grafts commercialized nowadays only satisfy the osteoconduction pre-requisite [11, 17, 18].

On a previous investigation project, novel biodegradable nano-hydroxyapatite/chitosan (nHAp/CS) scaffolds for bone regeneration were developed through different preparation methods at the Laboratory of Separation and Reaction Engineering (LSRE), Department of Chemical Engineering, Faculty of Engineering of the University of Porto (FEUP) (the reference is available at the Supplementary Material in Chapter VII) [19]. The different nHAp/CS scaffolds were characterized and compared for their chemical composition, morphology, swelling profile and mechanical resistance [19]. The results of the biological preliminary tests performed with the most suitable nHAp/CS scaffold showed that it was not contaminated by microorganisms, and also that it allowed osteoblast-like cells (MG63) adhesion and proliferation [19]. Moreover, its preparation method was comprised of three simple steps, reducing production time and costs, in a sustainable process and suitable for large scale manufacture [19].

The present research project aimed to accomplish a thorough *in vitro* and *in vivo* characterization of the nHAp/CS composite scaffold, as an alternative biodegradable graft biomaterial for bone tissue regeneration, namely for periodontal treatment applications. In terms of *in vitro* experiments, the main objectives were to:

- Evaluate a three-dimensional (3D) scaffold with high porosity and appropriate architecture (microstructure);

- Evaluate the cytocompatibility, biodegradability, bioactivity and the biomechanical properties of a composite scaffold under physiological conditions;
- Evaluate the antimicrobial effect against representative Gram-positive and Gram-negative bacterial cultures;
- Evaluate *in vitro* the osteogenic differentiation of isolated mesenchymal cells from patients.

Additionally, pre-clinical experiments were performed in small animal models to:

- Demonstrate appropriate *in vivo* degradation, inflammation response and angiogenesis after subcutaneous implantation in mice;
- Evaluate the *in vivo* bone regeneration in calvaria critical size defects in rats (pre-clinical evaluation).

The research developed in the present thesis is organized in the following chapters:

In **Chapter II**, an extensive literature review will be focused on the state of the art of biomaterials that are being developed for bone tissue regeneration, emphasizing the context of Periodontology. A specific type of biomaterial, nHAp/CS composites, will be analyzed in detail as a potential graft material for regeneration of periodontal and peri-implant osseous defects.

Chapter III is based on a published review article [20] of the most recent literature on aerogel-based composite scaffolds for bone regeneration. This article highlighted the importance of biomimetics in bone tissue engineering and reviewed the most frequently used preparation methods of aerogel-based composite scaffolds for bone regeneration. Then, the outcomes in terms of their porous microstructure, mechanical properties and *in vivo* bone regeneration were analyzed. Future research pathways were also proposed, including the need of developing new *in vitro* 3D models for bone regeneration to overcome the necessity of using *in vivo* animal models for pre-clinical testing of this type of biomaterials.

In **Chapter IV**, a full initial characterization of relevant properties of the nHAp/CS scaffold is presented, compared to a plain CS control scaffold [21]. This chapter is introduced with a description of the most relevant features of the ideal scaffolds for periodontal bone regeneration, followed by a brief review of the advantages and applications of supercritical CO_2 ($scCO_2$), with particular focus on the use of this methodology for biomaterials sterilization. The nHAp/CS scaffold was firstly characterized in terms of its microstructure, *in vitro* bioactivity, biodegradation and biomechanical profile. Then, *in vitro* biological tests assessed its antimicrobial activity, cytotoxicity of its extracts, the proliferation and osteogenic expression of an osteoblast-like cell line seeded on the scaffolds. Finally, a preliminary *in vivo* assessment of the scaffolds' biocompatibility and biodegradation was performed in a subcutaneous implantation model in mice.

Chapter V is devoted to evaluating the nHAp/CS bioaerogel scaffold´s ability to promote the osteogenic differentiation of primary human dental follicle stem cells. Moreover, both nHAp/CS and CS bioaerogel scaffolds were implanted in calvaria critical size defects in a rat

model for *in vivo* bone regeneration assessment. Besides the terminal histological evaluation, bone regeneration was accompanied throughout 12 weeks by microcomputed tomography (microCT), which is a non-invasive technique, so that the number of animals used in the experiments could be reduced.

An overall discussion of the experimental results is presented in **Chapter VI**, as well as future research perspectives related to the improvement of the aerogel scaffolds and the development of 3D *in vitro* models for bone regeneration. Also, the main conclusions of the research are presented.

Finally, supplementary material is presented in **Chapter VII**, that includes a table with additional information, as well as the article published by Ruphuy *et al.* (2018) that was a starting point for the present research, and to which this thesis' author also contributed [19].

I. References

[1] International Organization for Standardization. ISO 22442-1:2015(E). Medical devices utilizing animal tissues and their derivatives — Part 1: Application of risk management. Switzerland. 2015.

[2] Amirazad, H.; Dadashpour, M.; Zarghami, N. Application of decellularized bone matrix as a bioscaffold in bone tissue engineering. J Biol Eng. 2022, 16, 1-18. doi: 10.1186/s13036-021-00282-5

[3] Bellucci, D.; Sola, A.; Gazzarri, M.; Chiellini, F.; Cannillo, V. A new hydroxyapatite-based biocomposite for bone replacement. Mater Sci Eng C Mater Biol Appl. 2013, 33, 1091-1101. doi: 10.1016/j.msec.2012.11.038

[4] Cao, L.; Su, H.; Si, M.; Xu, J.; Chang, X.; Lv, J.; Zhai, Y. Tissue engineering in stomatology: a review of potential approaches for oral disease treatments. Front Bioeng Biotechnol. 2021, 9, 662418. doi: 10.3389/fbioe.2021.662418

[5] Lai, G.-J.; Shalumon, K.; Chen, J.-P. Response of human mesenchymal stem cells to intrafibrillar nanohydroxyapatite content and extrafibrillar nanohydroxyapatite in biomimetic chitosan/silk fibroin/nanohydroxyapatite nanofibrous membrane scaffolds. Int J Nanomedicine. 2015, 10, 567. doi: 10.2147/IJN.S73780

[6] Anastasio, A. T.; Paniagua, A.; Diamond, C.; Ferlauto, H. R.; Fernandez-Moure, J. S. Nanomaterial nitric oxide delivery in traumatic orthopedic regenerative medicine. Front Bioeng Biotechnol. 2021, 8, 592008. doi: 10.3389/fbioe.2020.592008

[7] García-González, C. A.; Budtova, T.; Durães, L.; Erkey, C.; Del Gaudio, P.; Gurikov, P.; Koebel, M.; Liebner, F.; Neagu, M.; Smirnova, I. An opinion paper on aerogels for biomedical and environmental applications. Molecules. 2019, 24, 1815. doi: 10.3390/molecules24091815

[8] Gill, S.; Prakash, M.; Forghany, M.; Vaderhobli, R. M. An ethical perspective to using bone grafts in dentistry. J Am Dent Assoc. 2022, 153, 88-91. doi: 10.1016/j.adaj.2021.09.011

[9] Iglesias-Mejuto, A.; García-González, C. A. 3D-printed alginate-hydroxyapatite aerogel scaffolds for bone tissue engineering. Mater Sci Eng C Mater Biol Appl. 2021, 131, 112525. doi: 10.1016/j.msec.2021.112525

[10] Weng, L.; Boda, S. K.; Wang, H.; Teusink, M. J.; Shuler, F. D.; Xie, J. Novel 3D hybrid nanofiber aerogels coupled with BMP-2 peptides for cranial bone regeneration. Adv Healthc Mater. 2018, 7, 1701415. doi: 10.1002/adhm.201701415

[11] Zhao, R.; Yang, R.; Cooper, P. R.; Khurshid, Z.; Shavandi, A.; Ratnayake, J. Bone grafts and substitutes in dentistry: A review of current trends and developments. Molecules. 2021, 26, 3007. doi: 10.3390/molecules26103007

[12] Lauritano, D.; Limongelli, L.; Moreo, G.; Favia, G.; Carinci, F. Nanomaterials for periodontal tissue engineering: chitosan-based scaffolds. A systematic review. Nanomaterials. 2020, 10, 605. doi: 10.3390/nano10040605

[13] Papapanou, P. N.; Sanz, M.; Buduneli, N.; Dietrich, T.; Feres, M.; Fine, D. H.; Flemmig, T. F.; Garcia, R.; Giannobile, W. V.; Graziani, F.; Greenwell, H.; Herrera, D.; Kao, R. T.; Kebschull, M.; Kinane, D. F.; Kirkwood, K. L.; Kocher, T.; Kornman, K. S.; Kumar, P. S.; Loos, B. G.; Machtei, E.; Meng, H.; Mombelli, A.; Needleman, I.; Offenbacher, S.; Seymour, G. J.; Teles, R.; Tonetti, M. S. Periodontitis: Consensus report of workgroup 2 of the 2017 World Workshop on the classification of eriodontal and peri-implant diseases and conditions. J Clin Periodontol. 2018, 45, S162-S170. doi: 10.1111/jcpe.12946

[14] Pieles, O.; Höring, M.; Adel, S.; Reichert, T. E.; Liebisch, G.; Morsczeck, C. Energy metabolism and Lipidome are highly regulated during osteogenic differentiation of dental follicle cells. Stem Cells Int. 2022, 2022, 3674931. doi: 10.1155/2022/3674931

[15] Chapple, I. L.; Mealey, B. L.; Van Dyke, T. E.; Bartold, P. M.; Dommisch, H.; Eickholz, P.; Geisinger, M. L.; Genco, R. J.; Glogauer, M.; Goldstein, M.; Griffin, T. J.; Holmstrup, P.; Johnson, G. K.; Kapila, Y.; Lang, N. P.; Meyle, J.; Murakami, S.; Plemons, J.; Romito, G. A.; Shapira, L.; Tatakis, D. N.; Teughels, W.; Trombelli, L.; Walter, C.; Wimmer, G.; Xenoudi, P.; Yoshie, H. Periodontal health and gingival diseases and conditions on an intact and a reduced periodontium: Consensus report of workgroup 1 of the 2017 World Workshop on the Classification of Periodontal and Peri-Implant Diseases and Conditions. J Clin Periodontol. 2018, 45, S68-S77. doi: 10.1111/jcpe.12940

[16] Golafshan, N.; Castilho, M.; Daghrery, A.; Alehosseini, M.; van de Kemp, T.; Krikonis, K.; de Ruijter, M.; Dal-Fabbro, R.; Dolatshahi-Pirouz, A.; Bhaduri, S. B.; Bottino, M. C.; Malda, J. Composite Graded Melt Electrowritten Scaffolds for Regeneration of the Periodontal Ligament-to-Bone Interface. ACS Appl Mater Interfaces. 2023, 15, 12735-12749. doi: 10.1021/acsami.2c21256

[17] Zhang, L.; Dong, Y.; Liu, Y.; Liu, X.; Wang, Z.; Wan, J.; Yu, X.; Wang, S. Multifunctional hydrogel/platelet-rich fibrin/nanofibers scaffolds with cell barrier and osteogenesis for guided tissue regeneration/guided bone regeneration applications. Int J Biol Macromol. 2023, 253, 126960. doi: 10.1016/j.ijbiomac.2023.126960

[18] Zhang, L.; Dong, Y.; Xue, Y.; Shi, J.; Zhang, X.; Liu, Y.; Midgley, A. C.; Wang, S. Multifunctional triple-layered composite scaffolds combining platelet-rich fibrin promote bone regeneration. ACS Biomater Sci Eng. 2019, 5, 6691-6702. doi: 10.1021/acsbiomaterials.9b01022

[19] Ruphuy, G.; Souto-Lopes, M.; Paiva, D.; Costa, P.; Rodrigues, A.; Monteiro, F.; Salgado, C.; Fernandes, M.; Lopes, J.; Dias, M. Supercritical CO_2 assisted process for the production of high-purity and sterile nano-hydroxyapatite/chitosan hybrid scaffolds. J Biomed Mater Res B Appl Biomater. 2018, 106, 965-975. doi: 10.1002/jbm.b.33903

[20] Souto-Lopes, M.; Fernandes, M. H.; Monteiro, F. J.; Salgado, C. L. Bioengineering Composite Aerogel-Based Scaffolds That Influence Porous Microstructure, Mechanical Properties and *In Vivo* Regeneration for Bone Tissue Application. Materials. 2023, 16, 4483. doi: 10.3390/ma16124483.

[21] Souto-Lopes, M.; Grenho, L.; Manrique, Y.; Dias, M. M.; Fernandes, M. H.; Monteiro, F. J.; Salgado, C. L. Full physicochemical and biocompatibility characterization of a supercritical CO_2 sterilized nano-hydroxyapatite/chitosan biodegradable scaffold for periodontal bone regeneration. Biomater Adv. 2023, 146, 213280. doi: 10.1016/j.bioadv.2023.213280

CHAPTER II

State of the Art

A. PERIODONTAL AND PERI-IMPLANT ANATOMY, PATHOLOGY AND TREATMENT

A. 1. The periodontal and peri-implant apparatus

The periodontium is an organ also called the “attachment apparatus”, which main function is to support and attach the teeth to the jaws bone, as well as to maintain the integrity of the masticatory mucosa [1] (Figure 1). It is comprised of four specialized tissues: the gingiva, the periodontal ligament (PDL), the root cementum and the alveolar bone [1-4].

At an embryonic phase, the tissues from the periodontal attachment derive from the ectomesenchymal cells in the first branchial arch of the neural tube that form the dental lamina [1, 5]. Throughout the tooth development, these ectomesenchymal cells differentiate into the dental papilla, that will form the dentin and the pulp, [1, 2] and the dental follicle (DF), from which the surrounding supporting tissues derive [1-3, 5]. The ectomesenchymal cells from the DF, which interact with the Hertwig’s epithelial root sheath, give rise to the cementum [1, 2, 5, 6]. Simultaneously, neighboring DF ectomesenchymal cells differentiate into either periodontal fibroblasts, that secrete the collagenous periodontal fibers, and osteoblasts, which generate the alveolar bone proper to attach the periodontal fibers [1-3, 5, 6].

The most external tissue of the periodontium is the gingiva (Figure 1a and b), which is continuous with the oral masticatory mucosa, covering the alveolar process of the jaws [1], and its main function is the protection of the underlying structures of the periodontal apparatus. Histologically, the gingiva is composed of an oral stratified orto/parakeratinized squamous epithelium (Figure 1a) and an underlying dense conjunctive tissue [5] (lamina propria) (Figure 1b) [1].

Underneath the gingiva, the teeth are connected to the alveolar bone by the PDL (Figure 1c), which is a soft connective tissue that occupies the narrow space (0.2 – 0.4 mm) between the root cementum (Figure 1d) and the lamina dura of the alveolar wall (Figure 1e), connecting them through collagen fibers (Sharpey’s fibers) (black lines in Figure 1) [1, 3, 5]. Moreover, it is sensitive to mechanical stimuli [7], distributing the masticatory forces to be resorbed throughout the alveolar bone and enabling teeth mobility [1, 8]. The PDL is highly vascularized, innervated [2, 5] and has a varied population of cells: mostly fibroblasts, but also osteoblasts, cementoblasts, osteoclasts, epithelial cell rests of Mallassez [1, 2] and inflammatory cells [5]. There is more recent evidence that it also contains mesenchymal stem cells (MSCs) (e.g. dental follicular tissue) that can

migrate, proliferate and differentiate into osteoblastic, cementum-forming and fibroblastic cells, contributing to the PDL regenerative capacity [6].

The connection between the PDL and the teeth occurs through the cementum (Figure 1d), which is a thin mineralized tissue that covers the external surface of the teeth roots [1]. The cementum shares some similar features with bone [3], despite it is neither vascularized nor innervated and it does not undergo remodeling [1]. It has an extracellular matrix (ECM) composed of an organic phase of mostly type I collagen [1], but also proteoglycans and glycoproteins [5], and an inorganic phase of hydroxyapatite (HAp) (65% of total weight) [1].

The PDL connects teeth to the jaws by the alveolar process (Figure 1f), which besides supporting teeth in its sockets (Figure 1g), also distributes forces resulting from the masticatory and occlusal contacts into the maxillary/mandibular basal bone [1]. The buccal, palatal/lingual (Figure 1h) and socket walls (alveolar bone proper or bundle bone in Figure 1e) of the alveolar process are made of cortical bone (lamina dura) and its central part is trabecular bone (Figure 1i), which is highly vascularized [1, 5]. The bundle bone, to which large Sharpey's fibers are inserted and connect with the principal fibers of the PDL, is characterized by a high turnover rate [1].

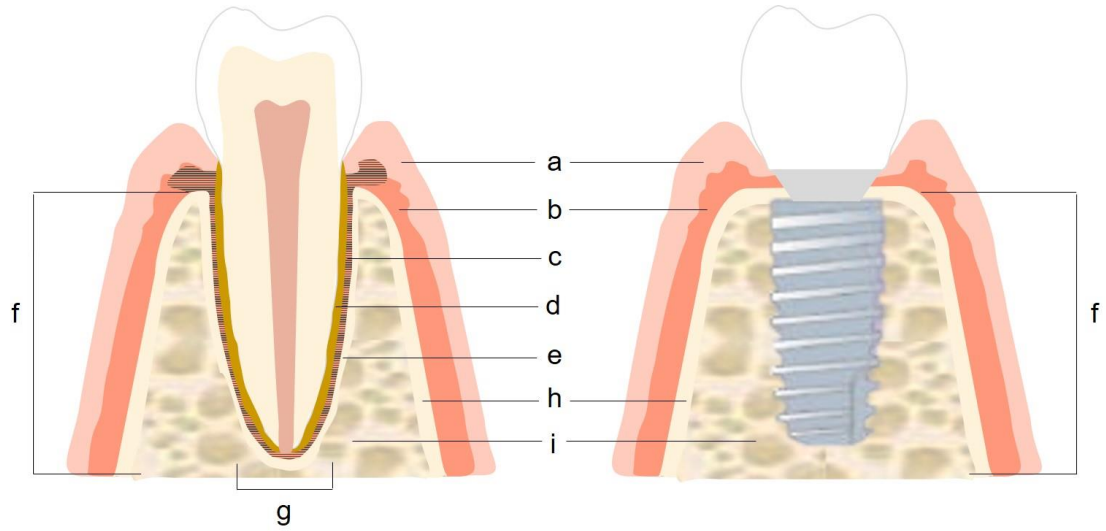

Figure 1. The anatomic differences between the periodontal (left image) and the peri-implant (right image) attachment apparatus. a) gingiva's squamous epithelium; b) gingiva's dense conjunctive tissue; c) periodontal ligament (black lines represent the Sharpey's fibers); d) cementum; e) alveolar wall/bundle bone; f) alveolar process; g) tooth socket; h) cortical bone of the buccal and palatal/lingual walls of the alveolar process; i) trabecular bone of the alveolar process. (adapted from [9])

A major difference between the supporting apparatus of a dental implant and a tooth is the lack of cementum and PDL in the case of implants [10], as illustrated in Figure 1. The mucosa around implants is similar to the gingiva around teeth, being a keratinized epithelium (masticatory mucosa) [1, 11] (Figure 1a and b) or even non-keratinized (lining mucosa) [10]. Since there is no PDL, it implies that most of the intrabony part of the implant is in direct contact with the trabecular bone (Figure 1i) [10]. "Osteointegration" (a term originally coined by Brånemark *et al.* in 1969) or "functional ankylosis" is the process by which "new bone is laid down directly upon the implant

surface, provided that the rules for atraumatic implant placement are followed and the implant exhibits primary stability" [1].

A. 2. Bone as a dynamic tissue

Bone's particular features make it a dynamic tissue that presents several important mechanic and metabolic functions in the organism, including resistance to external load, locomotion, protection of sensitive organs, hematopoiesis and contribution to homeostasis through the regulation (storage and releasing) of mineral ions (especially Ca^{2+}) and cells [1, 12]. Therefore, bone is able to adapt to the functional demands, which can be exerted by biochemical, hormonal, cellular and biomechanical factors [1, 13, 14].

Macroscopically, bone is composed of osseous tissue, periosteum, endosteum and bone marrow [1, 5] (Figure 2). Two types of bone structures can be distinguished according to their density: the external surface is cortical bone (compact bone), which is very dense and provides strength (porosity 5 – 15 %); the inner central cavity includes the trabecular bone (cancellous bone) [5, 12-15] comprised of an open interconnected porous network of ramified trabeculae (porosity 40 – 90 %) (Figure 2a), which due to their anisotropy contribute for redirecting stresses into the cortical bone [12-14]. The cancellous architecture is characterized by the number of trabeculae (Tb.N), their thickness (Tb.Th) and their separation (Tb.Sp), which may vary according to the location, direction and amount of load, age and pathology [12]. Histologically, cortical bone is composed of thin circumferential concentric lamellar systems (Haversian systems or osteons) with a central vascular channel (Haversian channel) that provides bone vascularization [5, 12, 14], with an anisotropic distribution as well [13] (Figure 2a) (a more detailed description is also presented on Section 1.1 and Figure 1 in Chapter III).

The outer surface of bone is covered by a fibrous connective tissue, the periosteum, (Figure 2a) except on the synovial articulating areas [1], tendon and muscle insertions [5]. The periosteum is connected to the cortical osseous tissue through Sharpey's fibers [1, 5]. Its outer layer is more fibrous, dense and vascularized with many fibroblasts and nociceptive receptors, while its inner osteogenic layer is loosely arranged and contains osteoprogenitor cells [1, 5, 12].

The trabecular bone inside the inner central cavity is lined by the endosteum [1, 5] (Figure 2a), which is a thin connective tissue with osteoprogenitor cells and osteoblasts [5, 12]. Moreover, this central cavity also houses the bone marrow stroma comprised of hematopoietic cells, stromal cells, adipocytes and vascular structures (Figure 2b) [1].

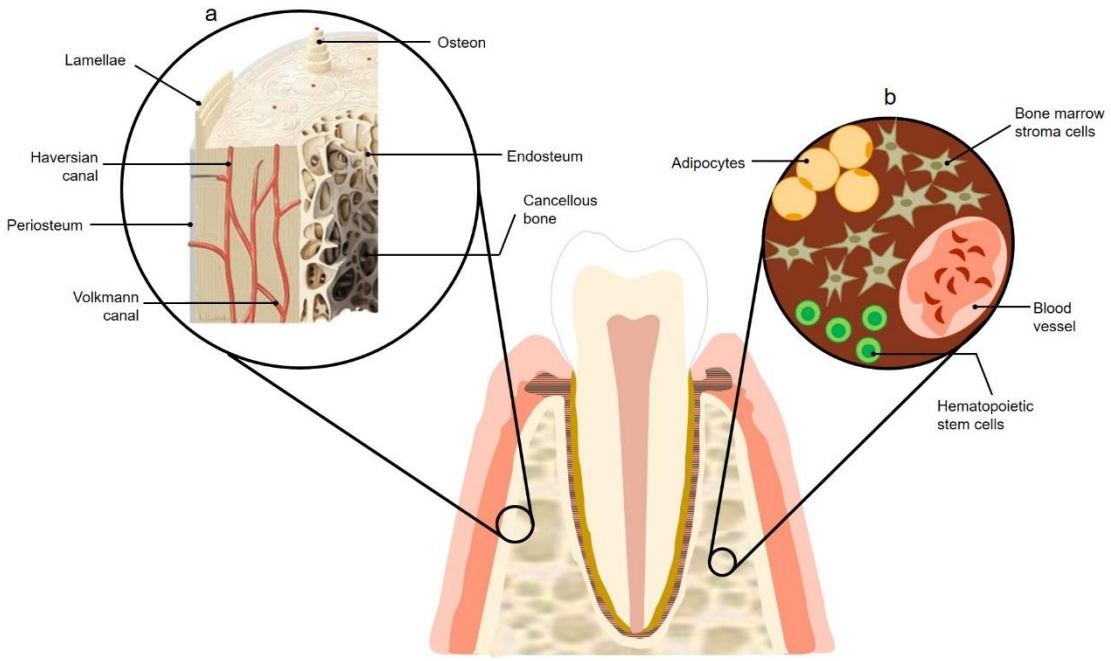

Figure 2. Macro and microscopic structure of bone tissue. a) organization of cortical and cancellous bone (adapted from [16] licensed under a Creative Commons Attribution 4.0 (CC BY 4.0) International License (https://creativecommons.org/licenses/by/4.0/)); b) bone marrow tissue cells (adapted from [1]).

The osseous tissue is a specialized connective tissue [5] with an ECM composed of organic and inorganic elements [17]. The bone ECM's organic phase (30 – 35 % wt. of bone) is 90 % of polymeric nature (collagen) [5, 18]; it has 10 % of other non-collagenous proteins (NCPs), carbohydrates and lipids [13, 19]; as well as water (9 % wt. of bone) [12, 20]. This polymeric phase is mostly type I collagen nanofibers [12, 21] (and also type III) [17] aligned in the direction of stress forces suffered by bone [12, 19]. Collagen and fibronectin possess peptides such as the RGD sequence (arginine-glycine-aspartic acid tripeptide), which connect to specific cell membrane receptors (some integrins subtypes), promoting cell binding to the ECM [22-25]. Despite only representing 2 % wt. of bone, NCPs are essential regulatory proteins for signaling and attachment of bone cells during ECM production and maintenance, playing vital roles in bone embryogenesis and repair [12].

About 69% wt. of the osseous tissue resides on a calcium phosphate ceramic, nano-hydroxyapatite (nHAp) ($Ca_{10}(PO_4)_6(OH)_2$) crystals [13, 15, 20, 26], which measure about 40 – 50 (length) x 25 (width) x 2 – 5 (thickness) nm [5, 12, 21, 27]. Mineralization initiates with the deposition of amorphous calcium phosphate, as well as calcium carbonate, and with maturation the mineral crystals grow and become oriented parallel to each other, along the collagen fibrils and the longitudinal axis of bone [12]. However, most HAp found in natural bone is non-stoichiometric [15], meaning that it has a variable chemical composition, which results in a Ca/P ratio different from that of pure $Ca_{10}(PO_4)_6(OH)_2$ (1.67) [23, 28-30]. With bone maturation, some of the Ca^{2+} and PO_4^{3-} ions in the apatite molecule might be substituted by trace molecules/elements such as carbonates, citrates, Na^+, Mg^{2+}, Cl^-, F^-, K^+, Sr^{2+}, Pb^{2+}, Zn^{2+}, Cu^{2+} and

Fe^{2+} [5, 12, 19, 23, 28, 31, 32]. Consequently, it changes natural bone HAp crystallinity and specific surface area, and thus its biological properties [28, 29].

The dispersed ceramic phase is the main responsible for the toughness and strength of bone (at moderate mechanical forces) [5, 19]. However, if bone was only made of the calcium phosphate ceramic it would be extremely brittle to higher tension and shear stress forces because of its lack of elasticity [5, 19]. Therefore, the polymeric ECM provides viscoelasticity, granting superior mechanical properties [19, 20]. On the other hand, when bone is decalcified, it becomes viscoelastic, with low stiffness to compression [5, 19]. Moreover, the cortical bone biomechanical response to load is dependent on the direction of the force, showing better performances towards longitudinal than transversal forces [20, 33]. In addition to the hierarchical architecture of bone, its mechanical properties are dependent as well on the type of bone anatomy and between distinct regions of the same bone, on an individual's age, physical activity, existence of chronic diseases and nutritional state [13, 34], systemic levels of hormones, growth factors and stress [35].

Besides its ECM, bone presents a variety of cell populations with specific characteristics and functions, which interact with each other and contribute to bone function and maintenance [1] (Figure 3). Osteoblasts are cuboid to columnar cells located in the inner and outer bone tissue surface, presenting a large rough endoplasmic reticulum and Golgi apparatus, which allows them to secrete the organic components of the bone ECM [5, 13]. The osteoblastic differentiation pathway is divided in three stages (cell proliferation, maturation and mineralization of the ECM), each characterized by up and downregulation of specific genes [17, 36, 37]. The first stage begins with the secretion of the ECM type I collagen [37], forming the immature organic matrix (osteoid) [1, 38]. At the second stage, the osteoblasts proliferate less and highly express bone alkaline phosphatase membrane-bound enzyme (ALP) [18, 37-40] that hydrolyses the organic phosphate esters and increases the phosphate ions local concentration [17, 41]. The mineralization process starts with the deposition of calcium and phosphate ions [1, 17] (amorphous calcium phosphate) [23], which will serve as templates for the subsequent crystal nucleation [15]. In the third stage, the mature osteoblasts produce osteocalcin (OCN) [18, 37, 40] which regulates the mineralization [36, 42]; bone sialoprotein (BSP), which is a crystal nucleator; osteopontin (OPN), which contributes to the formation of apatite crystals with the correct structure [36, 38, 41]. The nHAp crystals nucleated in circular structures [1] are orderly deposited (aligned with their *c*-axis) and propagate onto the polymeric collagen nanofibers [1, 21, 43, 44], in a maturation process that may take several months [1].

Since osteoblasts do not migrate, they become "trapped" inside lacunae in the newly formed and mineralized ECM and differentiate into stellate-shaped osteocytes [1, 5, 13, 15, 23], comprising 85 % – 90 % of all adult bone cells [14]. The lacunae are connected through canaliculi, allowing the circulation of fluids, nutrients and wastes by the blood vessels and enabling the osteocytes to communicate through cytoplasmic projections (dendrites) [5, 14, 15]. Moreover, the osteocyte network is sensitive to the mechanical loads to which bone is subjected (fluid shear stress) [14], thus responding with paracrine biochemical mediators (mechanotransduction) that regulate the metabolic functions like bone remodeling and blood calcium homeostasis [5, 14, 15,

23]. Moreover, the osteoblasts may also become bone lining cells, which are located in the surface of bone and are incapable of dividing [1, 13], though they could be reactivated for synthetic activity if stimulated [5].

Another important bone cell type is the specialized multinucleated osteoclast, which is derived from the monocyte/macrophage hematopoietic lineage in the bone marrow and presents receptors to a variety of signaling molecules like RANK, osteoprotegerin (OPG) and calcitonin [5, 13, 23]. The osteoclasts are responsible for the bone resorption, which is a process coupled with the bone formation performed by the osteoblasts, resulting in bone remodeling [13, 14, 23], as illustrated in Figure 3.

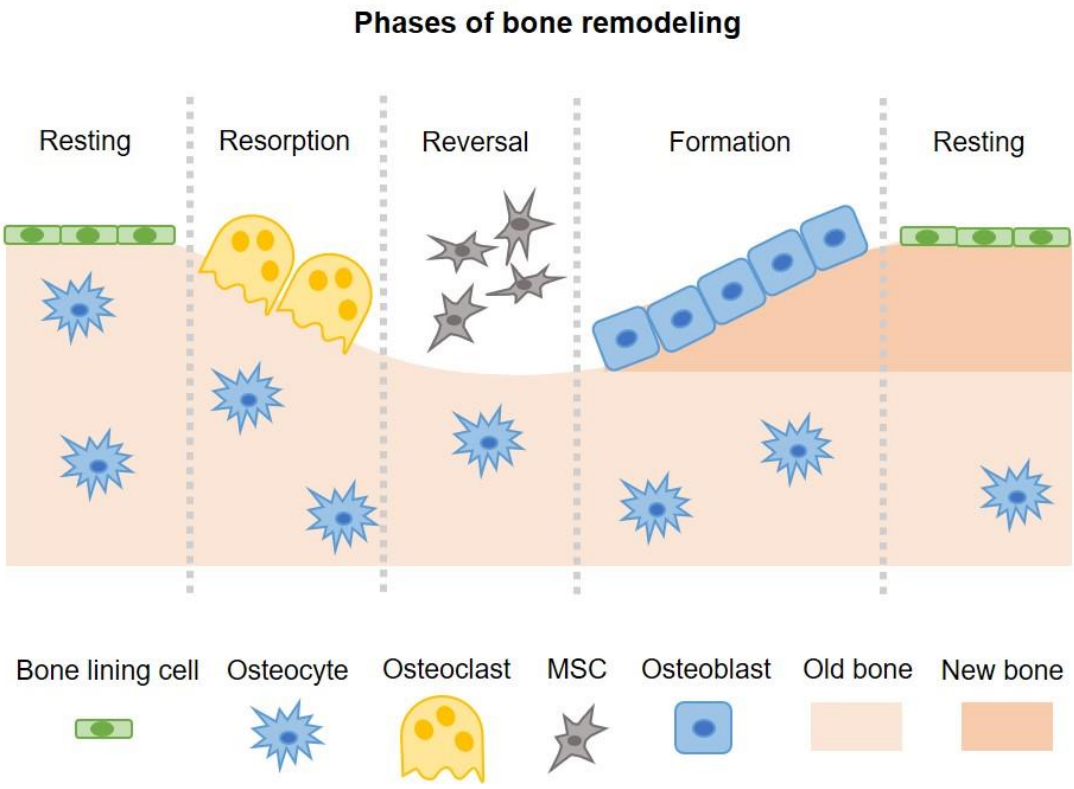

Figure 3. Bone cell types involved in bone remodeling steps (adapted from [13]) (MSC, mesenchymal stem cell).

During the resorption phase, the active osteoclast attaches to the bone surface and undergoes a cytoskeletal and membrane polarization. The osteoclasts produce hydrochloric acid that decreases the pH at the Howship lacuna, which is a sealed microcompartment between the ruffled border and the resorbing matrix surface [1, 5] and an ideal microenvironment for the dissolution of the bone mineral phase [5, 23]. Consequently, the proteinaceous component of the ECM becomes exposed and can be degraded by the proteolytic enzymes [1, 5].

Following the osteoclasts activity (takes approximately three to four weeks), the reversal phase is characterized by the migration of MSCs [1]. MSCs are stimulated by osteoinductive growth factors (GFs), such as bone morphogenetic proteins (BMPs), insulin-like growth factor

(IGF), platelet-derived growth factor (PDGF) and fibroblast growth factor (FGF) [1, 45], to differentiate into osteoprogenitor cells by the expression of the Indian hedgehog (Ihh) gene and Runt-related transcription factor 2 (RUNX2) [1]. The osteoprogenitor cells are located in the periosteum, endosteum and Havers channels [1, 5] and are able to migrate, proliferate and differentiate into osteoblasts to begin bone formation (takes about three to four months) [1].

This coordinated and proportioned process between the activity of osteoclasts and osteoblasts (basic multicellular unit (BMU)) is known as coupling [1]. Moreover, it has been described that osteoclasts are attracted to mechanically compromised bone sites (upon trauma, disease or disuse); thus, bone remodeling is essential to maintain skeletal integrity and quality [14, 15, 23].

A. 2.1. Bone repair and regeneration

The type of tissue healing response will depend on the nature of the lesion [1], and it can be either simple tissue repair, which “does not fully restore the architecture or function of the original part” or, ideally, tissue regeneration which is the “reproduction or reconstitution of a lost or injured part in a manner similar or identical to its original form” (definitions according to the American Academy of Periodontology’s Glossary of Periodontal Terms [46]).

In general, when bone tissue is damaged, e. g. a fracture or defect created by surgical removal of a tumor or cyst, there is rupture of blood vessels and bleeding, disruption of bone ECM and cell death [5]. In a normal response, a blood clot forms (24 hours) and the damaged cells release cytokines, which induce an inflammatory response that lasts for about two weeks [1].The clot fills the empty space and the fibrin network functions as a matrix for the cells migrating from the tissue surrounding the bone defect [1, 47]. The clot suffers fibrinolysis while the fibroblasts and endothelial cells migrate, forming the granulation tissue [5] (2 – 3 days) [1]. The cytokines attract inflammatory cells to the lesion site like neutrophils and macrophages, which phagocyte the injured tissue and cells, and osteoclasts that begin the resorption of the damaged bone [1]. The osteoclast activity stimulates the osteoprogenitor cells to quickly proliferate and differentiate [1, 5]. Moreover, macrophages express BMPs, which induce MSCs to differentiate into osteoblasts or chondrocytes [45, 48], as well as other osteoinductive factors like endothelial growth factor (EGF), vascular endothelial growth factor (VEGF), tumor necrosis factor alpha (TNF-α), transforming growth factor beta (TGF-β), PDGF and interleukins (ILs), [45, 49].

However, since the osteoprogenitor cells proliferate at a higher rate than the endothelial cells form new capillaries, the low oxygen concentration induces these cells to differentiate into chondroblasts, which produce a soft callous of hyaline cartilage [5] that functions as a scaffold [1] bridging the fracture site [48]. Conversely, the osteoprogenitor cells in the periphery of the lesion differentiate into osteoblasts, which produce bone ECM and induce the mineralization of the soft callus, becoming a hard callus of immature woven bone [1] (endochondral ossification) [5]. This

process is mediated by IL-6, OPG, VEGF, and BMPs and occurs at 6 to 12 weeks after the lesion [1].

For complete bone regeneration to occur, osteoblast/osteoclast coupling must lead to the remodeling of the immature woven bone into mature lamellar bone [48] through intramembranous ossification [5], in a process that may take three to four months after the reversal phase [1]. It has been shown that BMP-2 exerts a crucial influence on the process of intramembranous bone formation, and thus in bone regeneration [45, 50].

As stated before, bone is in a constant process of self-renewal to maintain its integrity, at an average turnover rate of 10% (trabecular bone shows a higher turnover rate than cortical bone) [1]. However, sometimes the size of the defect is so large that bone is not capable of regenerating it through simple remodeling (critical size defect) [1, 15] or it is necessary to achieve regeneration quicker than through normal biologic processes [1]. Moreover, systemic or local disease conditions (cancer, menopause, use of drugs, genetic conditions, nutritional deficiencies or infection) may impair the bone capacity of remodeling and self-regenerate [1].

A. 3. Periodontal and peri-implant diseases

The state of gingival/periodontal health corresponds clinically to “the absence of bleeding on probing, erythema and edema, patient symptoms” [51] (Figure 1 left). Even at a physiologic state, there is always a homeostatic level of host immune surveillance, comprised mostly of a neutrophilic infiltrate [51]. This is due to the fact that the oral cavity exhibits particular features that predispose to the formation of biofilms: it possesses hard non-shedding structures (teeth, implants and prosthetic devices) that open breaches in the mucosal epithelial surface and allow its colonization by bacteria in direct contact with the soft tissues [1].

Periodontal and peri-implant diseases are multifactorial (Figure 4) and include a variety of microbially-associated and host-mediated inflammatory conditions [52-55] that affect the health of periodontal and peri-implant tissues [56], and which if left untreated may lead to teeth (or dental implants) loss [3, 6, 9]. It is well established nowadays that the etiology of periodontal and peri-implant diseases is related to the presence of a dysbiotic microbiota (defined as an unfavorable alteration of the commensal microbiota), with a consequent disruption of the homeostatic balance with its susceptible host, leading to disease [1, 57].

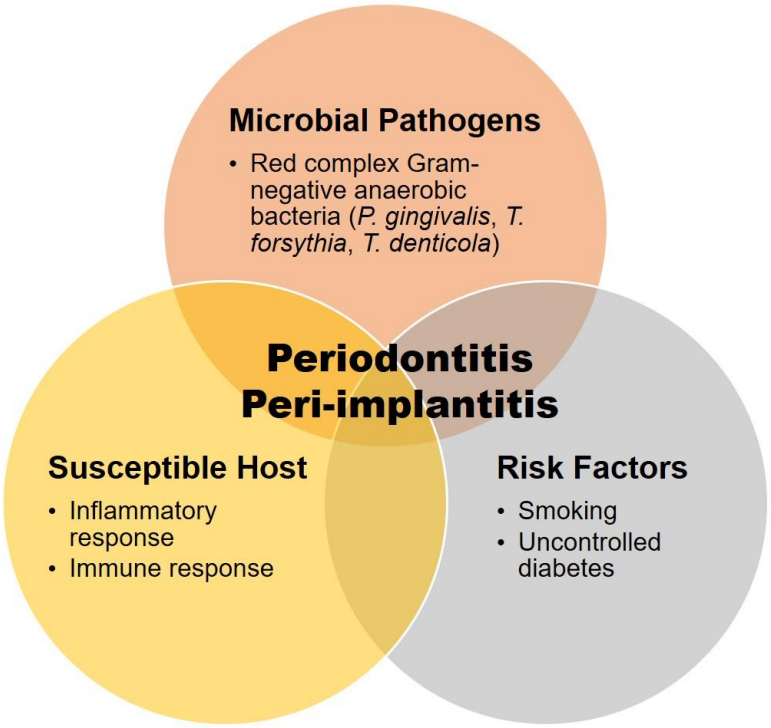

Figure 4. The multifactorial characteristics of periodontitis and peri-implantitis: it includes the interaction between the increased counts of periodontal pathogenic flora, the host susceptibility and environmental and systemic risk factors (adapted from [54]).

The classification system of periodontal diseases was reviewed in a 2017 consensus (2017 World Workshop on the Classification of Periodontal and Peri-Implant Diseases and Conditions) and further developed to include peri-implant conditions as well [56], as briefly presented in Table 1.

Table 1. 2017 Classification of periodontal and peri-implant diseases and conditions (adapted from [56])

Periodontal diseases and conditions	Periodontal health, gingival diseases and conditions
	Periodontitis
	Other conditions affecting the periodontium
Peri-implant diseases and conditions	Peri-implant health
	Peri-implant mucositis
	Peri-implantitis
	Peri-implant soft and hard tissue deficiencies

A. 3.1. Periodontal diseases

Most gingivitis cases are dental biofilm-induced, which causes a site-specific inflammation characterized by erythema, edema, bleeding and an increased flow of crevicular fluid [58] (Figure 5a). The inflammation is confined to the gingiva without extending to the periodontal attachment [51]. Once careful improvement of oral hygiene is implemented, it is totally reversible and can be solved without clinical attachment and bone loss [58].

In contrast with gingivitis, besides the signs of gingival inflammation and bleeding, all clinical forms of periodontitis present an irreversible loss of the connective tissue, periodontal ligament and alveolar bone resorption [1, 59] (Figure 5b). Periodontal bone loss is classified according to the morphology of the lesions, as presented in Table 1S (in the supplementary material of Chapter VII). Most periodontitis cases progress with episodic bursts, depending on the local site and on the patient, and it has been shown an alternation between active periods of periodontitis progression with periods of disease inactivity [1, 54]. Although epidemiological studies have shown that only some sites with gingivitis progress to periodontitis, prevention and treatment of gingivitis are still crucial to avoid periodontitis onset [58]. Therefore, it is important to implement an anti-biofilm treatment, which includes full-mouth debridement with mechanical removal of supra and subgingival plaque and calculus [54, 60-62], that might be complemented by measures such as full-mouth disinfection with antiseptics, systemic and local antibiotics, host modulation therapy, laser therapy and chemical agents for local application in root surfaces [11, 54, 60, 61, 63]. Moreover, surgical approaches may also be performed, however many times they imply negative outcomes, such as dentinal hypersensitivity of the exposed teeth roots, transient increase in tooth mobility, loss of interproximal papilla, with consequent food impaction and impairment of esthetics and, sometimes, phonetics [11, 54, 63].

It has been demonstrated that it is essential to control the most critical risk factors for the progression of periodontitis, which are smoking and uncontrolled diabetes mellitus [53, 54, 64] (Figure 4). Moreover, genetics seems to make some individuals more prone to develop a dysbiotic oral microbiota and/or to exhibit a hyper-inflammatory response [52, 55]. Consequently, they show more severe and progressive forms of periodontitis, and a worse response to prevention and treatment, as well as having a higher systemic impact [52, 55]. Additionally, other systemic conditions may contribute to the individual susceptibility to the onset and progression of periodontitis: immunologic, metabolic and endocrine disorders; diseases that affect the oral mucosa, gingival and connective tissues; acquired immunodeficiencies (human immunodeficiency virus (HIV) infection); inflammatory diseases; neoplasms and metastasis; some prescribed medications; abusing illegal drugs use; psychosocial factors like stress, depression and connected to the socio-economic status [1, 53, 64, 65]. On the other hand, the connection between periodontitis and the emergence or aggravation of conditions in other organ systems has been demonstrated, like in cardiovascular diseases, diabetes [53, 64, 66], chronic obstructive pulmonary disease, chronic kidney disease [66] and adverse pregnancy outcomes [53].

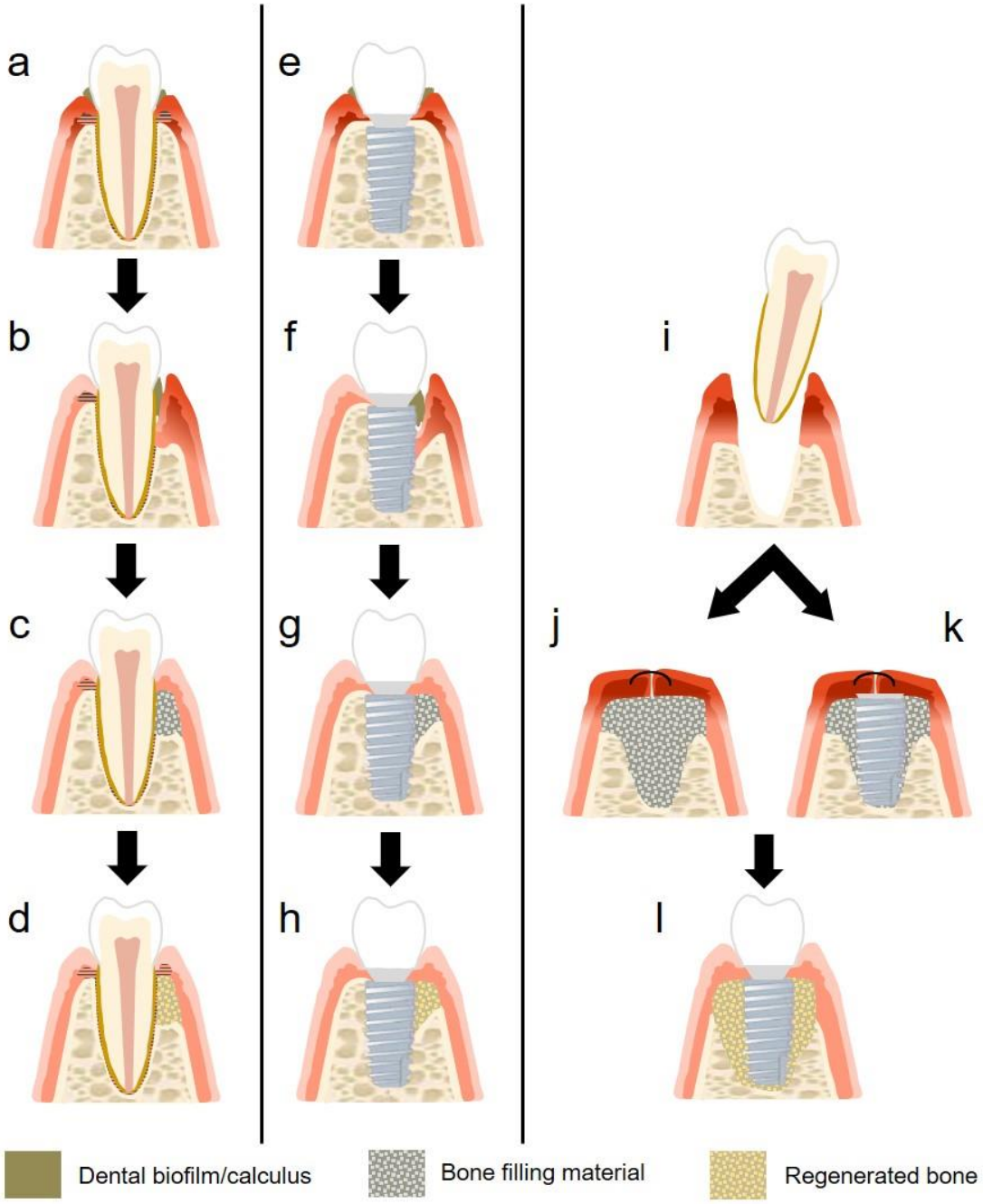

Figure 5. Representation of the evolution of periodontal and peri-implant diseases and their regenerative treatment: (a) gingivitis; (b) periodontitis; c) periodontal bone defect grafting with bone-filling material; d) ideal periodontal regeneration outcome; e) peri-implant mucositis; f) peri-implantitis; g) peri-implant bone defect grafting with bone-filling material; h) ideal peri-implant regeneration outcome; i) alveolar ridge defect upon tooth extraction; j) alveolar ridge reconstruction in a two-stage or k) one-stage bone augmentation approach (with simultaneous implant placement); l) alveolar defect regeneration with ideal implant placement (adapted from [9]).

Periodontitis is one of the most prevalent non-communicable public health chronic diseases worldwide [67]. The epidemiologic findings (from 2011 to 2020) of a recent meta-analysis estimated that the pooled prevalence of periodontitis in general was currently nearly

62%, in which moderate to severe forms of the disease represented 53.2%, while severe cases affected 23.6% of the population covered by the meta-analysis [67].

A. 3.2. Peri-implant diseases

Peri-implant health, similarly to periodontal health, is also defined by the “absence of erythema, bleeding on probing, swelling, and suppuration” [10] (Figure 1 right). Implant success was consensually defined in 2008 as “no pain or tenderness upon function, absence of mobility, < 2 mm radiographic bone loss from the initial surgery and no presence of exudate” [63].

Peri-implant mucositis is in implants the equivalent disease to biofilm-induced gingivitis in teeth, in which there is bleeding at probing, and there may be as well other clinical signs of inflammation as erythema, edema and/or suppuration [1, 10, 11, 63] (Figure 5e). Similarly to biofilm-induced gingivitis, peri-implant mucositis inflammatory signs resolve in 3 weeks upon a correct biofilm control, but the resolution of this condition may be negatively influenced by conditions like smoking, uncontrolled diabetes (Figure 4) and irradiation therapy at the implant zone [1, 10, 64].

Besides the clinical signs of inflammation, in peri-implantitis there is a progressive destruction of the supporting bone around the implant [1, 10, 11, 63] (Figure 5f). Suppuration at probing is a frequent finding, but mobility of the implant is only detected at the final stages of peri-implantitis, indicating the complete loss of osseointegration [1, 63]. There is evidence that peri-implant mucositis precedes peri-implantitis if no biofilm control measures and regular maintenance care are timely implemented [1, 10, 11]. Moreover, it has been demonstrated that patients with a previous history of severe periodontitis (and associated modifying factors like uncontrolled diabetes and smoking) are at higher risk of developing peri-implantitis [1, 10, 11, 54, 63, 64]. Additionally, studies suggest that bone loss progression in peri-implantitis occurs at an unpredictable higher rate than in periodontitis, because peri-implant connective tissues are less organized and respond poorly to progressive biofilm-associated lesions [1, 10, 11, 63, 68]. Still, if an anti-biofilm treatment is implemented with implant surface mechanical and/or chemical decontamination, it is possible to diminish the soft tissue inflammation and arrest bone destruction [10, 11].

It has been reported that the 5- and 10-year success rate of dental implants is 90 % worldwide [54, 68]. In terms of the prevalence of peri-implant diseases, it can be stated that peri-implant mucositis is a quite common finding, with a prevalence ranging from 40 to 48 % [1, 63] of patients and in 16 to 50 % [1, 63] of implant sites. Some studies indicate that peri-implantitis is a common disease in dental implant rehabilitated patients, ranging between 30 and 55 % [1, 63], while others indicate a mean prevalence of 12.8 % of implant sites and 18.5 % of patients [63].

Moreover, it is important to acknowledge that, very often, there are hard and soft tissue deficiencies in the alveolar ridge (Figure 5i) that may compromise the placement of dental implants in the most appropriate site from the prosthetic point of view [69]. These defects may

exhibit a wide range of sizes and according to Berglundh *et al.* (2018) they may be due to factors such as bone loss caused by periodontitis, endodontic infections, root fractures, thin cortical bone envelopes, mispositioning of teeth in relation to the arch, traumatic teeth extractions, injuries, pneumatization of the maxillary sinus and reduction of the amount of bone formation due to drug intake, systemic diseases, agenesis or prolonged absence of teeth and the mechanical pressure from removable prosthesis [10]. Therefore, in order to achieve a correct prosthetic rehabilitation, it is frequently necessary to regain the lost volume of bone and/or gingiva before (Figure 5j) or during the implants' installation (Figure 5k) through bone augmentation procedures [69].

A. 4. Periodontal and peri-implant regenerative treatments

Periodontal regeneration has become a main goal of periodontal therapy, ideally with full formation of new gingiva, bone, cementum and PDL with perpendicularly oriented collagen fibers [60, 62, 70-73] (Figure 5d). Additionally, regenerative approaches of peri-implantitis treatments (Figure 5h) aim to reduce probing depth (the distance between the gingival margin of a tooth/implant and the most apical location of the bone crest), increase bone levels and implant attachment (re-osseointegration), while minimizing soft tissues recession and improving esthetic outcomes [1, 11].

Periodontal and peri-implant regeneration may be accomplished by a single or a combination of procedures, including soft tissue grafts, bone replacement grafts (Figure 5c and g), root biomodifications, guided tissue/bone regeneration (GTR/GBR) and delivery of GFs (e.g. enamel matrix-derived (EMD) proteins and others), [1, 3, 9, 11, 54], and, still under development, stem cell delivery or gene therapies [1, 3, 9, 60, 62, 74, 75]. However, the success of regenerative treatments is dependent on the morphology of the infrabony defect (Table 1S), i.e., better outcomes are achieved for three-walled than for two- and one-walled lesions, and if the defect angulation is less than 45º [11, 54, 63], since better blood supply and mechanical support can be provided [9, 69]. Nevertheless, the clinical outcomes of such therapeutic approaches in humans are still quite unpredictable [11], in part due to the great variety of hard/soft tissues and cell types which are present in the periodontal apparatus [7, 74], but also because the cells' microenvironment at periodontium maturity is different from the one that led to its initial formation [3]. The outcomes of regenerative treatments for bone augmentation in ridge deficiencies and around diseased implants are also highly dependent on the characteristics of the implant surface (more favorable with smoother surfaces) and on the degree of local decontamination [1], as well as the systemic conditions of the patient [69].

The aim of filling osseous defects with bone replacement grafts is to stimulate the regrowth of alveolar bone [1, 60, 70, 75], many times in conjunction with GBR procedures. Bone graft materials (Table 2) offer mechanical support if membranes are used, avoiding their collapse to the defect, stabilize the blood clot and act as a scaffold for bone ingrowth [3, 60, 70, 74]. Also, bone graft biomaterials are useful to solve hard tissue deficiencies prior, during or after implant

surgery in more than 50% of the cases (Figure 5j and k) [69, 76-78]. However, there may be some negative outcomes when e.g. bone filling materials are placed in direct contact with the root cement, like teeth ankylosis [1]. Moreover, the crucial primary closure of soft tissue around the grafted area may compress the graft and compromise the space maintenance, especially in vertical augmentations [69].

Table 2. Types of bone graft materials according to their biological effect

Osteogenic	if it contains osteocompetent cells [1, 69, 75, 79]
Osteoconductive	if it functions as a three-dimensional scaffold that promotes the migration of osteoprogenitor cells through a porous structure for ingrowth of surrounding bone [1, 62, 69, 75, 79]
Osteoinductive	if it contains bone-inducing substances like growth regulatory molecules, which alter osteoblast gene expression, enhancing the bone healing process [1, 15, 60, 62, 69, 75, 79]. An osteoinductive material stimulates bone growth in ectopic (non-bone) sites [75, 80]

Bone graft materials may be classified as autogenous, allogenous, xenogenous or alloplastic (synthetic) [9, 62, 76, 81], or even a combination of two or more types of grafts (composite grafts) from different sources in order to achieve optimal results [69, 77]. Table 3 shows some examples of bone graft biomaterials currently commercialized in Portugal.

In the case of autografts, the donor tissue comes from the same individual who is receiving the graft (from either oral or extra-oral sites), comprising cortical and cancellous bone [1, 62, 76, 78]. Cancellous autograft is considered the “gold standard” bone graft material [42, 62, 69, 76, 78, 79, 81-83] since it presents the advantages of immune compatibility (no risk of rejection), a favorable composition and morphology (osteoconductive) [31, 83] and osteogenic potential [73] (bone GFs and viable cells) [69, 78, 81]. However, this treatment option has some disadvantages, since it is a more invasive procedure that implies a second (donor) surgical site (intra or extra-oral), increasing the patients’ morbidity (risk for pain and infection), and also the limitation of bone volume that can be collected from the donor site, and its unpredictable resorption rate [21, 31, 42, 62, 69, 76, 78, 79, 82-84]. Bone slurry collected during surgery can be used, though it might be contaminated by oral microorganisms [62, 69].

Alternatively, in order to avoid the second surgical site, allografts (grafts from cadaver donors) [1, 62] from commercial tissue banks have also been used, including human iliac cancellous bone and marrow (fresh frozen bone, FFB), freeze-dried bone allografts (FDBA) and demineralized freeze-dried bone allografts (DFDBA) [1, 4, 60, 73, 77]. Since it maintains its remaining proteins like BMPs, an allograft has osteoinductive properties (especially FFB) apart from being osteoconductive [62, 78]. Nevertheless, factors such as the age of the tissue donor and the variable content in GFs may influence the osteoinductive performance of some allografts, thus the efficacy of these grafts is controversial [60, 69, 81]. Despite allografts are often clinically

used on American patients, their use is more restricted inside the European Union [60, 78], since they raise several concerns on the risk of the transmission of diseases [21, 31, 78, 81-83] and adverse immune reactions, unpredictable resorption rates [60], as well as high cost [85] and short shelf-life [78]. Moreover, osteoinductive properties of the DFDBA may be affected by the sterilization method, being worse with gamma irradiation compared to ethylene oxide [69, 81]. The DFDBA matrix is an acid-treated allograft to remove the mineral mesh and provide a trabecular framework rich in BMPs and GFs, such as TGF-β and FGF, though its osteoinductive potential may be limited by its preparation methods and its mechanical properties are lower when compared to other grafts [78].

Xenografts (heterografts) are usually inorganic slowly absorbable bone scaffolds, which are used as volumetric fillers [47, 81]. Xenografts are retrieved from a donor of a different species [1, 62, 78] (bovine, equine, porcine), from which all cells and proteins were removed [47, 73], in order to minimize diseases transmission and undesirable immune reactions [78]. Since these graft materials are only osteoconductive [78], with a lack osteoinductivity, they must be implanted close to the bone defect margin, otherwise foreign body host response with fibrous encapsulation might occur [60]. Polymeric-based xenografts like collagen, chitosan and silk fibroin which are also derived from animals [78] will be further explored in section B2 in this chapter.

Alloplastic biomaterials are synthetic grafts which application is to full fill bone defects [1, 15, 69, 73], preferably promoting its guided regeneration (osteoconduction) [15, 69, 75]. Since alloplastic materials are produced from synthetic matrices, there is no risk of diseases transmission, the quantity of graft material is unlimited and there is no need of a donor surgical site [62, 81]. However, osteoinductive or osteogenic properties are absent and they lack of defined resorption rates [81] (if it is not resorbable, the material will remain in between the tissue ingrowth, limiting the space to bone tissue properly grow), so nowadays their clinical application is limited to smaller bone defects with surrounding tissue [69].

Table 3. List of some bone graft biomaterials for regenerative dentistry and maxillo-facial surgery commercialized in Portugal (source: Infarmed, 20-09-2023 and manufacturers' informative brochures)

Manufacturer/ Distributer	Commercial name	Type of bone graft	Source/ Composition	Clinical format
Augma ™ Biomaterials Ltd./ Biofix	Augma Bond Apatite	Alloplastic	Biphasic calcium sulphate	Bone graft cement
Botissdental GmbH	Cerabone®	Xenograft	Bovine pure bone mineral	Granules
	Cerabone® Plus	Xenograft	Bovine pure bone mineral with hyaluronic acid	Sticky granules
	Maxresorb®	Alloplastic	60 % hydroxyapatite (HAp) and 40 % beta-tricalcium phosphate (β-TCP) – Biphasic calcium phosphate (BCP)	Granules
Chiyewon Co., Ltd/ Nobel Biocare	Creos™ Xenoform	Xenograft	Bovine mineral cancellous bone	Granules
Chiyewon Co., Ltd/ GMI	Iceberg.Oss™	Xenograft	Bovine mineral cancellous bone (100 % HAp)	Granules, porous blocks
Curasan Ag/ Zimmer Dental	IngeniOs™	Alloplastic	Silicated β-TCP	Particles
Geistlich Pharma AG	Bio-Oss®	Xenograft	Bovine spongious bone	Granules, spongious bone blocks
	Bio-Oss® Collagen	Xenograft	90 % wt. bovine spongious bone and 10 % wt. porcine collagen fibers	Granules with fibers in a preformed block form
Institut Straumann AG	Straumann® BoneCeramic™	Alloplastic	60 % HAp and 40 % β-TCP (BCP)	Granules

Table 3. *cont.*				
Manufacturer/ Distributer	**Commercial name**	**Type of bone graft**	**Source/ Composition**	**Clinical format**
Noraker	ActivIoss® granules	Alloplastic	Bioactive glass 45S5	Granules
	ActivIoss® injectable putty	Alloplastic	Bioactive glass 45S5 and polyethylene glycol and glycerol (binder)	Injectable non-hardening putty
NovaBone Products, LLC/ Megagen	NovaBone® Dental Morsels	Alloplastic	Bioactive glass	Granules
	NovaBone® Dental Putty	Alloplastic	Calcium-phospho-silicate particulate and polyethylene glycol and glycerin (binder)	Injectable non-hardening putty
Tecnoss S.r.l.	OsteoBiol® Gel 40	Xenograft	60 % Cortico-cancellous porcine bone mix and 40 % collagen gel	Injectable gel
	OsteoBiol® Sp-Block	Xenograft	Collagenated cancellous equine bone	Rigid dried block
	OsteoBiol® Dual-Block	Xenograft	Collagenated cortico-cancellous porcine bone	Rigid dried block

B. BONE TISSUE ENGINEERING

B. 1. Properties of biomaterials for bone regeneration

Bone tissue engineering is a specific branch of tissue engineering which involves the integration of artificial porous and biodegradable 3D scaffolds, GFs and osteogenic cells to promote and accelerate bone regeneration [25, 32]. The development of scaffold biomaterials with adequate properties is essential to make full use of the body's innate regenerative capacity, which relies on the host's stem cells populations and GFs [86] and an adequate blood supply (vascularization) [74]. The scaffold itself may also function as a carrier of progenitor cells and GFs [74]. According to the European Society of Biomaterials (Second Consensus Conference on Definitions in Biomaterials, 1992), a biomaterial is a "material intended to interface with biological systems to evaluate, treat, augment or replace any tissue, organ or function of the body" [87]. Biomaterials are considered medical devices, which according to the International Organization for Standardization (ISO) are defined as: "any instrument, apparatus, implement, machine, appliance, implant, *in vitro* reagent or calibrator, software, material or other similar or related article, intended by the manufacturer to be used, alone or in combination, for human beings for one or more of the specific purpose(s) […]" [88]. Accordingly, a medical device may be as simple as a single material or it may be a complex apparatus made of different parts and materials [88].

With the fast development of a wide range of new technologies, equipment and devices for medical care, it has emerged the necessity of classifying the medical devices in order to guarantee their safe utilization. The European Regulation 2017/745 classifies medical devices according to the purpose of intended use and the potential risk they may pose to the human organism, considering several criteria [89]. Since the more invasive and/or longer duration of contact, the higher risk is implied in the device utilization [89], it is important to carry out appropriate testing on medical devices within a risk management process [88].

Biomaterials which are implanted in intimate and permanent contact with the organism are classified in classes IIb or III (European Regulation 2017/745) [89] and those which interact actively with tissues are class III devices [33]. Moreover, graft biomaterials can be classified according to their activity degree upon implantation in the organism, which is dependent on the tissue response towards the implant surface [79]:

- Bioinert – there is minimal interaction with the surrounding tissue, thus these biomaterials do not bond to tissue and might be encapsulated by fibrous tissue [26, 79].

- Bioactive – in a broader sense it is a biomaterial which upon chemical modifications of its surface, actively interacts with the hard and/or soft tissues nearby, eliciting a beneficial specific response from the host [26, 79, 80, 90]. Moreover, in a narrower sense, this concept also describes the ion-exchange of the biomaterial with body fluids that promotes a chemical strong bond to the bone interface through the formation of an apatite layer *in vitro* (in simulated body fluid (SBF)) and/or *in vivo*, contributing to its osteointegration [20, 33, 78-80, 90].
- Biodegradable/bioresorbable – upon implantation, the biomaterial starts to degrade at a variable rate, depending on its chemical features, and is gradually substituted by new tissue [26, 79].

The most common raw materials that have been used in synthetic bone graft biomaterials preparation include biopolymers (section B2 of Chapter II), bioceramics (section B3 of Chapter II), metals/metallic alloys [79, 91] and, more recently, combinations of these raw materials [3, 91].

In recent years research focus has been shifting towards the development of new biomaterials, medical devices and systems that mimic the natural elements, structures and models [3, 19, 79]. Bone is a composite tissue with complex hierarchical architecture, consisting of a fibrous organic ECM with dispersed inorganic nano-crystals [20, 27, 44, 80, 92]. A composite is a solid material that consists of a combination of two main types of phases: a continuous phase/matrix and one (or more) dispersed phase(s), which altogether result in a final product with superior properties than those of the individual raw materials [19]. The matrix confers the volume and supports the dispersed phase(s), which fills and enhances the properties of the matrix [19]. Thus, developing biomimetic bone alloplast grafts is an option that has been explored in bone tissue engineering, by designing 3D biodegradable porous nano-composite (polymeric matrix and dispersed ceramic particles) scaffolds that reproduce bone ECM [3, 9, 19, 44, 93, 94]. The physicochemical structure and composition of the biomaterial is recognized by the host stem cells, which could be induced towards cellular differentiation [70, 80]. The dispersed ceramic phase contributes for the material's bioactivity and strength, while the polymeric matrix promotes its flexibility and deformation capacity under mechanical load [3, 95].

However, as it has been mentioned before, bone is a very complex and organized tissue [21] from the chemical and mechanical points of view, directly influencing its biological responses, which make it difficult to reproduce [20]. It has been demonstrated that composites produced at the nano-scale show improved biological and mechanical responses when compared to micro-scale materials [75, 80, 93, 96, 97], because they mimic the natural bone surface topography [98]. Nano-scale materials present a higher specific surface area, which increases cell binding capacity, protein adsorption, ion release and bioactivity [97, 99], as well as stimulation of the proliferation and attachment of various cells types like MSCs, osteoblasts, osteoclasts, endothelial cells and PDL cells [27, 36, 75, 93, 98].

A biomaterial intended as a scaffold for bone regeneration should ideally:

a) be biocompatible with the living organism [70, 78, 80, 100-102], and not inducing acute or chronic inflammatory reactions *in vivo* [19, 100, 102, 103];

b) have a highly interconnected multiscale porous structure [20, 27] (porosity > 50 %) [34] (mean pore diameter > 100 – 200 μm) [19, 31, 44, 79, 97, 100], mimicking cancellous bone [80], to allow the circulation of oxygen, nutrients and wastes, cell migration, to promote neovascularization/angiogenesis and bone guided ingrowth [15, 25, 70, 78-80, 99, 103]. This type of porous structure also increases surface area [82]. This topic will be further explored in Chapter III.

c) be biodegradable into non-toxic sub-products and at a rate that keeps up with simultaneous new bone formation [15, 70, 78, 100, 101, 103]. Also, in the case of composite scaffolds, the different phases should be degraded in an appropriate rate [70, 80];

d) be hydrophilic, with a proper water-uptake (swelling) capability [104, 105], increasing the internal surface area, facilitating the cell migration, transport of oxygen, nutrients and metabolic wastes [25];

e) be osteoconductive [78, 82, 101], with a hydrophilic surface, morphology and topology suitable for osteoblast migration, adhesion, proliferation and differentiation towards osteocytes [15, 20, 102];

f) be osteogenic and osteoinductive by serving as a vehicle of osteoprogenitor viable cells [78, 79, 100, 101] and GFs [15, 70, 71, 78, 79, 100, 101];

g) be bioactive by interacting and establishing direct chemical bonds with the interface of the adjacent bone [26, 78-80], without forming a fibrous tissue layer in between [80], which promotes a strong bioactive fixation of the scaffold to the bone [20, 23, 26] (osteointegration) [19, 21, 23, 78];

h) have enough mechanical strength [20, 70, 75, 78, 82] (similar to bone) [80, 100, 102] to maintain the tissue volume, support bone growth, remodeling and mechanotransduction properties [15, 27], especially in load-bearing sites [84], and maintain its properties despite its initial degradation [34, 80]; This topic will be further explored in Chapter III.

i) have an antimicrobial activity [33] or at least a surface that does not favor microorganism adhesion [106];

j) be easy to handle clinically and/or cut into shape [70, 78, 80, 91, 102, 103], so it can be fixed into the bone defect and adapt to its complex shape [70, 80], as well as having the possibility of being manufactured and available in multiple forms like 3D scaffolds, sponges, foams, hydrogels, fibers, membranes, micro-spheres or cements [3, 20, 102];

k) be sterile [19, 27, 78, 80, 90] through validated processes that assure it is “free from all forms of viable microorganisms” [107], but without modifying the structural and chemical characteristics of the biomaterial [19];

l) be safe in general [62], i.e. “freedom from unacceptable risk” [108];

m) be scalable, commercially viable, affordable and have a long shelf life in regular storage conditions [19, 27, 80, 90, 91].

Obviously, it is very difficult that a single biomaterial can fulfill all the above-mentioned properties [19, 20, 93].

B. 2. Biopolymers

Natural biopolymers are ubiquitous and play important structural roles in every living being, since animals to plants and fungi [22, 109]. These biopolymers show valuable properties like abundancy, biocompatibility, low immunogenicity and biodegradation into non-toxic molecules [22, 109]. The mechanism of degradation of some natural biopolymers can be mediated by enzymes of the organism [80]. Biopolymers possess ligands to cell receptors that can induce cell differentiation [25] and upon chemical and physical modifications they may become versatile biomaterials [22]. Therefore, in the past years, so-called smart polymers derived from biological sources have been exploited for their use in medical devices [105]. However, because of their natural source, the reproducibility of these biopolymers is more difficult to achieve and the same polymer might present chemical differences according to its origin [80]. Table 4 presents some of the most common biopolymers used in bone tissue engineering.

Polysaccharides are composed of repeating monosaccharide units connected by glycosidic bonds forming carbohydrate structures [110] and are the most prominent group of smart polymers in tissue engineering nowadays [105]. Most of their sources are quite abundant and economically accessible, and they are in general physically and chemically versatile [110].

Table 4. Biopolymers used in tissue engineering

Type of molecule	Examples
Natural source [15, 22, 70, 102]	
Proteins	Collagen; gelatin and silk fibroin
Polysaccharides	Starch; alginate; carrageenan; cellulose and chitin/chitosan
Glycosaminoglycans	Chondroitin sulfate and hyaluronic acid
Synthetic source [19, 27, 70, 74, 78, 111]	
Polyesters	Poly (lactic acid) (PLA); Poly (glycolic acid); co-polymer Poly *d*, *l*-lactic-co-glycolic acid (PGLA); Poly-e-caprolactone (PCL)
Other molecules (very slow biodegradation)	Polyurethane, polyesterurethane

B. 2.2. Chitosan

The biopolymer chitin is the second most abundant after cellulose and it has been obtained mostly from the crustacean exoskeleton (shrimp, crab, lobster), but also from insect cuticles, mushroom envelopes, green algae and yeasts [15, 20, 70, 102, 112], where it has an important structural role comparable to collagen in animals and cellulose in plants [20, 22, 27]. Thus, there are three polymeric forms of chitin, presenting different features and functions: α-chitin that is stiffer, in comparison to β- and γ-chitins, which are more flexible [20]. However, chitin's practical use is very limited due to its poor solubility in water [102], and despite its abundancy, it is difficult to collect and to obtain a final product with reproducibility and standardized properties [20].

Chitosan (CS), which is a linear, semi-crystalline polysaccharide comprising co-polymers of N-acetyl D-glucosamine (2-acetamido-2-deoxy-D-glucose) and D-glucosamine (β-1,4-linked 2-amino-2-deoxy-D-glucose), linked by β(1-4) glycoside bonds, can be obtained from the partial deacetylation of chitin [15, 36, 70, 93, 102], rendering a more reactive polymer [20]. CS may have varying degrees of deacetylation between 50 and 95 %, corresponding to the ratio of D-glucosamine groups compared to the sum of N-acetyl D-glucosamine and D-glucosamine groups along the chains [15, 102]. Upon removal of the proteins and minerals from chitin through alkali and acid treatments respectively, the deacetylation process of CS can be obtained by either chemical hydrolysis in alkaline conditions at high temperatures [20, 70, 112] or by enzymatic hydrolysis with chitin deacetylase [70, 102, 112]. Its molecular weight can vary between 300 and 1000 kDA [15, 70, 102, 112]. Therefore, factors like the chitin source, presence of organic and inorganic impurities and the preparation method influence the molecular mass, the deacetylation degree (DD) and the distribution of the deacetylated amino groups, which widely modify its chemical features (crystallinity, solubility, degradation) and consequently CS's biological properties [15, 70, 102, 112].

CS is insoluble in neutral and alkaline solutions, but its protonated amino groups make it soluble in acid solutions (pH < 6) [15, 44, 102]. One of the most remarkable and differentiating property of the CS chain is its cationic nature provided by its D-glucosamine amino groups, which might be protonated and form polyelectrolyte complexes with anionic ions and molecules, including other polysaccharides, polymers, DNA, proteins and lipids [15, 22, 102, 112]. The higher the DD, the higher the number of positively charged free amino groups [15] and the higher functionalization can occur along the CS polymeric chain. CS derivatives such as carboxymethyl CS, N-carboxyethyl CS, quaterinized CS (QCS) and hydroxypropyl CS have been reported in previous studies to improve water solubility [112-115].

Because of its unique chemical features, CS's diverse biological properties make it a versatile biopolymer for biomedical applications [105]. Firstly, CS is highly biocompatible [70, 105, 112, 116], showing no toxicity when tested *in vitro* or *in vivo* in rats and humans [117, 118]. When implanted *in vivo*, CS materials show no inflammatory response [118] (low immunogenicity) [78, 119], with minimal foreign body response or fibrous encapsulation [15, 78, 94, 117] for CS with

higher DD (closer to 95 %) [120, 121]. Besides, CS with different DD shall be able to promote inflammatory cells recruitment and polarization that can lead to wound healing [15, 105]. CS biocompatibility increases with its DD, but it is dependent on the preparation method and the eventual presence of residual proteins (e.g. from crustaceans), which may induce allergic reactions [102].

Specifically, in the case of bone tissue regeneration, CS chain structure resembles the glycosaminoglycan of the bone tissue ECM, contributing to the regulation of cell behavior [25, 27, 36, 37, 70]. It has been demonstrated that osteoblast-like cells are able to adhere and proliferate on 2D CS films and 3D sponges with degrees of DD higher than 87 % [122, 123].

An interesting characteristic of CS is its biodegradability because it may be modified according to the final use of the material (e.g. to fit the tissue regeneration rate), since it largely depends on CS's DD and preparation method [15, 70, 102]. The biodegradation rate is inversely proportional to CS's crystallinity and, consequently, to its DD and molecular mass [15, 70, 102]. Therefore, the degradation rate is the lowest for a DD of 100 % (fully deacetylated, maximum crystallinity) and increases as the polymer becomes semi-crystalline and its DD is closest to 60 % [15, 70, 102]. Also, the biodegradation kinetics is affected by the distribution of the N-acetyl D-glucosamine residues along the polymer chains [102]. CS is degraded by hydrolysis due to interactions of the water molecules which break the polymer chain network [97]. Moreover, it must be considered that CS is a polysaccharide with β(1-4) glycoside bonds that are degraded *in vivo* by enzymes, primarily lysozyme [36, 70] (normal serum concentration in humans is 10 mg/L) [124] and also by hydrolyzation in about 3 to 7 weeks [15, 39, 102]. When degraded, CS forms non-toxic neutral oligosaccharides (saccharides and glucosamines) of variable molecular size that can be metabolized and excreted [15, 97, 102, 119]. Accordingly, the lower the DD, crosslinking and the smaller molecular mass of the CS chains, the fastest is its degradation rate [102, 119].

The polycationic nature of CS contributes for many biological properties that are very useful for tissue engineering. The positive charges of its amino groups can interact with the negative charges of cells membranes [40, 78], as well as with the glycoprotein mucin in acidic medium, which contributes to CS's mucoadhesion [70, 102, 119]. Once more, a higher DD correlates with increased mucoadhesion [102]. Besides, the CS amino residues react with the anionic membrane surface of the erythrocytes, creating a hemostatic effect by binding the cells and forming a clot that contributes to wound healing [15, 70, 102, 119]. With the same mechanism, CS is capable of causing the permeation of cells tight junctions by interacting with the negatively charged proteins of the membranes [78, 102]. In addition to its immunomodulatory effect, CS amino residues (polycationic nature) release proton ions that have an analgesic effect in the inflammatory area [102].

Furthermore, CS has shown natural antibacterial (examples of oral bacteria: Gram positive *like S. mutans* and Gram negative like *A. actinomycetemcomitans*) and antifungal properties, though the mechanisms of action are not totally clear yet [62, 118]. One of the possible explanations is related to CS being an alkali polysaccharide with a polycationic structure, which interacts with the anions of the Gram negative bacteria membranes and modifies its permeability,

weakening their barrier function, interfering with the mass transport of essential molecules through the cell wall and consequently reducing bacteria viability [15, 36, 102, 118, 125]. It is also possible that CS amino residues bind to bacterial DNA and inhibit the subsequent RNA synthesis [102]. Studies have also shown that CS is able to permeate fungal biofilms and interfere with these cells' metabolism and viability [118].

Also, because of its protonated amino groups, CS shows a great affinity to water. Therefore, its hydrophilicity is favorable for the adhesion, proliferation and differentiation of animal cells *in vitro* and *in vivo*, and thus, to tissue regeneration [15, 70, 78, 117]. *In vitro* studies have shown that it preferably supports the attachment and growth of osteoblasts when compared to fibroblasts [42].

Moreover, CS has been used in medical devices and pharmaceutical preparations as drug (e.g. heparin) and GF delivery (e.g. BMP-2) and gene carrier systems [42, 62, 118], on its own or in combination with alginate, collagen or gelatin [22, 118]. It forms colloidal hydrogels that carry the desired molecules such as antibiotics, GFs, protein or peptide drugs and vaccines that are released in a controlled way (in time and concentration) at the target tissues [102, 118]. It can also interact with bioactive molecules such as DNA through chemical crosslinking, ionic crosslinking and ionic complexation [118].

Despite its osteoconductivity [17, 37, 82] and versatility to be used in different forms (beads, films, hydrogels, scaffolds) [78, 96], pure CS biomaterials cannot support bone regeneration due to their weak mechanical properties [17, 78, 82, 96, 112], especially when immersed in solution [40], thus CS has been combined with other polymers like alginate, gelatin, hyaluronic acid and silk fibroin [17]. Moreover, CS does not present bioactive properties, so it does not directly bond to bone through an apatite layer [17, 18, 82, 105], therefore it should be combined with other bioactive materials like bioceramics, such as HAp [82].

B. 3. Bioceramics

Bioceramics are a class of inorganic non-metallic crystalline biomaterials [79] that can be derived from metallic oxides, calcium phosphates, glass ceramics, [26, 80] or calcium sulfate [79] (Table 5). Their molecules are connected by ionic bonds, rendering a strong structure, which density can be enhanced by sintering [79, 126]. However, these materials lack elasticity and have a brittle nature [21].

Bioceramics have been used as biomaterials for bone grafting because they resemble the inorganic phase of the osseous ECM [26]. Calcium phosphate (CaP)-based bioceramics are chemically and structurally the most similar to the inorganic phase of bone, are biocompatible, osteoconductive and form a strong chemical bond to bone (bioactivity) *in vivo*, which makes them an optimal choice as bone graft materials [23, 37, 44, 90, 112]. CaP ceramics are partially dissolved when in contact with physiological fluids and increase the concentration of Ca^{2+} and PO_3^{4-}, which stimulates the osteoblasts activity [27, 62]. Their degradation rate is dependent on

the ceramic crystallinity, porosity, chemical purity and surface roughness [35]. Properties like the chemical composition, crystallinity, particle size and surface structure directly influence the cells' responses [127].

Table 5. Bioceramics used in medical devices [26, 79, 80]

Molecular group	Biomaterials examples
Metallic oxides	Carbon, alumina (Al_2O_3), zirconia (ZrO_2), single oxide ceramics
Calcium phosphates (CaP)	HAp, α- and β-tricalcium phosphate (α-, β-TCP), biphasic calcium phosphate (BCP), calcium phosphate cement (CPC)
Glass ceramics	Bioactive glass (BG): Bioglass® (45S5), PerioGlas®, Novamin
Calcium sulfate (plaster of Paris)	

B. 3.1. Hydroxyapatite

HAp of either natural or synthetic origin has been extensively used as a graft biomaterial for bone regeneration [39, 96, 97, 117, 128] in a range of orthopedic and dental surgical techniques as bone fillers [20, 26, 86, 93, 96, 117]. This can be explained by the HAp similarity with the inorganic phase of bone ECM [25-27, 75, 93, 99, 112] in terms of chemical composition, crystal size and morphology [27, 44, 86]. Its chemical formula is $Ca_{10}(PO_4)_6(OH)_2$ (Ca/P molar ratio 1.67) [23, 112], the molar mass is 502.31 g/mol and the density is 3.16 g/cm^3 [26].

Synthetic HAp is very often prepared by wet-chemical processes (co-precipitation, hydrolysis, hydrothermal and sol-gel), but it can also be prepared by dry processes (solid-state reactions and mechanochemical) and high-temperature synthesis (spray pyrolysis, combustion, and thermal decomposition) [112, 129]. In the co-precipitation method [21, 23], calcium and phosphorous-based inorganic salts are combined in an aqueous solution at low temperature [26, 129], followed by aging, precipitation and drying [112], with the production of highly pure HAp rods [26]. Moreover, trace elements can also be incorporated to the HAp formula [130], resulting in non-stoichiometric crystals to enhance physicochemical and biological effects [23, 27, 79, 129, 130]. In the hydrothermal method [23] the reagents in aqueous solution react at high temperature [112] and pressure inside a sealed system, obtaining a crystallized nanophase rod-like HAp powder [26, 129]. The hydrolysis technique inhibits the agglomeration of the obtained HAp particles through the transformation of another calcium phosphate phase in an aqueous solution, followed by emulsion synthesis [112]. The sol-gel method involves molecular-level mixing of calcium and phosphorous usually at low temperature and pressure, forming a colloidal suspension [26, 112], which improves the homogeneity of the final precipitated HAp powder [26, 129]. Besides, a biomimetic approach has also been described, involving the nucleation and growth of HAp in SBF at 37ºC, forming a carbonated HAp, which is more similar to natural bone

crystals [26]. HAp nano-fibers can also be obtained by electrospinning [26, 27], as well as flexible ultralong HAp nanowires prepared by a solvothermal method [131]. Finally, HAp from natural origin (mammalian, marine, shells and plant sources) [112, 129] can be prepared by e.g. thermal calcination, resulting in HAp micro-particles; alkaline hydrolysis, producing carbonated nano-particles [96]; sol-gel, co-precipitation, among others, or a combination of methods [112]. The features of the final HAp product obtained by each of the described methods are influenced by the reaction times, pH, temperature, starting materials and surface modification treatments [23, 26, 27].

When implanted in the physiological medium, HAp biomaterials release calcium and phosphate ions and precipitate an active carbonated layer structural and chemically similar to bone [26, 97, 130]. Therefore, it has been shown that HAp is a bioactive biomaterial *in vitro* in SBF and *in vivo* directly bonds to bone without fibrous tissue interposition [86, 93, 99, 132]. HAp coatings of metal implants have been successfully employed to enhance their osseointegration [26, 79, 93, 112].

Due to its chemical composition, HAp presents several valuable features like biocompatibility, non-inflammatory inducement, osteoconductivity, osteoinductivity [20, 23, 25, 39, 93, 94, 97], pro-angiogenic properties [117, 128] and hydrophilicity due to its large amount of -OH groups [109]. HAp nanoparticles (1 – 100 nm) are more similar to those found in natural bone when compared to microparticles [26], thus they are more osteoconductive since they show several advantages such as improved surface energy, with a subsequent enhancement of its bioactivity, as well as an increase in surface area and higher protein adsorption [26, 75, 78, 98]. Therefore, HAp nanocrystals on a scaffold surface are easily recognized by osteoblasts due to protein adsorption [23, 36, 133] and contribute to the nucleation process that initiates the mineralization process mediated by these cells [26, 27, 40, 96]. Studies confirmed that HAp nano-crystals promote the BMP expression by alveolar osteoblasts *in vitro*, inducing osteogenic differentiation [27, 31, 75]. It has been reported that HAp scaffolds seeded with MSCs may induce ectopic bone formation [62]. HAp nano-particles have also been used as delivery systems for drugs, GFs, enzymes and antigens [23, 26, 78, 93].

However, HAp also presents some drawbacks, namely its brittleness despite its high mechanical strength [39, 78, 93, 97]. Therefore, the clinical use of HAp biomaterials is quite limited to low load-bearing sites [44, 78, 130]. Besides, HAp biomaterials are very stable in physiological pH ranges [26] and are generally considered long-term biodegradable, since they take a long time to be replaced by new bone tissue [40, 78, 79, 86], which may impair some regenerative applications (e.g. periodontal GTR and normal bone remodeling) [27, 74]. The biodegradation rate depends on the porosity degree (higher degradation with higher porosity) [20, 79, 86, 133], size and shape, crystallinity [20] and composition such as the ratio of ion substitution of the carbonated groups (non-stoichiometric HAp has a higher degradation rate) [35, 78]. Also, the patient's individual characteristics such as age, gender, bone type, hormonal and genetic factors affect the cell-mediated HAp rate of degradation during bone remodeling [20]. One of the strategies to improve the biodegradation of HAp materials is to combine them with other highly

resorbable CaP bioceramics like tricalcium phosphate (TCP) [35]. Moreover, some HAp presentations like micro-spheres and granules are difficult to handle clinically and they can migrate from the defect sites [39, 97, 117].

In order to solve these limitations, HAp has been combined with biopolymers, resulting in composite biomaterials that mimic the bone tissue ECM [39, 93, 97, 112]. The HAp dispersed phase increases the mechanical strength of biopolymers, which in general present low mechanical properties [82, 97]. Moreover, composites with HAp in their composition contribute to an increased adhesion and proliferation of osteoblast cells [93, 97].

C. NANO-HYDROXYAPATITE/CHITOSAN COMPOSITES

The use of CS combined with HAp (Figure 6) is considered an attractive biomimetic alternative [23, 25, 134] to the use of collagen in bone tissue regeneration [27, 112]. The concept is to simultaneously increase the mechanical properties and the biological responses [25, 70, 93, 112, 135]. Since that CS is mechanically weak and it is not bioactive [82, 93, 96], it can be combined with HAp, which provides mechanical strength to the composite, resulting in a bioactive, biodegradable and osteoconductive biomaterial [15, 82, 112, 136]. On the other hand, CS increases the compressive/tensile strength of HAp, providing elasticity, decreasing brittleness [19, 42, 93] and improving the clinical handling [42]. Additionally, since the biodegradation rate of HAp is generally difficult to adjust to clinical demands and normal bone healing, the combination with CS improves the control over the scaffolds' degradation to become more adjusted to the bone tissue formation [42, 112]. Biocomposites of nHAp and CS have been studied not only as bone regeneration biomaterials (membranes [97], scaffolds), but also as drug delivery systems, gene delivery carriers and coatings of metal implants [112].

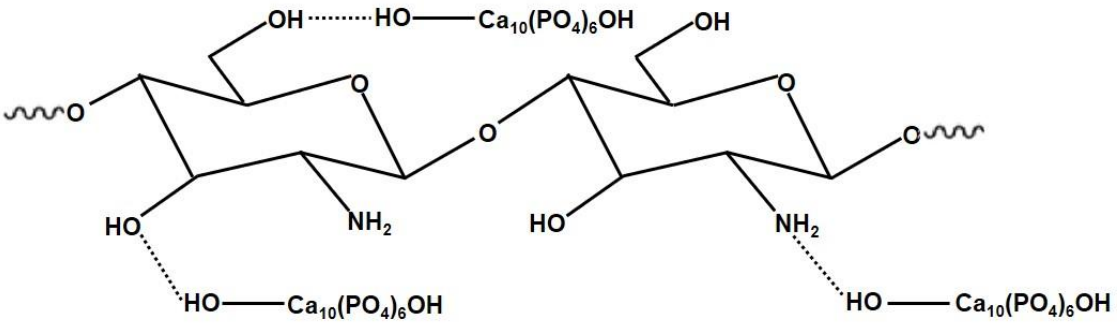

Figure 6. Hydrogen bonds between the CS monomer and HAp (adapted from [20, 112]).

C. 1. Preparation methods

During the preparation process of such 3D scaffolds there is the difficulty of balancing properties like porosity, mechanical strength and biodegradation [21, 25]. As described before, composites prepared at the nano-scale present improved biological and mechanical properties when compared to micro-scale materials [28, 96]. However, the preparation processes of these biomaterials are also challenging due to the tendency of nanoparticles to agglomerate [28]. Quite often it is reported the use of crosslinking agents (e.g. genipin [18], $CaCl_2$ [82]) to reinforce the

scaffolds structure and mechanical resistance [136]. Crosslinking degree is defined as the ratio of consumed amino groups in the crosslinked samples to the free amino groups in the corresponding uncrosslinked samples [18, 137].

Generally, the synthesis of biopolymer/bioceramic composite porous scaffolds is comprised of two main stages: in the first stage a dispersion/slurry of the two phases is prepared; in the second stage the porous structure is formed and the solvents are eliminated. Both stages can be pursued using different methods and respective variations, which results in a final product with different physicochemical and biological properties [19, 30].

Therefore, for the first stage, one of the simplest, quickest and most popular method is the mechanical stirring [15, 44, 112], in which separate polymer solution and ceramic powder/paste are previously prepared in the intended proportions [18, 29]. Then, the two components must be thoroughly mixed in order to achieve a homogenous, and thus stable, dispersion [19, 29, 112]. However, it can be difficult to obtain a homogenous mixture [18, 29], since miscibility between two phases is dependent on physicochemical properties like the wettability and hydrophilicity/polarity of the polymer and the ceramic [19, 28, 44]. Preferably, both components should establish an interface through strong and stable bonds (covalent or ionic bonds) rather than through van der Waal forces or hydrogen bonds, in order to avoid early mechanical failure of the final product because of lack of adhesion [18, 19, 28] or unwanted migration of the HAp particles in the organism [42].

Also, a common method is the co-precipitation, in which the mineral crystals are precipitated and formed inside the polymer solution [29]. This process is also called *in situ* co-precipitation [44, 82, 112] or biomimetic method because it resembles the natural process that happens during bone mineralization [28, 29], which is the formation and precipitation of the nano-sized apatite crystals uniformly distributed and strongly bonded upon a pre-existing polymeric extracellular matrix [42]. For example, in the case of an nHAp/CS composite, an acid CS solution containing Ca^{2+} ions is mixed with a basic solution containing PO_4^{3-} precursor [30, 112]. The pH of the final solution is increased, which causes the simultaneous precipitation of CS (at pH > 6) and HAp crystals [15]. Although with this cost-effective and reproducible method, it is easier to obtain a homogenous distribution of the biopolymer and the bioceramic [112], it might be more difficult to control the size and purity of the inorganic crystals [82]. Since this method is performed at room temperature, it allows the incorporation of thermally sensitive molecules (drugs, GFs, proteins) [112].

Another biomimetic method includes the coating of a previously prepared biopolymer scaffold with an apatite layer [15, 18]. This can be achieved by either soaking the scaffolds in SBF in mild processing conditions [15, 18, 30] or in a water/ethanol solution with Ca^{2+} and PO_4^{3-} ions at 80 ºC [138]. This apatite layer can also be obtained by electrochemical and electrophoretic procedures [29].

In a second stage of scaffold preparation, the porosity is formed and the solvent is eliminated by phase separation. This stage might be accomplished by solvent casting, gas foaming or freeze drying [28]. The solvent casting technique consists in pouring the

polymer/organic solvent solution in a mould with porogen particles [28], which can be a foaming agent (e.g. hydrogen peroxide solution), a hydrophobic liquid (oil), calcium sulfate or degradable polymer microparticles [139]. Once the solvent evaporates, the composite is poured in another adequate solvent of the porogen, leaving pores in the place of the particles [28]. The fact of having to use an extra and potentially hazardous organic solvent constitutes a disadvantage, hence the gas foaming technique uses a gas (CO_2) instead of porogen particles, which is eliminated inside a high-pressure chamber [25, 28, 140]. The latter technique takes a long time to perform (several days), it does not leave an interconnected pore structure and uses excessive heat that may damage the polymer structure [28].

The most commonly employed thermally induced phase separation technique is freeze drying [25, 82, 112], since it is quite simple and does not require porogen particles or gases [28, 44]. Upon scaffold freezing, solvent ice crystals nucleation occurs inside the scaffold, which sublime afterwards with the vacuum inside the freeze drying chamber [28]. The freezing temperature dictates to a great extent the size and distribution of the ice crystals and consequently the size and interconnection of the pores of the final scaffold [25, 97]. The mean pore diameter diminishes with the decreasing temperature [44], as well as with a higher concentration of CS and lower swelling ratios [25].

Moreover, composites with a polymer nanofiber or mesh structure (50 – 100 nm of diameter) similar to that of bone extracellular matrix can be obtained by electrospinning [28, 84, 141]. It has been described that the polymer nanofibrous scaffolds present high interconnectivity and resemble the fiber collagenous structure of bone ECM, but since their mechanical properties are weak [17], the dispersed nHAp phase can be either introduced in the polymer solution before electrospinning [15, 17, 92] or posteriorly deposited upon the scaffold by e.g. soaking mineralization [17]. In this inexpensive technique a high voltage electrical field is applied to the polymer solution that is being poured from a syringe or similar, which causes the solvent evaporation, transforming the liquid into a conical shape and therefore into a fiber before being collected [15, 80, 92, 102].

Despite during the phase separation stage (e.g. by freeze drying) the majority of the residual solvent is eliminated (in most CS-based biomaterials it is acetic acid), most of the preparation techniques described in the literature present a problem with the need of getting rid of unwanted potentially toxic solvents [28]. Most studies usually neutralize the scaffolds with alkaline solutions such as NaOH, wash it thoroughly with distilled water and then repeat the freeze drying step [42, 96, 112]. Nevertheless, this procedure increases the complexity of the whole process, time and costs of production, and might leave more unwanted solutions and precipitated salts from the neutralizing solutions inside the porous scaffold structure.

An alternative procedure to overcome this is the $scCO_2$ extraction technique [140]. The supercritical state is when a certain molecule is simultaneously a liquid and a gas in conditions beyond its specific critical temperature (T_C) and pressure (P_C) [140]. As a result, the molecule preserves the properties of a liquid (dissolution capacity) and of a gas (high diffusion and low viscosity) [140, 142]. CO_2 is quite an available and affordable non-inflammable gas [142-144],

environment friendly and recyclable [143], which is only hazardous by inhalation [144]. The supercritical conditions of CO_2 are T_C 31.1ºC (near-ambient temperature) and P_C 7.39 MPa (73.9 bar), which are relatively mild conditions for sensitive polymers [140, 142-146]. Also, $scCO_2$ is an inert gas to most polymers and since it has high density, low viscosity and no superficial tension, it is appropriate for highly porous scaffolds [140, 142-144, 146]. Since CO_2 is a non-polar molecule, $scCO_2$ is a suitable solvent for molecules with a low hydrophilic/hydrophobic character, low molecular weight and low polarity [140].

C. 2. Sterilization methods

Furthermore, upon the scaffold preparation, it must be sterilized in an efficient and convenient way, so it can contact directly with cell culture medium for *in vitro* tests [15] or *in vivo* with living body fluids [20]. Sterilization is only considered to have been achieved after the inactivation of spore preparations of *Bacillus subtilis* and *Bacillus stearothermophilus* (most resistant bioindicators), with a reduction in bacterial spore colony forming units (CFUs) of 10^{-6} (sterility assurance level (SAL)) [143, 147].

Published reports employed disinfection methods such as immersion in ethanol [17, 44, 97, 101, 109, 113, 125, 148] or sterilization methods such as ethylene oxide [37, 42, 131, 149, 150], irradiation with ultraviolet light [18, 32, 38, 44, 115, 125, 151, 152], gamma irradiation [83, 153, 154], but without much consensus on the sterilization protocols, which might produce irreversible physicochemical structural alterations to the polymer chain matrix [15, 19, 20], hindering the properties of the polymer-based biomaterials.

It has been described in the literature that $scCO_2$ has been used in the food and pharmaceutical industry as a sterilization method of food and biomaterials respectively, being effective against a range of bacteria, viruses and insects [142, 146]. Nevertheless, its sterilization effectiveness is variable and dependent on the working conditions and the type of microorganism contamination, namely bacterial spores [142, 144, 146]. Spilimbergo *et al.* (2003) reported that *Bacillus subtilis* spores can be totally inactivated after $scCO_2$ treatment at 75 ºC for 2 hours [142]. Moreover, Wehmeyer *et al.* (2015) reported the sterilization of an amniotic membrane for transplantation through the $scCO_2$ method for 10 – 30 min at constant 9900 kPa and 35 ºC, with the addition of 2 mL of peracetic acid (PAA) as a chemical co-adjuvant [147]. The literature has been showing that probably the $scCO_2$ modifies the microorganisms' membrane permeability and synergistically causes an intracellular pH decrease due to increased mass transfer of CO_2 [142, 143, 146, 147]. In the case of spore bacteria, the mild heat firstly induces the pore activation and germination, which is subsequently inactivated by the former mechanisms described [142, 143].

II. References

[1] Lang, N. P.; Berglundh, T.; Giannobile, W. V.; Sanz, M., Eds. Lindhe's Clinical Periodontology and Implant Dentistry, 7th Ed.; Wiley-Blackwell: Oxford, 2021. doi: -

[2] Nagata, M.; English, J. D.; Ono, N.; Ono, W. Diverse stem cells for periodontal tissue formation and regeneration. Genesis. 2022, 60, e23495. doi: 10.1002/dvg.23495

[3] Liang, Y.; Luan, X.; Liu, X. Recent advances in periodontal regeneration: A biomaterial perspective. Bioact Mater. 2020, 5, 297-308. doi: 10.1016/j.bioactmat.2020.02.012

[4] Giannobile, W. V.; Nevins, M., Eds. Osteology guidelines for oral and maxillofacial regeneration: preclinical models for translational research, 1st Ed.; Quintessence Publishing: London, 2011. doi: -

[5] Gartner, L. P. Textbook of Histology, 4th Ed.; Elsevier: Philadelphia, USA, 2017. doi: -

[6] Pieles, O.; Höring, M.; Adel, S.; Reichert, T. E.; Liebisch, G.; Morsczeck, C. Energy metabolism and Lipidome are highly regulated during osteogenic differentiation of dental follicle cells. Stem Cells Int. 2022, 2022, 3674931. doi: 10.1155/2022/3674931

[7] Gauthier, R.; Attik, N.; Chevalier, C.; Salles, V.; Grosgogeat, B.; Gritsch, K.; Trunfio-Sfarghiu, A.-M. 3D Electrospun Polycaprolactone Scaffolds to Assess Human Periodontal Ligament Cells Mechanobiological Behaviour. Biomimetics. 2023, 8, 108. doi: 10.3390/biomimetics8010108

[8] Golafshan, N.; Castilho, M.; Daghrery, A.; Alehosseini, M.; van de Kemp, T.; Krikonis, K.; de Ruijter, M.; Dal-Fabbro, R.; Dolatshahi-Pirouz, A.; Bhaduri, S. B.; Bottino, M. C.; Malda, J. Composite Graded Melt Electrowritten Scaffolds for Regeneration of the Periodontal Ligament-to-Bone Interface. ACS Appl Mater Interfaces. 2023, 15, 12735-12749. doi: 10.1021/acsami.2c21256

[9] Larsson, L.; Decker, A.; Nibali, L.; Pilipchuk, S.; Berglundh, T.; Giannobile, W. Regenerative medicine for periodontal and peri-implant diseases. J Dent Res. 2016, 95, 255-266. doi: 10.1177/0022034515618887

[10] Berglundh, T.; Armitage, G.; Araujo, M.; Avila-Ortiz, G.; Blanco, J.; Camargo, P. M.; Chen, S.; Cochran, D.; Derks, J.; Figuero, E.; Hämmerle, C. H. F.; Heitz-Mayfield, L. J. A.; Huynh-Ba, G.; Iacono, V.; Koo, K.-T.; Lambert, F.; McCauley, L.; Quirynen, M.; Renvert, S.; Salvi, G. E.; Schwarz, F.; Tarnow, D.; Tomasi, C.; Wang, H.-L.; Zitzmann, N. Peri-implant diseases and conditions: Consensus report of workgroup 4 of the 2017 World Workshop on the Classification of Periodontal and Peri-Implant Diseases and Conditions. J Clin Periodontol. 2018, 45, S286-S291. doi: 10.1111/jcpe.12957

[11] Barootchi, S.; Wang, H.-L. Peri-implant diseases: Current understanding and management. Int J Oral Implantol (Berl). 2021, 14, 263-82. doi: -

[12] Burr, D. B.; Allen, M. R. Basic and Applied Bone Biology, 2nd Ed.; Elsevier: London, UK, 2019. doi: -

[13] Yuste, I.; Luciano, F. C.; González-Burgos, E.; Lalatsa, A.; Serrano, D. Mimicking bone microenvironment: 2D and 3D *in vitro* models of human osteoblasts. Pharmacol Res. 2021, 169, 105626. doi: 10.1016/j.phrs.2021.105626

[14] Wang, L.; You, X.; Zhang, L.; Zhang, C.; Zou, W. Mechanical regulation of bone remodeling. Bone Res. 2022, 10, 16. doi: 10.1038/s41413-022-00190-4

[15] Levengood, S. K. L.; Zhang, M. Chitosan-based scaffolds for bone tissue engineering. J Mater Chem B. 2014, 2, 3161-3184. doi: 10.1039/C4TB00027G

[16] Akbari, S.; Khazaeinejad, P. Geometrical and mechanical analysis of polylactic acid and polyvinylidine fluoride scaffolds for bone tissue engineering. Eng Comput. 2023, 39, 4153–4165. doi: 10.1007/s00366-023-01902-y

[17] Lai, G.-J.; Shalumon, K.; Chen, J.-P. Response of human mesenchymal stem cells to intrafibrillar nanohydroxyapatite content and extrafibrillar nanohydroxyapatite in biomimetic chitosan/silk fibroin/nanohydroxyapatite nanofibrous membrane scaffolds. Int J Nanomedicine. 2015, 10, 567. doi: 10.2147/IJN.S73780

[18] Xu, F.; Ding, H.; Song, F.; Wang, J. Effects of preparation methods on the bone formation potential of apatite-coated chitosan microspheres. J Biomater Sci Polym Ed. 2014, 25, 2080-2093. doi: 10.1080/09205063.2014.970604

[19] Dorozhkin, S. V. Biocomposites and hybrid biomaterials based on calcium orthophosphates. Biomatter. 2011, 1, 3-56. doi: 10.4161/biom.1.1.16782

[20] Pighinelli, L.; Kucharska, M. Chitosan–hydroxyapatite composites. Carbohydr Polym. 2013, 93, 256-262. doi: 10.1016/j.carbpol.2012.06.004

[21] Venkatesan, J.; Kim, S.-K. Nano-hydroxyapatite composite biomaterials for bone tissue engineering—A review. J Biomed Nanotechnol. 2014, 10, 3124-3140. doi: 10.1166/jbn.2014.1893

[22] Venkatesan, J.; Bhatnagar, I.; Manivasagan, P.; Kang, K.-H.; Kim, S.-K. Alginate composites for bone tissue engineering: a review. Int J Biol Macromol. 2015, 72, 269-281. doi: 10.1016/j.ijbiomac.2014.07.008

[23] Sugimoto, K.; Zhou, Y.; Galindo, T. G. P.; Kimura, R.; Tagaya, M. Investigation of Surface Layers on Biological and Synthetic Hydroxyapatites Based on Bone Mineralization Process. Biomimetics. 2023, 8, 184. doi: 10.3390/biomimetics8020184

[24] Moshaverinia, A.; Chen, C.; Xu, X.; Akiyama, K.; Ansari, S.; Zadeh, H. H.; Shi, S. Bone regeneration potential of stem cells derived from periodontal ligament or gingival tissue sources encapsulated in RGD-modified alginate scaffold. Tissue Engineering Part A. 2014, 20, 611-621. doi: 10.1089/ten.TEA.2013.0229

[25] Jamalpoor, Z.; Mirzadeh, H.; Joghataei, M. T.; Zeini, D.; Bagheri-Khoulenjani, S.; Nourani, M. R. Fabrication of cancellous biomimetic chitosan-based nanocomposite scaffolds applying a combinational method for bone tissue engineering. J Biomed Mater Res A. 2015, 103, 1882-1892. doi: 10.1002/jbm.a.35320

[26] Zakaria, S. M.; Sharif Zein, S. H.; Othman, M. R.; Yang, F.; Jansen, J. A. Nanophase hydroxyapatite as a biomaterial in advanced hard tissue engineering: a review. Tissue Eng Part B Rev. 2013, 19, 431-441. doi: 10.1089/ten.TEB.2012.0624

[27] Venugopal, J.; Prabhakaran, M. P.; Zhang, Y.; Low, S.; Choon, A. T.; Ramakrishna, S. Biomimetic hydroxyapatite-containing composite nanofibrous substrates for bone tissue engineering. Philos Trans A Math Phys Eng Sci. 2010, 368, 2065-2081. doi: 10.1098/rsta.2010.0012

[28] Šupová, M. Problem of hydroxyapatite dispersion in polymer matrices: a review. J Mater Sci Mater Med. 2009, 20, 1201-1213. doi: 10.1007/s10856-009-3696-2

[29] Peniche, C.; Solís, Y.; Davidenko, N.; García, R. Chitosan/hydroxyapatite-based composites. Biotecnol Apl. 2010, 27, 202-210. doi: -

[30] Danilchenko, S. N.; Kalinkevich, O. V.; Pogorelov, M. V.; Kalinkevich, A. N.; Sklyar, A. M.; Kalinichenko, T. G.; Ilyashenko, V. Y.; Starikov, V. V.; Bumeyster, V. I.; Sikora, V. Z. Characterization and *in vivo* evaluation of chitosan-hydroxyapatite bone scaffolds made by one step coprecipitation method. J Biomed Mater Res A. 2011, 96, 639-647. doi: 10.1002/jbm.a.33017

[31] Wang, H.; Zhi, W.; Lu, X.; Li, X.; Duan, K.; Duan, R.; Mu, Y.; Weng, J. Comparative studies on ectopic bone formation in porous hydroxyapatite scaffolds with complementary pore structures. Acta Biomater. 2013, 9, 8413-8421. doi: 10.1016/j.actbio.2013.05.026

[32] Bozorgi, A.; Mozafari, M.; Khazaei, M.; Soleimani, M.; Jamalpoor, Z. Fabrication, characterization, and optimization of a novel copper-incorporated chitosan/gelatin-based scaffold for bone tissue engineering applications. Bioimpacts. 2022, 12, 233. doi: 10.34172/bi.2021.23451

[33] Vallittu, P. K.; Närhi, T. O.; Hupa, L. Fiber glass–bioactive glass composite for bone replacing and bone anchoring implants. Dent Mater. 2015, 31, 371-381. doi: 10.1016/j.dental.2015.01.003

[34] Fu, Q.; Saiz, E.; Rahaman, M. N.; Tomsia, A. P. Bioactive glass scaffolds for bone tissue engineering: state of the art and future perspectives. Mater Sci Eng C Mater Biol Appl. 2011, 31, 1245-1256. doi: 10.1016/j.msec.2011.04.022

[35] Hoppe, A.; Güldal, N. S.; Boccaccini, A. R. A review of the biological response to ionic dissolution products from bioactive glasses and glass-ceramics. Biomaterials. 2011, 32, 2757-2774. doi: 10.1016/j.biomaterials.2011.01.004

[36] Zia, I.; Jolly, R.; Mirza, S.; Umar, M. S.; Owais, M.; Shakir, M. Hydroxyapatite Nanoparticles Fortified Xanthan Gum–Chitosan Based Polyelectrolyte Complex Scaffolds for Supporting the Osteo-Friendly Environment. ACS Appl Bio Mater. 2020, 3, 7133-7146. doi: 10.1021/acsabm.0c00948

[37] Przekora, A.; Ginalska, G. Enhanced differentiation of osteoblastic cells on novel chitosan/β-1, 3-glucan/bioceramic scaffolds for bone tissue regeneration. Biomed Mater. 2015, 10, 015009. doi: 10.1088/1748-6041/10/1/015009

[38] Zhang, L.; Dong, Y.; Xue, Y.; Shi, J.; Zhang, X.; Liu, Y.; Midgley, A. C.; Wang, S. Multifunctional triple-layered composite scaffolds combining platelet-rich fibrin promote bone regeneration. ACS Biomater Sci Eng. 2019, 5, 6691-6702. doi: 10.1021/acsbiomaterials.9b01022

[39] Yao, A.-H.; Li, X.-D.; Xiong, L.; Zeng, J.-H.; Xu, J.; Wang, D.-P. Hollow hydroxyapatite microspheres/chitosan composite as a sustained delivery vehicle for rhBMP-2 in the treatment of bone defects. J Mater Sci Mater Med. 2015, 26, 1-12. doi: 10.1007/s10856-014-5336-8

[40] Wang, F.; Zhang, Y. C.; Zhou, H.; Guo, Y. C.; Su, X. X. Evaluation of *in vitro* and *in vivo* osteogenic differentiation of nano-hydroxyapatite/chitosan/poly (lactide-co-glycolide) scaffolds with human umbilical cord mesenchymal stem cells. J Biomed Mater Res A. 2014, 102, 760-768. doi: 10.1002/jbm.a.34747

[41] Nasello, G.; Alamán-Díez, P.; Schiavi, J.; Pérez, M. Á.; McNamara, L.; García-Aznar, J. M. Primary Human Osteoblasts Cultured in a 3D Microenvironment Create a Unique Representative Model of Their Differentiation Into Osteocytes. Front Bioeng Biotechnol. 2020, 8, 336. doi: 10.3389/fbioe.2020.00336

[42] Chesnutt, B. M.; Yuan, Y.; Buddington, K.; Haggard, W. O.; Bumgardner, J. D. Composite chitosan/nano-hydroxyapatite scaffolds induce osteocalcin production by osteoblasts *in vitro* and support bone formation *in vivo*. Tissue Eng Part A. 2009, 15, 2571-2579. doi: 10.1089/ten.tea.2008.0054

[43] Liu, X.; Zhang, G.; Hou, C.; Wang, H.; Yang, Y.; Guan, G.; Dong, W.; Gao, H.; Feng, Q. Vascularized bone tissue formation induced by fiber-reinforced scaffolds cultured with osteoblasts and endothelial cells. Biomed Res Int. 2013, 2013, doi: 10.1155/2013/854917

[44] Zhang, J.; Nie, J.; Zhang, Q.; Li, Y.; Wang, Z.; Hu, Q. Preparation and characterization of bionic bone structure chitosan/hydroxyapatite scaffold for bone tissue engineering. J Biomater Sci Polym Ed. 2014, 25, 61-74. doi: 10.1080/09205063.2013.836950

[45] Bhat, A.; Wooten, R. M.; Jayasuriya, A. C. Secretion of growth factors from macrophages when cultured with microparticles. J Biomed Mater Res A. 2013, 101, 3170-3180. doi: 10.1002/jbm.a.34604

[46] Glossary of Periodontal Terms. Available online: https://members.perio.org/libraries/glossary (assessed on 14-01-2024)

[47] Bojar, W.; Kucharska, M.; Ciach, T.; Koperski, Ł.; Jastrzębski, Z.; Szałwiński, M. Bone regeneration potential of the new chitosan-based alloplastic biomaterial. J Biomater Appl. 2014, 28, 1060-1068. doi: 10.1177/0885328213493682

[48] Guzmán, R.; Nardecchia, S.; Gutiérrez, M. C.; Ferrer, M. L.; Ramos, V.; del Monte, F.; Abarrategi, A.; López-Lacomba, J. L. Chitosan scaffolds containing calcium phosphate salts and rhBMP-2: *in vitro* and *in vivo* testing for bone tissue regeneration. PloS One. 2014, 9, e87149. doi: 10.1371/journal.pone.0087149

[49] Dagtekin, G.; Schiffer, R.; Klein, B.; Jahnen-Dechent, W.; Zwadlo-Klarwasser, G. Modulation of angiogenic functions in human macrophages by biomaterials. Biomaterials. 2003, 24, 3395-3401. doi: 10.1016/s0142-9612(03)00201-1

[50] Dean, D. B.; Watson, J. T.; Moed, B. R.; Zhang, Z. Role of bone morphogenetic proteins and their antagonists in healing of bone fracture. Front Biosci (Landmark Ed). 2009, 14, 2878-2888. doi: doi.org/10.2741/3419

[51] Chapple, I. L.; Mealey, B. L.; Van Dyke, T. E.; Bartold, P. M.; Dommisch, H.; Eickholz, P.; Geisinger, M. L.; Genco, R. J.; Glogauer, M.; Goldstein, M.; Griffin, T. J.; Holmstrup, P.; Johnson, G. K.; Kapila, Y.; Lang, N. P.; Meyle, J.; Murakami, S.; Plemons, J.; Romito, G. A.; Shapira, L.; Tatakis, D. N.; Teughels, W.; Trombelli, L.; Walter, C.; Wimmer, G.; Xenoudi, P.; Yoshie, H. Periodontal health and gingival diseases and conditions on an intact and a reduced periodontium: Consensus report of workgroup 1 of the 2017 World Workshop on the Classification of Periodontal and Peri-Implant Diseases and Conditions. J Clin Periodontol. 2018, 45, S68-S77. doi: 10.1111/jcpe.12940

[52] Tonetti, M. S.; Greenwell, H.; Kornman, K. S. Staging and grading of periodontitis: Framework and proposal of a new classification and case definition. J Clin Periodontol. 2018, 45, S149-S161. doi: 10.1111/jcpe.12945

[53] Lim, G.; Janu, U.; Chiou, L.-L.; Gandhi, K. K.; Palomo, L.; John, V. Periodontal health and systemic conditions. Dent J (Basel). 2020, 8, 130. doi: 10.3390/dj8040130

[54] Kwon, T.; Lamster, I. B.; Levin, L. Current concepts in the management of periodontitis. Int Dent J. 2021, 71, 462-476. doi: 10.1111/idj.12630

[55] Balta, M.; Papathanasiou, E.; Blix, I.; Van Dyke, T. Host modulation and treatment of periodontal disease. J Dent Res. 2021, 100, 798-809. doi: 10.1177/0022034521995157

[56] Caton, J. G.; Armitage, G.; Berglundh, T.; Chapple, I. L.; Jepsen, S.; Kornman, K. S.; Mealey, B. L.; Papapanou, P. N.; Sanz, M.; Tonetti, M. S. A new classification scheme for periodontal and peri-implant diseases and conditions - Introduction and key changes from the 1999 classification. J Clin Periodontol. 2018, 45, S1-S8. doi: 10.1111/jcpe.12935

[57] Mehta, J.; Eaton, C.; AlAmri, M.; Lin, G. H.; Nibali, L. The association between *Aggregatibacter actinomycetemcomitans* JP2 clone and periodontitis: A systematic review and meta-analysis. J Periodontal Res. 2023, 58, 465-482. doi: 10.1111/jre.13102

[58] Trombelli, L.; Farina, R.; Silva, C. O.; Tatakis, D. N. Plaque-induced gingivitis: Case definition and diagnostic considerations. J Clin Periodontol. 2018, 45, S44-S67. doi: 10.1111/jcpe.12939

[59] Papapanou, P. N.; Sanz, M.; Buduneli, N.; Dietrich, T.; Feres, M.; Fine, D. H.; Flemmig, T. F.; Garcia, R.; Giannobile, W. V.; Graziani, F.; Greenwell, H.; Herrera, D.; Kao, R. T.; Kebschull, M.; Kinane, D. F.; Kirkwood, K. L.; Kocher, T.; Kornman, K. S.; Kumar, P. S.; Loos, B. G.; Machtei, E.; Meng, H.; Mombelli, A.; Needleman, I.; Offenbacher, S.; Seymour, G. J.; Teles, R.; Tonetti, M. S. Periodontitis: Consensus report of workgroup 2 of the 2017 World Workshop on the classification of eriodontal and peri-implant diseases and conditions. J Clin Periodontol. 2018, 45, S162-S170. doi: 10.1111/jcpe.12946

[60] Bosshardt, D. D.; Sculean, A. Does periodontal tissue regeneration really work? Periodontol 2000. 2009, 51, 208-219. doi: 10.1111/j.1600-0757.2009.00317.x.

[61] Plessas, A. Nonsurgical periodontal treatment: review of the evidence. Oral Health Dent Manag. 2014, 13, 71-80. doi: -

[62] Shue, L.; Yufeng, Z.; Mony, U. Biomaterials for periodontal regeneration: a review of ceramics and polymers. Biomatter. 2012, 2, 271-277. doi: 10.4161/biom.22948

[63] Kormas, I.; Pedercini, C.; Pedercini, A.; Raptopoulos, M.; Alassy, H.; Wolff, L. F. Peri-implant diseases: diagnosis, clinical, histological, microbiological characteristics and treatment strategies. A narrative review. Antibiotics. 2020, 9, 835. doi: 10.3390/antibiotics9110835

[64] Darby, I. Risk factors for periodontitis & peri-implantitis. Periodontol 2000. 2022, 90, 9-12. doi: 10.1111/prd.12447

[65] Jepsen, S.; Caton, J. G.; Albandar, J. M.; Bissada, N. F.; Bouchard, P.; Cortellini, P.; Demirel, K.; de Sanctis, M.; Ercoli, C.; Fan, J.; Geurs, N. C.; Hughes, F. J.; Jin, L.; Kantarci, A.; Lalla, E.; Madianos, P. N.; Matthews, D.; McGuire, M. K.; Mills, M. P.; Preshaw, P. M.; Reynolds, M. A.; Sculean, A.; Susin, C.; West, N. X.; Yamazaki, K. Periodontal manifestations of systemic diseases and developmental and acquired conditions: Consensus report of workgroup 3 of the 2017 World Workshop on the Classification of Periodontal and Peri-Implant Diseases and Conditions. J Clin Periodontol. 2018, 45, S219-S229. doi: 10.1111/jcpe.12951

[66] Sanz, M.; Marco del Castillo, A.; Jepsen, S.; Gonzalez-Juanatey, J. R.; D'Aiuto, F.; Bouchard, P.; Chapple, I.; Dietrich, T.; Gotsman, I.; Graziani, F.; Herrera, D.; Loos, B.; Madianos, P.; Michel, J.-B.; Perel, P.; Pieske, B.; Shapira, L.; Shechter, M.; Tonetti, M.; Vlachopoulos, C.; Wimmer, G. Periodontitis and cardiovascular diseases: Consensus report. J Clin Periodontol. 2020, 47, 268-288. doi: 10.1111/jcpe.13189

[67] Trindade, D.; Carvalho, R.; Machado, V.; Chambrone, L.; Mendes, J. J.; Botelho, J. Prevalence of periodontitis in dentate people between 2011 and 2020: a systematic review and meta-analysis of epidemiological studies. J Clin Periodontol. 2023, 50, 604-626. doi: 10.1111/jcpe.13769

[68] Gazil, V.; Bandiaky, O. N.; Renard, E.; Idiri, K.; Struillou, X.; Soueidan, A. Current data on oral peri-implant and periodontal microbiota and its pathological changes: A systematic review. Microorganisms. 2022, 10, 2466. doi: 10.3390/microorganisms10122466

[69] Moy, P. K.; Aghaloo, T. Risk factors in bone augmentation procedures. Periodontol 2000. 2019, 81, 76-90. doi: 10.1111/prd.12285

[70] Lauritano, D.; Limongelli, L.; Moreo, G.; Favia, G.; Carinci, F. Nanomaterials for periodontal tissue engineering: chitosan-based scaffolds. A systematic review. Nanomaterials. 2020, 10, 605. doi: 10.3390/nano10040605

[71] Liao, F.; Chen, Y.; Li, Z.; Wang, Y.; Shi, B.; Gong, Z.; Cheng, X. A novel bioactive three-dimensional β-tricalcium phosphate/chitosan scaffold for periodontal tissue engineering. J Mater Sci Mater Med. 2010, 21, 489-496. doi: 10.1007/s10856-009-3931-x

[72] Soares, M. P. C. M.; Soares, P. V.; Pereira, A. G.; Moura, C. C. G.; Soares, P. B. F.; Naves, L. Z.; de Magalhães, D. Biocompatibility of three bioabsorbable membranes assessed in FGH fibroblasts and human osteoblast like cells culture. Head Face Med. 2014, 10, 1-6. doi: 10.1186/1746-160X-10-29

[73] Wang HL; Greenwell H; Fiorellini J; Giannobile W; Offenbacher S; Salkin L; Townsend C; Sheridan P; RJ;, G.; Research, S. a. T. C. Periodontal regeneration. J Periodontol. 2005, 76, 1601-22. doi: 10.1902/jop.2005.76.9.1601

[74] Akita, D.; Morokuma, M.; Saito, Y.; Yamanaka, K.; Akiyama, Y.; Sato, M.; Mashimo, T.; Toriumi, T.; Arai, Y.; Kaneko, T. Periodontal tissue regeneration by transplantation of rat adipose-derived stromal cells in combination with PLGA-based solid scaffolds. Biomed Res. 2014, 35, 91-103. doi: 10.2220/biomedres.35.91

[75] Pilloni, A.; Pompa, G.; Saccucci, M.; Di Carlo, G.; Rimondini, L.; Brama, M.; Zeza, B.; Wannenes, F.; Migliaccio, S. Analysis of human alveolar osteoblast behavior on a nano-hydroxyapatite substrate: an *in vitro* study. BMC Oral Health. 2014, 14, 1-7. doi: 10.1186/1472-6831-14-22

[76] Bucchi, C.; Del Fabbro, M.; Arias, A.; Fuentes, R.; Mendes, J. M.; Ordonneau, M.; Orti, V.; Manzanares-Céspedes, M.-C. Multicenter study of patients' preferences and concerns regarding the origin of bone grafts utilized in dentistry. Patient Prefer Adherence. 2019, 18, 179-185. doi: 10.2147/PPA.S186846

[77] Gill, S.; Prakash, M.; Forghany, M.; Vaderhobli, R. M. An ethical perspective to using bone grafts in dentistry. J Am Dent Assoc. 2022, 153, 88-91. doi: 10.1016/j.adaj.2021.09.011

[78] Zhao, R.; Yang, R.; Cooper, P. R.; Khurshid, Z.; Shavandi, A.; Ratnayake, J. Bone grafts and substitutes in dentistry: A review of current trends and developments. Molecules. 2021, 26, 3007. doi: 10.3390/molecules26103007

[79] Rai, J. J.; Kalantharakath, T. Biomimetic ceramics for periodontal regeneration in infrabony defects: A systematic review. J Int Soc Prev Community Dent. 2014, 4, S78. doi: 10.4103/2231-0762.146207

[80] Jones, J. R. Review of bioactive glass: from Hench to hybrids. Acta Biomater. 2013, 9, 4457-4486. doi: 10.1016/j.actbio.2012.08.023

[81] Salem, D.; Natto, Z.; Elangovan, S.; Karimbux, N. Usage of bone replacement grafts in periodontics and oral implantology and their current levels of clinical evidence—A systematic assessment. J Periodontol. 2016, 87, 872-879. doi: 10.1902/jop.2016.150512

[82] He, X.; Liu, Y.; Yuan, X.; Lu, L. Enhanced healing of rat calvarial defects with MSCs loaded on BMP-2 releasing chitosan/alginate/hydroxyapatite scaffolds. PloS One. 2014, 9, e104061. doi: 10.1371/journal.pone.0104061

[83] Zhang, X.; Zhu, L.; Lv, H.; Cao, Y.; Liu, Y.; Xu, Y.; Ye, W.; Wang, J. Repair of rabbit femoral condyle bone defects with injectable nanohydroxyapatite/chitosan composites. J Mater Sci Mater Med. 2012, 23, 1941-1949. doi: 10.1007/s10856-012-4662-y

[84] Swetha, M.; Sahithi, K.; Moorthi, A.; Srinivasan, N.; Ramasamy, K.; Selvamurugan, N. Biocomposites containing natural polymers and hydroxyapatite for bone tissue engineering. Int J Biol Macromol. 2010, 47, 1-4. doi: 10.1016/j.ijbiomac.2010.03.015

[85] Wang, L.; Li, C.; Chen, Y.; Dong, S.; Chen, X.; Zhou, Y. Poly (lactic-co-glycolic) acid/nanohydroxyapatite scaffold containing chitosan microspheres with adrenomedullin delivery for modulation activity of osteoblasts and vascular endothelial cells. Biomed Res Int. 2013, 2013, doi: 10.1155/2013/530712

[86] Bellucci, D.; Sola, A.; Gazzarri, M.; Chiellini, F.; Cannillo, V. A new hydroxyapatite-based biocomposite for bone replacement. Mater Sci Eng C Mater Biol Appl. 2013, 33, 1091-1101. doi: 10.1016/j.msec.2012.11.038

[87] Williams, D. F.; Black, J.; Doherty, P. J. Advances in Biomateriais: Biomaterial-Tissue Interfaces. In Second consensus conference on definitions in biomateriais, Doherty, P. J.; Williams, R. L.; Williams, D. F., Eds.; Elsevier Science Publishers: Amsterdam, 1992; 10, 525-533. doi: -

[88] International Organization for Standardization. ISO 10993-1:2018(E). Biological evaluation of medical devices — Part 1: Evaluation and testing within a risk management process. Switzerland. 2018.

[89] Regulation (EU) 2017/745 of the European Parliment and of the Council of 5 April 2017 on medical devices. 2017

[90] Rahaman, M. N.; Day, D. E.; Bal, B. S.; Fu, Q.; Jung, S. B.; Bonewald, L. F.; Tomsia, A. P. Bioactive glass in tissue engineering. Acta Biomater. 2011, 7, 2355-2373. doi: 10.1016/j.actbio.2011.03.016

[91] Seyedmajidi, M.; Rabiee, S.; Haghanifar, S.; Seyedmajidi, S.; Alaghehmand, H.; Jamaatlu, N.; Bijani, A. Histopathological, Histomorphometrical, and Radiographical Evaluation of Injectable Glass-Ceramic-Chitosan Nanocomposite in Bone Reconstruction of Rat. Int J Biomater. 2015, 2015, doi: 10.1155/2015/719574

[92] Liu, H.; Peng, H.; Wu, Y.; Zhang, C.; Cai, Y.; Xu, G.; Li, Q.; Chen, X.; Ji, J.; Zhang, Y. The promotion of bone regeneration by nanofibrous hydroxyapatite/chitosan scaffolds by effects on integrin-BMP/Smad signaling pathway in BMSCs. Biomaterials. 2013, 34, 4404-4417. doi: 10.1016/j.biomaterials.2013.02.048

[93] Soleymani, S.; Naghib, S. M. 3D and 4D printing hydroxyapatite-based scaffolds for bone tissue engineering and regeneration. Heliyon. 2023, 9, e19363. doi: 10.1016/j.heliyon.2023.e19363

[94] Tsiourvas, D.; Sapalidis, A.; Papadopoulos, T. Hydroxyapatite/chitosan-based porous three-dimensional scaffolds with complex geometries. Mater. Today Commun. 2016, 7, 59-66. doi: 10.1016/j.mtcomm.2016.03.006

[95] Boccaccini, A. R.; Erol, M.; Stark, W. J.; Mohn, D.; Hong, Z.; Mano, J. F. Polymer/bioactive glass nanocomposites for biomedical applications: a review. Compos Sci Technol. 2010, 70, 1764-1776. doi: 10.1016/j.compscitech.2010.06.002

[96] Lee, J. S.; Baek, S. D.; Venkatesan, J.; Bhatnagar, I.; Chang, H. K.; Kim, H. T.; Kim, S.-K. *In vivo* study of chitosan-natural nano hydroxyapatite scaffolds for bone tissue regeneration. Int J Biol Macromol. 2014, 67, 360-366. doi: 10.1016/j.ijbiomac.2014.03.053

[97] Qasim, S. B.; Delaine-Smith, R. M.; Fey, T.; Rawlinson, A.; Rehman, I. U. Freeze gelated porous membranes for periodontal tissue regeneration. Acta Biomater. 2015, 23, 317-328. doi: 10.1016/j.actbio.2015.05.001

[98] Laranjeira, M.; Fernandes, M.; Monteiro, F. Response of monocultured and co-cultured human microvascular endothelial cells and mesenchymal stem cells to macroporous granules of nanostructured-hydroxyapatite agglomerates. J Biomed Nanotechnol. 2013, 9, 1594-1606. doi: 10.1166/jbn.2013.1664

[99] Laranjeira, M.; Fernandes, M.; Monteiro, F. Innovative macroporous granules of nanostructured-hydroxyapatite agglomerates: Bioactivity and osteoblast-like cell behaviour. J Biomed Mater Res A. 2010, 95, 891-900. doi: 10.1002/jbm.a.32916

[100] Amirazad, H.; Dadashpour, M.; Zarghami, N. Application of decellularized bone matrix as a bioscaffold in bone tissue engineering. J Biol Eng. 2022, 16, 1-18. doi: 10.1186/s13036-021-00282-5

[101] Chatzipetros, E.; Yfanti, Z.; Christopoulos, P.; Donta, C.; Damaskos, S.; Tsiambas, E.; Tsiourvas, D.; Kalogirou, E.-M.; Tosios, K. I.; Tsiklakis, K. Imaging of nano-hydroxyapatite/chitosan scaffolds using a cone beam computed tomography device on rat calvarial defects with histological verification. Clin Oral Investig. 2020, 24, 437-446. doi: 10.1007/s00784-019-02939-4

[102] Croisier, F.; Jérôme, C. Chitosan-based biomaterials for tissue engineering. European Polym J. 2013, 49, 780-792. doi: 10.1016/j.eurpolymj.2012.12.009

[103] Martins, M.; Barros, A. A.; Quraishi, S.; Gurikov, P.; Raman, S.; Smirnova, I.; Duarte, A. R. C.; Reis, R. L. Preparation of macroporous alginate-based aerogels for biomedical applications. J Supercrit Fluids. 2015, 106, 152-159. doi: 10.1016/j.supflu.2015.05.010

[104] Chen, C.; Li, H.; Pan, J.; Yan, Z.; Yao, Z.; Fan, W.; Guo, C. Biodegradable composite scaffolds of bioactive glass/chitosan/carboxymethyl cellulose for hemostatic and bone regeneration. Biotechnol Lett. 2015, 37, 457-465. doi: 10.1007/s10529-014-1697-9

[105] Correia, C. O.; Leite, Á. J.; Mano, J. F. Chitosan/bioactive glass nanoparticles scaffolds with shape memory properties. Carbohydr Polym. 2015, 123, 39-45. doi: 10.1016/j.carbpol.2014.12.076

[106] Song, F.; Koo, H.; Ren, D. Effects of material properties on bacterial adhesion and biofilm formation. J Dent Res. 2015, 94, 1027-1034. doi: 10.1177/0022034515587690

[107] International Organization for Standardization. ISO 22442-3:2007(E). Medical devices utilizing animal tissues and their derivatives — Part 3: Validation of the elimination and/or inactivation of viruses and transmissible spongiform encephalopathy (TSE) agents. Switzerland. 2007.

[108] International Organization for Standardization. ISO 14971:2007(E). Medical devices — Application of risk management to medical devices. Switzerland. 2007.

[109] Jiang, H.; Zuo, Y.; Zou, Q.; Wang, H.; Du, J.; Li, Y.; Yang, X. Biomimetic spiral-cylindrical scaffold based on hybrid chitosan/cellulose/nano-hydroxyapatite membrane for bone regeneration. ACS Appl Mater Interfaces. 2013, 5, 12036-12044. doi: 10.1021/am4038432

[110] Yang, J.; Han, S.; Zheng, H.; Dong, H.; Liu, J. Preparation and application of micro/nanoparticles based on natural polysaccharides. Carbohydr Polym. 2015, 123, 53-66. doi: 10.1016/j.carbpol.2015.01.029

[111] Campos, D. M.; Gritsch, K.; Salles, V.; Attik, G. N.; Grosgogeat, B. Surface entrapment of fibronectin on electrospun PLGA scaffolds for periodontal tissue engineering. Biores Open Access. 2014, 3, 117-126. doi: 10.1089/biores.2014.0015

[112] Said, H. A.; Mabroum, H.; Lahcini, M.; Oudadesse, H.; Barroug, A.; Youcef, H. B.; Noukrati, H. Manufacturing methods, properties, and potential applications in bone tissue regeneration of hydroxyapatite-chitosan biocomposites: A review. Int J Biol Macromol. 2023, 125150. doi: 10.1016/j.ijbiomac.2023.125150

[113] Kang, Y.; Xu, J.; Su, Y.; Fang, H.; Liu, J.; Cheng, Y. Y.; Jiang, D.; Nie, Y.; Song, K. 3D bioprinting of dECM/Gel/QCS/nHAp hybrid scaffolds laden with mesenchymal stem cell-derived exosomes to improve angiogenesis and osteogenesis. Biofabrication. 2023, 15, 024103. doi: 10.1088/1758-5090/acb6b8

[114] Li, L.; Wang, P.; Liang, H.; Jin, J.; Zhang, Y.; Shi, J.; Zhang, Y.; He, S.; Mao, H.; Xue, B. Design of a Haversian system-like gradient porous scaffold based on triply periodic minimal surfaces for promoting bone regeneration. J Adv Res. 2023, doi: 10.1016/j.jare.2023.01.004

[115] Sun, Q.; Yu, L.; Zhang, Z.; Qian, C.; Fang, H.; Wang, J.; Wu, P.; Zhu, X.; Zhang, J.; Zhong, L. A novel gelatin/carboxymethyl chitosan/nano-hydroxyapatite/β-tricalcium phosphate biomimetic nanocomposite scaffold for bone tissue engineering applications. Front Chem. 2022, 10, 958420. doi: 10.3389/fchem.2022.958420

[116] Shen, S.; Fu, D.; Xu, F.; Long, T.; Hong, F.; Wang, J. The design and features of apatite-coated chitosan microspheres as injectable scaffold for bone tissue engineering. Biomed Mater. 2013, 8, 025007. doi: 10.1088/1748-6041/8/2/025007

[117] Song, J. M.; Shin, S. H.; Kim, Y. D.; Lee, J. Y.; Baek, Y. J.; Yoon, S. Y.; Kim, H. S. Comparative study of chitosan/fibroin–hydroxyapatite and collagen membranes for guided bone regeneration in rat calvarial defects: micro-computed tomography analysis. Int J Oral Sci. 2014, 6, 87-93. doi: 10.1038/ijos.2014.16

[118] Xu, C.; Lei, C.; Meng, L.; Wang, C.; Song, Y. Chitosan as a barrier membrane material in periodontal tissue regeneration. J Biomed Mater Res B Appl Biomater. 2012, 100, 1435-1443. doi: 10.1002/jbm.b.32662

[119] Dessì, M.; Borzacchiello, A.; Mohamed, T. H.; Abdel-Fattah, W. I.; Ambrosio, L. Novel biomimetic thermosensitive β-tricalcium phosphate/chitosan-based hydrogels for bone tissue engineering. J Biomed Mater Res A. 2013, 101, 2984-2993. doi: 10.1002/jbm.a.34592

[120] Barbosa, J. N.; Amaral, I. F.; Aguas, A. P.; Barbosa, M. A. Evaluation of the effect of the degree of acetylation on the inflammatory response to 3D porous chitosan scaffolds. J Biomed Mater Res A. 2010, 93, 20-28. doi: 10.1002/jbm.a.32499

[121] Vasconcelos, D. P.; Fonseca, A. C.; Costa, M.; Amaral, I. F.; Barbosa, M. A.; Águas, A. P.; Barbosa, J. N. Macrophage polarization following chitosan implantation. Biomaterials. 2013, 34, 9952-9959. doi: 10.1016/j.biomaterials.2013.09.012

[122] Amaral, I.; Cordeiro, A.; Sampaio, P.; Barbosa, M. Attachment, spreading and short-term proliferation of human osteoblastic cells cultured on chitosan films with different degrees of acetylation. J Biomater Sci Polym Ed. 2007, 18, 469-485. doi: 10.1163/156856207780425068

[123] Amaral, I.; Sampaio, P.; Barbosa, M. Three-dimensional culture of human osteoblastic cells in chitosan sponges: The effect of the degree of acetylation. J Biomed Mater Res A. 2006, 76, 335-346. doi: 10.1002/jbm.a.30522

[124] Saravanan, S.; Nethala, S.; Pattnaik, S.; Tripathi, A.; Moorthi, A.; Selvamurugan, N. Preparation, characterization and antimicrobial activity of a bio-composite scaffold containing chitosan/nano-hydroxyapatite/nano-silver for bone tissue engineering. Int J Biol Macromol. 2011, 49, 188-193. doi: 10.1016/j.ijbiomac.2011.04.010

[125] Sadeghianmaryan, A.; Naghieh, S.; Yazdanpanah, Z.; Sardroud, H. A.; Sharma, N.; Wilson, L. D.; Chen, X. Fabrication of chitosan/alginate/hydroxyapatite hybrid scaffolds using 3D printing and impregnating techniques for potential cartilage regeneration. Int J Biol Macromol. 2022, 204, 62-75. doi: 10.1016/j.ijbiomac.2022.01.201

[126] Bueno, E. M.; Glowacki, J. Cell-free and cell-based approaches for bone regeneration. Nat Rev Rheumatol. 2009, 5, 685-697. doi: 10.1038/nrrheum.2009.228

[127] Lee, Y.-T.; Yu, B.-Y.; Shao, H.-J.; Chang, C.-H.; Sun, Y.-M.; Liu, H.-C.; Hou, S.-M.; Young, T.-H. Effects of the surface characteristics of nano-crystalline and micro-particle calcium phosphate/chitosan composite films on the behavior of human mesenchymal stem cells *in vitro*. J Biomater Sci Polym Ed. 2011, 22, 2369-2388. doi: 10.1163/092050610X540431

[128] Jun, S.-H.; Lee, E.-J.; Jang, T.-S.; Kim, H.-E.; Jang, J.-H.; Koh, Y.-H. Bone morphogenic protein-2 (BMP-2) loaded hybrid coating on porous hydroxyapatite scaffolds for bone tissue engineering. J Mater Sci Mater Med. 2013, 24, 773-782. doi: 10.1007/s10856-012-4822-0

[129] Radulescu, D.-E.; Vasile, O. R.; Andronescu, E.; Ficai, A. Latest Research of Doped Hydroxyapatite for Bone Tissue Engineering. Int J Mol Sci. 2023, 24, 13157. doi: 10.3390/ijms241713157

[130] Wang, Y.; Lv, P.; Ma, Z.; Zhang, J. Enhanced Healing of Rat Calvarial Critical Size Defect with Selenium-Doped Lamellar Biocomposites. Biol Trace Elem Res. 2013, 155, 72-81. doi: 10.1007/s12011-013-9763-z

[131] Huang, B.; Chen, M.; Tian, J.; Zhang, Y.; Dai, Z.; Li, J.; Zhang, W. Oxygen-Carrying and Antibacterial Fluorinated Nano-Hydroxyapatite Incorporated Hydrogels for Enhanced Bone Regeneration. Adv Healthc Mater. 2022, 11, 2102540. doi: 10.1002/adhm.202102540

[132] Kokubo, T.; Takadama, H. How useful is SBF in predicting in vivo bone bioactivity? Biomaterials. 2006, 27, 2907-2915. doi: 10.1016/j.biomaterials.2006.01.017

[133] Figliuzzi, M. M.; De Fazio, R.; Tiano, R.; De Franceschi, S.; Pacifico, D.; Mangano, F.; Fortunato, L. Histological evaluation of a biomimetic material in bone regeneration after one year from graft. Ann Stomatol (Roma). 2014, 5, 103. doi: -

[134] Azevedo, A.; Sá, M.; Fook, M.; Neto, P. N.; Sousa, O.; Azevedo, S.; Teixeira, M.; Costa, F.; Araújo, A. Use of chitosan and β-tricalcium phosphate, alone and in combination, for bone healing in rabbits. J Mater Sci Mater Med. 2014, 25, 481-486. doi: 10.1007/s10856-013-5091-2

[135] Nguyen, D.; McCanless, J.; Mecwan, M.; Noblett, A.; Haggard, W.; Smith, R.; Bumgardner, J. Balancing mechanical strength with bioactivity in chitosan–calcium phosphate 3D microsphere scaffolds for bone tissue engineering: air-vs. freeze-drying processes. J Biomater Sci Polym Ed. 2013, 24, 1071-1083. doi: 10.1080/09205063.2012.735099

[136] Fonseca-García, A.; Mota-Morales, J. D.; Quintero-Ortega, I. A.; García-Carvajal, Z. Y.; Martínez-López, V.; Ruvalcaba, E.; Landa-Solís, C.; Solis, L.; Ibarra, C.; Gutiérrez, M. C. Effect of doping in carbon nanotubes on the viability of biomimetic chitosan-carbon nanotubes-hydroxyapatite scaffolds. J Biomed Mater Res A. 2014, 102, 3341-3351. doi: 10.1002/jbm.a.34893

[137] Yan, L. P.; Wang, Y. J.; Ren, L.; Wu, G.; Caridade, S. G.; Fan, J. B.; Wang, L. Y.; Ji, P. H.; Oliveira, J. M.; Oliveira, J. T.; Mano, J. F.; Reis, R. L. Genipin-cross-linked collagen/chitosan biomimetic scaffolds for articular cartilage tissue engineering applications. J Biomed Mater Res A. 2010, 95, 465-475. doi: 10.1002/jbm.a.32869

[138] Li, L.; Li, B.; Zhao, M.; Ding, S.; Zhou, C. Single-step mineralization of woodpile chitosan scaffolds with improved cell compatibility. J Biomed Mater Res B Appl Biomater. 2011, 98, 230-237. doi: 10.1002/jbm.b.31811

[139] Xu, H. H.; Burguera, E. F.; Carey, L. E. Strong, macroporous, and *in situ*-setting calcium phosphate cement-layered structures. Biomaterials. 2007, 28, 3786-3796. doi: 10.1016/j.biomaterials.2007.05.015

[140] García-González, C. A.; Concheiro, A.; Alvarez-Lorenzo, C. Processing of materials for regenerative medicine using supercritical fluid technology. Bioconjug Chem. 2015, 26, 1159-1171. doi: 10.1021/bc5005922

[141] Cao, L.; Su, H.; Si, M.; Xu, J.; Chang, X.; Lv, J.; Zhai, Y. Tissue engineering in stomatology: a review of potential approaches for oral disease treatments. Front Bioeng Biotechnol. 2021, 9, 662418. doi: 10.3389/fbioe.2021.662418

[142] Spilimbergo, S.; Bertucco, A.; Lauro, F.; Bertoloni, G. Inactivation of *Bacillus subtilis* spores by supercritical CO_2 treatment. Innov Food Sci Emerg Technol. 2003, 4, 161-165. doi: 10.1016/S1466-8564(02)00089-9

[143] Soares, G. C.; Learmonth, D. A.; Vallejo, M. C.; Davila, S. P.; González, P.; Sousa, R. A.; Oliveira, A. L. Supercritical CO_2 technology: The next standard sterilization technique? Mater Sci Eng C Mater Biol Appl. 2019, 99, 520-540. doi: 10.1016/j.msec.2019.01.121

[144] Zhang, J.; Davis, T. A.; Matthews, M. A.; Drews, M. J.; LaBerge, M.; An, Y. H. Sterilization using high-pressure carbon dioxide. J Supercrit Fluids. 2006, 38, 354-372. doi: 10.1016/j.supflu.2005.05.005

[145] Gomes, P. B.; Mata, V. G.; Rodrigues, A. E. Production of rose geranium oil using supercritical fluid extraction. J Supercrit Fluids. 2007, 41, 50-60. doi: 10.1016/j.supflu.2006.08.018

[146] Ribeiro, N.; Soares, G. C.; Santos-Rosales, V.; Concheiro, A.; Alvarez-Lorenzo, C.; García-González, C. A.; Oliveira, A. L. A new era for sterilization based on supercritical CO_2 technology. J Biomed Mater Res B Appl Biomater. 2020, 108, 399-428. doi: 10.1002/jbm.b.34398

[147] Wehmeyer, J. L.; Natesan, S.; Christy, R. J. Development of a sterile amniotic membrane tissue graft using supercritical carbon dioxide. Tissue Eng Part C Methods. 2015, 21, 649-659. doi: 10.1089/ten.TEC.2014.0304

[148] Pitrolino, K. A.; Felfel, R. M.; Pellizzeri, L. M.; McLaren, J.; Popov, A. A.; Sottile, V.; Scotchford, C. A.; Scammell, B. E.; Roberts, G. A.; Grant, D. M. Development and *in vitro* assessment of a bi-layered chitosan-nano-hydroxyapatite osteochondral scaffold. Carbohydr Polym. 2022, 282, 119126. doi: 10.1016/j.carbpol.2022.119126

[149] He, Y.; Dong, Y.; Cui, F.; Chen, X.; Lin, R. Ectopic osteogenesis and scaffold biodegradation of nano-hydroxyapatite-chitosan in a rat model. PLoS One. 2015, 10, e0135366. doi: 10.1371/journal.pone.0135366

[150] Kumar, P.; Saini, M.; Dehiya, B. S.; Umar, A.; Sindhu, A.; Mohammed, H.; Al-Hadeethi, Y.; Guo, Z. Fabrication and *in-vitro* biocompatibility of freeze-dried CTS-nHA and CTS-nBG scaffolds for bone regeneration applications. Int J Biol Macromol. 2020, 149, 1-10. doi: 10.1016/j.ijbiomac.2020.01.035

[151] Hu, X.; Zheng, S.; Zhang, R.; Wang, Y.; Jiao, Z.; Li, W.; Nie, Y.; Liu, T.; Song, K. Dynamic process enhancement on chitosan/gelatin/nano-hydroxyapatite-bone derived multilayer scaffold for osteochondral tissue repair. Biomater Adv. 2022, 133, 112662. doi: 10.1016/j.msec.2022.112662

[152] Lazarevic, M.; Petrovic, S.; Pierfelice, T. V.; Ignjatovic, N.; Piattelli, A.; Vlajic Tovilovic, T.; Radunovic, M. Antimicrobial and Osteogenic Effects of Collagen Membrane Decorated with Chitosan–Nano-Hydroxyapatite. Biomolecules. 2023, 13, 579. doi: 10.3390/biom13040579

[153] Samie, M.; Khan, A. F.; Rahman, S. U.; Iqbal, H.; Yameen, M. A.; Chaudhry, A. A.; Galeb, H. A.; Halcovitch, N. R.; Hardy, J. G. Drug/bioactive eluting chitosan composite foams for osteochondral tissue engineering. Int J Biol Macromol. 2023, 229, 561-574. doi: 10.1016/j.ijbiomac.2022.12.293

[154] Sun, T. W.; Yu, W. L.; Zhu, Y. J.; Chen, F.; Zhang, Y. G.; Jiang, Y. Y.; He, Y. H. Porous Nanocomposite Comprising Ultralong Hydroxyapatite Nanowires Decorated with Zinc-Containing Nanoparticles and Chitosan: Synthesis and Application in Bone Defect Repair. Chemistry. 2018, 24, 8809-8821. doi: 10.1002/chem.201800425

CHAPTER III

Bioengineering Composite Aerogel-Based Scaffolds That Influence Porous Microstructure, Mechanical Properties and *In Vivo* Regeneration for Bone Tissue Application

Bioengineering Composite Aerogel-Based Scaffolds That Influence Porous Microstructure, Mechanical Properties and *In Vivo* Regeneration for Bone Tissue Application

Souto-Lopes M [a,b,c], Fernandes MH [d,e], Monteiro FJ [a,b,c,f], Salgado CL [a,b]

a – i3S – Instituto de Investigação e Inovação em Saúde da Universidade do Porto, R. Alfredo Allen 208, 4200-135 Porto, Portugal

b – INEB Instituto de Engenharia Biomédica, Universidade do Porto, R. Alfredo Allen 208, 4200-135 Porto, Portugal

c – Faculty of Engineering of the University of Porto, Rua Dr. Roberto Frias, 4200-465 Porto, Portugal

d – Faculty of Dental Medicine of the University of Porto, R. Dr. Manuel Pereira da Silva, 4200-393 Porto, Portugal

e – LAQV/REQUIMTE – Laboratório Associado para a Química Verde/ Rede de Química e Tecnologia, Portugal

f – Porto Comprehensive Cancer Center (P.CCC), R. Dr. António Bernardino de Almeida, 4200-072, Porto, Portugal

Materials, 2023, 16:4483. doi: 10.3390/ma16124483.

ABSTRACT

Tissue regeneration of large bone defects is still a clinical challenge. Bone tissue engineering employs biomimetic strategies to produce graft composite scaffolds that resemble the bone extracellular matrix to guide and promote osteogenic differentiation of the host precursor cells. Aerogel-based bone scaffold preparation methods have been increasingly improved to overcome the difficulties in balancing the need for an open highly porous and hierarchically organized microstructure with compression resistance to withstand bone physiological loads, especially in wet conditions. Moreover, these improved aerogel scaffolds have been implanted *in vivo* in critical bone defects, in order to test their bone regeneration potential. This review addresses recently published studies on aerogel composite (organic/inorganic)-based scaffolds, having in mind the various cutting-edge technologies and raw biomaterials used, as well as the improvements that are still a challenge in terms of their relevant properties. Finally, the lack of 3D *in vitro* models of bone tissue for regeneration studies is emphasized, as well as the need for further developments to overcome and minimize the requirement for studies using *in vivo* animal models.

KEYWORDS

Aerogels; Bone regeneration; Composite scaffolds; Porous microstructure; Mechanical properties; Biomaterial

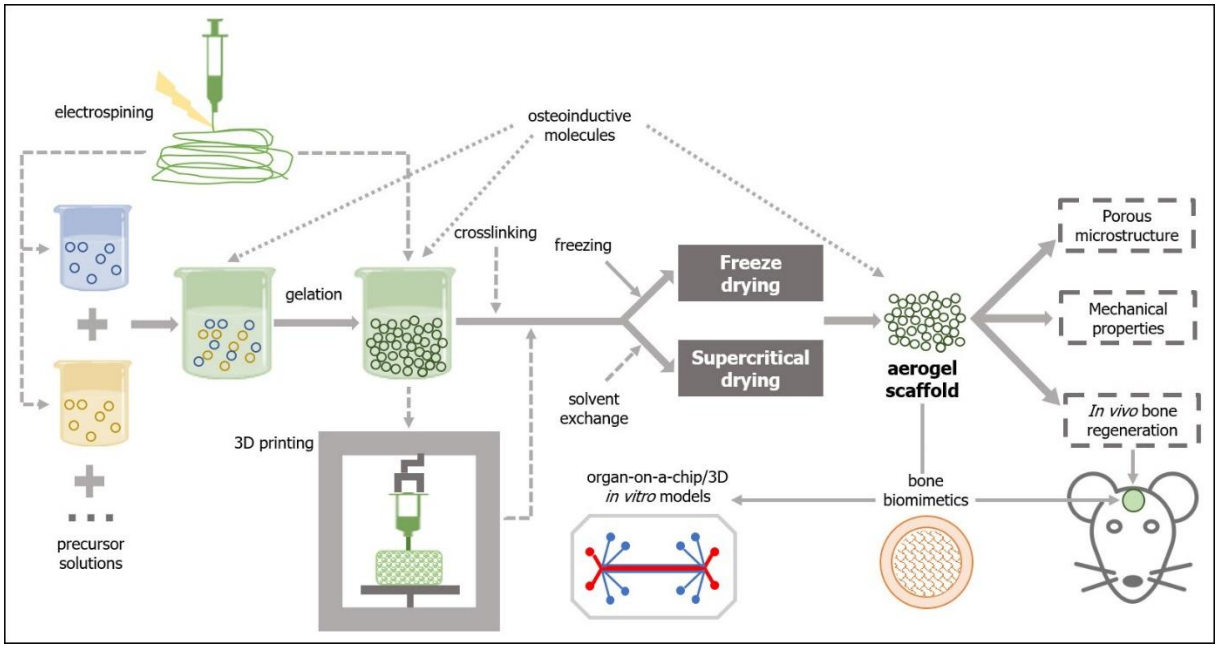

Graphical abstract

1. INTRODUCTION

1.1. Biomimetic graft biomaterials for bone regeneration

Bone is a highly specialized hard connective tissue with a macroscopic and microscopic hierarchical structure that is continuously being remodeled through the concerted activities of bone-forming osteoblasts and bone-resorbing osteoclasts [1]. As schematized in Figure 1, macroscopically, bone encompasses a dense outer layer, the cortical or compact bone, which surrounds the inner highly porous (total porosity of 40 to 90 % [2]) marrow cavity formed by trabecular or cancellous bone [3, 4]. The microscopic arrangement of mature cortical bone is composed of the Harversian canal systems (osteons) surrounded by parallel or concentric lamellar systems [3, 4]. On the other hand, trabeculae and spicules of cancellous bone are extensions of the inner circumferential lamellae of cortical bone into the marrow space, but their lamellar configuration is irregular and does not have osteons [3, 4]. While the lamellae of compact bone enclose a high number of dispersed lacunae, each with an osteocyte and a network of interconnecting canaliculi to maintain cell signaling and bone metabolism, in cancellous bone, the osteocytes inside the lamellae perform metabolic exchanges by diffusion from the bone marrow [3, 4].

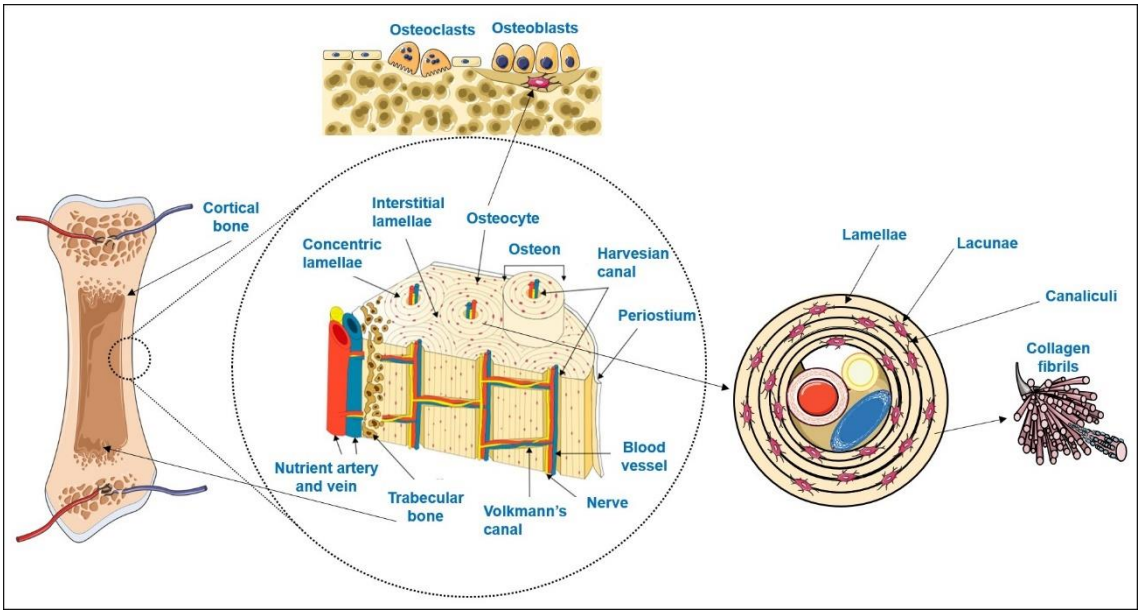

Figure 1. Schematic representation of bone hierarchical macro, micro and nanostructure and main cellular populations (adapted from [5]). Parts of the figure were drawn by using pictures from Servier Medical Art. Servier Medical Art by Servier is licensed under a Creative Commons Attribution 3.0 Unported License (https://creativecommons.org/licenses/by/3.0/).

Osteocytes, the more abundant bone cells, are the mature cells that result from osteoblasts becoming trapped in their own lacunae upon calcification of the extracellular matrix (ECM) [3, 6, 7]. Bone ECM is composed of an organic phase, 30 % w/w, mostly of collagen type I crosslinked fibers secreted by the osteoblasts. On top of these fibers, hydroxyapatite nanocrystals are orderly deposited which, together with amorphous calcium phosphate, comprise the inorganic phase of bone (70 % w/w) [2, 8, 9]. The combination of both organic and inorganic phases decisively contributes to the simultaneous hardness and flexibility of bone, making it able to withstand the forces exerted by physiologic body functions [2, 10, 11].

Though bone is a dynamic tissue that is able to continuously remodel, and also to repair itself in case of injury, some traumatic and pathologic lesions are so extensive that they exceed the organism's regeneration capacity [12-16]. Moreover, with an increasingly aging world population, and increased demand for higher health standards and quality of life, it has become imperative to develop strategies to overcome bone regeneration obstacles [12, 17-19]. Since there are limitations to the use of autografts and allografts for surgical filling of large bone void defects [14-16, 18-20], in recent decades, bone tissue engineering has been developing biomimetic alloplastic graft biomaterials inspired by the above-mentioned macro and microstructure of bone, as well as by its ECM physicochemical features [2, 11, 13, 14, 16, 21, 22].

From a materials science point of view, bone ECM can be considered a composite due to its organic/inorganic synergistic nature [8]. Therefore, efforts have been made to develop bone substitute materials that combine an organic flexible polymeric matrix reinforced by an inorganic dispersed phase [7-10, 20]. Furthermore, the raw materials chosen for the bone graft composition should be biocompatible, as well as bioactive to stimulate osteoprogenitor cells to migrate and differentiate into osteoblasts that will secrete collagen for the new bone tissue [16, 18]. Moreover, the structure and texture of these graft scaffolds should display high hierarchical open porosity, with meso (nano), micro and macropores (100 – 500 µm) to allow the migration and attachment of osteoblasts, as well as the ingrowth of new blood vessels [7, 15, 18, 20, 23] and the circulation of oxygen, nutrients, metabolites and signaling molecules, and consequently a large inner hydrophilic surface area to allow water uptake, protein adsorption and ion exchange [23, 24]. Moreover, bone graft scaffolds should exhibit mechanical properties comparable to native bone (cancellous bone demonstrates compressive strengths ranging between 7 and 10 MPa [25], ultimate tensile strength near 1.2 MPa and bending strength around 8 MPa [9]), which can be promoted by the existence of nanosized pores, to reach ideally 5 – 10 MPa of compressive strength [26].

This review offers an up-to-date overview of the advances in aerogel-based composite biomaterials that provide biomimetic structures for bone regeneration. Recently published data (last 5 years) of aerogel composite scaffolds for bone regeneration are analyzed, and the outcomes are compared in terms of the scaffolds' different production methods, porous microstructure, mechanical properties and *in vivo* bone regeneration capacity.

1.2. Aerogel-based biomaterials

Though the number of scientific publications on aerogel-based materials has been increasing exponentially in the last years (Figure 2a), it is in fact a concept that goes back to 1931, when Kistler produced a highly porous solid material after replacing the liquid phase from a gel by air through supercritical conditions with minimal volume shrinking [27, 28] (usually below 25 %) [28]. Since then, aerogel materials have been developed and applied to a wide variety of scientific and technological areas, e.g., civil engineering, electrical engineering, aerospace engineering, chemical engineering and environmental applications, due to their remarkable physicochemical properties [29, 30]. Most of these materials are silica-based [29] and zeolites [31].

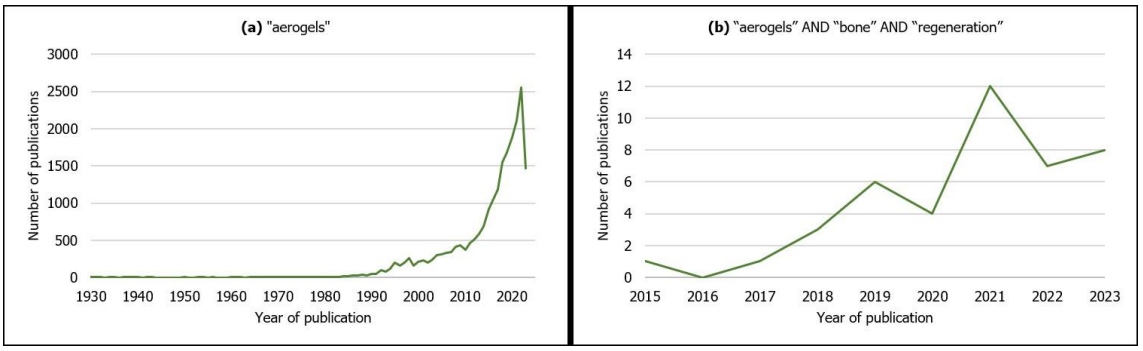

Figure 2. Evolution in the number of publications by year of publication on (a) aerogels from all scientific fields (search keyword: “aerogels”); (b) aerogels for bone regeneration (search keywords: “aerogels” AND “bone” AND “regeneration”). Source: Scopus (search date: 9 June 2023).

According to IUPAC, aerogel is a “gel comprised of a microporous solid in which the dispersed phase is a gas” [31], and additionally exhibits features such as high porosity (> 80 %), open pore network, high mesoporosity [32], low bulk density (< 0.5 $g \cdot cm^{-3}$), high specific surface area (500 – 1200 $m^2 \cdot g^{-1}$), low thermal conductivity, low speed of sound propagation and low dielectric constant [26, 29, 33-35]. More recently, due to these outstanding characteristics, as well as the possibility of using a variety of raw materials in their composition [32, 36], aerogels are also being applied in the biomedical and pharmaceutical fields, namely as scaffolds for tissue regeneration, wound healing dressings, carriers for drug delivery, biosensors for diagnostics [29, 33, 34, 36, 37], antimicrobial activity agents and decontaminating compounds [34]. Accordingly, as observed in Figure 2b, aerogel-based scaffolds are being developed specifically for bone tissue regeneration, resorting to organic natural (silk fibroin, chitosan, cellulose, starch, alginate) [14, 15, 17, 24, 32, 38] or synthetic polymers (poly(e-caprolactone) (PCL)) [17] and inorganic compounds (cellulose nanocrystals, β-tricalcium phosphate, silica, hydroxyapatite) [18, 20, 36, 39], or a combination of both (composite/hybrid) (e.g., silica-silk fibroin) [11, 30, 33].

2. PREPARATION METHODS OF COMPOSITE AEROGELS FOR BONE REGENERATION

Generally, the first step to obtain a composite aerogel is to prepare a homogeneous colloidal solution with the precursor compounds [33, 37]. These precursors can be solely the monomers or precursors dissolved in water or organic solvents [35] or may already include the inorganic phase or other target components (*in situ*) before the sol-gel process [16, 30]. At this stage, polymer gelation occurs through chemical, physical [35] or enzymatic crosslinking [40], forming a wet gel/aquagel [33] (hydrogel [32] in the case the swelling agent is water, alcogel in the case of alcohols [31]). Moreover, gelation can be ionically promoted by biopolymers such as chitosan [7, 15, 24] and alginate in the colloidal solution [41]. Chemical crosslinking tends to form stronger bonds than physical crosslinking [24, 33, 35, 42].

Furthermore, often micro and nanofabrication techniques such as electrospinning and 3D printing have been employed in order to obtain aerogel scaffolds that mimic the ECM 3D morphology with tunable features [10]. Therefore, electrospinning is a versatile technique that may be applied either to the precursor (organic or inorganic) solutions [10, 15, 43-46] or after the sol-gel process [43]. However, the direct deposition of the nanofiber layers obtained by conventional electrospinning results in 2D densely packed nanofiber mats [16, 43, 44, 47] that are inadequate for tissue regeneration [48] and require additional processing methods to obtain 3D scaffolds [16, 43, 47]. Moreover, a frequently used strategy is to cut the as-spun continuous nanofibers into shorter nanofibers [48] to incorporate into scaffolds in order to improve simultaneously compression strength and flexibility [15, 43, 47], as well as to enhance ECM biomimetics [15, 16, 43, 44].

Three-dimensional printing has been rapidly developing due to the need to customize the scaffolds to the irregular shapes of the bone defects through computer-aided design (CAD) technology [21, 23, 39, 41], in a reproducible, automated and scalable way [41]. Additionally, 3D printing enables the manufacturing of scaffolds of various compositions with complex architectures and controlled porous interconnected microstructures [11, 21, 23, 41]. Micro-extrusion-based 3D printing is an additive technique that has been commonly used for producing hydrogels for bone scaffolds, in which adjusting the formulation of the bioink gel (viscosity and rheology) is crucial to obtain an optimized extrudability [11, 41], but at the same time solid enough to maintain its tailored 3D geometry upon layer-by-layer deposition and to achieve maximum shape fidelity and printing accuracy [41].

Finally, in order to obtain a solid material, it is necessary to remove the liquid phase from the wet gel by a method that respects its porous structure, maintains its volume and prevents it from collapsing [33-35]. Therefore, the drying technique is considered the most critical step in aerogel preparation [30]. Furthermore, if the inorganic phase (or other target substance) is not included in the precursor solutions before the sol-gel process, it may be added to the aerogel in an additional final processing step (*ex situ*) by adsorption or precipitation [8], loaded by a liquid or gas phase [30].

Depending on the chosen drying technique, three types of solid porous materials have been distinguished: (1) xerogels are obtained after drying for several days at room temperature and pressure;

(2) cryogels are obtained upon freezing of the wet gel, followed by sublimation of the frozen solvent crystals by freeze drying; (3) aerogels are achieved when drying is accomplished in supercritical (CO_2, ethanol, acetone or methanol) drying conditions [30, 34, 35]. However, in recent years, with advances in materials science, the aerogel concept has been extended to porous materials that may be produced by a liquid phase removal (e.g., freeze drying) [2, 28] and display aerogel-like properties; therefore, this strict classification of solid porous materials based solely on the drying technique may not always be applied [28]. Nevertheless, from the same gel composition it is possible to obtain materials with different final properties according to the performed drying technique, since their properties depend on the final configuration of the porous matrix [28]. Due to the particularities of supercritical drying techniques, these are the ones with the least impact on the gels' structure for obtaining aerogels when compared with other techniques [28]. The most relevant drying techniques employed for aerogel-based scaffolds for bone regeneration are elucidated below.

2.1. Supercritical drying

Supercritical drying is based on the principle that when a certain molecule is simultaneously a liquid and a gas in conditions beyond its specific critical temperature point (T_C) and pressure (P_C), it is in a supercritical state [49, 50]. As a result, the molecule preserves the properties of a liquid (dissolution capacity) and of a gas (high diffusion and low viscosity) [49, 50].

Depending on the nature of the wet gel compounds and respective solvents, two types of supercritical drying may be applied. High-temperature supercritical drying (HTSD) operates at temperatures and pressures higher than the solvent's (usually ethanol) critical point, and this supercritical fluid is slowly extracted from the gel [28, 35]. This technique has been often used to produce silica-based aerogels with large porosity and specific surface and very low densities, as well as other inorganic and metal oxide-based aerogels [35]. However, these conditions imply more operating risks and very often are not appropriate for sensitive biopolymers (e.g., polysaccharide-based polymers such as chitosan and alginate or proteins such as collagen, gelatin and silk-fibroin) [35]. Therefore, low-temperature supercritical drying (LTSD) has been introduced [35], by either dissolving the wet gel organic solvent in soluble CO_2, raising the pressure until CO_2 reaches the supercritical state and flushing it out [28, 33] or by continuously pumping a supercritical CO_2 ($scCO_2$) flow through the wet gel [28].

CO_2 is a fairly widely available and affordable non-inflammable gas [50, 51], which is environmentally friendly and recyclable [50]. The supercritical conditions of CO_2 are T_C 31.1 ºC (304.25 K or 87.98 ºF/near-room temperature) and P_C 7.39 MPa (72.9 atm or 1.071 psi or 73.9 bar), which are relatively mild conditions for sensitive biopolymers [49-52]. Moreover, $scCO_2$ is inert with respect to most polymers, and since it has high density, low viscosity and no surface tension (no capillary forces), it is appropriate for producing highly porous scaffolds [33, 49, 51]. However, in the case of some polysaccharide-based aerogels (e.g., alginate), the solvent used is water (hydrogel) [41], which is poorly

soluble in $scCO_2$. Consequently, in those particular cases, an extra processing step of solvent exchange (for an organic solvent) must be performed before supercritical drying [32, 33, 35, 38, 41]. Nevertheless, LTSD usually takes longer to remove all the solvent from the aerogel than HTSD [35], which may be a drawback in terms of technological scale-up.

Table 1 summarizes the most relevant outcomes in terms of porous configuration, mechanical properties and bone regeneration *in vivo* for supercritical-dried composite aerogels.

Table 1. Aerogel composite scaffolds prepared by $scCO_2$ drying.

References	Material	Preparation Methodology	Porous Properties	*In Vitro* Mechanical Properties	Bone Regeneration *In Vivo* (MicroCT Analysis)
Perez-Moreno *et al.* (2020) [7]	Silica (SiO_2)/chitosan (CS 0, 4, 8, 16, 20 wt.%) (SCS) composite aerogels	Ultrasonic preparation of precursors, ultrasonic sol-gel, aging and solvent exchange, $scCO_2$ drying (40 ºC, 10 MPa)	Pore size (nm): 11.211 (SCS8) – 14.108 (SCS16) (BJH method)	Young's modulus (MPa): 0.66 (SCS16) – 11.57 (SiO_2)	-
Perez-Moreno *et al.* (2023) [53]	Chitosan (CS 8 wt.%)-silica (SiO_2) hybrid	Ultrasonic preparation of precursors, ultrasonic sol-gel, aging and solvent exchange, $scCO_2$ drying (40 ºC, 10 MPa)	Pore size (nm): 16.9 (SiO_2A), 17.3 (SCS8A) (BJH method)	Young's modulus (MPa): 30.81 (SG15) – 78.55 (SG30) (dry); 1.65 (SG30) – 3.71 (SG15) (wet)	-
Reyes-Peces *et al.* (2023) [54]	Hybrid silica-3-glycidoxypropyltrimethoxysilane (GPTMS)-gelatin (SG) (15, 25, 30 wt.% of gelatin content)-based aerogel	One-step sol-gel (with crosslinking), $scCO_2$ drying (90 bar, 40 ºC)	Mean pore diameter (nm): 8.6 (SG30) – 10.8 (SG15) (BJH method)	Young's modulus (MPa): 30.81 (SG15) – 78.55 (SG30) (dry); 1.65 (SG30) – 3.71 (SG15) (wet) Compressive strength (MPa): 3.69 (SG15) – 9.90 (SG30) (dry); 0.10 (SG30) – 0.33 (SG15) (wet) Maximum compressive strain (%): 14.06 (SG30) – 27.67 (SG25) (dry); 4.08 (SG30) – 4.55 (SG15) (wet)	-

Table 1. *cont.*

References	Material	Preparation Methodology	Porous Properties	*In Vitro* Mechanical Properties	Bone Regeneration *In Vivo* (MicroCT Analysis)
Iglesias-Mejuto *et al.* (2021) [41]	3D-printed alginate (Alg 6 %)-hydroxyapatite (HA 0, 8, 16, 24 wt.%) aerogel scaffolds	Sol-gel to obtain bioinks, 3D printing of hydrogels, gelation, conversion into alcogels, $scCO_2$ drying (40 ºC, CO_2 flow rate 5 – 7 g/min, 120 bar, 4 h)	Mean pore diameter (nm): 19 (Alg 6 %, HA 0 %, $CaCl_2$ 1 M) – 31 (Alg 6 %, HA 24 %, $CaCl_2$ 1 M) (BJH method) Macropores (SEM imaging) Total porosity (%): 80.33 (Alg 6 %, HA 24 %, $CaCl_2$ 1 M) – 88.56 (Alg 6 %, HA 0 %, $CaCl_2$ 1 M) (helium pycnometer)	-	-
Maleki *et al.* (2019) [26]	Silica-silk fibroin (SF) aerogel hybrids	One step aqueous-based sol-gel, unidirectional freeze casting (slow (33 cm/h) or rapid (66 cm/h) cooling rate until -10 ºC or -196 ºC), $scCO_2$ drying	Porosity (%): 91 (silica-SF 10-33) – 94 (silica-SF-196-33 and silica-SF-196-66) (helium pycnometer) Pore diameter (nm): 16 (silica-SF-10-66 and silica-SF-196-66) – 18 (silica-SF-10-33) (BJH method) Macropore diameter (µm): 0.52 (silica-SF-10-66) – 17.84 (silica-SF-196-33) (SEM imaging)	Maximum compression strength (MPa): 0.36 (silica-SF-10-66) – 1.6 (silica-SF-196-33) Young' s modulus (MPa): 4.03 (silica-SF-10-33) – 7.3 (silica-SF-196-33)	Femur defect in rats – 25 days New bone density of scaffold (silica-SF-196-33) implanted defect was similar to native bone

BJH – Barrett-Joyner-Halenda method; SEM – scanning electron microscopy.

2.2. Freeze drying

The most commonly employed aerogel drying technique for biomedical applications (including bone tissue regeneration, as shown in Table 2) is freeze drying, due to its simplicity, low cost, being environmentally friendly, low working pressures and the fact that it does not require porogen particles, gases or flammable liquids [33, 42]. Through this drying process, it is possible to obtain biomaterials with high porosity and high surface area, preserved micro and nanopore structure, with low volume shrinkage and low density [33, 42].

In terms of the resulting aerogel configuration, the most critical step is the freezing stage. Most solvents freeze between -5 and -20 ºC, which are quite accessible freezing temperatures [35]. However, some studies have been published describing -80 ºC freezing temperatures [10, 55] and -196 ºC (liquid N_2) [11, 21, 44], as well as tailored freezing protocols to obtain specific results, such as in the case of freeze casting or cryostructuring (directional freezing) [15, 23, 42, 44], in order to obtain, for example, anisotropic materials [26, 42]. The freezing temperature and freezing rate dictate, to a great extent, the size and distribution of the ice crystals and, consequently, the size and interconnection of the pores of the final aerogel structure [42]. The pores' mean diameter and their interconnectivity diminish with decreasing temperature and increasing freezing rate [35, 42, 44].

Table 2. Aerogel composite scaffolds prepared by freeze drying.					
References	**Material**	**Preparation Methodology**	**Porous Properties**	***In Vitro* Mechanical Properties**	**Bone Regeneration *In Vivo* (MicroCT Analysis)**
Karamat-Ullah *et al.* (2021) [23]	Silica (0.6 or 3 ratio)-silk fibroin gel-based ink for hybrid aerogel-based scaffold conjugated with CM (cecropin melittin)-RGD peptide (60 or 120 µg)	Sol-gel-based hybrid ink, 3D printing, unidirectional freeze casting, freeze drying (-60 ºC for 24 h)	Mesopore diameter (nm): 15.6 (Silica-3-SF-CM-RGD-60) – 17.2 (Silica-3-SF) (BJH method) Micropore size (µm): 18 – 20 (nanoCT and SEM imaging) Macropore size (µm): 500 – 1000 (microCT analysis and SEM imaging)	Young's modulus (kPa): 31.98 (Silica-0.6-SF-CM-RGD-60) – 283.5 (Silica-3-SF-CM-RGD-60) along the pore (freezing) direction	-
Ng *et al.* (2022) [11]	Methacrylated silk fibroin (SF-MA) and ciprofloxacin-loaded methacrylated hollow mesoporous silica microcapsules (HMSC-MA) aerogel-based composite scaffolds (SF-MA-HMSC)	Self-assembled SF methacrylation, synthesis of HMSC, HMSC methacrylation, sol-gel of HMSC-MA and SF-MA-15 and 30 (4 and 2 w/v%), 3D printing of the hydrogel ink, ciprofloxacin-loading, UV photopolymerization/crosslinking, freeze casting (liquid N_2), freeze drying (-60 ºC, 24 h)	Pore size (µm): ~100(macropores); ~100 – 120 (interconnected micropores) (micro and nanoCT analysis); mesoporosities	-	-

Table 2. *cont.*

References	Material	Preparation Methodology	Porous Properties	*In Vitro* Mechanical Properties	Bone Regeneration *In Vivo* (MicroCT Analysis)
Al-Jawuschi *et al.* (2023) [21]	Silk fibroin methacrylate (SF-MA) incorporated with methacrylate polyvinyl pyrrolidine (PVP)-bismuth sulfide (Bi_2S_3) nanobelts 3D aerogel-based composite scaffold loaded with sorafenib (SFN) (SF-MA-20-PVP-Bi_2S_3-MA-x) (x = 5, 10 and 15 mass of loaded nanobelts)	Self-assembled SF methacrylation, PVP-Bi_2S_3 nanobelts prepared by hydrothermal method, PVP-Bi_2S_3 nanobelts methacrylation, sol-gel of SF-MA-20-PVP-Bi_2S_3-MA-x, 3D printing of the hydrogel ink, UV photopolymerization/crosslinking, freeze casting (liquid N_2), freeze drying (-40 ºC, 24 h), SFN loading	Pore size (µm): ~1000 (macropores) (SEM imaging); 7 – 23 (interconnected micropores) (SEM imaging); no meso- or nanopores	-	-
Chen *et al.* (2021) [9]	Dual network silk fibroin (SF)/cellulose/nHA (S-C-H) composite aerogel	Sol-gel, crosslinking, freeze drying (24 h)	-	Tensile strength (MPa): 7.73 (S-C-H (1:8:1 ratio)) Bending strength (MPa): 25.91 (S-C-H (1:8:1 ratio))	-
Chen *et al.* (2022) [25]	Mineralized (hydroxyapatite) silk fibroin (SF)/cellulose (M-S-C) interpenetrating network composite aerogel	Sol-gel, mineralization *in situ* (24 h), freeze drying (-56 ºC, 48 h)	Interconnected (SEM imaging) porosity increased from 98.4 % (S-C) to 99.2 % (M-S-C) after *in situ* mineralization (ethanol liquid immersion method)	Compressive strength (MPa): 22.4 (M-S-C), 11.1 (M-C) Elastic modulus (MPa): ~600 (M-S-C) – ~375 (M-C and S-C)	-

Table 2. *cont.*

References	Material	Preparation Methodology	Porous Properties	*In Vitro* Mechanical Properties	Bone Regeneration *In Vivo* (MicroCT Analysis)
Liu *et al.* (2022a) [10]	Poly(lactic acid)/gelatin (PLA/Gel)/silica (SiO_2 0, 20, 40, 60 %) nanofiber composite aerogel	Electrospinning of PLA/Gel nanofibers and SiO_2 nanofibers, sol-gel, freezing (-80 ºC 12 h), freeze drying (72 h), muffle furnace for crosslinking	PLA/Gel exhibited compact nanofiber sheets along with mesopores; PLA/Gel/SiO_2 aerogels showed loose fibers morphology and uniform pores with increasing SiO_2 (SEM imaging)	Ultimate compressive strength (kPa): 516.7 (PLA/Gel/SiO_2-60) – 866.6 (PLA/Gel/SiO_2-40) (dry state) Compressive modulus (kPa): ~60 (PLA/Gel/SiO_2-40) – ~30 (PLA/Gel/SiO_2-60) (dry state) Shape recovery rate (wet state) of PLA/Gel/SiO_2-40 was 94 % and 91 % after 50 and 100 cycles	Calvaria defect (diameter 5 mm) in rats – 12 weeks New bone coverage (%): 93 (PLA/Gel/SiO_2-40), ~60 (PLA/Gel), ~35 (control) BV/TV (%): ~65 (PLA/Gel/SiO_2-40), ~35 (PLA/Gel), ~30 (control) BMD ($g \cdot cm^{-3}$): 0.213 (PLA/Gel/SiO_2-40), 0.131 (PLA/Gel), 0.097 (control)
Liu *et al.* (2022b) [22]	Polyvinyl alcohol (PVA)/modified carbon nanotubes (MCNTs 0.05, 0.10 or 0.15 wt.%)/hydroxyapatite (HAp) aerogel scaffolds	PVA/MCNTs suspension, freezing (liquid N_2 for 10 min), freeze drying (48 h); suspension of PVA/MCNTs (0.05 wt.%) aerogels in SBF for 3 days for mineralization	Main pore size distribution 1000 – 1700 nm Porosity (%): 70.10 (PVA/MCNTs (0.05 wt.%)/HAp) – 76.03 (PVA) (mercury porosimetry)	Stiffness (at 70 % deformation, MPa): ~1.5 (PVA/MCNTs (0.10 and 0.15 wt.%)) – 4.2 (PVA/MCNTs (0.05 wt.%)/HAp)	Calvaria defect (diameter 5 mm) in rats – 8 weeks BV/TV and BS/TS (%): ~100 (PVA/MCNTs (0.05 wt.%)/HAp), ~80 (PVA/MCNTs (0.05 wt.%)) BMD ($g \cdot cm^{-3}$): ~0.5 (PVA/MCNTs (0.05 wt.%)/HAp), ~0.4 (PVA/MCNTs (0.05 wt.%))

Table 2. *cont.*

References	Material	Preparation Methodology	Porous Properties	*In Vitro* Mechanical Properties	Bone Regeneration *In Vivo* (MicroCT Analysis)
Weng *et al.* (2018) [44]	3D hybrid nanofiber aerogels of PLGA-collagen-gelatin (PCG) and Sr-Cu codoped bioactive glass (BG) nanofibers (60:40) loaded with E7-BMP (bone morphogenetic protein)-2 peptide	Sol-gel, electrospinning, crosslinking; fragmentation of nanofibers, sol-gel of nanofibers, rapid freeze casting (-30 ºC, -50 ºC or -80 ºC in ethanol for 1 min or -196 ºC in liquid N_2), freeze drying (-55 ºC for 72 h), thermal crosslinking, solvent exchange, freeze drying	Size of pores was around 30 µm (for freezing temperatures -30 ºC to -80 ºC) Much smaller pores for -196 ºC freezing temperatures (SEM imaging)	Compression modulus (MPa): ~0.25 (PCG-BG (25:75)) – ~2.25 (PCG-BG (100:0))	Calvaria defect (diameter 8 mm) in rats – 8 weeks BV/TV (%): 65 (PCG-BG (60:40) E7-BMP) Bone formation area (%): 68 (PCG-BG (60:40) E7-BMP)
Li *et al.* (2021) [43]	3D hybrid nanofiber aerogels of PLGA-collagen-gelatin (PCG) and bioactive glass (BG) nanofibers (60:40) loaded with polycation miR-26a nanoparticles (NPs)	Sol-gel, electrospinning of PCG and BG nanofibers, crosslinking; fragmentation of nanofibers, sol-gel of nanofibers, freezing (-20 ºC for 3 h and -80 ºC for 15 min), freeze drying, thermal crosslinking, freeze drying	Interconnected pores, diameter 100 µm (SEM imaging)	-	Calvaria defect (diameter 8 mm) in rats – 4 weeks Bone volume (mm^3): 2.1 (Blank), 7.5 (aerogel/miR-NC NPs), 21.8 (aerogel/miR-26a NPs) BV/TV (%): 6.0 (Blank), 21.4 (aerogel/miR-NC NPs), 62.2 (aerogel/miR-26a NPs) Bone formation area (%): 7.3 (Blank), 19.7 (aerogel/miR-NC NPs), 56.4 (aerogel/miR-26a NPs)

Table 2. *cont.*					
References	**Material**	**Preparation Methodology**	**Porous Properties**	***In Vitro* Mechanical Properties**	**Bone Regeneration *In Vivo* (MicroCT Analysis)**
Ruphuy *et al.* (2018) [56]	Nano-hydroxyapatite/chitosan (nHApCS, 70/30) hybrid scaffold (different neutralization methods: untreated, NaOHEtOH, $scCO_2$-75/75)	nHAp and CS dispersion, freezing (-20 ºC overnight), freeze drying (24 h) and: – immersion in NaOH/ethanol, washing, freeze drying or – $scCO_2$ (2 cycles at 75 ºC, 8.0 MPa) residual solvent removal and sterilization	Total porosity (%): 81 (n-HApCS-$scCO_2$-75/75), 83 (nHApCS-untreated), 93 (nHApCS-NaOHEtOH) (gas pycnometer) Mean pore size (μm): 86 (nHApCS-untreated), 72 (nHApCS-$scCO_2$-75/75), 63 (nHApCS-NaOHEtOH) (SEM imaging)	Storage modulus (at 1 Hz after 1 h in PBS, kPa): 6.8 (nHApCS-untreated), 20.5 (nHApCS-$scCO_2$-75/75), 13.3 (nHApCS-NaOHEtOH)	-
Souto-Lopes *et al.* (2023) [57]	3D nanohydroxyapatite/chitosan (nHAp/CS, 70/30) or CS scaffold	nHAp and CS dispersion, freezing (-20 ºC overnight), freeze drying (24 h), $scCO_2$ (continuous batch cycles at 75 ºC, 8.0 MPa for 2 h) residual solvent removal and sterilization	Total porosity (%): 77 (CS), 78 (nHAp/CS). Full interconnectivity Pore diameter (μm): 152 (CS), 201 (nHAp/CS) (microCT analysis)	Storage modulus (at 1 Hz, kPa): 37.0 (nHAp/CS 1 h in PBS) – 38.8 (nHAp/CS 28 days in PBS); 11.9 (CS 1 h in PBS) – 7.8 (CS 28 days in PBS). Storage modulus (at 10 Hz, kPa): 47.1 (nHAp/CS 1 h in PBS) – 42.3 (nHAp/CS 28 days in PBS); 16.3 (CS 1 h in PBS) – 8.7 (CS 28 days in PBS).	-

Table 2. *cont.*					
References	**Material**	**Preparation Methodology**	**Porous Properties**	***In Vitro* Mechanical Properties**	**Bone Regeneration *In Vivo* (MicroCT Analysis)**
Liu *et al.* (2019) [58]	Graphene oxide (0, 0.05, 0.1, 0.2 % GO)-collagen (COL) aerogels	Sol-gel, freezing, freeze drying (-50 ºC for 8 h), crosslinking, freeze drying	Porosity (%): 78.1 (0.2 % GO-COL) – 83.6 (0.1 % GO-COL) (liquid displacement method) Pore size (µm): 100 – 160 (SEM imaging)	Elastic modulus (compression, MPa): 0.20 (COL) – 0.51 (0.2 % GO-COL)	2 craniofacial bone defects (diameter 5 mm) in rats – 12 weeks BV (mm^3): ~3 (0.05 % GO-COL) – ~6 (0.2 % GO-COL) BV/TV (%): ~8 (0.05 % GO-COL) – ~16 (0.2 % GO-COL)
Li *et al.* (2018) [55]	Sugarcane aerogel-derived borate bioglass scaffolds (SBBS)	Sol-gel preparation of borate glass, curing; freezing (-80 ºC for 48 h) of sugarcane carbon hydrogels, freeze drying; borate loading on sugarcane aerogels, oven drying	-	Compressive strength (MPa): ~0.55 (less concentrated curing solution) – ~0.75 (more concentrated curing solution) for 30-5B SBBS	Bilateral ulnar bone defect (7 mm radial length and 3 x 3 mm^2 cross-sectional area) in rabbits – 8 weeks The defect with vertically oriented SBBS was completely healed
Ye *et al.* (2019) [16]	Nanohydroxyapatite/ PLLA/gelatin (nHA/PLA/Gel)-peptide (PEP, BMP-2 derived peptides) 3D nanofibrous scaffolds	PLA and Gel solution homogenization, nHA dispersion, electrospinning, cut and dispersion of nanofibers, freeze drying (24 h), thermo-crosslinking, crosslinking, freeze drying (48 h), polydopamine (pDA) coating, immersion in BMP-2 peptide solution, freeze drying	Interconnected pores from tens of microns to 300 µm (SEM imaging)	Young's modulus (kPa): ~45 (PLA/Gel) – ~65 (nHA/PLA/Gel) (wet)	Calvaria defect (diameter 6 mm) in rats – 8 weeks BV/TV (%): ~15 (PLA/Gel) – ~45 (nHA/PLA/Gel-PEP)

Table 2. *cont.*					
References	**Material**	**Preparation Methodology**	**Porous Properties**	***In Vitro* Mechanical Properties**	**Bone Regeneration *In Vivo* (MicroCT Analysis)**
Zhang *et al.* (2021) [46]	Three-layered scaffold of poly(L-lactide)/gelatin/hyaluronic acid/chondroitin sulfate (PLA/Gel/HA/CS) fibers and PLA/Gel gradient biomineralized fiber composite aerogels grafted with E7-peptide (A-E7G)	Electrospinning of PLA/Gel/HA/CS and PLA/Gel fibers, porogen incorporation, freezing (liquid N_2), freeze drying (24 h), crosslinking heat treatment, porogen removal, soaking of PLA/Gel in 5SBF (24 or 48 h), aerogel layer adhesion with photocurable methacrylated gelatin (GelMA), photocrosslinking, E7-peptide grafting, freeze drying	-	Compressive stress (at 80 % strain, MPa): 0.23 (PLA/Gel/HA/CS aerogel layer), 0.62 (PLA/Gel 5SBF 24 h aerogel layer), ~0.6 (A-G trilayered scaffold), 1.4 (PLA/Gel 5SBF 48 h aerogel layer)	Bilateral double knee osteochondral full thickness defects (4 mm x 4 mm) in rabbits – 12 weeks BV/TV (%): ~20 (Blank), ~30 (PLA/Gel), ~35 (A-G) ~50 (A-E7G) Tb.Th (mm): ~0.2 (Blank) – ~0.35 (A-E7G) Tb.N (1/mm): ~1.25 (Blank) – ~2.0 (A-E7G)

BJH – Barrett-Joyner-Halenda method; SEM – scanning electron microscopy; PBS – phosphate buffer saline; BV/TV – bone volume/tissue volume; BMD – bone mineral density; BS/TS – bone surface/tissue surface; BV – bone volume; SBF – simulated body fluid; Tb.Th – trabecular thickness; Tb.N – trabecular number.

2.3. Ambient pressure drying

Ambient pressure (or evaporation) drying is a simple, economic technique with lower associated risks [59] for obtaining porous materials (xerogels) from wet-gel solutions [33, 59]. While it has been regularly utilized in industrial scale-up [33], however, this technique is slow [59], usually requires the substitution of water by an organic solvent such as ethanol or acetone [33] and typically takes several days to complete [35]. Compared to the drying techniques described in Sections 2.1 and 2.2, ambient pressure drying frequently leads to a higher shrinkage ratio of the material [33, 59] and pore structure collapses due to capillary tensions [28], depending on the precursor solutions and solvents employed [59]. The use of ionic gelation and crosslinking agents also influences the final morphology of the scaffold [59]. Consequently, these materials tend to exhibit higher bulk densities and lower porosities and surface areas, but also more stable mechanical properties [59]. Nevertheless, compared to other aerogels, these ambient-dried materials have been successfully employed in various applications. For example, they have shown promise in sustained drug delivery (where the slower delivery rate, compared to highly porous aerogels, is more beneficial in some biomedical applications) and in wound dressing and healing (due to their great absorbability of exudates) [59]. A few bone tissue engineering applications of composite xerogel scaffolds have also been studied in more recent years, as detailed in Table 3.

Table 3. Aerogel (xerogel) composite scaffolds prepared by ambient pressure drying.

References	Material	Preparation Methodology	Porous Properties	*In Vitro* Mechanical Properties	Bone Regeneration *In Vivo* (MicroCT Analysis)
Perez-Moreno *et al.* (2021) [60]	Silica (SiO_2)-chitosan (CS 8 wt.%)-tricalcium phosphate (TCP 10 or 20 wt.%) (SCS8T) xerogels	Ultrasonic preparation of precursors, ultrasonic sol-gel, washing (unwashed (U), in ethanol for 1 (E1) or 7 days (E7) or in water for 30 d (W30)), ambient pressure drying (80 ºC, 48 h)	Pore size (nm): 3.0 (SCS8T20_U) – 3.3 (SCS8_U, SCS8T10_U); 4.7 (SCS8T20_E1) – 6.7 (SCS8_E1); 6.0 (SCS8T20_E7) – 7.1 (SCS8_E7); 2.5 (SCS8_W30) – 2.7 (SCS8T10_W30, SCS8T20_W30) (BJH method)	-	-
Perez-Moreno *et al.* (2023) [53]	Chitosan (CS 8 wt.%)—silica (SiO_2) hybrid/tricalcium phosphate (TCP 10 wt.%) xerogel (SCS8T10X)	Ultrasonic preparation of precursors, ultrasonic sol-gel, aging and solvent exchange, ambient pressure drying (50 ºC)	Pore size (nm): 4.7 (SiO_2X), 5.0 (SCS8X), 7.5 (SCS8T10X) (BJH method)	-	-

BJH – Barrett-Joyner-Halenda method

3. PROPERTIES OF COMPOSITE AEROGELS FOR BONE REGENERATION

One of the most essential features of bone graft biomaterials is the existence of a highly interconnected porous structure, comprising a wide range of pore sizes and geometries, in order to meet the needs of a rough surface for adhesion of osteoblasts and osteoclasts [15, 41, 61], as well as the circulation of cells, oxygen, nutrients and metabolites and the formation of new vessels [10, 25, 37]. Moreover, this type of architecture should be balanced with the scaffolds' ability to withstand compressive stress from the functional demands of bone [10, 15, 24, 61]. Otherwise, if the scaffold does not recover upon compression, its porous configuration is lost and it might jeopardize its osteoconductivity effect *in vivo* [7, 10, 15]. Despite the importance of the chosen drying technique, the performance of the hybrid/composite scaffold still depends to a great extent on its composition, including factors such as the type and degree of crosslinking, concentration and molecular weight of polymers and inorganic phases [19, 42].

3.1. Aerogels' porous structure

When comparing Tables 1 – 3, it is clear that most aerogel composite scaffolds for bone regeneration were prepared through freeze drying instead of the classical supercritical drying or even ambient pressure drying techniques. Generally, biomaterials prepared by $scCO_2$ drying tend to exhibit higher porosity (Figure 3), but smaller pore diameters when compared to freeze-dried materials [33]. They usually lack macropores [41] (pores above 100 µm). While in freeze-dried materials the pore diameters tend to range from 20 to 160 µm (micro/macroporosity) [37], $scCO_2$-dried biomaterials show high mesoporosity (nanometer range pore size) [41]. Nevertheless, freeze-dried materials may also show mesoporosity and therefore feature aerogel-like properties [28].

However, it is important to consider the methodologies used to analyze and quantify the scaffolds' porosity and pore size, since the limitations of each method can bias these values and the perception of the aerogel structure [18, 28]. Therefore, SEM (scanning electron microscopy) imaging, micro and nanoCT analysis are adequate for the assessment of macro and micropores [23, 28, 56, 57, 62], while mesoporosity and textural parameters (specific pore volume, pore size distributions and mean pore diameter) are usually determined from the desorption branch of N_2 sorption isotherm by the Barrett-Joyner-Halenda (BJH) method, and specific surface area is calculated with the Brunauer-Emmett-Teller (BET) five-point method [18, 23, 32, 41, 54]. Surface area, volume, density and porosity have also been determined by mercury intrusion [22, 62]; helium pycnometer has been used to estimate apparent density and porosity [26, 41, 56, 62]; the ethanol liquid immersion method [25] and liquid displacement method have been used for porosity measurement [58].

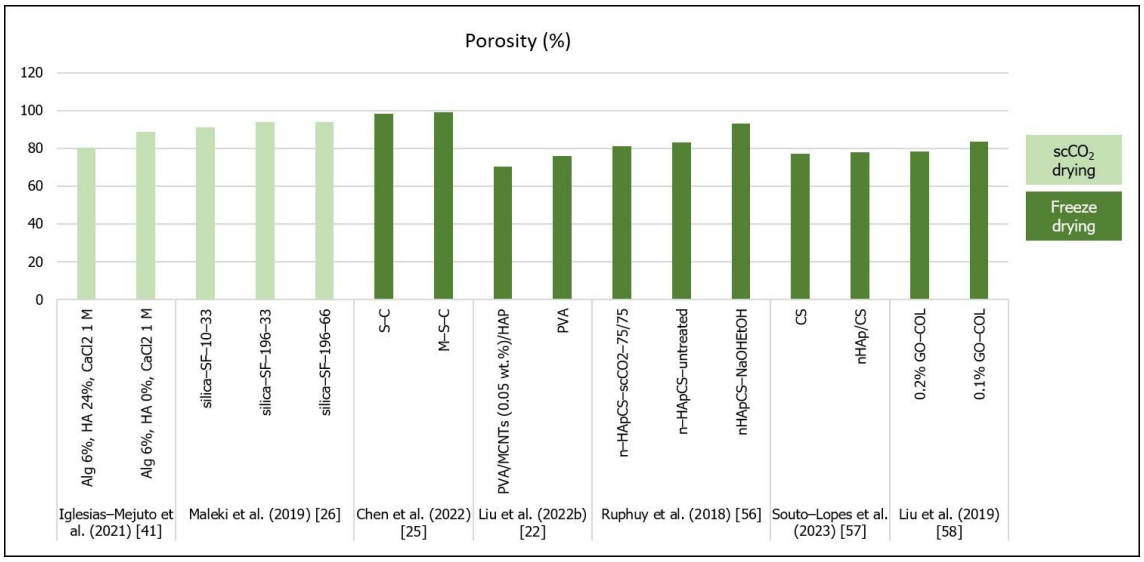

Figure 3. Porosity (%) of aerogel scaffolds prepared through different drying methods (data from [22, 25, 26, 41, 56-58]).

In terms of pore size, the studies' results in Table 1 showed that the pore size scale ranges from 8.6 [54] to 31 nm [41] (mesopores) to a few micrometers [26]. Perez-Moreno *et al.* (2020) developed silica (SiO_2)/chitosan (CS 0, 4, 8, 16, 20 wt.%) (SCS) composite aerogels with mesopores ranging from 11 to 14 nm [7]. The authors noticed that there was not a defined pore size behavior with the variations in CS content, but pore interconnectivity was higher for pure SiO_2 and SCS20 aerogels, which suggested that CS had a distorting influence on the aerogel network [7]. In a 2021 (Table 3) study, Perez-Moreno *et al.* developed ambient-dried silica (SiO_2)-chitosan (CS 8 wt.%) xerogels incorporating tricalcium phosphate (TCP 10 or 20 wt.%) (SCS8T) to enhance bioactivity [60]. They compared the effect of several washing methods (ethanol or water) before drying and concluded that ethanol washing, in general, was more effective in reducing unreacted chemical residues, and thus exhibited higher mesopore diameters (from 4.7 to 7.1 nm) than in water or no washing (from 2.5 to 3.3 nm) [60]. Moreover, the authors verified that the incorporation of TCP in the ethanol-washed xerogels increased the density by 40 to 50 %, while in water-washed xerogels the density increased by only 4 to 7 %, showing that TCP was released from the biomaterial by water [60]. Furthermore, the pore diameters tended to decrease with the higher TCP contents in ethanol-washed samples (4.7 nm for SCS8T20_E1 vs. 5.5 for SCS8T10_E1 and 6.0 nm for SCS8T20_E7 vs. 6.3 for SCS8T10_E7) [60]. Furthermore, Perez-Moreno *et al.*'s (2023) study (Tables 1 and 3) compared the effect of $scCO_2$ and ambient pressure drying on the scaffolds' properties [53]. Firstly, they came to the conclusion that $scCO_2$ drying impaired the TCP incorporation, since it would be leached by the $scCO_2$ procedure from the aerogel [53]. They also reported that the xerogel scaffolds showed lower pore diameters (between 4.7 and 7.5 nm) than the aerogels (16.9 to 17.3 nm), and the incorporation of CS 8 wt.% and TCP 10 wt.% increased the pore diameters when compared to both types of pure silica matrices (SiO_2A and SiO_2X) [53].

The hybrid silica-gelatin-based aerogels developed by Reyes-Peces *et al.* (2023) (Table 1) exhibited lower mean pore diameters (in a nanometer scale), specific surface area and total pore

volume with increasing contents of gelatin (from 15 to 30 % wt.) and crosslinker (organosilaner 3-glycidoxypropyltrimethoxysilane – GPTMS) [54]. The authors attributed these results to a more intertwined hybrid structure, due to higher organic network content. Moreover, these hybrid aerogels did not show a micro or macropore distribution [54]. In a study by Iglesias-Mejuto *et al.* (2021) 3D-printed alginate-hydroxyapatite (Alg-HA) aerogel scaffolds were obtained after $scCO_2$ drying [41]. They compared their scaffolds' structure properties with and without hydroxyapatite included in the alginate aerogel, and concluded that although the hybrid scaffolds displayed a markedly lower specific surface area and total pore volume, the differences in the mean pore diameter were not meaningful (19 nm for Alg 6 %, HA 0 %, $CaCl_2$ 1 M formulation; 31 nm for Alg 6 %, HA 24 %, $CaCl_2$ 1 M) [41]. The authors compensated the lack of macropores through the scaffold design obtained by 3D printing (with the aligned microfibers separated by microporous gaps), which allowed for reaching high total porosity values (80 to 88 %) and a pore size range (from nanopores to macropores) more favorable for bone tissue engineering [41]. When developing scaffolds for bone regeneration, it is desirable to improve the macroporosity to enhance cell migration, neovascularization and mass transfer [32]. Furthermore, the presence of mesoporosity has a relevant impact on implant topography and scaffold bioactivity [35], and high porosity is an essential feature of scaffolds for expanding cells and their interactions *in vivo* [37, 44].

In order to overcome the drawbacks in establishing a hierarchical oriented microstructure composed of macropores as well as mesopores, Maleki *et al.* (2019) (Table 1) developed a silica-silk fibroin hybrid aerogel prepared through a combination of freeze casting followed by $scCO_2$ drying [26]. In that particular case, the hybrid aerogel that exhibited more equilibrated outcomes in general was the one obtained at lower cooling constant temperature and rate (silica-SF-196-33) [26]. This aerogel was the lightest (bulk density 0.075 g/cm^3) and displayed the highest macro-sized honeycomb-like pores (17.84 µm) and the highest total porosity (94 %) [26]. After that study, Karamat-Ullah *et al.* (2021) (Table 2) developed a silica (0.6 or 3 ratio)-silk fibroin gel-based ink for a 3D-printed hybrid aerogel-based scaffold conjugated with CM (cecropin melittin)-RGD peptide (60 or 120 µg), which showed antimicrobial and cell adhesive properties [23]. However, in that work, the scaffolds' hierarchically organized porous structure was also evaluated, but instead of using unidirectional freeze casting followed by supercritical drying, they performed freeze casting and drying [23]. Therefore, the aerogel showed mesopores from the sol-gel process, micropores after the freeze casting, and macropores through the 3D printing [23]. In the same research subject, Ng *et al.* (2022) (Table 2) developed 3D-printed methacrylated silk fibroin (SF-MA) and ciprofloxacin-loaded methacrylated hollow mesoporous silica microcapsules (HMSC-MA) aerogel-based composite scaffolds (SF-MA-HMSC), with hierarchical interconnected porosity [11]. Similarly, pores of around 1000 µm were observed from CAD 3D model and printing, micropores of 100 to 120 µm were formed from freeze casting and drying, and mesoporosity derived from the self-assembled SF methacrylation and photo-crosslinking processes [11]. Finally, based on the 3D-printing methodologies developed by Ng *et al.* (2022) [11], the authors showed the development of silk fibroin methacrylate (SF-MA) incorporated with methacrylate polyvinyl pyrrolidine (PVP) – bismuth sulfide (Bi_2S_3) nanobelts 3D aerogel-based

composite scaffold loaded with sorafenib (SFN) (SF-MA-20-PVP-Bi_2S_3-MA-x) for photothermally anticancer drug (SFN) release and cancer cell ablation. They reported similar macropores (1000 µm) resulting from the 3D printing, but smaller micropores (7 to 23 µm) from unidirectional freeze casting and drying, and absence of mesopores [21].

Weng *et al.* (2018) produced 3D hybrid nanofiber aerogels of PLGA-collagen-gelatin (PCG) and Sr-Cu co-doped bioactive glass (BG) nanofibers at different freezing temperatures, thermal crosslinking conditions and PCG:BG ratios [44]. Their results showed that despite the overall porosity being unaffected, the pore size (from SEM image analysis) was highly influenced by the high freezing temperature gradients, i.e., freezing temperatures between -30 ºC and -80 ºC did not make differences in pore size (around 30 µm), but when frozen in liquid N_2, the pore size was so reduced that the aerogel should not be appropriate for bone regeneration [44]. In another study, Li *et al.* (2021) prepared the PCG-BG (60:40) (without Sr-Cu doping) aerogel by a slower freezing protocol (-20 ºC for 3 h and then -80 ºC for 15 min), using shorter BG nanofiber segments and different thermal crosslinking conditions (48 ºC for 10 min) [43]. As a consequence of the freezing conditions and shorter nanofibers, the scaffolds featured larger interconnected pores with a 100 µm diameter, when compared to the Weng *et al.* (2018) study [44], which should improve both cell infiltration and vascularization [43].

In an earlier study, Chen *et al.* (2021) developed a dual-network silk fibroin/cellulose/nHA (S-C-H) aerogel scaffold through freeze drying [9]. Afterwards, they kept the same interpenetrating dual organic phase but tested different *in situ* mineralization times before freeze drying, instead of dispersing nHA in the sol-gel [25]. Their extremely porous M-S-C aerogel scaffold (mineralized for 24 h) showed significantly higher interconnected porosity (99.2 %) than the S-C (non-mineralized) aerogel (98.4 %) [25]. Another study by Liu *et al.* (2022a) produced a composite aerogel by electrospinning PLA/Gel nanofibers and SiO_2 nanofibers (0 to 60 % w/w), followed by -80 ºC freezing and freeze drying [10]. The PLA/Gel/SiO_2 scaffolds displayed more favorable porous morphologies than the plain PLA/Gel scaffold, which suffered shrinkage upon thermal crosslinking [10]. These studies showed how the reinforcement of the microstructure through the inclusion of an inorganic phase might improve the general porous configuration of the scaffolds.

Additionally, Ruphuy *et al.* (2018) developed freeze-dried nano-hydroxyapatite/chitosan (n-Hap/CS, 70/30) hybrid scaffolds with pore size ranging between 50 and 100 µm, using different methods for solvent (acetic acid) neutralization [56]. Their SEM imaging analysis showed that the freeze-dried scaffolds without any further treatment exhibited a favorable interconnected porous structure (86 µm mean pore size, 83 % porosity), and the supercritical process kept a similar porous structure (72 µm, 81 %) [56]. By contrast, NaOH/ethanol neutralization altered the scaffold's morphology and decreased the mean pore size (63 µm) but increased the overall porosity (93 %), probably due to the second freeze drying step [56].

Souto-Lopes *et al.* (2023) tested the freeze-dried nHAp/CS scaffolds processed by continuous supercritical CO_2, instead of two independent cycles, and the microCT results showed total porosity of 78 %, without statistical difference from the CS scaffold (77 %) [57]. Moreover, the nHAp/CS scaffolds showed a wider range of pore sizes, though there was no significant difference

between the mean pore size of the nHAp/CS (201 µm) and CS (152 µm) scaffolds [57].

Liu *et al.* (2022b) prepared PVA and PVA/MCNTs (0.05, 0.10 or 0.15 wt.%) freeze-dried aerogels that simulated the natural cuttlebone porous configuration and mimicked its bone structure [22]. Since a fast deep-freeze method (10 min in liquid N_2) of the suspensions was used, the final aerogels featured a lower pore size (1000 to 1700 nm) [22] when compared to the other previously mentioned freeze-dried scaffolds [11, 16, 21, 23, 43, 58]. However, these pore sizes did not fall into the mesoporous range. The porosity of the PVA aerogels (76 %) diminished with the addition of the inorganic phase (MCNTs) and it was lower (around 70 %) for the PVA/MCNTs (0.05 wt.%) and PVA/MCNTs (0.05 wt.%)/HAp [22], which contrasted with the results from Chen *et al.* (2022) [25]. Ye *et al.* (2019) incorporated BMP-2 peptides into nano-hydroxyapatite/PLLA/gelatin (nHA/PLA/Gel-PEP) 3D nanofibrous scaffolds prepared by freeze drying of short nanofibers [16]. The produced scaffolds showed a range of pore sizes from tens of microns to 300 µm. The pore sizes were higher in the PLA/Gel scaffolds when compared to nHA/PLA/Gel and nHA/PLA/Gel-PEP, but there were more pores and more uniform distribution in nHA/PLA/Gel and nHA/PLA/Gel-PEP when compared to PLA/Gel scaffolds [16]. The freeze-dried graphene oxide (GO)-collagen (COL) aerogels developed by Liu *et al.* (2019) did not show significant differences in terms of pore size ranges (100 to 160 µm) and total porosity (around 80 %) with different GO ratios (0, 0.05, 0.1, 0.2 %), but these values were appropriate for bone regeneration [58].

3.2. Aerogels' *in vitro* mechanical properties

In both Tables 1 and 2, the results from the reported mechanical tests were performed under dry conditions, unless stated otherwise. When evaluating the mechanical properties of aerogel scaffolds for bone regeneration, it is important to consider the conditions in which the tests were performed, since there are usually differences in the mechanical performance of these biomaterials in dry or wet conditions, as discussed below.

This material behavior is observed in the study of the hybrid silica-GPTMS-gelatin-based aerogels developed by Reyes-Peces *et al.* (2023) (Table 1) [54]. The supercritical-dried aerogels showed an elastic behavior to compression and higher stiffness in dry conditions with increasing gelatin content (maximum compressive strain for SG25 was 27.67 %) and crosslinking agents [54]. However, since the aim of these biomaterials was to be implanted in a living organism with moisture from blood and organic fluids, when tested in wet conditions, the performance of these hybrid aerogels decreased for all compression parameters (though still in the MPa scale), with the lowest stiffness shown for the aerogels with higher organic phase contents [54]. This phenomenon may be explained by the fact that gelatin allowed the swelling of phosphate buffer saline (PBS), which showed the respective swelling ratios of 2.32, 3.42 and 3.04 for 15, 25 and 30 % of gelatin content, respectively [54]. Ye *et al.* (2019) (Table 2) also tested the nHA/PLA/Gel-PEP 3D nanofibrous scaffolds under wet conditions and concluded that the presence of nHA significantly increased the material's Young's modulus (~65 kPa) [16]. However, the pDA-assisted coating for

the incorporation of BPM-2 peptide significantly decreased the Young's modulus (~50 kPa). Nonetheless, the range of the Young's modulus is quite different from that obtained by Reyes-Peces *et al.* (2023) (1.65 to 3.71 MPa) [54], which showed very low-sized pores (mesoporosity) through $scCO_2$ treatment, when compared to the micrometric range pore diameter up to 300 µm obtained after freeze drying [16].

Furthermore, in Ruphuy *et al.*'s study (2018), the freeze-dried nHAp/CS scaffolds were subjected to dynamic mechanical analysis after 1 h in PBS [56]. Despite all scaffold types exhibiting a fast swelling (24 g g^{-1} in 10 min for the nHApCS-$scCO_2$-75/75 scaffold), both the untreated and NaOH/EtOH neutralized-scaffolds showed structural disruption, which impaired their mechanical performance (storage modulus at 1 Hz was ~7 and 13 kPa, respectively) compared to the materials produced with $scCO_2$ technology (20.5 kPa) [56]. Nevertheless, all tested scaffolds showed an increase in the storage modulus (from 6.8 to ~15 kPa for nHApCS-untreated, from 13.3 to ~15 kPa for nHApCS-NaOHEtOH and from 20.5 to ~28 kPa for nHApCS-$scCO_2$-75/75, at 1 and 10 Hz, respectively) and Tan Delta (loss factor, from ~0.3 to ~0.5 for nHApCS-untreated, from ~0.1 to ~0.3 for nHApCS–NaOHEtOH and from ~0.1 to ~0.4 for nHApCS-$scCO_2$-75/75, at 1 and 10 Hz, respectively) [56]. These parameters were also evaluated by Souto-Lopes *et al.* (2023) [57]. Moreover, the work showed differences in the compressive storage modulus between the scaffolds with (37.0 kPa after 1 h in PBS and 38.8 kPa after 28 days in PBS at 1 Hz; 47.1 kPa after 1 h in PBS and 42.5 kPa after 28 days in PBS at 10 Hz) and without (11.9 kPa after 1 h in PBS and 7.8 kPa after 28 days in PBS at 1 Hz; 16.3 kPa after 1 h in PBS and 8.7 kPa after 28 days in PBS at 10 Hz) nHAp in their composition [57]. The storage modulus results for the nHAp/CS scaffold were approximately three-fold higher (at both 1 and 10 Hz) when compared to the CS material after swelling in PBS and five-fold higher after 28 days of incubation in PBS. Therefore, the increased biodegradation with time after CS scaffold incubation in saline solution explains the biomechanical response of the different biomaterials [57].

When comparing the mechanical strength only in dry conditions, the hybrid silica-gelatin-based aerogels developed by Reyes-Peces *et al.* (2023) exhibited the best performance [54] (Table 1). The $scCO_2$-dried silica/chitosan composite aerogel developed by Perez-Moreno *et al.* (2020) showed a viscoelastic behavior and a marked decrease in the Young's modulus with the incorporation of CS (from 11.57 MPa in SiO_2 to 2.61 MPa in SCS4) [7]. On the other hand, those authors reported that the aerogel with lower CS content (SCS4) exhibited increased compressive strength but decreased toughness, when compared to the pure SiO_2 aerogel, which was driven by the loss of pore interconnectivity, as referred to in a previous section (Section 3.1) [7]. Water absorption occurred in a linear way for aerogels with and without CS, being expected a swelling behavior of the CS network [7]. The $scCO_2$-dried hybrid silica-silk fibroin aerogel developed by Maleki *et al.* (2019) with more favorable structural parameters in general (silica-SF-196-33) also featured the highest maximum strength (1.6 MPa) and Young's modulus (7.3 MPa) [26]. In order to improve the hierarchical porous structure of the aerogels, Karamat-Ullah *et al.* (2021) showed that freeze casting and drying instead of $scCO_2$ drying (Maleki *et al.* (2019) [26]) changed the scaffolds' porous structure and influenced the scaffolds' stiffness (compression test), since their

Young's modulus decreased significantly from a range of 4.03 – 7.3 MPa [26] to 31.98 – 283.5 kPa [23].

When evaluating the mechanical performance considering the organic/inorganic ratio of the freeze-dried aerogels, Chen *et al.* (2022) observed that the M-S-C composite aerogel showed the highest compressive strength results (22.4 MPa) after 24 h of *in situ* mineralization (a comparative study along times of 1, 3, 6 and 12 h of *in situ* mineralization) [25]. Moreover, despite there being no differences in the microstructural parameters between the freeze-dried GO-COL aerogels developed by Liu *et al.* (2019), the compression elastic modulus increased with GO contents (value for 0.2 % GO-COL was significantly higher than that for 0, 0.05 and 0.1 % of GO) [58]. These authors also determined that 0.1 % and 0.2 % GO-COL scaffolds absorbed more than 1500 % of water (about 1.27-fold and 1.35-fold more than the COL scaffold, respectively), showing that increasing GO content contributed to the increase in materials' hydrophilicity [58]. However, higher inorganic phase content could not necessarily mean higher mechanical strength, as shown by Liu *et al.* (2022a) with their study of PLA/Gel/SiO_2 (0 to 60 % w/w) scaffolds [10]. In that case, the PLA/Gel/SiO_2-40 aerogel displayed significantly higher mechanical properties when compared to the other aerogels tested with different SiO_2 contents (PLA/Gel/SiO_2-60 showed lower compressive strength when compared to the PLA/Gel-control) [10]. Moreover, the PVA/MCNT (0.05 wt.%) freeze-dried aerogels developed by Liu *et al.* (2022b) also showed higher stiffness (3.5 MPa at 70 % strain) than the PVA/MCNTs (0.1 wt.%) and PVA/MCNTs (0.15 wt.%) (~1.5 MPa for both), due to higher content of MCNTs that jeopardizes their own particle dispersion in the aerogel [22]. Nevertheless, the stiffness of PVA/MCNTs (0.05 wt.%) increased with the addition of HAp after 3 days of SBF mineralization (~4.0 to 4.2 MPa) [22]. By contrast, Weng *et al.* (2018) observed an exponential increase in the Young's modulus with the increase in the polymer content of the PCG-BG aerogel [44]. They showed the highest results with PCG 100 %, after optimal thermal crosslinking at 52 ºC for 10 min [44]. Even though their initial objective was to incorporate the highest possible ratio of Sr-Cu co-doped BG nanofibers, in order to achieve the best outcomes in terms of osteoinduction and neovascularization, the opposite in terms of the materials' mechanical properties was observed [44].

In terms of biomimetic strategies for aerogel scaffold development, Li *et al.* (2018) prepared sugarcane-derived borate bioglass (tetraethyl orthosilicate (TEOS), tributyl borate (TBB), triethyl phosphate (TEP)) aerogel scaffolds by freeze drying with anisotropic properties due to the multilevel structure of the sugarcane, in order to match the internal structure of natural bone [55]. The aerogel prepared with a ratio of two of TEOS to TBB (named 30-5B) showed more favorable biodegradation and bioactivity properties and, after reinforcement with different concentrations of a phosphate curing solution, the composite showed the highest compression strength (~0.75 MPa) with higher concentration of curing solution when compared with the composite prepared with the lowest concentration of curing solution (~0.55 MPa) [55]. Another study by Zhang *et al.* (2021) developed an aerogel-based three-layered scaffold (A-G) made of electrospun fibers (poly(L-lactide)/gelatin/hyaluronic acid/chondroitin sulfate – PLA/Gel/HA/CS) using the aerogel technology for osteochondral regeneration [46]. The scaffolds were

subsequently freeze-dried, crosslinked, gradient biomineralized and grafted with E7 peptide (A-E7G) [46]. The upper (chondral) layer (A-C) composed of PLA/Gel/HA/CS aerogel showed the lowest compressive resistance (0.23 MPa), followed by the middle (intermediate calcified cartilage zone) layer (A-M) made of PLA/Gel aerogel soaked in 5SBF for 24 h (0.62 MPa), as well as the three-layered scaffold (A-G, ~0.6 MPa) and crosslinked PLA/Gel aerogel (A-U, ~0.6 MPa) [46]. The highest compressive stress was observed with PLA/Gel aerogel that was biomineralized for 48 h (A-B, 1.4 MPa) referring to the bottom (osseous) layer [46].

3.3. Aerogels and *in vivo* bone regeneration potential

The final goal of the development of aerogel scaffolds for bone regeneration is their capacity for guiding bone cell migration and inducing differentiation of host mesenchymal stem cells into osteoblasts, in order to secrete collagen fibers and promote new bone formation in a tissue defect [23]. At this stage, every property of a biomaterial, from the composition and morphology to the mechanical and biocompatibility performance, is an important aspect that may contribute or not to promote bone regeneration [26]. Figure 4 summarizes the most relevant results of *in vivo* bone regeneration from most of the studies analyzed below in this section.

From the studies detailed in Table 1 (aerogel scaffolds prepared by $scCO_2$ drying), Maleki *et al.* (2019) reported that their silica-SF-196-33 scaffold (which exhibited more appropriate microstructural architecture and mechanical properties) was chosen to be tested *in vivo* in a rat femur defect model [26]. Despite the low macropore mean diameter (17.84 µm), but high porosity (94 %), after 25 days, the microCT analysis revealed that bone density in the defect containing the implanted scaffold was similar to that of native bone [26]. Moreover, no evidence of inflammation, negative tissue response or systemic toxicity was observed [26].

Several freeze-dried aerogels (Table 2) have already been tested *in vivo* in critical size bone defects. Liu *et al.* (2022b) observed that the PVA/MCNTs (0.05 wt.%)/HAp scaffold's BV/TV and BS/TS was nearly 100 % (the defect was almost fully filled by new bone tissue) after 8 weeks in rat calvaria model [22]. All bone formation quantifications measured by microCT were significantly higher for the scaffold with HAp when compared to the other groups (empty control defect, PVA and PVA/MCNTs – 0.05 wt.%), due to the osteoinduction triggered by the presence of the HAp nanoparticles [22]. Liu *et al.* (2022a) observed that the PLA/Gel/SiO_2-40 scaffold showed increasing BV/TV, BMD and new bone formation (93 % after 12 weeks in rat calvaria model) with time, with significant differences compared to the plain PLA/Gel and the empty controls at all time points [10]. On the other hand, Liu *et al.* (2019) showed lower bone formation after 12 weeks post implantation in rat calvaria model [58]. According to these authors' conclusions, the 0.1 and 0.2 % GO-COL groups showed a > 1.5-fold higher BV (~6 mm^3) and BV/TV ratio (~16 %) when compared to the other two groups [58].

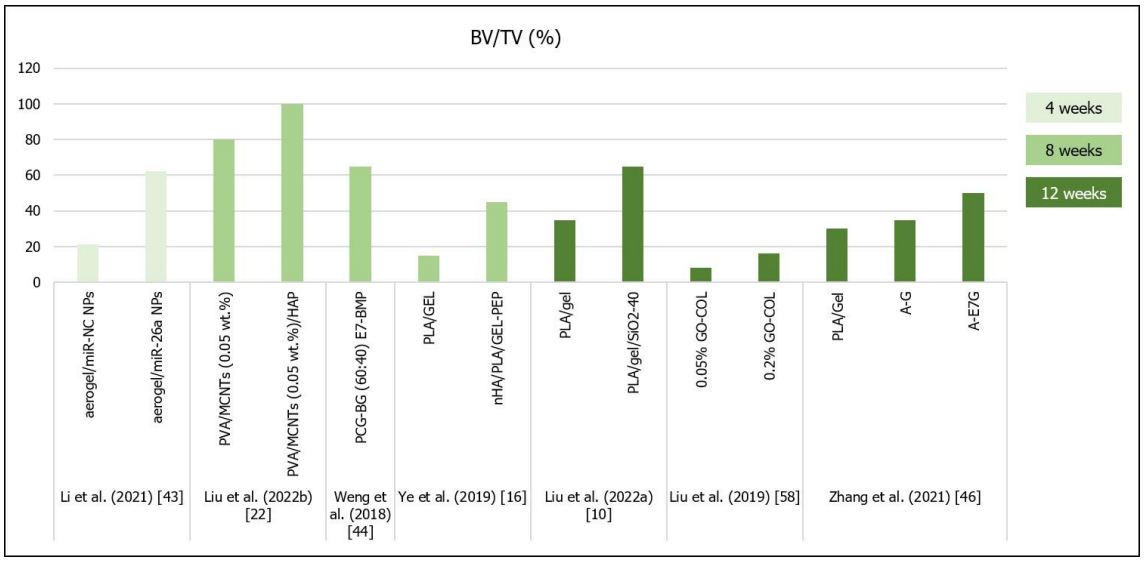

Figure 4. Results (bone volume/tissue volume (BV/TV %)) from bone regeneration *in vivo* (obtained by microCT analysis) with the implantation of aerogel scaffolds of different materials (data from [10, 16, 22, 43, 44, 46, 58]). All scaffolds were implanted in rat calvaria model, except for the study from ref. [46] (rabbit knee).

There were also some published results that described the inclusion of osteoinductive molecules in the proposed aerogel's composition, in order to improve their regeneration outcomes. Weng *et al.* (2018) performed a bone implant of PCG-BG (60:40) scaffolds and compared the mineralized tissue formation in rat calvaria defects with and without the introduction E7-BMP peptide [44]. After 8 weeks, there was no difference in terms of bone volume and bone formation area when compared the PCG-BG (60:40) scaffolds and the empty defects (~25 % and ~30 %, respectively), but the PCG-BG (60:40) E7-BMP scaffold showed 65 % bone formation inside the defect and 68 % of new bone area [44]. Li *et al.* (2021) incorporated nanoparticles (NPs) of microRNAs-26a (miR-26a) in the PCG-BG (60:40) aerogels to promote bone mesenchymal stem cell osteogenic differentiation and tissue vascularization [43]. In terms of *in vivo* bone regeneration in rat calvaria defects at the 4th week of implantation, aerogel with miR-NC NPs (negative control – without miR-26a) promoted significantly more bone formation (7.5 mm^3 of bone volume, 21.4 % of BV/TV, 19.7 % of bone formation area) than that observed in the empty defect (2.1 mm^3 of bone volume, 6.0 % of BV/TV, 7.3 % of bone formation area), and the addition of the miR-26a significantly increased the bone regeneration (21.8 mm^3 of bone volume, 62.2 % of BV/TV, 56.4 % of bone formation area) [43]. However, despite the larger pore diameters in the Li *et al.* (2021) study (100 µm) [43], the bone regeneration results were similar to the two types of PCG-BG (60:40) aerogels prepared in the two different studies [43, 44].

Another study involving BMP-2-derived peptides was conducted by Ye *et al.* (2019), which stated that the presence of nHA significantly increased the *in vivo* new bone formation in rat calvaria defects implanted with nHA/PLA/Gel 3D nanofibrous scaffolds when compared to the control material, but the presence of BMP-2 peptides further increased the BV/TV results (~45 %)

[16]. Moreover, after 12 weeks, Zhang *et al.* (2021) showed that although both three-layered aerogel scaffolds (A-G and A-E7G) for osteochondral regeneration tended to increase new bone formation, only the scaffolds modified with E7-peptide showed significant differences (BV/TV ~50 %; Tb.Th ~0.35 mm; Tb.N ~2.0 mm^{-1}) when compared to the control defects [46]. Furthermore, upon nanoindentation tests, the regenerated osteochondral tissue in the A-E7G aerogel-implanted defect exhibited significantly higher reduced modulus (~20 MPa) and hardness (~400 kPa) when compared with the other tested groups [46].

An interesting approach was reported by Li *et al.* (2018) with the 30-5B sugarcane-derived borate bioglass aerogel scaffold with anisotropic properties [55]. They implanted their scaffold in either a horizontal or vertical orientation of the sugarcane microstructure in bilateral ulnar bone defects in rabbits [55]. After 8 weeks, the vertically oriented aerogel scaffolds that were parallel to the long axis of the rabbit ulna showed complete bone formation along the defect, when compared to the control and horizontally oriented scaffold, which showed lower tissue formation [55].

4. FUTURE RESEARCH APPROACHES FOR AEROGELS AND BONE REGENERATION

Despite the recent advances in aerogel technology for biomedical applications, particularly for bone regeneration, there are still some issues that must be overcome in order to successfully obtain reliable clinical results with these graft materials. Robust production methods must be further developed to obtain aerogels comprising both mesopores and micro/macropores, which might be accomplished by combining several techniques such as 3D printing, freeze casting and freeze drying [11, 23]. It would also be interesting to further develop anisotropic scaffolds with oriented porous structures matching the surrounding native bone [55, 63].

Mainly, there is also the need to improve the balance between high porosity and mechanical strength of composite aerogels, specifically under wet conditions. The plasticizing effect of aqueous solutions in the polymeric matrices is very significant, and it is necessary to increase the stiffness after swelling. Further testing of crosslinking conditions/agents, as well as nanofiber technologies (namely the use of short nanofibers) could improve the materials' properties, mechanically reinforcing the aerogel structure [16, 43, 44].

Additionally, reducing the use of solvents and chemicals used in the scaffolds' synthesis would improve the biocompatibility and decrease the production costs and the environmental impact. Moreover, there is a need to perform more studies regarding the incorporation of important biological molecules to provide higher osteoinduction properties and to boost host cellular response and tissue regeneration [16, 43, 44].

Another research line in the bone bioengineering technologies is the development of tissue regeneration based on *in vitro* 3D tissue models (organ-on-a-chip) instead of using *in vivo* animal experiments. By using microfluidic systems, this approach overcomes the limitations of

simplistic 2D cell cultures [1], while avoiding the obstacles related to ethical issues and high costs associated with animal experiments [64]. Although significant efforts have already been made in the development of organ-on-a-chip technology for the gastrointestinal tract, vasculature, lung, kidney and others, there are not yet so many effective examples of bone-on-a-chip models [64, 65]. In fact, most of the bone-on-a-chip devices produced so far were developed to study diseases such as osteoporosis or cancer/metastasis and related therapies [66], but those for bone tissue development or regeneration are scarce [64]. Microfluidic systems allow the simulation of biomechanical cues that are important for bone cell functionality through shear stresses caused by the fluid flow [1, 65]. Both natural and synthetic-based organic/inorganic compounds have been employed for the obtention of 3D hydrogels for bone-on-a-chip devices [1, 65]. Three-dimensional bioprinting has also proved to be useful in developing these devices [1, 64, 66, 67], as well as other scaffold preparation methods frequently employed for bone regeneration [66]. Additionally, co-culture cells, such as primary human osteoblasts (HOBs) [6] or human bone marrow-derived mesenchymal stem cells (hBM-MSCs) and human umbilical vein endothelial cells (HUVECs) [68], human adipose-derived stem cells (ADSCs) [69] or metastatic breast cancer (BrCa) cells [70], and joining specific growth factors such as BMP-2 could be employed to better mimic bone microenvironment [68] in either physiological or pathological conditions.

5. CONCLUSIONS

The present review compared the preparation methods of composite aerogels for bone regeneration and the outcomes in terms of their porous structure, mechanical performance, swelling and *in vivo* bone repair in small animal models. Having in mind the recent changes in the aerogel definition, it was noticeable that most authors have been preparing their aerogel-based bone scaffolds through freeze drying instead of supercritical and ambient pressure drying, due to the need for achieving a wider range of pore sizes, including micro/macropores. Supercritical drying technology may produce scaffolds with very high total porosities, but mainly exhibit mesoporosity, which, despite providing a favorable texture and high surface area for cell attachment, may not be so effective for vascularization, cell proliferation and migration and molecular transport. Other production methods such as printing and freeze casting, should be used more to overcome these drawbacks. On the other hand, supercritical-dried aerogels seemed to provide better mechanical compressive strength in dry conditions when compared with similar freeze-dried composite aerogels, though other important key factors such as the precursors (organic and inorganic), crosslinking agent and technologies such as electrospinning seemed to play relevant roles in the mechanical performance. However, the mechanical tests in wet conditions deserve to be further studied, because they should provide more reliable viscoelastic properties after swelling. This review highlighted the performance of aerogels towards the relevance of the inorganic phase, as well as the presence of osteoinductive molecules such as BPM-2-derived peptides for new bone formation *in vivo* in critical size defects. Though microCT

technology enabled reducing the number of animals used for assessing *in vivo* bone regeneration quantification, research in this field should focus on improving knowledge in areas such as 3D *in vitro* bone regeneration models for replacing/reducing live animal experimentation, in order to avoid unethical procedures.

Author Contributions: Conceptualization, M.S.-L., M.H.F. and C.L.S.; methodology, M.S.-L.; validation, M.S.-L. and C.L.S.; formal analysis, M.S.-L. and C.L.S.; data curation, M.S.-L. and C.L.S.; writing—original draft preparation, M.S.-L.; writing—review and editing, M.S.-L., M.H.F., F.J.M. and C.L.S.; supervision, M.H.F. and C.L.S.; project administration, M.H.F. and C.L.S.; funding acquisition, M.H.F. and C.L.S. All authors have read and agreed to the published version of the manuscript.

Funding: The authors acknowledge i3S—Instituto de Investigação e Inovação em Saúde da Universidade do Porto, which is supported by Portuguese funds through FCT/MCTES (Fundação para a Ciência e a Tecnologia)—UIDB/04293/2020 and LAQV/REQUIMTE through projects UIDB/50006/2020 and UIDP/50006/2020. The last author, C.L.S., gratefully acknowledges FCT for financial support (CEECINST/00091/2018/CP1500/CT0019).

Institutional Review Board Statement: Not applicable.

Informed Consent Statement: Not applicable.

Data Availability Statement: The data are unavailable.

Conflicts of Interest: The authors declare no conflict of interest.

III. References

[1] Yuste, I.; Luciano, F. C.; González-Burgos, E.; Lalatsa, A.; Serrano, D. Mimicking bone microenvironment: 2D and 3D *in vitro* models of human osteoblasts. Pharmacol Res. 2021, 169, 105626. doi: 10.1016/j.phrs.2021.105626

[2] Zheng, L.; Zhang, S.; Ying, Z.; Liu, J.; Zhou, Y.; Chen, F. Engineering of aerogel-based biomaterials for biomedical applications. Int J Nanomedicine. 2020, 15, 2363-2378. doi: 10.2147/IJN.S238005

[3] Gartner, L. P. Textbook of Histology, 4th Ed.; Elsevier: Philadelphia, USA, 2017. doi: -

[4] Burr, D. B.; Allen, M. R. Basic and Applied Bone Biology, 2nd Ed.; Elsevier: London, UK, 2019. doi: -

[5] Robles-Linares, J. A.; Ramírez-Cedillo, E.; Siller, H. R.; Rodríguez, C. A.; Martínez-López, J. I. Parametric modeling of biomimetic cortical bone microstructure for additive manufacturing. Materials. 2019, 12, 913. doi: 10.3390/ma12060913

[6] Nasello, G.; Alamán-Díez, P.; Schiavi, J.; Pérez, M. Á.; McNamara, L.; García-Aznar, J. M. Primary Human Osteoblasts Cultured in a 3D Microenvironment Create a Unique Representative Model of Their Differentiation Into Osteocytes. Front Bioeng Biotechnol. 2020, 8, 336. doi: 10.3389/fbioe.2020.00336

[7] Perez-Moreno, A.; Reyes-Peces, M. d. l. V.; de Los Santos, D. M.; Pinaglia-Tobaruela, G.; de la Orden, E.; Vilches-Pérez, J. I.; Salido, M.; Piñero, M.; de la Rosa-Fox, N. Hydroxyl groups induce bioactivity in silica/chitosan aerogels designed for bone tissue engineering. In vitro model for the assessment of osteoblasts behavior. Polymers (Basel). 2020, 12, 2802. doi: 10.3390/polym12122802

[8] Asha, S.; Ananth, A. N.; Jose, S. P.; Rajan, M. J. Reduced graphene oxide aerogel networks with soft interfacial template for applications in bone tissue regeneration. Appl Nanosci. 2018, 8, 395-405. doi: 10.1007/s13204-018-0803-z

[9] Chen, Z.-J.; Shi, H.-H.; Zheng, L.; Zhang, H.; Cha, Y.-Y.; Ruan, H.-X.; Zhang, Y.; Zhang, X.-C. A new cancellous bone material of silk fibroin/cellulose dual network composite aerogel reinforced by nano-hydroxyapatite filler. Int J Biol Macromol. 2021, 182, 286-297. doi: 10.1016/j.ijbiomac.2021.03.204

[10] Liu, M.; Shafiq, M.; Sun, B.; Wu, J.; Wang, W.; EL-Newehy, M.; EL-Hamshary, H.; Morsi, Y.; Ali, O.; Khan, A. u. R. Composite superelastic aerogel scaffolds containing flexible SiO_2 nanofibers promote bone regeneration. Adv Healthc Mater. 2022, 11, 2200499. doi: 10.1002/adhm.202200499

[11] Ng, P.; Pinho, A. R.; Gomes, M. C.; Demidov, Y.; Krakor, E.; Grume, D.; Herb, M.; Lê, K.; Mano, J.; Mathur, S. Fabrication of Antibacterial, Osteo-Inductor 3D Printed Aerogel-Based Scaffolds by Incorporation of Drug Laden Hollow Mesoporous Silica Microparticles into the Self-Assembled Silk Fibroin Biopolymer. Macromol Biosci. 2022, 22, 2100442. doi: 10.1002/mabi.202100442

[12] Anastasio, A. T.; Paniagua, A.; Diamond, C.; Ferlauto, H. R.; Fernandez-Moure, J. S. Nanomaterial nitric oxide delivery in traumatic orthopedic regenerative medicine. Front Bioeng Biotechnol. 2021, 8, 592008. doi: 10.3389/fbioe.2020.592008

[13] Berrio, M.; Oñate, A.; Salas, A.; Fernández, K.; Meléndrez, M. Synthesis and applications of graphene oxide aerogels in bone tissue regeneration: a review. Mater Today Chem. 2021, 20, 100422. doi: 10.1016/j.mtchem.2021.100422

[14] Guo, J.; Yang, X.; Chen, J.; Wang, C.; Kang, Y.; Jiang, T.; Chen, M.; Li, W.; Zhou, C.; Chen, Z. Accelerated Bone Regeneration by an Astaxanthin-Modified Antioxidant Aerogel through Relieving Oxidative Stress via the NRF2 Signaling Pathway. ACS Biomater Sci Eng. 2022, 8, 4524-4534. doi: 10.1021/acsbiomaterials.2c00596

[15] Rong, R.; Li, H.; Dong, X.; Hu, L.; Shi, X.; Du, Y.; Deng, H.; Sa, Y. Silk fibroin-chitosan aerogel reinforced by nanofibers for enhanced osteogenic differentiation in MC3T3-E1 cells. Int J Biol Macromol. 2023, 233, 123501. doi: 10.1016/j.ijbiomac.2023.123501

[16] Ye, K.; Liu, D.; Kuang, H.; Cai, J.; Chen, W.; Sun, B.; Xia, L.; Fang, B.; Morsi, Y.; Mo, X. Three-dimensional electrospun nanofibrous scaffolds displaying bone morphogenetic protein-2-derived peptides for the promotion of osteogenic differentiation of stem cells and bone regeneration. J Colloid Interface Sci. 2019, 534, 625-636. doi: 10.1016/j.jcis.2018.09.071

[17] Goimil, L.; Braga, M. E.; Dias, A. M.; Gomez-Amoza, J. L.; Concheiro, A.; Alvarez-Lorenzo, C.; de Sousa, H. C.; Garcia-Gonzalez, C. A. Supercritical processing of starch aerogels and aerogel-loaded poly (ε-caprolactone) scaffolds for sustained release of ketoprofen for bone regeneration. J CO2 Util. 2017, 18, 237-249. doi: 10.1016/j.jcou.2017.01.028

[18] Osorio, D. A.; Lee, B. E.; Kwiecien, J. M.; Wang, X.; Shahid, I.; Hurley, A. L.; Cranston, E. D.; Grandfield, K. Cross-linked cellulose nanocrystal aerogels as viable bone tissue scaffolds. Acta Biomater. 2019, 87, 152-165. doi: 10.1016/j.actbio.2019.01.049

[19] Santos-Rosales, V.; Iglesias-Mejuto, A.; García-González, C. A. Solvent-free approaches for the processing of scaffolds in regenerative medicine. Polymers (Basel). 2020, 12, 533. doi: 10.3390/polym12030533

[20] Huang, G.-J.; Yu, H.-P.; Wang, X.-L.; Ning, B.-B.; Gao, J.; Shi, Y.-Q.; Zhu, Y.-J.; Duan, J.-L. Correction: Highly porous and elastic aerogel based on ultralong hydroxyapatite nanowires for high-performance bone regeneration and neovascularization. J Mater Chem B. 2021, 9, 7566-7566. doi: 10.1039/d1tb90128a

[21] Al-Jawuschi, N.; Chen, S.; Abie, N.; Fischer, T.; Fare, S.; Maleki, H. H. Self-Assembly-Driven Bi_2S_3 Nanobelts Integrated a Silk-Fibroin-Based 3D-Printed Aerogel-Based Scaffold with a Dual-Network Structure for Photothermal Bone Cancer Therapy. Langmuir. 2023, 39, 4326-4337. doi: 10.1021/acs.langmuir.2c03334

[22] Liu, S.; Li, D.; Chen, X.; Jiang, L. Biomimetic cuttlebone polyvinyl alcohol/carbon nanotubes/hydroxyapatite aerogel scaffolds enhanced bone regeneration. Colloids Surf B Biointerfaces. 2022, 210, 112221. doi: 10.1016/j.colsurfb.2021.112221

[23] Karamat-Ullah, N.; Demidov, Y.; Schramm, M.; Grumme, D.; Auer, J.; Bohr, C.; Brachvogel, B.; Maleki, H. 3D printing of antibacterial, biocompatible, and biomimetic hybrid aerogel-based scaffolds with hierarchical porosities via integrating antibacterial peptide-modified silk fibroin with silica nanostructure. ACS Biomater Sci Eng. 2021, 7, 4545-4556. doi: 10.1021/acsbiomaterials.1c00483

[24] El-Wakil, N.; Kamel, R.; Mahmoud, A. A.; Dufresne, A.; Abouzeid, R. E.; Abo El-Fadl, M. T.; Maged, A. Risedronate-loaded aerogel scaffolds for bone regeneration. Drug Deliv. 2023, 30, 51-63. doi: 10.1080/10717544.2022.2152135

[25] Chen, Z.-J.; Zhang, Y.; Zheng, L.; Zhang, H.; Shi, H.-H.; Zhang, X.-C.; Liu, B. Mineralized self-assembled silk fibroin/cellulose interpenetrating network aerogel for bone tissue engineering. Biomater Adv. 2022, 134, 112549. doi: 10.1016/j.msec.2021.112549

[26] Maleki, H.; Shahbazi, M.-A.; Montes, S.; Hosseini, S. H.; Eskandari, M. R.; Zaunschirm, S.; Verwanger, T.; Mathur, S.; Milow, B.; Krammer, B. Mechanically strong silica-silk fibroin bioaerogel: a hybrid scaffold with ordered honeycomb micromorphology and multiscale porosity for bone regeneration. ACS Appl Mater Interfaces. 2019, 11, 17256-17269. doi: 10.1021/acsami.9b04283

[27] Kistler, S. S. Coherent expanded aerogels and jellies. Nature. 1931, 127, 741-741. doi: 10.1038/127741a0

[28] Vareda, J. P.; Lamy-Mendes, A.; Durães, L. A reconsideration on the definition of the term aerogel based on current drying trends. Microporous Mesoporous Mater. 2018, 258, 211-216. doi: 10.1016/j.micromeso.2017.09.016

[29] García-González, C. A.; Budtova, T.; Durães, L.; Erkey, C.; Del Gaudio, P.; Gurikov, P.; Koebel, M.; Liebner, F.; Neagu, M.; Smirnova, I. An opinion paper on aerogels for biomedical and environmental applications. Molecules. 2019, 24, 1815. doi: 10.3390/molecules24091815

[30] Stergar, J.; Maver, U. Review of aerogel-based materials in biomedical applications. J Sol-Gel Sci Technol. 2016, 77, 738-752. doi: 10.1007/s10971-016-3968-5

[31] Alemán, J.; Chadwick, A. V.; He, J.; Hess, M.; Horie, K.; Jones, R. G.; Kratochvíl, P.; Meisel, I.; Mita, I.; Moad, G. Definitions of terms relating to the structure and processing of sols, gels, networks, and inorganic-organic hybrid materials (IUPAC Recommendations 2007). Pure Appl Chem. 2007, 79, 1801-1829. doi: 10.1351/pac200779101801

[32] Martins, M.; Barros, A. A.; Quraishi, S.; Gurikov, P.; Raman, S.; Smirnova, I.; Duarte, A. R. C.; Reis, R. L. Preparation of macroporous alginate-based aerogels for biomedical applications. J Supercrit Fluids. 2015, 106, 152-159. doi: 10.1016/j.supflu.2015.05.010

[33] El-Naggar, M. E.; Othman, S. I.; Allam, A. A.; Morsy, O. M. Synthesis, drying process and medical application of polysaccharide-based aerogels. Int J Biol Macromol. 2020, 145, 1115-1128. doi: 10.1016/j.ijbiomac.2019.10.037

[34] Ferreira-Gonçalves, T.; Constantin, C.; Neagu, M.; Reis, C. P.; Sabri, F.; Simón-Vázquez, R. Safety and efficacy assessment of aerogels for biomedical applications. Biomed Pharmacother. 2021, 144, 112356. doi: 10.1016/j.biopha.2021.112356

[35] Guastaferro, M.; Reverchon, E.; Baldino, L. Polysaccharide-based aerogel production for biomedical applications: A comparative review. Materials (Basel). 2021, 14, 1631. doi: 10.3390/ma14071631

[36] Hegedűs, C.; Czibulya, Z.; Tóth, F.; Dezső, B.; Hegedűs, V.; Boda, R.; Horváth, D.; Csík, A.; Fábián, I.; Tóth-Győri, E. The Effect of Heat Treatment of β-Tricalcium Phosphate-Containing Silica-Based Bioactive Aerogels on the Cellular Metabolism and Proliferation of MG63 Cells. Biomedicines. 2022, 10, 662. doi: 10.3390/biomedicines10030662

[37] Yahya, E. B.; Amirul, A.; HPS, A. K.; Olaiya, N. G.; Iqbal, M. O.; Jummaat, F.; AK, A. S.; Adnan, A. Insights into the role of biopolymer aerogel scaffolds in tissue engineering and regenerative medicine. Polymers (Basel). 2021, 13, 1612. doi: 10.3390/polym13101612

[38] Goimil, L.; Santos-Rosales, V.; Delgado, A.; Evora, C.; Reyes, R.; Lozano-Perez, A. A.; Aznar-Cervantes, S. D.; Cenis, J. L.; Gómez-Amoza, J. L.; Concheiro, A. scCO_2-foamed silk fibroin aerogel/poly (ε-caprolactone) scaffolds containing dexamethasone for bone regeneration. J CO2 Util. 2019, 31, 51-64. doi: 10.1016/j.jcou.2019.02.016

[39] Dong, S.; Zhang, Y.-n.; Wan, J.; Cui, R.; Yu, X.; Zhao, G.; Lin, K. A novel multifunctional carbon aerogel-coated platform for osteosarcoma therapy and enhanced bone regeneration. J Mater Chem B. 2020, 8, 368-379. doi: 10.1039/c9tb02383f

[40] Li, D.; Chen, K.; Duan, L.; Fu, T.; Li, J.; Mu, Z.; Wang, S.; Zou, Q.; Chen, L.; Feng, Y. Strontium ranelate incorporated enzyme-cross-linked gelatin nanoparticle/silk fibroin aerogel for osteogenesis in OVX-induced osteoporosis. ACS Biomater Sci Eng. 2019, 5, 1440-1451. doi: 10.1021/acsbiomaterials.8b01298

[41] Iglesias-Mejuto, A.; García-González, C. A. 3D-printed alginate-hydroxyapatite aerogel scaffolds for bone tissue engineering. Mater Sci Eng C Mater Biol Appl. 2021, 131, 112525. doi: 10.1016/j.msec.2021.112525

[42] Tyshkunova, I. V.; Poshina, D. N.; Skorik, Y. A. Cellulose cryogels as promising materials for biomedical applications. Int J Mol Sci. 2022, 23, 2037. doi: 10.3390/ijms23042037

[43] Li, Y.; Wang, J.; Qian, D.; Chen, L.; Mo, X.; Wang, L.; Wang, Y.; Cui, W. Electrospun fibrous sponge via short fiber for mimicking 3D ECM. J Nanobiotechnology. 2021, 19, 131. doi: 10.1186/s12951-021-00878-5.

[44] Weng, L.; Boda, S. K.; Wang, H.; Teusink, M. J.; Shuler, F. D.; Xie, J. Novel 3D hybrid nanofiber aerogels coupled with BMP-2 peptides for cranial bone regeneration. Adv Healthc Mater. 2018, 7, 1701415. doi: 10.1002/adhm.201701415

[45] Yuan, Z.; Ren, Y.; Shafiq, M.; Chen, Y.; Tang, H.; Li, B.; EL-Newehy, M.; EL-Hamshary, H.; Morsi, Y.; Zheng, H. Converging 3D printing and electrospinning: effect of poly (L-lactide)/gelatin based short nanofibers aerogels on tracheal regeneration. Macromol Biosci. 2022, 22, 2100342. doi: 10.1002/mabi.202100342

[46] Zhang, L.; Fang, J.; Fu, L.; Chen, L.; Dai, W.; Huang, H.; Wang, J.; Zhang, X.; Cai, Q.; Yang, X. Gradient fibrous aerogel conjugated with chemokine peptide for regulating cell differentiation and facilitating osteochondral regeneration. Chem Eng J. 2021, 422, 130428. doi: 10.1016/j.cej.2021.130428

[47] Chen, Y.; Shafiq, M.; Liu, M.; Morsi, Y.; Mo, X. Advanced fabrication for electrospun three-dimensional nanofiber aerogels and scaffolds. Bioact Mater. 2020, 5, 963-979. doi: 10.1016/j.bioactmat.2020.06.023

[48] Chen, S.; John, J. V.; McCarthy, A.; Xie, J. New forms of electrospun nanofiber materials for biomedical applications. Journal of materials chemistry B. 2020, 8, 3733-3746. doi: 10.1039/d0tb00271b

[49] García-González, C. A.; Concheiro, A.; Alvarez-Lorenzo, C. Processing of materials for regenerative medicine using supercritical fluid technology. Bioconjug Chem. 2015, 26, 1159-1171. doi: 10.1021/bc5005922

[50] Gupta, R. B.; Shim, J.-J. Solubility in supercritical carbon dioxide, 1st Ed.; CRC press: Boca Raton, USA, 2006. doi: 10.1201/9781420005998

[51] Zhang, J.; Davis, T. A.; Matthews, M. A.; Drews, M. J.; LaBerge, M.; An, Y. H. Sterilization using high-pressure carbon dioxide. J Supercrit Fluids. 2006, 38, 354-372. doi: 10.1016/j.supflu.2005.05.005

[52] Gomes, P. B.; Mata, V. G.; Rodrigues, A. E. Production of rose geranium oil using supercritical fluid extraction. J Supercrit Fluids. 2007, 41, 50-60. doi: 10.1016/j.supflu.2006.08.018

[53] Pérez-Moreno, A.; Piñero, M.; Fernández-Montesinos, R.; Pinaglia-Tobaruela, G.; Reyes-Peces, M. V.; Mesa-Díaz, M. d. M.; Vilches-Pérez, J. I.; Esquivias, L.; de la Rosa-Fox, N.; Salido, M. Chitosan-Silica Hybrid Biomaterials for Bone Tissue Engineering: A Comparative Study of Xerogels and Aerogels. Gels. 2023, 9, 383. doi: 10.3390/gels9050383

[54] Reyes-Peces, M. V.; Fernández-Montesinos, R.; Mesa-Díaz, M. d. M.; Vilches-Pérez, J. I.; Cárdenas-Leal, J. L.; de la Rosa-Fox, N.; Salido, M.; Piñero, M. Structure-Related Mechanical Properties and Bioactivity of Silica–Gelatin Hybrid Aerogels for Bone Regeneration. Gels. 2023, 9, 67. doi: 10.3390/gels9010067

[55] Li, T.; Ai, F.; Shen, W.; Yang, Y.; Zhou, Y.; Deng, J.; Li, C.; Ding, X.; Xin, H.; Wang, X. Microstructural orientation and precise regeneration: a proof-of-concept study on the sugar-cane-derived implants with bone-mimetic hierarchical structure. ACS Biomater Sci Eng. 2018, 4, 4331-4337. doi: 10.1021/acsbiomaterials.8b01052

[56] Ruphuy, G.; Souto-Lopes, M.; Paiva, D.; Costa, P.; Rodrigues, A.; Monteiro, F.; Salgado, C.; Fernandes, M.; Lopes, J.; Dias, M. Supercritical CO_2 assisted process for the production of high-purity and sterile nano-hydroxyapatite/chitosan hybrid scaffolds. J Biomed Mater Res B Appl Biomater. 2018, 106, 965-975. doi: 10.1002/jbm.b.33903

[57] Souto-Lopes, M.; Grenho, L.; Manrique, Y.; Dias, M. M.; Fernandes, M. H.; Monteiro, F. J.; Salgado, C. L. Full physicochemical and biocompatibility characterization of a supercritical CO_2 sterilized nano-hydroxyapatite/chitosan biodegradable scaffold for periodontal bone regeneration. Biomater Adv. 2023, 146, 213280. doi: 10.1016/j.bioadv.2023.213280

[58] Liu, S.; Zhou, C.; Mou, S.; Li, J.; Zhou, M.; Zeng, Y.; Luo, C.; Sun, J.; Wang, Z.; Xu, W. Biocompatible graphene oxide–collagen composite aerogel for enhanced stiffness and *in situ* bone regeneration. Mater Sci Eng C Mater Biol Appl. 2019, 105, 110137. doi: 10.1016/j.msec.2019.110137

[59] Abdul Khalil, H. P. S.; Yahya, E. B.; Tajarudin, H. A.; Balakrishnan, V.; Nasution, H. Insights into the role of biopolymer-based xerogels in biomedical applications. Gels. 2022, 8, 334. doi: 10.3390/gels8060334

[60] Pérez-Moreno, A.; Reyes-Peces, M. V.; Vilches-Pérez, J. I.; Fernández-Montesinos, R.; Pinaglia-Tobaruela, G.; Salido, M.; De la Rosa-Fox, N.; Piñero, M. Effect of washing treatment on the textural properties and bioactivity of silica/chitosan/TCP xerogels for bone regeneration. Int J Mol Sci. 2021, 22, 8321. doi: 10.3390/ijms22158321

[61] Li, L.; Wang, P.; Liang, H.; Jin, J.; Zhang, Y.; Shi, J.; Zhang, Y.; He, S.; Mao, H.; Xue, B. Design of a Haversian system-like gradient porous scaffold based on triply periodic minimal surfaces for promoting bone regeneration. J Adv Res. 2023, doi: 10.1016/j.jare.2023.01.004

[62] Santos-Rosales, V.; Gallo, M.; Jaeger, P.; Alvarez-Lorenzo, C.; Gómez-Amoza, J. L.; García-González, C. A. New insights in the morphological characterization and modelling of poly (ε-caprolactone) bone scaffolds obtained by supercritical CO_2 foaming. J Supercrit Fluids. 2020, 166, 105012. doi: 10.1016/j.supflu.2020.105012

[63] John, J.V.; McCarthy, A.; Wang, H.; Luo, Z.; Li, H.; Wang, Z.; Cheng, F.; Zhang, Y.S.; Xie, J. Freeze-Casting with 3D-Printed Templates Creates Anisotropic Microchannels and Patterned Macrochannels within Biomimetic Nanofiber Aerogels for Rapid Cellular Infiltration. Adv. Healthc. Mater. 2021, 10, 2100238.

[64] Galván-Chacón, V. P.; Zampouka, A.; Hesse, B.; Bohner, M.; Habibovic, P.; Barata, D. Bone-on-a-Chip: A Microscale 3D Biomimetic Model to Study Bone Regeneration. Adv Eng Mater. 2022, 24, 2101467. doi: 10.1002/adem.202101467

[65] Monteduro, A. G.; Rizzato, S.; Caragnano, G.; Trapani, A.; Giannelli, G.; Maruccio, G. Organs-on-chips technologies – A guide from disease models to opportunities for drug development. Biosens Bioelectron. 2023, 231, 115271. doi: 10.1016/j.bios.2023.115271

[66] Almela, T.; Al-Sahaf, S.; Brook, I. M.; Khoshroo, K.; Rasoulianboroujeni, M.; Fahimipour, F.; Tahriri, M.; Dashtimoghadam, E.; Bolt, R.; Tayebi, L. 3D printed tissue engineered model for bone invasion of oral cancer. Tissue Cell. 2018, 52, 71-77. doi: 10.1016/j.tice.2018.03.009

[67] Sharma, R.; Perez, M. R.; da Silva, V. A.; Thomsen, J.; Bhardwaj, L.; Andrade, T. A.; Alhussan, A.; Willerth, S. M. 3D bioprinting complex models of cancer. Biomater Sci. 2023, doi: 10.1039/d2bm02060b

[68] Blache, U.; Metzger, S.; Vallmajo-Martin, Q.; Martin, I.; Djonov, V.; Ehrbar, M. Dual role of mesenchymal stem cells allows for microvascularized bone tissue-like environments in PEG hydrogels. Adv Healthc Mater. 2016, 5, 489-498. doi: 10.1002/adhm.201500795

[69] Kim, H.; Han, S. H.; Kook, Y.-M.; Lee, K.-M.; Jin, Y.-Z.; Koh, W.-G.; Lee, J. H.; Lee, K. A novel 3D indirect co-culture system based on a collagen hydrogel scaffold for enhancing the osteogenesis of stem cells. J Mater Chem B. 2020, 8, 9481-9491. doi: 10.1039/d0tb01770a

[70] Cui, H.; Esworthy, T.; Zhou, X.; Hann, S. Y.; Glazer, R. I.; Li, R.; Zhang, L. G. Engineering a Novel 3D Printed Vascularized Tissue Model for Investigating Breast Cancer Metastasis to Bone. Adv Healthc Mater. 2020, 9, 1900924. doi: 10.1002/adhm.201900924

CHAPTER IV

Full Physicochemical and Biocompatibility Characterization of a Supercritical CO_2 Sterilized Nano-hydroxyapatite/Chitosan Biodegradable Scaffold for Periodontal Bone Regeneration

Full Physicochemical and Biocompatibility Characterization of a Supercritical CO_2 Sterilized Nano-hydroxyapatite/Chitosan Biodegradable Scaffold for Periodontal Bone Regeneration

Souto-Lopes M [a,b,c], Grenho L [d,e], Manrique Y [f,g], Dias MM [f,g], Fernandes MH [d,e], Monteiro FJ [a,b,c,h], Salgado CL [a,b]

a – i3S – Instituto de Investigação e Inovação em Saúde da Universidade do Porto, R. Alfredo Allen 208, 4200-135 Porto, Portugal

b – INEB – Instituto de Engenharia Biomédica, Universidade do Porto, R. Alfredo Allen 208, 4200-135 Porto, Portugal

c – Faculty of Engineering of the University of Porto, Rua Dr. Roberto Frias, 4200-465 Porto, Portugal

d – Faculty of Dental Medicine of the University of Porto, R. Dr. Manuel Pereira da Silva, 4200-393 Porto, Portugal

e – LAQV/REQUIMTE – Laboratório Associado para a Química Verde/ Rede de Química e Tecnologia, Portugal

f – LSRE-LCM – Laboratory of Separation and Reaction Engineering – Laboratory of Catalysis and Materials, Faculty of Engineering of the University of Porto, Rua Dr. Roberto Frias, 4200-465 Porto, Portugal

g – ALiCE – Associate Laboratory in Chemical Engineering, Faculty of Engineering of the University of Porto, Rua Dr. Roberto Frias, 4200-465 Porto, Portugal

h – Porto Comprehensive Cancer Center (P.CCC), R. Dr. António Bernardino de Almeida, 4200-072, Porto, Portugal

Biomaterials Advances, 2023, 146:213280. doi: 10.1016/j.bioadv.2023.213280

ABSTRACT

Despite bone's innate self-renewal capability, some periodontal pathologic and traumatic defects' size inhibits full spontaneous regeneration. This current research characterized a 3D porous biodegradable nano-hydroxyapatite/chitosan (nHAp/CS, 70/30) scaffold for periodontal bone regeneration, which preparation method includes the final solvent extraction and sterilization through supercritical CO_2 ($scCO_2$).

MicroCT analysis revealed the fully interconnected porous microstructure of the nHAp/CS scaffold (total porosity 78 %, medium pore size 200 μm) which is critical for bone regeneration. Scanning electron microscopy (SEM) showed HAp crystals forming on the surface of the nHAp/CS scaffold after 21 days in simulated body fluid, demonstrating its bioactivity *in vitro*. The presence of nHAp in the scaffolds promoted a significantly lower biodegradation rate compared to a plain CS scaffold in PBS. Dynamic mechanical analysis confirmed their viscoelasticity, but the presence of nHAp significantly enhanced the storage modulus (42.34 ± 6.09 kPa at 10 Hz after 28 days in PBS), showing that it may support bone ingrowth at low-load bearing bone defects. Both scaffold types significantly inhibited the growth, attachment and colony formation abilities of *S. aureus* and *E. coli*, enhancing the relevance of chitosan in the grafts' composition for the naturally contaminated oral environment. At SEM and confocal laser scanning microscopy, MG63 cells showed normal morphology and could adhere and proliferate inside the biomaterials' porous structure, especially for the nHAp/CS scaffold, reaching higher proliferative rate at day 14. MG63 cells seeded within nHAp/CS scaffolds presented a higher expression of RUNX2, collagen A1 and Sp7 osteogenic genes compared to the CS samples.

The *in vivo* subcutaneous implantation in mice of both scaffold types showed lower biodegradability with the preservation of the scaffolds porous structure that allowed the ingrowth of connective tissue until 5 weeks. Histology shows an intensive and progressive ingrowth of new vessels and collagen between the 3rd and the 5th week, especially for the nHAp/CS scaffold.

So far, the $scCO_2$ method enabled the production of a cost-effective and environment-friendly ready-to-use nHAp/CS scaffold with microstructural, chemical, mechanical and biocompatibility features that make it a suitable bone graft alternative for defect sites in an adverse environment as in periodontitis and peri-implantitis.

KEYWORDS

Biomimetics, Nano-hydroxyapatite/chitosan scaffold, Highly-porous 3D microstructure, Antimicrobial activity, Osteogenic differentiation, Biomaterials

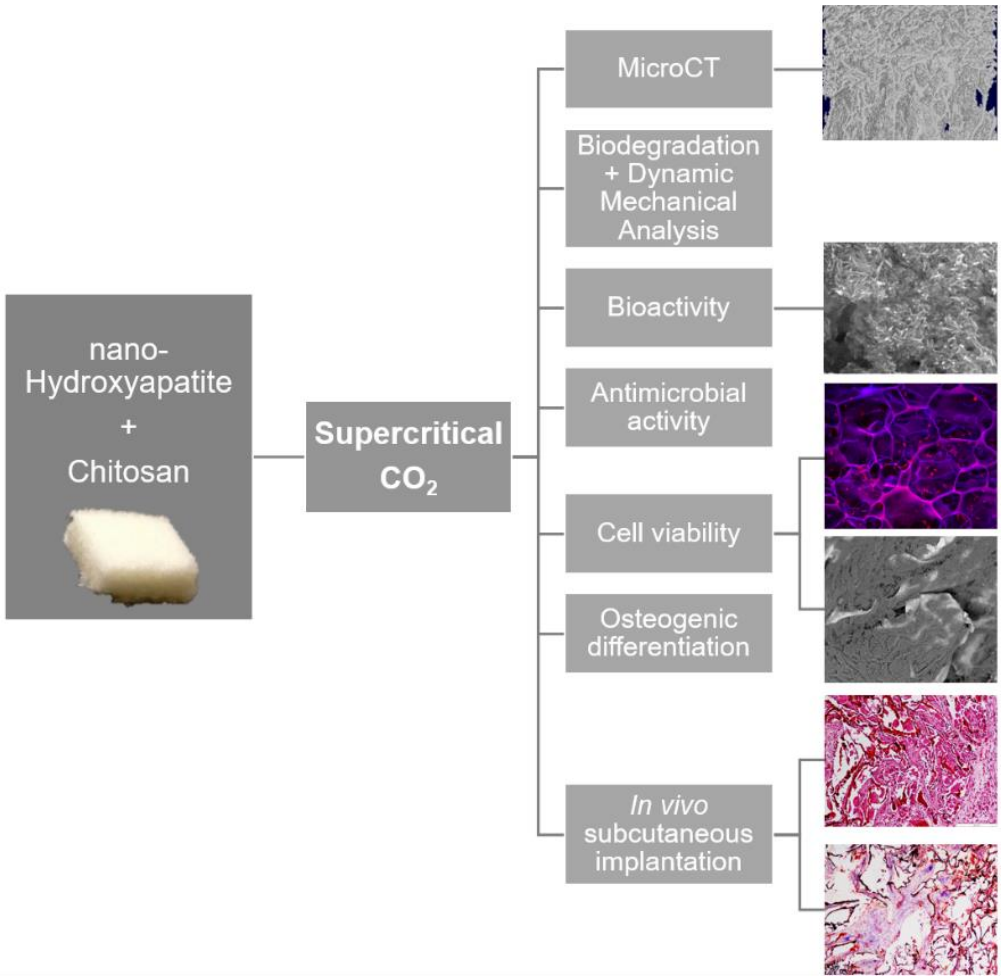

Graphical abstract

1. INTRODUCTION

Despite bone innate capability of constant self-renewal to maintain its integrity [1, 2], some periodontal pathologic and traumatic lesions are so large that full spontaneous regeneration is not possible [3]. In recent years, periodontal therapy goal has shifted from simply arresting the progression of periodontal tissues breakdown through conventional procedures, to guided tissue/bone regeneration to promote full neo-formation of the periodontal apparatus [3-7]. Therefore, bone tissue engineering has been developing biodegradable scaffold biomaterials that fill the empty spaces, guide and stimulate bone regrowth by relying on the host's stem cells populations and growth factors [4, 5, 8, 9]. The focus has been on the development of biomimetic composite scaffolds containing an organic polymeric extracellular matrix with dispersed inorganic nanocrystals that mimic bone architecture and chemical composition [4, 9-14].

These biomaterials should ideally be biocompatible, highly porous, biodegradable, hydrophilic, osteoconductive, osteogenic and osteoinductive, have enough mechanical strength, show antimicrobial activity, being sterile, clinically versatile, scalable and safe [4, 9, 15-19]. However, the most challenging task has been to fulfill all of these often antagonistic pre-requisites to obtain a balanced final product [13, 20]. For instance, scaffolds should withstand physiological compression in order to maintain bone volume and cells homeostasis, while at the same time having a highly biodegradable interconnective large porous structure [9, 21-23]. Moreover, many hazardous chemicals that are used to prepare homogeneous mixtures (*e.g.* solvents), crosslinking agents, foamers or pore-forming agents and drug carriers, as well as neutralizers of all the previous reagents, might leave byproducts and trace residues that compromise the biomaterials biocompatibility and safety, increase the production costs and are environmentally harmful [8]. Another difficult issue is to sterilize the final scaffold without modifying the structural and chemical characteristics of the biomaterial, especially because conventional sterilization techniques employ extreme conditions of heat and pressure, chemicals or radiation that damage the sensitive polymeric matrices [13, 16, 20, 24-28], making it imperative to find alternative sterilization solutions.

In the supercritical fluid state, CO_2 shows intermediate properties between a liquid and a gas, with no surface tension which enables its easy penetration into the complex macro and microstructures of biomaterials at mild operating conditions (critical temperature (T_C) = 31.1 ºC, critical pressure (P_C) = 7.39 MPa), that can be tuned to change its diffusivity, viscosity and density [8, 24, 28-30]. Therefore, according to Garcia-Gonzalez *et al.* supercritical CO_2 ($scCO_2$) has been employed in scaffold designing for example as a foaming promoter; as a non-solvent in the immersion-precipitation (phase inversion) technique; as an aerogel dryer without collapsing the highly porous structures; as a plasticizer of polymer matrices; as an adjunct in the preparation and impregnation of microparticles and fibers that work as vehicles for drugs/bioactive compounds; as a purification agent to remove cells and other antigens from allo/xenogenic grafts; and finally as a sterilization method with or without the use of chemical co-adjuvants [8].

In our previous work, Ruphuy *et al.*, we have developed a nano-hydroxyapatite/chitosan

(nHAp/CS) hybrid scaffold (weight ratio of 70:30 % w/w, similar to bone) for non-load bearing bone regeneration [31]. Further in Ruphuy *et al.*, nHAp/CS dispersions were produced in a continuous reactor for industrial scale-up implementation [32]. CS combined with HAp is an attractive alternative to the use of collagen [3, 19], since CS's cationic nature enables the formation of poly-electrolyte complexes with anionic ions and molecules, making it a versatile biopolymer for biomedical applications [16, 33, 34]. Besides, CS is biocompatible, biodegradable, mucoadhesive, antibacterial, anti-fungal, hydrophilic [3, 16, 21, 34, 35] and can provide elasticity and decrease brittleness to HAp-based scaffolds [3, 13, 36, 37]. The present work intended to further characterize *in vitro* the nHAp/CS scaffold in terms of its structural and physical features, potential innate antimicrobial abilities, the cytotoxicity level of its leachable in different conditions and the expression of osteogenic differentiation markers of MG63 cells, comparing with a CS scaffold as a control material. Moreover, nHAp/CS and CS scaffolds were implanted subcutaneously in CBA nude mice to evaluate *in vivo* their biodegradation and tissue biocompatibility. The characterization of these properties is a fundamental first step to assess the general safety, viability and biodegradation of the nHAp/CS scaffold as a bone graft biomaterial, before moving on to more specific assays concerning its periodontal application.

2. MATERIALS AND METHODS

2.1. Preparation of nHAp/CS and CS scaffolds

nHAp/CS scaffolds were produced using CS granules from marine animals' exoskeleton with a deacetylation degree 91.9 % and dynamic viscosity of 128 mPa·s (1 % at 20 ºC in 1 % acetic acid solution) (90/200/A1, Biolog-Heppe), and nHAp aqueous paste 15 % w/w, pH 9–10 (nanoXIM-HAp102, Fluidinova). The preparation method was described in our previous published work [31]. Briefly, nHAp paste was homogenously dispersed in a viscous CS solution (3.0 % w/v in acetic acid) in a 70:30 % w/w proportion. The nHAp/CS dispersion was poured into Petri plates and stored at -20 ºC overnight. Control samples of CS were prepared following the same protocol except for the addition of the nHAp paste. The phase separation was achieved through a standard freeze drying procedure (VirTis BenchTop 6 K, model nº 6KBTEL) for 24 h. The residual solvent removal and sterilization was performed by $scCO_2$ (in-house built unit) in continuous batch cycles at 8.0 MPa (80 bar) and 75 ºC for 2 h. Finally, the samples were collected from the sample carrier unit in sterile conditions, individually packed in sterile plastic packages (Nasco Whirl-Pak® standard bags 2 oz.) and stored at room temperature (RT). Unless stated otherwise in the next sections, the scaffolds were cut into 5 x 5 x 4 mm samples in sterile conditions to perform the experiments.

2.2. Physicochemical characterization of nHAp/CS and CS scaffolds

2.2.1. Microstructure analysis

nHAp/CS and CS samples (*n* = 3) were used to perform microCT analysis to assess scaffolds' morphology. The microCT equipment (Skyscan1276, Bruker) was operated at 40 kV, with 180º rotation and each sample scan took about 60 min. Bruker software programs were used for image reconstruction (NRecon) and observation (DataViewer), data analysis (CTAn) and 3D models obtaining (CTVol).

2.2.2. *In vitro* biodegradation and biomechanical analysis

nHAp/CS and CS samples (10 x 10 x 4 mm) were used to perform the biodegradation and biomechanical analysis in simulated physiologic conditions *i.e.* PBS with or without lysozyme at human blood serum concentration – 10 mg/L (Sigma), at 37 ºC, pH 7.4 and 100 rpm. Each dry sample was initially weighted (W_0) and then individually soaked (*n* = 5). Solutions were replaced weekly. After 7, 14 and 28 days of incubation, samples were collected and the compressive strength was obtained by Dynamic Mechanical Analysis (DMA, Tritec 2000, Triton Technology). Each wet sample was cyclically tested for 10 min at increasing frequencies from 0.1 to 20 Hz (dislocation 0.1 mm) at RT. The control conditions group samples (nHAp/CS and CS in PBS only) were collected after 1 h of incubation. The final weight (W_x) was determined when the samples were completely air-dried at RT and the biodegradation rate (B_x %) was calculated according to the following equation:

$$B_x\ \% = (W_0 - W_x)/W_0 \times 100$$

2.2.3. *In vitro* bioactivity analysis

Simulated body fluid (SBF) was prepared according to the reference protocol established by Kokubo and Takadama in 2006 [38] to evaluate the bioactivity of nHAp/CS and CS scaffolds after 7, 14, 21 and 28 days of incubation. Each sample was individually soaked in SBF, which was replaced every week. Dry nHAp/CS and CS samples (not soaked in SBF) were used as blank samples for comparing purposes. After each time-point, the samples were left to dry at RT, and then set-up on metal holders and sputter-coated (SPI-Module) with a thin gold/palladium film for observation by scanning electron microscopy (SEM, 15 kV, FEI Quanta 400FEG ESEM) and elemental analysis (EDS, EDAX Genesis X4M).

2.3. *In vitro* biological activity of nHAp/CS and CS scaffolds

2.3.1. *In vitro* antimicrobial activity analysis

The innate antimicrobial properties of nHAp/CS and CS scaffolds were evaluated against Gram-positive *Staphylococcus aureus* ATCC 25923 and Gram-negative *Escherichia coli* ATCC 25922. Overnight cultures were re-inoculated in fresh tryptic soy broth (TSB, Liofilchem) and further incubated under agitation for 3 h at 37 ºC. Each bacteria in exponential phase was then diluted in TSB to obtain an initial suspension of 10^6 colony forming units (CFU)/mL. After swelling at 37 ºC for 1 h in TSB, nHAp/CS and CS samples (n = 3) were incubated with each bacterial suspension for 24 h at 37 ºC and 100 rpm. Bacterial suspensions with no scaffold samples were used as controls. Planktonic bacteria were quantified by (i) optical density (OD) at 600 nm in a microplate reader (Synergy HT, BioTek Instruments); (ii) Alamar blue assay by adding 10 % (v/v) resazurin (0.1 mg/mL, Sigma) and reading the fluorescence intensity in the microplate reader (λex = 530 nm and λem = 590 nm); and (iii) colony counts (CFU/mL). For this, suspension samples from each well were serially diluted and plated in nutrient agar (NA, Liofilchem). Sessile bacteria on nHAp/CS and CS were evaluated by Alamar blue assay. Briefly, pre-washed scaffolds were incubated with TSB supplemented with resazurin and the fluorescence intensity was determined at 530/590 nm with the microplate reader after 30 min at 37 ºC and 100 rpm.

2.3.2. Cell culture conditions

MG63 osteoblastic-like cells (MG63 cell line, ATCC number CRL-1427™) were incubated in alpha-Minimal Essential Medium (α-MEM) supplemented with 10 % (v/v) fetal bovine serum (FBS), 100 U/mL penicillin, 100 µg/mL streptomycin and 0.25 µg/mL amphotericin B (all reagents from Gibco), in a humidified atmosphere of 5 % CO_2 at 37 ºC. At 70 – 80 % confluence, cells were detached with TrypLE Express (Gibco) for 5 min at 37 ºC to be subsequently used.

2.3.3. *In vitro* cytotoxicity analysis – indirect assay

This indirect assay was performed according to the ISO 10993-5:2009 guidelines, with slight alterations. Extract solutions were prepared by soaking nHAp/CS and CS samples in 1 mL of supplemented α-MEM for 1 and 24 h at 37 ºC in individual tubes. Half of the samples were re-soaked for another hour in new tubes with fresh medium. After centrifuging at 13500 rpm for 2 min, the pure extract solutions were added to MG63 cells (at 10^4 cells/cm^2 previously cultured for 24 h) (n = 3). Negative control cell cultures were incubated in medium without extracts. After 24

h of exposure, cells metabolic activity and viability were evaluated by MTT and live/dead assays, respectively. Briefly, 10 % of MTT solution (0.5 mg/mL, Sigma) was added to each well and incubated at 37 ºC for 3 h. Formazan crystals were dissolved with dimethyl sulfoxide (DMSO, Panreac) and the absorbance was read at 550 nm in a microplate reader. To perform the live/dead assay, cells were incubated with Calcein AM (1 µM, Bioloegend) and propidium iodide (BD Pharmingen, BD Biosciences) for 10 min at 37 ºC. The cells were observed using the Celena S digital imaging system (Logos Biosystems).

2.3.4. *In vitro* cytotoxicity analysis – direct assay

nHAp/CS and CS samples were soaked in 1 mL of supplemented α-MEM for 1 h at 37 ºC in 24-well plates with non-adherent surface. The medium was removed and 1 x 10^5 cells in 50 µL were seeded into each sample [39]. The cells were allowed to adhere for 4 h, after which the culture medium was added. Cells seeded at 5 x 10^3 cells/mL in 13 mm coverslips (Sarstedt) were used as negative controls. Cells were incubated up to 21 days at 37 ºC in a 5 % CO_2 humidified atmosphere.

Metabolic activity was assessed by Alamar blue assay on days 2, 7, 14 and 21. At each time point, after medium removal, the seeded materials were transferred to new wells and incubated with fresh medium containing 10 % resazurin (0.1 mg/mL, Sigma-Aldrich), for 3 h in standard culture conditions. The fluorescence of the supernatant was read in a microplate reader at 530/590 nm.

Immunostaining of the F-actin cytoskeleton and nucleus of MG63 cells were evaluated after 7, 14 and 21 days of culture. Briefly, nHAp/CS and CS samples were washed with PBS and fixed with 3.7 % formaldehyde for 10 min. Cells were permeabilized with 0.1 % Triton X-100 for 15 min and incubated with 1 % bovine serum albumin (BSA, Sigma-Aldrich) for 30 min to reduce non-specific binding. Cells were stained for F-actin cytoskeleton with Alexa Fluor-conjugated Phalloidin 594 nm (1:25, BioLegend) for 1 h, and nucleus with Hoechst (8 µg/mL, Enzo) for 10 min. Images were obtained using laser scanning confocal microscope (CLSM, Leica SP5).

Cell morphology and distribution were also evaluated after 7, 14 and 21 days of culture by SEM. Briefly, nHAp/CS and CS samples were washed with PBS and fixed with 1.5 % glutaraldehyde (TAAB) in 0.14 M sodium cacodylate buffer (pH = 7.3, Sigma-Aldrich) during 10 min. Samples were dehydrated in increasing concentrations of ethanol aqueous solutions for 30 min each and subsequently critical point dried (CPD 7501, Polaron Range). Samples were fixed to metal holders with carbon tape and observed in a SEM equipment (Phenom ProX; software ProSuite, Phenom World).

2.3.5. *In vitro* osteogenic differentiation analysis

To assess the osteogenic induction potential of nHAp/CS and CS scaffolds, the levels of osteogenic differentiation of MG63 cells were evaluated.

ALP activity of MG63 cells was evaluated at day 7, 14, and 21 of culture in cell lysates. Briefly, nHAp/CS and CS samples were washed with PBS and individually submersed in 300 µL of sterile ultra-pure water. After 1 h of incubation at 37 ºC, samples were frozen at -80 ºC for 1 h and then thawed at RT to promote cells lysis. Samples were cut into small pieces, vortexed and centrifuged at 13500 rpm for 2 min. ALP activity was evaluated in the supernatants by the hydrolysis of *p*-nitro-phenyl phosphate substrate (Sigma-Aldrich) in alkaline buffer solution (pH 10, 30 min, 37 ºC) and determination of p-nitrophenol at 405 nm in a microplate reader. These results were normalized to total protein content (using the same supernatant) with the BioRad DC™ protein assay kit (Lowry's method), following the manufacturer's instructions.

Cell proliferation was determined through quantification of DNA content in the supernatants using the Quant-iT™ PicoGreen™ dsDNA assay kit (Invitrogen), according to the manufacturer's instructions.

Lastly, the expression of relevant osteogenic genes was analyzed at day 7, 14 and 21 of culture by real-time quantitative polymerase chain reaction (RT-qPCR). Briefly, total RNA was extracted with NucleoSpin kit (NucleoSpin RNA, Macherey-Nagel), and reverse-transcribed into complementary DNA (cDNA) with the iScriptTM cDNA Synthesis Kit (BioRad), as recommended by the manufacturers. The expression of the target genes was quantitatively determined on RT-PCR equipment (CFX384, BioRad) using iTaq™ Universal SYBR® Green Supermix (BioRad, Hercules). All genes were normalized to the reference gene beta-actin (ACTB, BioRad) and are described in Table 1. Relative quantification of gene amplification by qPCR was performed using the cycle threshold (Ct) values and relative expression levels were calculated using the $2^{\wedge}(-\Delta\Delta Ct)$ method. For each qPCR, samples were analyzed in duplicate and three independent experiments were performed.

Table 1. Gene name and respective primers assay ID (BioRad) for RT-qPCR.

Gene name (abbreviation)	Assay ID
Runt-related transcription factor 2 (RUNX-2)	qHsaCED0044067
Sp7 transcription factor (SP7)	qHsaCED0003759
Collagen type I (COL1A1)	qHsaCED0043248
Beta-actin (ACTB)	qHsaCED0036269

2.4. *In vivo* animal experiment

2.4.1. Animal model and surgical conditions

The experimental models were six specimens of 9 weeks-old female CBA nude mice (*Mus musculus*) weighting an average of 21.1 g. The study was performed and approved by the Animal based studies Ethical Committee and fulfilled all legal requirements (i3S Animal Ethical Committee and DGAV, Portugal). The animals were allowed to acclimatize for 2 weeks before the experimental procedures.

Before the experimental procedures, 4 x 4 x 4 mm nHAp/CS and CS samples were swelled in sterile saline solution (NaCl 0.9 %, Braun) for 1 h at RT. Anesthesia was induced with isoflurane 5 % (IsoFlo, Abbott) by inhalation during approximately 2 min and maintained with isoflurane 1 – 2 %. The surgical field was disinfected with topical antiseptic povidone-iodine 10 % (Betadine, MEDA Pharma) and all surgical procedures were performed in standard aseptic conditions. A midline incision through the dorsal skin was performed and two subcutaneous pockets were created, one on the right side (CS sample) and one on the left side (nHAp/CS sample). The dorsal wound was then closed with surgical staples. Post-surgical pain control was achieved with buprenorphine 0.01 mg/Kg twice a day for 2 days.

After recovery, the mice were caged in pairs and allowed to move in their cages without restriction. They were fed with commercial mice chow and water for 3 and 5 weeks *ad lib*. After the foreseen period, the mice were euthanized with carbon dioxide asphyxiation. The samples (scaffolds and surrounding tissue) were explanted and were individually stored in formaldehyde solution 4 % for 3 days at 4 ºC.

2.4.2. Histological analysis

Fixed samples were processed for histology, embedded in paraffin and sectioned with a microtome (5 – 7 μm thickness) (Microm HM335E). The sections were stained with hematoxylin-eosin (H&E) and Masson's trichrome for light microscopy (Olympus DP 25 Camera, Software Cell B) observation.

2.5. Statistical analysis

The results were showed as the arithmetic mean ± standard deviation. The data was statistically analyzed with Graphpad Prism (*vs.* 8) software. Depending on the number of independent groups for each experiment, data was analyzed with either *t*-test, one- or two-way

ANOVA, followed by *post hoc* Tukey HSD or Fisher's LSD multiple comparison tests. Differences between groups were considered significant for $p < 0.05$.

3. RESULTS

3.1. Physicochemical characterization of nHAp/CS and CS scaffolds

3.1.1. *In vitro* microCT analysis

The created 3D models of the nHAp/CS and CS scaffolds' microstructure (Figure 1a) and b)) confirmed that both porous scaffolds are highly interconnected and closed porosity is practically non-existent. Table 2 shows the quantitative analysis of relevant parameters of the scaffolds' microstructure. For all parameters no significant differences were found between nHAp/CS and CS scaffolds. Figure 1c) and d) plots the pore diameters distribution of nHAp/CS and CS scaffolds, respectively.

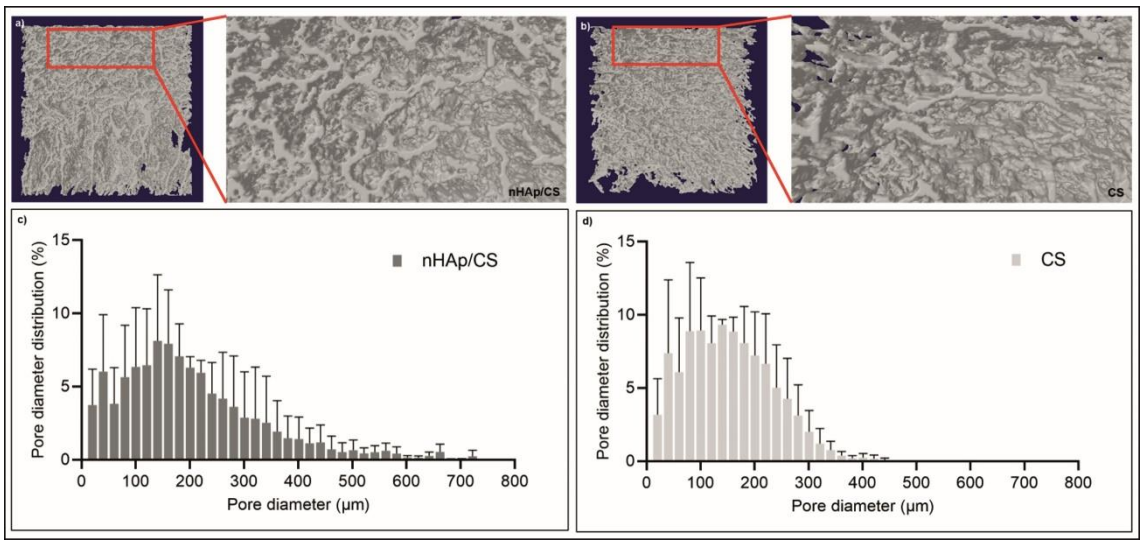

Figure 1. a) MicroCT models of nHAp/CS and b) CS scaffolds' microstructure; c) pore diameter distribution of nHAp/CS and d) CS scaffolds.

Table 2. Quantitative analysis of the scaffolds' microstructure (mean ± SD).					
Scaffold material	**Total porosity (%)**	**Open porosity (%)**	**Closed porosity (%)**	**Pore diameter (μm)**	**Wall thickness (μm)**
nHAp/CS	78.01 ± 6.74	78.01 ± 6.74	0.00 ± 0.00	201.53 ± 63.85	40.53 ± 2.06
CS	77.41 ± 5.04	77.41 ± 5.04	0.00 ± 0.00	152.63 ± 31.05	38.39 ± 0.94

3.1.2. *In vitro* biodegradation and biomechanical analysis

The biodegradation rate and dynamic compression strength were simultaneously tested in aqueous medium in simulated physiologic conditions up to 28 days. As depicted in Figure 2a) the presence of nHAp in the scaffolds' composition promoted a significantly lower biodegradation rate when compared to the CS scaffold (# $p < 0.05$). It is also noticeable in both scaffold types that most of the degradation occurs within the first hour of immersion in PBS, independently of the presence of lysozyme, but afterwards the scaffolds seem to maintain their structure stable with time. The addition of lysozyme only affected the nHAp/ CS degradation after 28 days (* $p < 0.05$).

Additionally, the DMA analysis results are shown in Figure 2b). The presence of nHAp in the scaffolds' composition tended to increase the storage modulus (E') with frequency. For all samples, Tan Delta (loss factor) also increased with frequency, showing that both materials presented viscoelastic properties. Figure 2c) compares the E' for the different conditions with time at 1 and 10 Hz. It is evident that the presence of nHAp significantly enhanced the samples E' under compression (# $p < 0.05$ at 1 and 10 Hz). The results show a slight tendency of a reduction in the compressive strength with time: at 10 Hz (high frequency) the E' value for the nHAp/CS scaffold immediately after swelling was 47.14 ± 6.86 and decreased to 42.34 ± 6.09 kPa after 28 days of incubation in PBS, however this difference is not statistically significant. Nevertheless, no significant differences were observed with or without lysozyme. CS scaffolds' strength at high frequencies (10 Hz) was more affected by the presence of lysozyme, since there is a statistically significant difference between the E' for all time points between this group and the control.

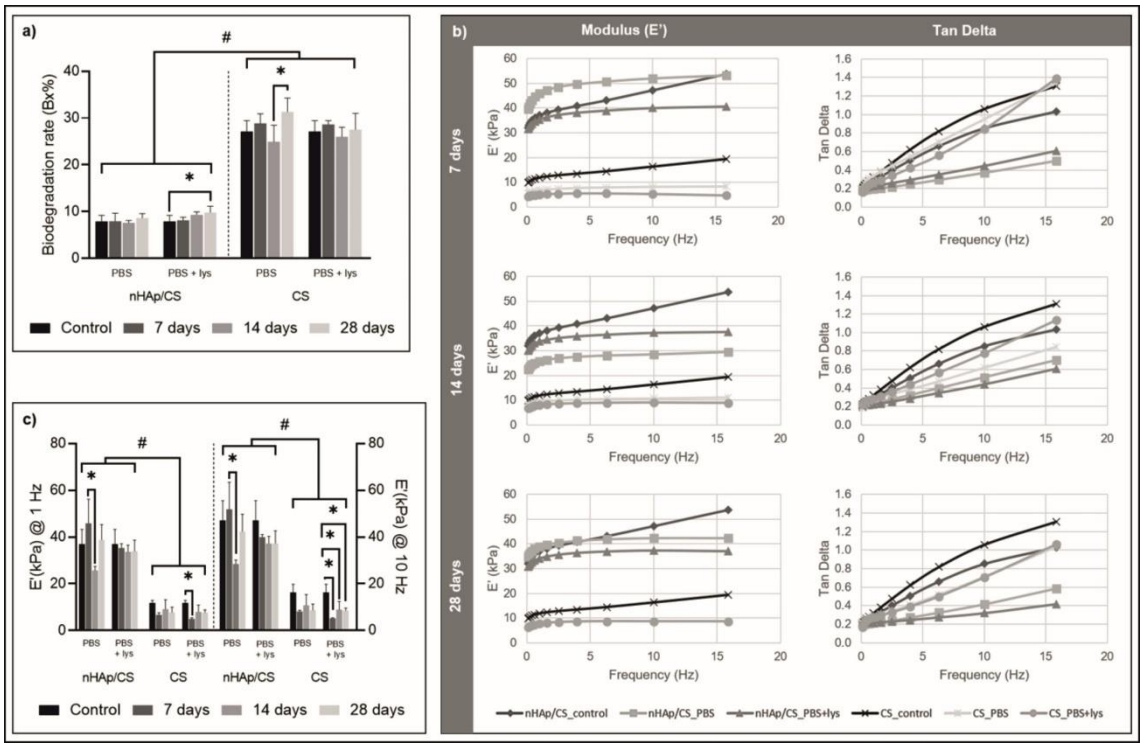

Figure 2. a). Biodegradation rate (B_x %) of nHAp/CS and CS samples after 1 h (control), 7, 14 and 28 days of incubation in PBS or PBS with lysozyme (lys). * Significantly different between time points; # significantly different between materials ($p < 0.05$). b) Storage modulus (E') and Tan Delta *versus* increasing frequencies (from 0.1 to 20 Hz) under dynamic compression for nHAp/CS and CS scaffolds, after incubation in PBS or PBS with lysozyme (PBS + lys) for 7, 14 and 28 days. Control samples (1 h of incubation) are presented in all plots. c) Storage modulus (E') at 1 and 10 Hz for nHAp/CS and CS samples in different incubation conditions and with time. * Significantly different between time points; # significantly different between materials ($p < 0.05$).

3.1.3. *In vitro* bioactivity analysis

Figure 3 depicts the increase in the apatite crystals growth on the surface of the scaffolds, showing that the formation of an amorphous apatite layer was already taking place at 7 days on nHAp/CS scaffolds. EDS graphs show an increase in P and Ca peaks since day 7 when compared with the blank nHAp/CS scaffolds. With time it is noticeable that these apatite crystals became more defined, presenting a needle-like shape after 21 days. The difference between the apatite layer in blank and 28 days nHAp/CS samples is clear. On the contrary, CS scaffolds present a smooth surface with no apatite deposition and an apparent gradual degradation with time.

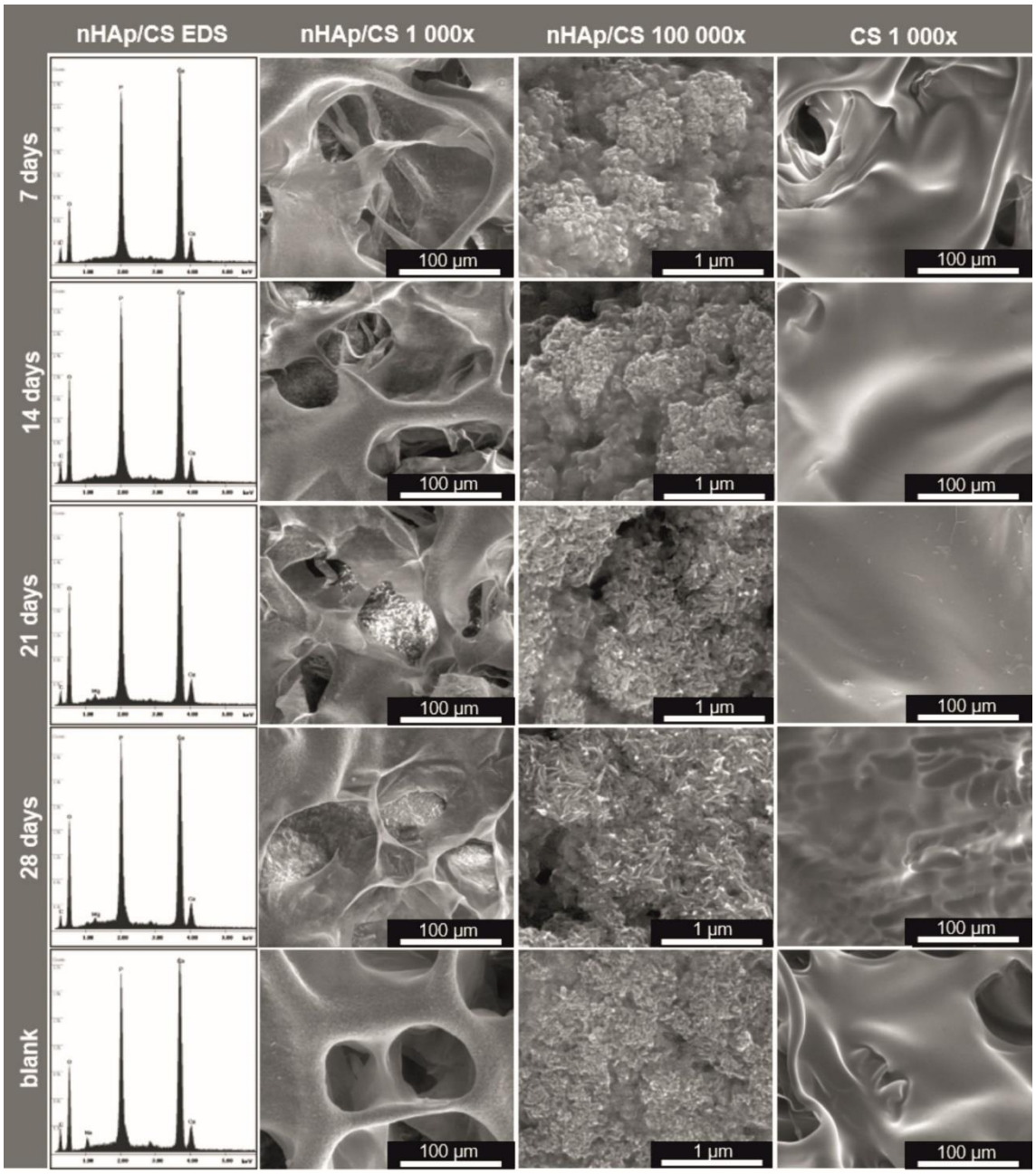

Figure 3. SEM images of nHAp/CS and CS scaffolds after incubation in SBF until the 28th day. Blank scaffolds that were not immersed in SBF solution are shown in the bottom row. EDS graphs show the elemental composition of the apatite layer.

3.2. *In vitro* biological activity of nHAp/CS and CS scaffolds

3.2.1. *In vitro* antimicrobial activity analysis

The ability of Gram-positive and Gram-negative bacteria strains to grow around and colonize the scaffolds was evaluated. Figure 4a) and b) shows that the nHAp/CS scaffold

significantly inhibited the planktonic growth either assessed by OD (2.4 % for *S. aureus*; 59.2 % for *E. coli*) or colony counts (10 log reduction for *S. aureus*; 1 log reduction for *E. coli*), though with a stronger effect on *S. aureus* than on *E. coli*. Also, the metabolic activity of *S. aureus* (2.1 % for nHAp/CS; 4.9 % for CS) was more affected by the scaffold presence than *E. coli* (71.3 % for nHAp/CS; 44.6 % for CS). CS scaffolds inhibitory effect was more noticeable by the colony counts method (8 log reduction for *S. aureus*; 1 log reduction for *E. coli*) (Figure 4b)). Regarding sessile bacteria (Figure 4c)), there was no significant difference between the two scaffolds, yet, again, *S. aureus*' viability was slightly lower when compared to *E. coli*.

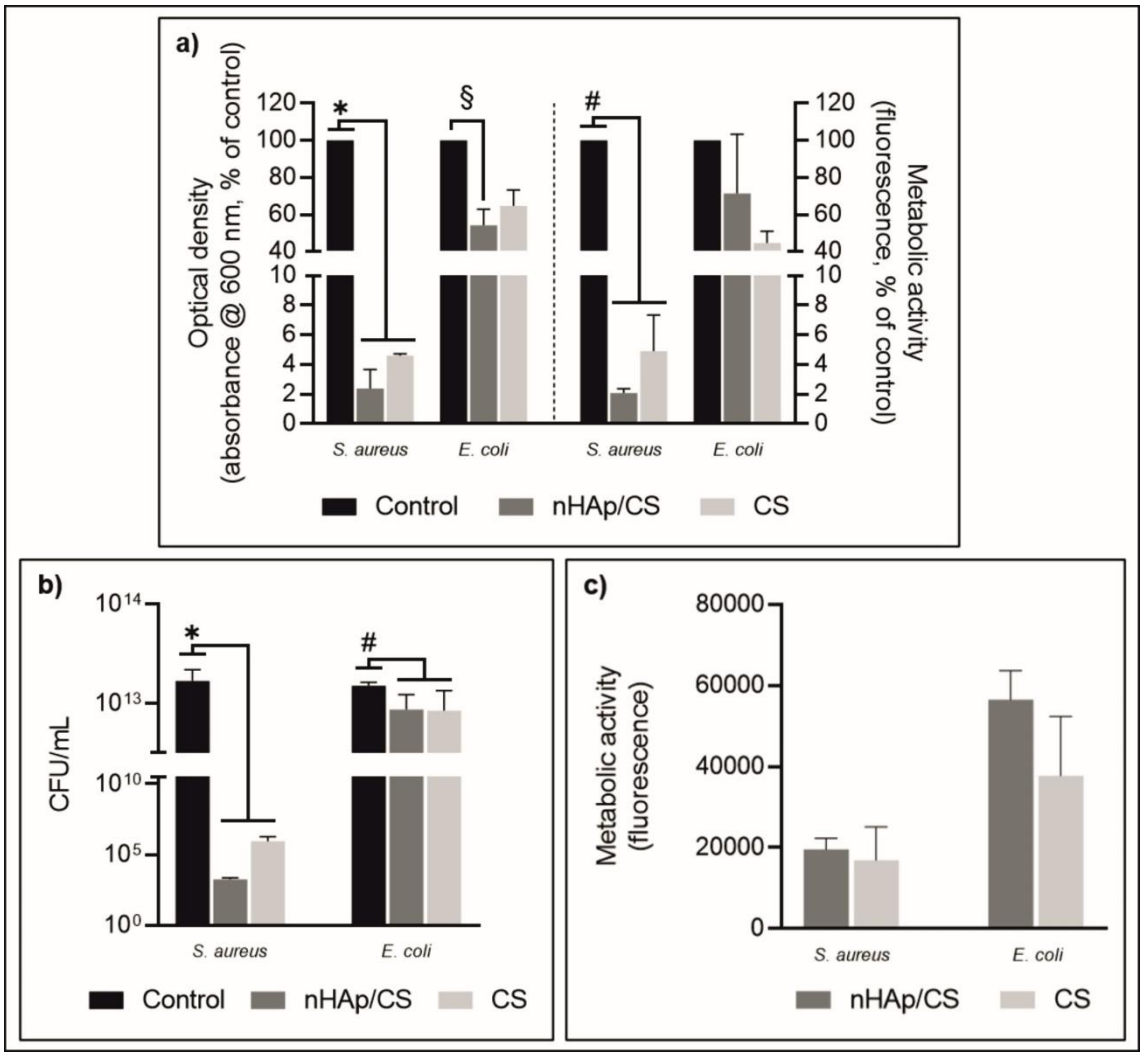

Figure 4. a) Quantification of planktonic bacteria growth with nHAp/CS and CS scaffolds when compared to control suspensions through optical density (OD) and metabolic activity assays. *, #, § Significant differences between control and materials ($p < 0.05$). b) Colony counts assay. *, # Significant differences between control and materials ($p < 0.05$). c) Quantification of the metabolic activity of sessile bacteria attached to nHAp/CS and CS scaffolds. No significant differences were found between the materials ($p < 0.05$).

3.2.2. *In vitro* cytotoxicity analysis – indirect assay

The cytotoxicity of nHAp/CS and CS leachable obtained in different conditions was evaluated according to the ISO 10993-5:2009 guidelines. Firstly, Figure 5a) shows that leachable from both scaffolds did not show cytotoxicity, with the cells' viability ranging from 86 to 124 %. Live/dead assay images (Figure 5b)) corroborate these results. For nHAp/CS scaffolds there is no difference between 1 h and 24 h leachable, but the cells survival increases if the scaffolds are incubated a second time for 1 h (* $p < 0.05$).

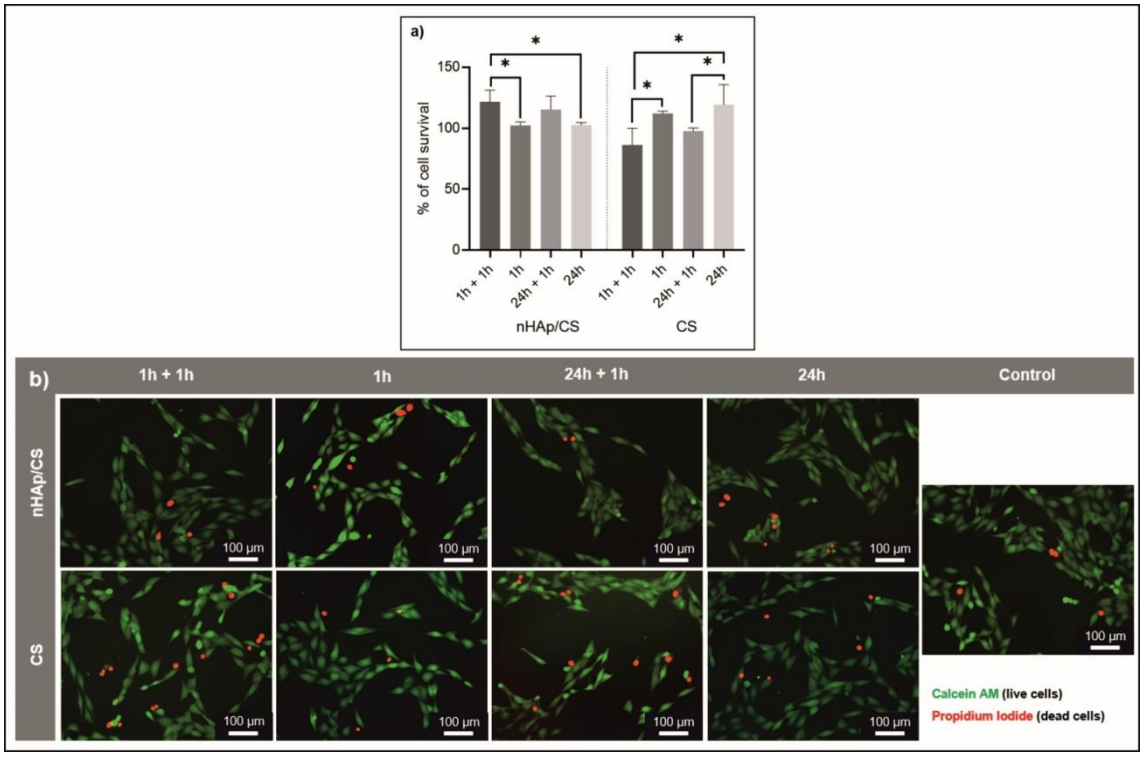

Figure 5. a) Quantification of MG63 cells survival (% of control) in leachables obtained in different time conditions through MTT assay (1 day). * Significant differences between leachable conditions ($p < 0.05$). b) Live/dead assay images of MG63 cells cultured for 1 day in leachables obtained in different time conditions.

3.2.3. *In vitro* cytotoxicity analysis – direct assay

MG63 are considered to be "osteoblast-like" cells and are frequently used in tissue engineering studies that investigate the impact of biomaterials on osteogenic differentiation, viability and proliferation [40]. The proliferation ability of MG63 seeded within the nHAp/CS and CS scaffolds was quantitatively assessed by its metabolic activity, proliferation rate (Alamar blue assay, Figure 6a)) and DNA quantification (Figure 6b)). The graphs show a significantly higher metabolic activity and DNA content of MG63 seeded into nHAp/CS scaffolds (* $p < 0.05$) when

compared to those on CS scaffolds. When seeded into nHAp/CS scaffolds, their metabolic activity reached a higher rate at day 14 (# $p < 0.05$), but the DNA content increases significantly until the 21st day of culture (# $p < 0.05$). These results suggest that the cells have favorable conditions to proliferate over the material surface throughout the total experimental period. Still, both the metabolic activity and DNA content of MG63 seeded on CS scaffolds increased significantly along the time until the 21st day of culture (§ $p < 0.05$).

To assess the morphology and distribution of MG63 seeded within the scaffolds CLSM (Figure 6c)) and SEM images (Figure 6d)) were analyzed. Through the biomaterials self-fluorescence, the CLSM representative images depict in detail their tridimensional interconnected porous structure where the cells migrate and adhere. At day 7, MG63 were adherent to the scaffolds structure and after day 14 they showed an elongated morphology of their F-actin fibers of the cytoskeleton (stained in red) and cell-to-cell contacts, which is more obvious at the nHAp/CS samples. Into CS scaffolds, the cells showed lower attachment and proliferation rate at early time-point. SEM images (Figure 6d) also indicate that MG63 were able to adhere and proliferate inside both biomaterials porous structure. However, the cells' proliferation was more evident in the nHAp/CS scaffolds, which seemed to offer better proliferative conditions in agreement with the obtained quantitative data (total DNA content). Also, the cells presented a normal morphology though it seemed to be more favorable when seeded on nHAp/CS scaffolds.

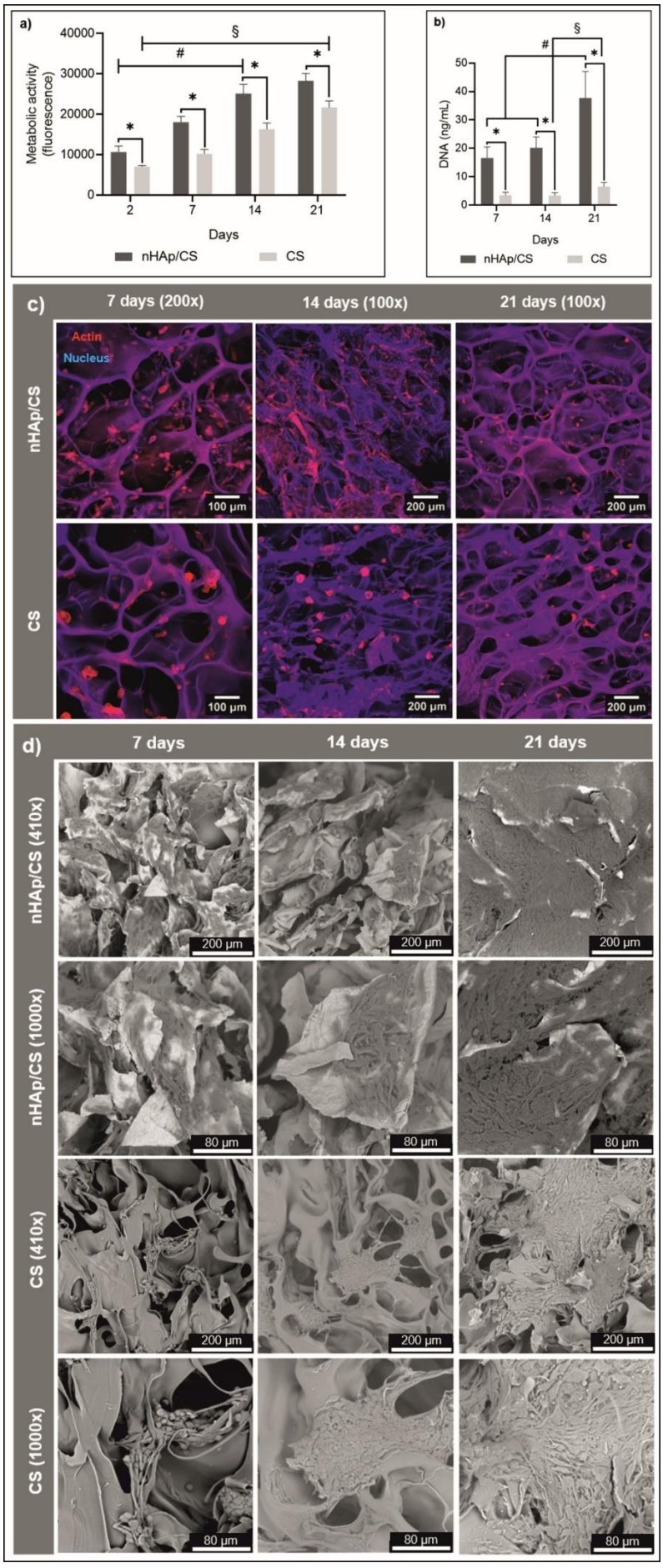

Figure 6. a) Quantification of the metabolic activity of MG63 cells seeded on nHAp/CS and CS scaffolds for 21 days through Alamar blue assay (longitudinal experiment). # Significant differences between time points for nHAp/CS ($p < 0.05$); § significant differences between time points for CS ($p < 0.05$); * significant differences between materials ($p < 0.05$). b) Total DNA content quantification of MG63 seeded into nHAp/CS and CS scaffolds for 21 days. # significant differences between time points for nHAp/CS ($p < 0.05$); § significant differences between time points for CS ($p < 0.05$); * significant differences between materials ($p < 0.05$). c) CLSM images of MG63 seeded into nHAp/CS and CS scaffolds for 7 to 21 days. The cells' cytoskeleton (actin fibers) was stained in red and the nuclei were counterstained in blue. The biomaterial's structure is visible due to its self-fluorescence (chitosan – blue). d) SEM images of MG63 seeded into nHAp/CS and CS scaffolds for 7 to 21 days.

3.2.4. *In vitro* osteogenic differentiation analysis

The MG63 cells' ALP activity was determined from 7 to 21 days of culture into the scaffolds after cells lysis and is plotted at Figure 7a). The results show that there is no significant difference in the ALP activity (nmol/mg/min) between the two biomaterials at any time point. Moreover, the ALP activity remained stable throughout the whole experiment, since there are no significant differences between all time points.

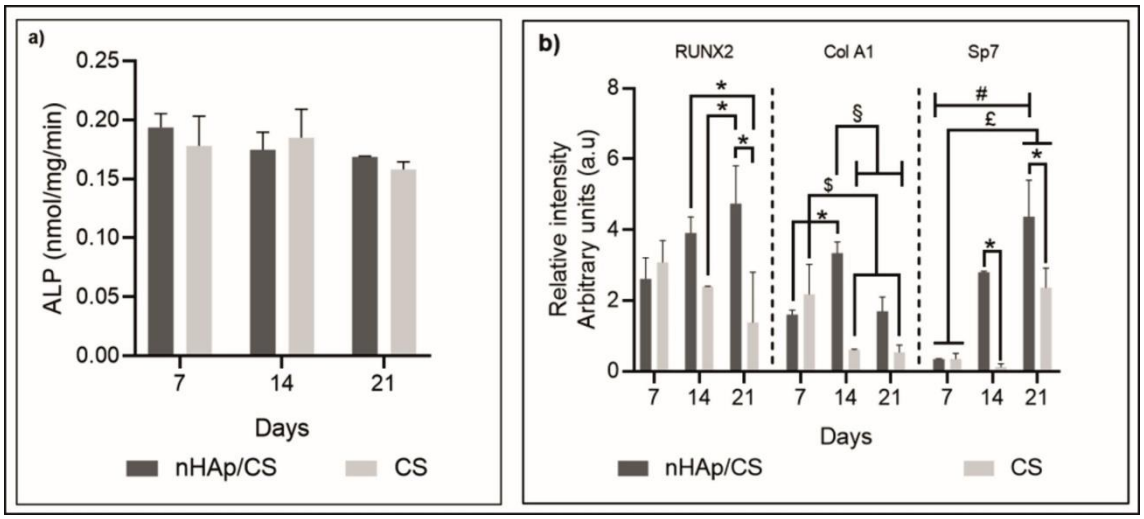

Figure 7. a) Quantification of ALP activity of MG63 seeded into nHAp/CS and CS scaffolds for 7 to 21 days. No significant differences between materials ($p < 0.05$). b) RT-qPCR quantitative results of the expression of RUNX2, collagen A1 and Sp7 genes by MG63 seeded within nHAp/CS and CS scaffolds from 7 to 21 days. * Significant differences between time points and/or materials ($p < 0.05$); §, $ significant differences in the expression of the collagen A1 gene ($p < 0.05$); #, £ significant differences in the expression of the Sp7 ($p < 0.05$).

The cells seeded within the scaffolds were also analyzed by RT-qPCR for the expression of relevant osteoblastic genes, using β-actin as a reference gene and cells cultured on TCPS well-plates as control. Figure 7b) shows the results of RUNX2, collagen A1 and Sp7 gene expression with time by the cells cultured into each type of scaffold. In terms of the RUNX2 expression, there is a tendency for an increasing expression with time for the nHAp/CS samples and a decrease for the CS samples, although these results are not statistically different. Nevertheless, there are significant differences amongst the two materials for time points 14 and 21 days (* $p < 0.05$). The collagen A1 gene expression showed an increase at the 7th day regarding CS samples, but significantly decreased after the 14th day ($ $p < 0.05$). On the other hand, cells within the nHAp/ CS scaffolds showed higher collagen A1 expression at the 14th day (*, § $p < 0.05$), but statistically significant when compared to other time points. Finally, the Sp7 gene, which codifies the osterix protein, presents a significant increase in its expression along with time in cells seeded into nHAp/CS scaffolds (# $p < 0.05$) when compared to the cells into CS scaffolds (* $p < 0.05$). Therefore, cells seeded within CS scaffolds showed a significantly higher Sp7 expression at the

21st day (£ $p < 0.05$) compared to the other time points. In this case, there is also a significant interaction between the materials and cells that influence their response along the time of culture according to the two-way ANOVA test.

3.3. *In vivo* subcutaneous implantation

To evaluate the materials' concerning the safety, biocompatibility and degradation rate, scaffolds were implanted into subcutaneous pockets in CBA nude mice. Nude mice have a suppressed immune system due to reduced number of T cells [41]. But these mice have myeloid cells, such as macrophages, myeloid-derived suppressor cells (MDSCs), and dendritic cells (DCs) that are present in the immune response [42]. Thus, nude mice are ideal for tumor and tissue studies because they have no specific antigen responses such as organ transplant rejection, but, in this work, they were used to follow the biodegradation process *in vivo*, since the macrophage are the primary cells responsible for the formation of giant cells and foreign body response, similar to human immune response to biomaterials' implantation [43]. The *in vivo* biocompatibility of the scaffolds explants was histologically evaluated after 3 and 5 weeks. Macroscopically, Figure 8a) shows at the subcutaneous implant of the nHAp/CS scaffold after the 3rd week of implantation, a large caliber blood vessel ingrowth towards the biomaterial graft. This important finding was already suggesting that the presence of the biomaterial could be promoting vasculogenesis/angiogenesis.

Microscopically, Figure 8b) and c) shows the histological sections of the *in vivo* subcutaneous implantation of both scaffold types stained with H&E and Masson's trichrome, respectively. At 3 weeks of implantation, for both nHAp/CS and CS scaffolds, there was no evidence of intense acute or chronical inflammatory response. An outer thin fibrous capsule with disorganized connective tissue and a few monocytes were present around the implanted scaffolds as a low foreign body response (non-specific reaction from host tissue) after biomaterial's implantation. Fewer areas of new connective tissue were observed from the periphery to the center of the scaffolds within the materials' porous structure. Between the 3rd and the 5th week of implantation, intensive and progressive ingrowth of new blood vessels within the scaffolds' porous structures were observed, with higher evidence into the nHAp/CS scaffold. Also, the Masson's trichrome images show (Figure 8c)) the presence of collagen fibers (blue) that became much more abundant at the 5th week and this feature is even more evident for the nHAp/CS scaffold. Both materials seemed to be structurally stable until at least the 5th week of implantation, which is important to support tissue ingrowth and regeneration.

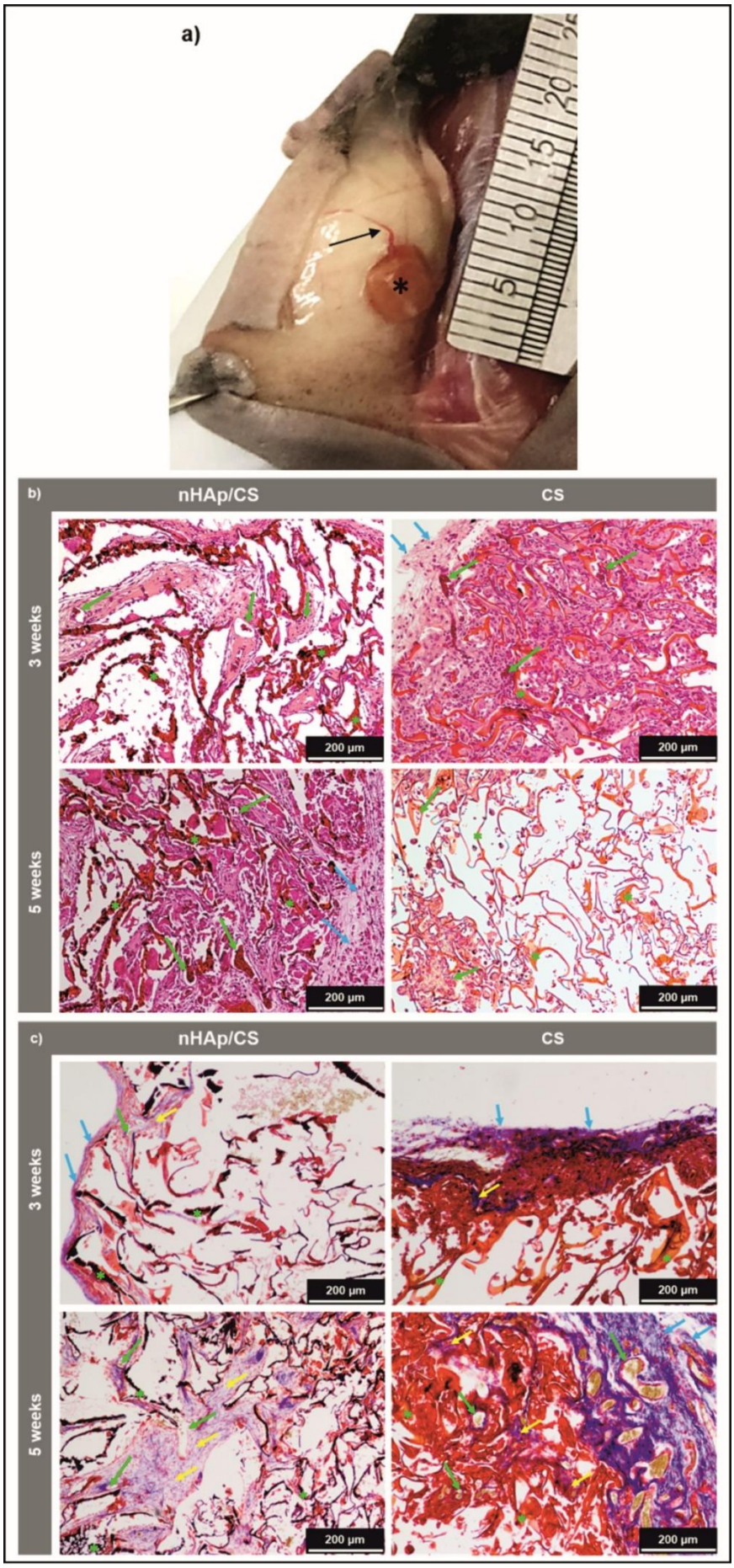

Figure 8. a) Macroscopic image of nHAp/CS subcutaneous implant after 3 weeks of implantation. A blood vessel (black arrow) is inosculating the scaffold implant (black *). b) Optical micrographs of histological samples stained with H&E and c) with Masson's trichrome. Green *: materials; green arrows: blood vessels; blue arrows: outer fibrous capsule; yellow arrows: diffuse connective tissue.

4. DISCUSSION

The development of engineered bone tissue graft biomaterials has been focusing in mimicking the bone extracellular matrix structure and composition [21]. One of the strategies is the use of biodegradable biopolymers to obtain a porous matrix and reinforcing it with osteoinductive ceramic nanoparticles [44]. However, often the production process involves the use of many potentially cytotoxic chemicals, numerous preparation steps and difficulties in the final sterilization process without jeopardizing the whole material [8]. These biopolymers, from proteins to polysaccharides, are very sensitive to the extreme physical conditions imposed by validated conventional sterilization methods like dry heat, steam, ethylene oxide and gamma irradiation and non-regulated methods like hydrogen peroxide, gas plasma, peracetic acid, ozone, E-Beam and UV irradiation, making it even more imperative to find viable alternatives that assure the integrity of the material's properties, but also their safety for clinical use [8, 24, 25].

Unlike most similar biomaterials published [3, 15, 39, 44-49], in this work, nHAp/CS scaffolds were prepared through a 3 steps process (dispersion preparation, freeze drying and $scCO_2$ extraction) [8, 24, 25], which included the final solvent extraction (removed the acetic acid and avoided pH changes) and provided the materials' sterilization through $scCO_2$, resulting in a cost-effective and eco-friendly bone graft.

This research aimed to develop a porous biodegradable nHAp/CS 70/30 scaffold for bone regeneration, in particular for periodontal application. Bone graft biomaterials should present enough mechanical strength [20, 50, 51] (similar to bone) [9, 17-19, 34], to keep the tissue volume, support bone growth, remodeling and mechano-transduction properties [16, 19, 51]. They should also maintain the stiffness despite their degradation [17, 51, 52], therefore, the degradation rate should be similar to the native bone's ingrowth [9, 53, 54]. Other authors such as Qasim *et al.* [3, 45, 55] have also been developing chitosan-hydroxyapatite membranes for periodontal guided bone regeneration (GBR) by freeze gelation [3, 55]. They compared membranes with different molecular weights, and their lower molecular weight membrane, chitosan 30:70 biomaterial that has similar composition to the nHAp/CS scaffold, promoted significantly higher cellular viability of MG63 from day 1 to 7 [45]. Tamburaci *et al.* have also developed chitosan-Si-nHAp periodontal GBR bilayer membranes, which presented significantly higher compression modulus (150 to 200 kPa in dry conditions), protein adsorption, antimicrobial effectiveness, increased ALP activity and osteocalcin expression by human osteossarcoma cell line (Saos-2) when higher contents (40 and 50 %) of nano-hydroxyapatite dispersed phase were incorporated [47].

It has been described that for bone regeneration to occur, scaffolds should mimic the microstructure of cancellous bone, and although there is some controversy concerning the porous structure, it means that total porosity should be above 60 % and the interconnected pores' diameter should be at least 100–200 μm [3, 10, 11, 13, 21, 23, 49, 51, 56-59]. In our previous work [31], the morphological features of nHAp/CS samples such as mean pore size (72 ± 35 μm) and pore size distributions (ranging proportionally from < 50 μm to > 100 μm) were obtained by SEM

image analysis, while porosity (81 %) was experimentally estimated with a gas pycnometer. Despite the frequent use of these methodologies, microCT is becoming a basilar method to analyze scaffolds microstructure [3, 39, 47, 48, 60] since it is not invasive and does not destroy the samples. In the present study, microCT analysis of the nHAp/CS scaffold revealed its highly interconnected porous microstructure and pores diameters suitable to assure the circulation of oxygen, nutrients and metabolites, cell migration, promote neovascularization/angiogenesis and bone guided ingrowth [9, 10, 16-18, 44, 51, 56, 61]. The porosity of the nHAp/CS is around 78 %, which is very similar to the previous experimentally determined value [31] and in line with other published studies like Qasim *et al.* (78 % for chitosan membranes containing HA particles) [3] and Belluzo *et al.* (70 % for chitosan and carboxymethyl cellulose with nHAp hydrogel scaffolds) [60], while Tamburaci *et al.* showed 86 % for the chitosan-50%Si-nHAp layer of their GBR membranes [47]. Scaffolds' porosities above 80 % tend to exhibit low values of compressive strength and should be considered for low-load bearing applications, while porosities lower than 70 % might present higher compressive strength, but these more compact scaffolds are not favorable for bone tissue ingrowth [57]. The pore interconnectivity is practically total (there are no closed pores in the samples), which is similar to a 3D plotted hydroxyapatite-chitosan-silica scaffold designed by Dong *et al.*, despite their porosity was much lower (around 58 %) [48]. Also, the nHAp/CS scaffold's pore size distribution has a wide range, with smaller pores around 50 μm, which are favorable for osteoblastic attachment and proliferation, and larger pores from 100 to > 700 μm that promote a fast swelling that allows nutrients and oxygen circulation [44].

Most published works studying the *in vitro* mechanical properties of biomaterials for bone regeneration, tend to perform their experiments in static conditions and on dry materials. However, these conditions hardly simulate the physiologic and clinical settings in which the biomaterials will be applied, since once the biomaterial is implanted it will be in contact with body fluids, swelling and becoming wet [3]. Moreover, once the surgical wound is closed, the graft biomaterial is subjected to dynamic compressive forces from healing process itself and tissue/organ function [1]. Besides, the scaffolds structural degradation will also be affected by their mechanical response (strength). The degradation rate should be slow and expected to occur in the mid-term (> 8 to 12 weeks) [46, 62-66] for these biomaterials. Also, scaffolds with polymeric matrices exhibit viscoelastic properties which are not adequately evaluated through such conventional static methods [67, 68]. For those reasons, in this study it was chosen to perform DMA with cyclic increasing compressive forces on pre-wetted scaffolds and repeat this analysis at different time points until the 28th day (using the same samples of the biodegradation test), so that a full picture of the biomaterials' performance will be achieved with similar conditions to *in vivo* experimentations. Some authors have also reported DMA/rheology experiments with chitosan/hydroxyapatite-based biomaterials which were previously immersed in aqueous solutions, but for shorter periods of time [39, 69]. Campos *et al.* immersed chitosan-collagen based scaffolds with a hydroxyapatite layer in water at 37 ºC until complete swelling (15 min) before performing dynamic frequency sweep tests (between 0.01 and 10 Hz) [39]. The scaffolds exhibited viscoelastic properties and at 1 Hz the storage modulus was 1.375 kPa (the E' of our

nHAp/CS scaffold tested at 1 Hz immediately after 1 h of swelling was 37.03 kPa), the loss modulus was 70 Pa and the tan delta was 0.05 [39]. Raina *et al.* tested a silk-fibroin, chitosan, agarose, hydroxyapatite-based crosslinked cryogel for its rheological properties after 1 h of immersion in PBS [69]. After 15 min of compression with a constant force of 1 N/s, the storage modulus of this cryogel decreased from 130 to 120 kPa and the loss modulus was approximately 15 kPa [69].

Despite one of the main goals of the present research being the development of a biodegradable scaffold, its biodegradation rate should be synchronized with the formation of new bone, while also maintaining the mechanical support. The present mid-term biodegradation/biomechanical experiment results show that for both scaffold types the degradation occurred immediately upon immersion in PBS, but it stays quite stable (or showing a little increase) until the 28th day of immersion in PBS. The high degree of deacetylation (91.9 %, high crystallinity) of the CS used in the scaffolds composition contributed to the low degradation rates, even with the presence of lysozyme [12, 16, 34, 35, 44, 54]. Therefore, the presence of sintered nHAp crystals seemed to play an important role in the mid-term stability of the scaffolds because nHAp/CS samples clearly degraded less than the plain CS scaffolds [60]. Similarly, Qasim *et al.* showed that the molecular interaction between nHAp crystals and CS matrix slightly reduced the swelling rate [3], which also decreased the materials' degradation by hydrolysis and increased strength [3, 44, 48, 60]. In a recent study, Qasim *et al.* also found that after the chitosan-hydroxyapatite membranes degradation, the final weight stayed quite stable until the 28th day of incubation in PBS with lysozyme (varied between 80 and near 100 % of initial mass), independently on the variations of chitosan molecular weight and percentage of HAp in the membrane's composition [45]. Moreover, the results of the enzymatic degradation (in PBS with lysozyme) of chitosan-Si-nHAp membranes studied by Tamburaci *et al.* showed a lower weight loss after 28 days for the samples with Si-nHAp (50 % of weight loss by the chitosan-50 %Si-nHAp and 79 % by the chitosan membrane) [47]. In the research developed by Raina *et al.*, the biodegradation of their silk-fibroin, chitosan, agarose, hydroxyapatite-based cryogel in PBS at the 4th week was about 20 % [69]. It has been described in published work that the nHAp dispersed phase within a polymeric matrix (*e.g.* collagen) improved the storage modulus and decreased the loss factor of the composite scaffolds [48, 52, 70]. Moreover, the biodegradation led to the decrease of the storage modulus and elasticity, and increased viscosity (tan delta) [70]. Caridade *et al.* showed that the storage modulus (stiffness) of CS membranes was negatively affected by the increasing relative humidity, but did not affect the tan delta [67]. After CS membranes were completely immersed, the storage modulus reduced drastically and the loss factor showed a higher peak, probably due to a plasticizing effect caused by water inside the CS structure, creating a strong cohesion between the polymer chains [67]. Despite nHAp/CS scaffold high porosity, the biomechanical tests performed indicated that the graft may support bone ingrowth at low-load bearing bone defects (like in periodontal treatment) [71] and for a longer period of time, when compared to the CS scaffold [9].

An important feature of bone graft materials is their capacity to interact and establish

direct chemical bonds with the interface of the adjacent bone, promoting a strong bioactive fixation of the scaffold to the surrounding bone tissue (osteointegration) [10, 13, 14, 17, 22, 72, 73]. nHAp-based biomaterials have been described as bioactive because they are able to form an apatite layer within 4 weeks when they are soaked in SBF *in vitro*. This surface characteristics should predict the materials' bone bonding ability *in vivo* [38, 44, 48]. Regarding nHAp/CS scaffold, a distinct layer of apatite crystals was already visible after 21 days, that will favor the materials' *in vivo* bonding to bone rapidly [38, 39]. Campos *et al.* achieved similar results of apatite deposition on the HAp-containing layer of their chitosan/collagen-based scaffold [39]. They described that some apatite nuclei were already visible at the 7th day of immersion in SBF, which almost covered the entire surface at the 21st day [39]. Dong *et al.* also described that the presence of HAp on the composition of their hybrid hydroxyapatite-chitosan-silica scaffold promoted a more homogenous deposition of a thick layer of platelet-like apatite crystals than on the chitosan-silica scaffold after only 3 days in SBF [48].

Since the aim of the present graft biomaterial is to fill periodontal bone defects, which are located in the naturally contaminated oral cavity environment, it was important to evaluate if the scaffolds would be easily colonized by Gram-positive and Gram-negative bacteria strains [1, 47]. The bacteria strains tested in this study are model Gram-positive (*S. aureus*) and Gram-negative (*E. coli*) [47, 74], as well as relevant strains usually present in severe intra-osseous infections (osteomyelitis) [71]. CS evaluations showed intrinsic antimicrobial effects on both Gram-positive and Gram-negative bacteria and also on fungi [7, 35, 75, 76], which is an advantage when compared to other biopolymers frequently used in biodegradable scaffolds. However, its antibacterial effects are dependent on several intrinsic and extrinsic polymer properties, such as the source of chitin, the degree of deacetylation, polymer molecular weight, the polymerization degree, the polymer concentration in the solution, the pH of the environment [4, 75], the type of target bacteria and the target tissue [75, 76], the presence of functional groups in the chitosan molecular structure, the formation of metal complexes [76]. Though the mechanisms of action are not fully understood yet, it seems that CS interacts with the peptidoglycan layer of Gram-positive bacteria, disturbing cell functions and resulting in cell death, while in the case of Gram-negative bacteria it disrupts the membrane integrity, causing leakage of intracellular material and interference with DNA/RNA synthesis [75, 76]. The CS used in this study was highly deacetylated and had low molecular weight, which have contributed to its antimicrobial effectiveness [75, 76]. The materials' results demonstrated the relevance of chitosan antimicrobial properties in the composition of the biomaterials, but the presence of nHAp crystals also seems to play a role in increasing the antimicrobial efficacy. Tamburaci *et al.* also found through inhibition zone method and colony counts assay, that higher contents (40 and 50 %) of the dispersed phase in their chitosan-Si-nHAp membranes for periodontal GBR significantly inhibited *E. coli* and *S. aureus* growth, though it was more effective on *E. coli* [47].

As expected, the viability values of the indirect cytotoxicity tests meet the ISO 10993-5:2009 standard criteria, which requires a minimum of 70 % of cell survival for non-cytotoxic materials. These results are in line with those published by other authors with similar materials

[39]. However, it seems that the nHAp/CS scaffold might leach an excess of unbonded nHAp. Those nanoparticles could be capable to introduce considerable local changes in pH [21, 44, 77]. MG63 osteoblast-like cells seeded within both scaffold types proliferated significantly until the 21st day of culture. Although the tests performed in this work have longer periods of time when compared to literature [3, 39, 44, 48, 78], the biocompatibility test (Alamar blue) and DNA quantification results are in line with those published by Qasim *et al.* [3]. The authors seeded MG63 cells on a CS/HAp (50:50) or plain CS porous membranes and evaluated cell viability with the Alamar blue assay that showed a significant increase (almost three-fold for CS/HAp and two-fold for plain CS) from the 1st to the 7th day of culture [3]. Campos *et al.* showed a considerable increase in the number of murine osteoblasts seeded on the HAp subchondral layer (live/dead assay) within the scaffolds from day 3 to 14 [39]. Pinto *et al.* also reported increasing metabolic activity from day 1 to day 7 of MG63 cells seeded on both on 0.2 % glutaraldehyde crosslinked chitosan scaffolds with either HAp or biphasic granules [78]. Evaluating this work quantitative and qualitative results, it is evident that the presence of nHAp crystals in the matrix surface is favorable for cells attachment, proliferation and spindle-like morphology, similarly to Kumar *et al.* results that also confirmed by SEM the MG63 cells early capacity to attach and proliferate on chitosan-nano-hydroxyapatite and chitosan-nano-bioglass scaffolds [44]. In the same way to the present study, Dong *et al.* study also concluded that murine bone marrow stem cells showed a better morphology at SEM and CLSM evaluation when attached to HAp-CS-silica hybrid than to simple CS-silica hybrid scaffolds, as well as a higher number of viable cells (live/dead assay) [48]. These results are probably due to the chemical microenvironment and topographical features of the scaffolds walls promoted by the nHAp presence, which better resembles the natural bone ECM [78].

In terms of osteogenic differentiation, ALP activity remained constant from the 7th to the 21st day of experiment and it was similar in both scaffold types. ALP is an early osteogenic differentiation marker [48, 79], responsible for increasing phosphate in the bone ECM microenvironment [79]. Pinto *et al.* managed to achieve a significant increase of ALP activity with MG63 seeded on 0.2 % glutaraldehyde crosslinked chitosan scaffolds with either HAp granules (at the 7th day of culture) or biphasic granules (at the 4th and 7th days) [78]. However, in the present study, nHAp/CS scaffolds promoted in general a significantly higher osteogenic expression of the genes tested, with RUNX2 slightly increasing for nHAp/CS and decreasing for CS scaffolds. RUNX2 is a critical transcription factor for osteoblastic differentiation commitment [78] and, in this work, it shows that nHAp is contributing for the cells' engagement with osteoblastic differentiation. Consequently, there is an upregulation of collagen A1 gene expression at the 14th day. The collagen type I is the protein with higher content into natural bone ECM [78, 80]. Pinto *et al.* also obtained higher RUNX2 and collagen A1 genes expressions for MG63 seeded on both 0.2 % glutaraldehyde crosslinked chitosan scaffolds with HAp or biphasic granules compared to matrix scaffolds with no HA granules [78]. Moreover, Sp7, a transcription factor regulated by RUNX2 and responsible for the late stages of osteoblastic differentiation [80], had a significant increase of gene expression with time, especially in nHAp/CS scaffolds, which demonstrates the

appropriate cellular environment promoted by the presence of the nHAp crystals (similar to those present in the extracellular bone matrix) for osteoblasts.

Upon *in vitro* evaluation of biocompatibility, it is essential to assess whether the biomaterials are safe before their application *in vivo*, due to the complexity of the living organisms which is not completely covered *in vitro*. The subcutaneous implantation of the scaffolds was performed in the small rodent model before assessing the bone regeneration with a non-periodontal critical size defects in the rat or rabbit model, allowing the evaluation of the biomaterial's stability and biocompatibility that will reduce the number of materials and experimental groups (time-points), reducing the average of animals used in the bone model, and applying the 3Rs in animal research. At the rat model scale, periodontal critical size defects are relatively small (0.5 to 2 mm [81]), making visualization as well as the execution challenging, since the high-risk surgery might expose their teeth apices, thus becoming prone to necrosis and pain and decreasing the animals' welfare and survival [82]. Therefore, when both scaffold types were implanted subcutaneously in mice, they did not induce adverse responses (inflammation) such as redness or swelling in the peripheral skin [56], or a higher presence of polymorphonuclear leukocytes (acute inflammatory response) or monocytes such as lymphocytes (chronic inflammatory response) [83]. The presence of CS seemed to promote muco-adhesion, which contributed for the stabilization of the graft materials and subsequent angiogenesis and collagen fibers deposition, which was more intensively observed into the nHAp/CS scaffold. This feature probably has a direct correlation between wettability of the materials' surface, which is determinant to define the final composition of the protein coating [84]. Similarly, Kaczmarek *et al.* also reported no local (acute or chronic) inflammatory changes, swelling or other adverse reactions after subcutaneous implantation of chitosan/collagen/hyaluronic acid HAp scaffolds with different ratio compositions in New Zealand rabbits for 6 months [83]. Moreover, their scaffolds with higher HAp content in their composition promoted the formation of blood vessels, higher presence of fibroblasts, as well as the long-term stability of the scaffolds [83]. In the present study, after 5 weeks of *in vivo* implantation, both scaffold types seem to maintain their structure, which is promising in terms of mid to long-term tissue regeneration support [39]. This structure stability is probably due to the presence of a CS matrix with a high degree of deacetylation, which slows down the biomaterials degradation rate [12, 16, 34, 44].

5. CONCLUSIONS

In this research we have been testing a nHAp/CS (and CS) scaffold produced by the $scCO_2$ method to overcome the challenges associated with porosity, sterilization of sensitive biopolymeric-based materials, as well as the extraction of cytotoxic solvents from the matrices. After the $scCO_2$ technique validation as a sterilization method, many benefits will be achieved such as the higher integrity of the biomaterials and increased physical properties (*i.e.*, total porosity, pore distribution), with reduced associated costs and higher scalability and less environmental

impact. Further studies will be needed to provide evidence of $scCO_2$ efficacy and safety in a wide range of biomedical devices.

In this work, the nHAp/CS scaffolds showed high porosity (78 %) with adequate pore dimensions (average of 200 μm), osteoconduction (after 21 days), low degradation rate (structurally stable for 28 days) with appropriated mechanical resistance (storage modulus: 40 – 50 kPa) that should be suitable for bone ingrowth when applied in low-load bearing defect sites like at periodontal disease treatment. nHAp/CS showed higher biocompatibility *in vitro* and in an ectopic *in vivo* model when compared to the CS scaffold. Further biological studies shall evaluate the performance of nHAp/CS against specific periodontal pathogenic bacteria (*e.g. P. gingivalis* and *A. actinomycetemcomitans*), *in vitro* osteoinduction properties regarding mesenchymal stem cells differentiation, as well as the *in vivo* pro-regenerative properties into critical bone defects.

CRediT authorship contribution statement

Mariana Souto-Lopes: Conceptualization, Methodology, Validation, Formal analysis, Investigation, Data curation, Writing – original draft, Visualization. **Liliana Grenho:** Methodology, Validation, Formal analysis, Investigation, Resources, Writing – review & editing. **Yaidelin Alves Manrique:** Methodology, Validation, Investigation, Resources, Writing – review & editing. **Madalena Maria Dias:** Methodology, Resources, Writing – review & editing, Supervision, Project administration, Funding acquisition. **Maria Helena Fernandes:** Conceptualization, Methodology, Validation, Resources, Writing – review & editing, Supervision, Project administration, Funding acquisition. **Fernando Jorge Monteiro:** Conceptualization, Resources, Writing – review & editing, Supervision, Project administration, Funding acquisition. **Christiane Laranjo Salgado:** Conceptualization, Methodology, Validation, Investigation, Resources, Data curation, Writing – review & editing, Supervision, Project administration, Funding acquisition.

Conflict of interest

The authors of the manuscript entitled “Full physicochemical and biocompatibility characterization of a supercritical CO_2 sterilized nano-hydroxyapatite/chitosan biodegradable scaffold for periodontal bone regeneration” declare no conflict of interest.

Data availability

Data will be made available on request.

Acknowledgements

The authors acknowledge i3S – Institute for Research and Innovation in Health (Unit: INEB – National Institute of Biomedical Engineering) that is supported by Portuguese funds through FCT/MCTES (Fundação para a Ciência e a Tecnologia) – UIDB/04293/2020. This article was also a result of LA/P/0045/2020 (ALiCE), UIDB/50020/2020 and UIDP/ 50020/2020 (LSRE-LCM) projects, funded by national funds through FCT/MCTES (PIDDAC). The last author, CLS, gratefully

acknowledges FCT for financial support (CEECINST/00091/2018/CP1500/CT0019). The authors acknowledge the support of Professor María Gomez Lázaro from the i3S Scientific Platform Bioimaging, member of the national infrastructure PPBI – Portuguese Platform of Bioimaging (PPBI-POCI-01-0145-FEDER-022122), for the use of microCT, CLSM and critical point dryer. The authors acknowledge the support of the i3S Scientific Platform Biointerfaces and Nanotechnology for the use of DMA. The authors acknowledge the support of the i3S Scientific Platform Cell Culture and Genotyping for the real-time PCRs. The authors acknowledge the support of the i3S Scientific Platform Animal Facility in *in vivo* experiments (Project – 022866/2020-12-31, DGAV, Portugal).

IV. References

[1] Basyuni, S.; Ferro, A.; Santhanam, V.; Birch, M.; McCaskie, A. Systematic scoping review of mandibular bone tissue engineering. Br J Oral Maxillofac Surg. 2020, 58, 632-642. doi: 10.1016/j.bjoms.2020.03.016

[2] Lang, N. P.; Lindhe, J., Eds. Clinical Periodontology and Implant Dentistry, 6th Ed.; Wiley Blackwell: Chichester, 2015. doi: -

[3] Qasim, S. B.; Delaine-Smith, R. M.; Fey, T.; Rawlinson, A.; Rehman, I. U. Freeze gelated porous membranes for periodontal tissue regeneration. Acta Biomater. 2015, 23, 317-328. doi: 10.1016/j.actbio.2015.05.001

[4] Fakhri, E.; Eslami, H.; Maroufi, P.; Pakdel, F.; Taghizadeh, S.; Ganbarov, K.; Yousefi, M.; Tanomand, A.; Yousefi, B.; Mahmoudi, S. Chitosan biomaterials application in dentistry. Int J Biol Macromol. 2020, 162, 956-974. doi: 10.1016/j.ijbiomac.2020.06.211

[5] Kim, J.; Park, C.; Perez, R.; Lee, H.; Jang, J.; Lee, H.; Wall, I.; Shi, S.; Kim, H. Advanced biomatrix designs for regenerative therapy of periodontal tissues. J Dent Res. 2014, 93, 1203-1211. doi: 10.1177/0022034514540682

[6] Soares, M. P. C. M.; Soares, P. V.; Pereira, A. G.; Moura, C. C. G.; Soares, P. B. F.; Naves, L. Z.; de Magalhães, D. Biocompatibility of three bioabsorbable membranes assessed in FGH fibroblasts and human osteoblast like cells culture. Head Face Med. 2014, 10, 1-6. doi: 10.1186/1746-160X-10-29

[7] Shue, L.; Yufeng, Z.; Mony, U. Biomaterials for periodontal regeneration: a review of ceramics and polymers. Biomatter. 2012, 2, 271-277. doi: 10.4161/biom.22948

[8] García-González, C. A.; Concheiro, A.; Alvarez-Lorenzo, C. Processing of materials for regenerative medicine using supercritical fluid technology. Bioconjug Chem. 2015, 26, 1159-1171. doi: 10.1021/bc5005922

[9] Bharadwaz, A.; Jayasuriya, A. C. Recent trends in the application of widely used natural and synthetic polymer nanocomposites in bone tissue regeneration. Mater Sci Eng C Mater Biol Appl. 2020, 110, 110698. doi: 10.1016/j.msec.2020.110698

[10] Rai, J. J.; Kalantharakath, T. Biomimetic ceramics for periodontal regeneration in infrabony defects: A systematic review. J Int Soc Prev Community Dent. 2014, 4, S78. doi: 10.4103/2231-0762.146207

[11] Zhang, J.; Nie, J.; Zhang, Q.; Li, Y.; Wang, Z.; Hu, Q. Preparation and characterization of bionic bone structure chitosan/hydroxyapatite scaffold for bone tissue engineering. J Biomater Sci Polym Ed. 2014, 25, 61-74. doi: 10.1080/09205063.2013.836950

[12] Dessì, M.; Borzacchiello, A.; Mohamed, T. H.; Abdel-Fattah, W. I.; Ambrosio, L. Novel biomimetic thermosensitive β-tricalcium phosphate/chitosan-based hydrogels for bone tissue engineering. J Biomed Mater Res A. 2013, 101, 2984-2993. doi: 10.1002/jbm.a.34592

[13] Dorozhkin, S. V. Biocomposites and hybrid biomaterials based on calcium orthophosphates. Biomatter. 2011, 1, 3-56. doi: 10.4161/biom.1.1.16782

[14] Swetha, M.; Sahithi, K.; Moorthi, A.; Srinivasan, N.; Ramasamy, K.; Selvamurugan, N. Biocomposites containing natural polymers and hydroxyapatite for bone tissue engineering. Int J Biol Macromol. 2010, 47, 1-4. doi: 10.1016/j.ijbiomac.2010.03.015

[15] Jamalpoor, Z.; Mirzadeh, H.; Joghataei, M. T.; Zeini, D.; Bagheri-Khoulenjani, S.; Nourani, M. R. Fabrication of cancellous biomimetic chitosan-based nanocomposite scaffolds applying a combinational method for bone tissue engineering. J Biomed Mater Res A. 2015, 103, 1882-1892. doi: 10.1002/jbm.a.35320

[16] Levengood, S. K. L.; Zhang, M. Chitosan-based scaffolds for bone tissue engineering. J Mater Chem B. 2014, 2, 3161-3184. doi: 10.1039/C4TB00027G

[17] Jones, J. R. Review of bioactive glass: from Hench to hybrids. Acta Biomater. 2013, 9, 4457-4486. doi: 10.1016/j.actbio.2012.08.023

[18] Rahaman, M. N.; Day, D. E.; Bal, B. S.; Fu, Q.; Jung, S. B.; Bonewald, L. F.; Tomsia, A. P. Bioactive glass in tissue engineering. Acta Biomater. 2011, 7, 2355-2373. doi: 10.1016/j.actbio.2011.03.016

[19] Venugopal, J.; Prabhakaran, M. P.; Zhang, Y.; Low, S.; Choon, A. T.; Ramakrishna, S. Biomimetic hydroxyapatite-containing composite nanofibrous substrates for bone tissue engineering. Philos Trans A Math Phys Eng Sci. 2010, 368, 2065-2081. doi: 10.1098/rsta.2010.0012

[20] Pighinelli, L.; Kucharska, M. Chitosan–hydroxyapatite composites. Carbohydr Polym. 2013, 93, 256-262. doi: 10.1016/j.carbpol.2012.06.004

[21] Zhao, Y.; Fan, T.; Chen, J.; Su, J.; Zhi, X.; Pan, P.; Zou, L.; Zhang, Q. Magnetic bioinspired micro/nanostructured composite scaffold for bone regeneration. Colloids Surf B Biointerfaces. 2019, 174, 70-79. doi: 10.1016/j.colsurfb.2018.11.003

[22] Venkatesan, J.; Kim, S.-K. Nano-hydroxyapatite composite biomaterials for bone tissue engineering—A review. J Biomed Nanotechnol. 2014, 10, 3124-3140. doi: 10.1166/jbn.2014.1893

[23] Kong, L.; Ao, Q.; Wang, A.; Gong, K.; Wang, X.; Lu, G.; Gong, Y.; Zhao, N.; Zhang, X. Preparation and characterization of a multilayer biomimetic scaffold for bone tissue engineering. J Biomater Appl. 2007, doi: 10.1177/0885328206073706

[24] Ribeiro, N.; Soares, G. C.; Santos-Rosales, V.; Concheiro, A.; Alvarez-Lorenzo, C.; García-González, C. A.; Oliveira, A. L. A new era for sterilization based on supercritical CO2 technology. J Biomed Mater Res B Appl Biomater. 2020, 108, 399-428. doi: 10.1002/jbm.b.34398

[25] Soares, G. C.; Learmonth, D. A.; Vallejo, M. C.; Davila, S. P.; González, P.; Sousa, R. A.; Oliveira, A. L. Supercritical CO_2 technology: The next standard sterilization technique? Mater Sci Eng C Mater Biol Appl. 2019, 99, 520-540. doi: 10.1016/j.msec.2019.01.121

[26] White, A.; Burns, D.; Christensen, T. W. Effective terminal sterilization using supercritical carbon dioxide. J Biotechnol. 2006, 123, 504-515. doi: 10.1016/j.jbiotec.2005.12.033

[27] Zhang, J.; Davis, T. A.; Matthews, M. A.; Drews, M. J.; LaBerge, M.; An, Y. H. Sterilization using high-pressure carbon dioxide. J Supercrit Fluids. 2006, 38, 354-372. doi: 10.1016/j.supflu.2005.05.005

[28] Spilimbergo, S.; Bertucco, A.; Lauro, F.; Bertoloni, G. Inactivation of *Bacillus subtilis* spores by supercritical CO_2 treatment. Innov Food Sci Emerg Technol. 2003, 4, 161-165. doi: 10.1016/S1466-8564(02)00089-9

[29] Wehmeyer, J. L.; Natesan, S.; Christy, R. J. Development of a sterile amniotic membrane tissue graft using supercritical carbon dioxide. Tissue Eng Part C Methods. 2015, 21, 649-659. doi: 10.1089/ten.TEC.2014.0304

[30] Gupta, R. B.; Shim, J.-J. Solubility in supercritical carbon dioxide, 1st Ed.; CRC press: Boca Raton, USA, 2006. doi: 10.1201/9781420005998

[31] Ruphuy, G.; Souto-Lopes, M.; Paiva, D.; Costa, P.; Rodrigues, A.; Monteiro, F.; Salgado, C.; Fernandes, M.; Lopes, J.; Dias, M. Supercritical CO_2 assisted process for the production of high-purity and sterile nano-hydroxyapatite/chitosan hybrid scaffolds. J Biomed Mater Res B Appl Biomater. 2018, 106, 965-975. doi: 10.1002/jbm.b.33903

[32] Ruphuy, G.; Weide, T.; Lopes, J.; Dias, M. M.; Barreiro, M. Preparation of nano-hydroxyapatite/chitosan aqueous dispersions: From lab scale to continuous production using an innovative static mixer. Carbohydr Polym. 2018, 202, 20-28. doi: 10.1016/j.carbpol.2018.08.123

[33] Venkatesan, J.; Bhatnagar, I.; Manivasagan, P.; Kang, K.-H.; Kim, S.-K. Alginate composites for bone tissue engineering: a review. Int J Biol Macromol. 2015, 72, 269-281. doi: 10.1016/j.ijbiomac.2014.07.008

[34] Croisier, F.; Jérôme, C. Chitosan-based biomaterials for tissue engineering. European Polym J. 2013, 49, 780-792. doi: 10.1016/j.eurpolymj.2012.12.009

[35] Xu, C.; Lei, C.; Meng, L.; Wang, C.; Song, Y. Chitosan as a barrier membrane material in periodontal tissue regeneration. J Biomed Mater Res B Appl Biomater. 2012, 100, 1435-1443. doi: 10.1002/jbm.b.32662

[36] Zhang, X.; Zhu, L.; Lv, H.; Cao, Y.; Liu, Y.; Xu, Y.; Ye, W.; Wang, J. Repair of rabbit femoral condyle bone defects with injectable nanohydroxyapatite/chitosan composites. J Mater Sci Mater Med. 2012, 23, 1941-1949. doi: 10.1007/s10856-012-4662-y

[37] Chesnutt, B. M.; Yuan, Y.; Buddington, K.; Haggard, W. O.; Bumgardner, J. D. Composite chitosan/nano-hydroxyapatite scaffolds induce osteocalcin production by osteoblasts *in vitro* and support bone formation *in vivo*. Tissue Eng Part A. 2009, 15, 2571-2579. doi: 10.1089/ten.tea.2008.0054

[38] Kokubo, T.; Takadama, H. How useful is SBF in predicting *in vivo* bone bioactivity? Biomaterials. 2006, 27, 2907-2915. doi: 10.1016/j.biomaterials.2006.01.017

[39] Campos, Y.; Sola, F. J.; Almirall, A.; Fuentes, G.; Eich, C.; Que, I.; Chan, A.; Kaijzel, E.; Tabata, Y.; Quintanilla, L. Design, construction, and biological testing of an implantable porous trilayer scaffold for repairing osteoarthritic cartilage. J Tissue Eng Regen Med. 2020, 14, 355-368. doi: 10.1002/term.3001

[40] Wilkesmann, S.; Fellenberg, J.; Nawaz, Q.; Reible, B.; Moghaddam, A.; Boccaccini, A. R.; Westhauser, F. Primary osteoblasts, osteoblast precursor cells or osteoblast-like cell lines: Which human cell types are (most) suitable for characterizing 45S5-bioactive glass? J Biomed Mater Res A. 2020, 108, 663-674. doi: 10.1002/jbm.a.36846. Epub 2019 Dec 4.

[41] Hoffman, R. M. Nude Mouse. In Reference Module in Life Sciences, Eds.; Elsevier: Amsterdam, 2017; doi: 10.1016/B978-0-12-809633-8.06825-4

[42] Masuda, J.; Shigehiro, T.; Matsumoto, T.; Satoh, A.; Mizutani, A.; Umemura, C.; Saito, S.; Kijihira, M.; Takayama, E.; Seno, A. Cytokine expression and macrophage localization in xenograft and allograft tumor models stimulated with lipopolysaccharide. Int J Mol Sci. 2018, 19, 1261. doi: 10.3390/ijms19041261

[43] Sheikh, Z.; Brooks, P. J.; Barzilay, O.; Fine, N.; Glogauer, M. Macrophages, foreign body giant cells and their response to implantable biomaterials. Materials (Basel). 2015, 8, 5671-5701. doi: 10.3390/ma8095269

[44] Kumar, P.; Saini, M.; Dehiya, B. S.; Umar, A.; Sindhu, A.; Mohammed, H.; Al-Hadeethi, Y.; Guo, Z. Fabrication and in-vitro biocompatibility of freeze-dried CTS-nHA and CTS-nBG scaffolds for bone regeneration applications. Int J Biol Macromol. 2020, 149, 1-10. doi: 10.1016/j.ijbiomac.2020.01.035

[45] Qasim, S. B.; Baig, M. R.; Matinlinna, J. P.; Daood, U.; Al-Asfour, A. Highly Segregated Biocomposite Membrane as a Functionally Graded Template for Periodontal Tissue Regeneration. Membranes (Basel). 2021, 11, 667. doi: 10.3390/membranes11090667

[46] Zhang, Z.; Wu, G.; Cao, Y.; Liu, C.; Jin, Y.; Wang, Y.; Yang, L.; Guo, J.; Zhu, L. Self-assembling peptide and nHA/CTS composite scaffolds promote bone regeneration through increasing seed cell adhesion. Mater Sci Eng C Mater Biol Appl. 2018, 93, 445-454. doi: 10.1016/j.msec.2018.07.079

[47] Tamburaci, S.; Tihminlioglu, F. Development of Si doped nano hydroxyapatite reinforced bilayer chitosan nanocomposite barrier membranes for guided bone regeneration. Mater Sci Eng C Mater Biol Appl. 2021, 128, 112298. doi: 10.1016/j.msec.2021.112298

[48] Dong, Y.; Liang, J.; Cui, Y.; Xu, S.; Zhao, N. Fabrication of novel bioactive hydroxyapatite-chitosan-silica hybrid scaffolds: Combined the sol-gel method with 3D plotting technique. Carbohydr Polym. 2018, 197, 183-193. doi: 10.1016/j.carbpol.2018.05.086

[49] He, X.; Liu, Y.; Yuan, X.; Lu, L. Enhanced healing of rat calvarial defects with MSCs loaded on BMP-2 releasing chitosan/alginate/hydroxyapatite scaffolds. PloS One. 2014, 9, e104061. doi: 10.1371/journal.pone.0104061

[50] Pilloni, A.; Pompa, G.; Saccucci, M.; Di Carlo, G.; Rimondini, L.; Brama, M.; Zeza, B.; Wannenes, F.; Migliaccio, S. Analysis of human alveolar osteoblast behavior on a nano-hydroxyapatite substrate: an *in vitro* study. BMC Oral Health. 2014, 14, 1-7. doi: 10.1186/1472-6831-14-22

[51] Fu, Q.; Saiz, E.; Rahaman, M. N.; Tomsia, A. P. Bioactive glass scaffolds for bone tissue engineering: state of the art and future perspectives. Mater Sci Eng C Mater Biol Appl. 2011, 31, 1245-1256. doi: 10.1016/j.msec.2011.04.022

[52] Rodrigues, S. C.; Salgado, C. L.; Sahu, A.; Garcia, M. P.; Fernandes, M. H.; Monteiro, F. J. Preparation and characterization of collagen-nanohydroxyapatite biocomposite scaffolds by cryogelation method for bone tissue engineering applications. J Biomed Mater Res A. 2013, 101, 1080-1094. doi: 10.1002/jbm.a.34394

[53] Xiong, Y.; Huang, J.; Fu, L.; Ren, H.; Li, S.; Xia, W.; Yan, Y. Enhancement of osteoblast cells osteogenic differentiation and bone regeneration by hydroxyapatite/phosphoester modified poly (amino acid). Mater Sci Eng C Mater Biol Appl. 2020, 111, 110769. doi: 10.1016/j.msec.2020.110769

[54] Lauritano, D.; Limongelli, L.; Moreo, G.; Favia, G.; Carinci, F. Nanomaterials for periodontal tissue engineering: chitosan-based scaffolds. A systematic review. Nanomaterials. 2020, 10, 605. doi: 10.3390/nano10040605

[55] Qasim, S. B.; Husain, S.; Huang, Y.; Pogorielov, M.; Deineka, V.; Lyndin, M.; Rawlinson, A.; Rehman, I. U. *In-vitro* and *in-vivo* degradation studies of freeze gelated porous chitosan composite scaffolds for tissue engineering applications. Polym Degrad Stab. 2017, 136, 31-38. doi: 10.1016/j.polymdegradstab.2016.11.018

[56] Liu, Y.; Gu, J.; Fan, D. Fabrication of high-strength and porous hybrid scaffolds based on nano-hydroxyapatite and human-like collagen for bone tissue regeneration. Polymers. 2020, 12, 61. doi: 10.3390/polym12010061

[57] Pilia, M.; Guda, T.; Appleford, M. Development of composite scaffolds for load-bearing segmental bone defects. Biomed Res Int. 2013, 2013, 458253. doi: 10.1155/2013/458253

[58] Peniche, C.; Solís, Y.; Davidenko, N.; García, R. Chitosan/hydroxyapatite-based composites. Biotecnol Apl. 2010, 27, 202-210. doi: -

[59] Xu, H. H.; Burguera, E. F.; Carey, L. E. Strong, macroporous, and *in situ*-setting calcium phosphate cement-layered structures. Biomaterials. 2007, 28, 3786-3796. doi: 10.1016/j.biomaterials.2007.05.015

[60] Belluzo, M. S.; Medina, L. F.; Molinuevo, M. S.; Cortizo, M. S.; Cortizo, A. M. Nanobiocomposite based on natural polyelectrolytes for bone regeneration. J Biomed Mater Res A. 2020, 108, 1467-1478. doi: 10.1002/jbm.a.36917

[61] Jun, S.-H.; Lee, E.-J.; Jang, T.-S.; Kim, H.-E.; Jang, J.-H.; Koh, Y.-H. Bone morphogenic protein-2 (BMP-2) loaded hybrid coating on porous hydroxyapatite scaffolds for bone tissue engineering. J Mater Sci Mater Med. 2013, 24, 773-782. doi: 10.1007/s10856-012-4822-0

[62] Bi, S.; Wang, P.; Hu, S.; Li, S.; Pang, J.; Zhou, Z.; Sun, G.; Huang, L.; Cheng, X.; Xing, S. Construction of physical-crosslink chitosan/PVA double-network hydrogel with surface mineralization for bone repair. Carbohydr Polym. 2019, 224, 115176. doi: 10.1016/j.carbpol.2019.115176

[63] Sun, T. W.; Yu, W. L.; Zhu, Y. J.; Chen, F.; Zhang, Y. G.; Jiang, Y. Y.; He, Y. H. Porous Nanocomposite Comprising Ultralong Hydroxyapatite Nanowires Decorated with Zinc-Containing Nanoparticles and Chitosan: Synthesis and Application in Bone Defect Repair. Chemistry. 2018, 24, 8809-8821. doi: 10.1002/chem.201800425

[64] Lee, J. S.; Baek, S. D.; Venkatesan, J.; Bhatnagar, I.; Chang, H. K.; Kim, H. T.; Kim, S.-K. *In vivo* study of chitosan-natural nano hydroxyapatite scaffolds for bone tissue regeneration. Int J Biol Macromol. 2014, 67, 360-366. doi: 10.1016/j.ijbiomac.2014.03.053

[65] Wang, Y.; Lv, P.; Ma, Z.; Zhang, J. Enhanced Healing of Rat Calvarial Critical Size Defect with Selenium-Doped Lamellar Biocomposites. Biol Trace Elem Res. 2013, 155, 72-81. doi: 10.1007/s12011-013-9763-z

[66] Liu, H.; Peng, H.; Wu, Y.; Zhang, C.; Cai, Y.; Xu, G.; Li, Q.; Chen, X.; Ji, J.; Zhang, Y. The promotion of bone regeneration by nanofibrous hydroxyapatite/chitosan scaffolds by effects on integrin-BMP/Smad signaling pathway in BMSCs. Biomaterials. 2013, 34, 4404-4417. doi: 10.1016/j.biomaterials.2013.02.048

[67] Caridade, S. G.; da Silva, R. M.; Reis, R. L.; Mano, J. F. Effect of solvent-dependent viscoelastic properties of chitosan membranes on the permeation of 2-phenylethanol. Carbohydr Polym. 2009, 75, 651-659. doi: 10.1016/j.carbpol.2008.09.011

[68] Mano, J. F. Viscoelastic properties of chitosan with different hydration degrees as studied by dynamic mechanical analysis. Macromol Biosci. 2008, 8, 69-76. doi: 10.1002/mabi.200700139

[69] Raina, D. B.; Isaksson, H.; Teotia, A. K.; Lidgren, L.; Tägil, M.; Kumar, A. Biocomposite macroporous cryogels as potential carrier scaffolds for bone active agents augmenting bone regeneration. J Control Release. 2016, 235, 365-378. doi: 10.1016/j.jconrel.2016.05.061

[70] Salgado, C. L.; Grenho, L.; Fernandes, M. H.; Colaço, B. J.; Monteiro, F. J. Biodegradation, biocompatibility, and osteoconduction evaluation of collagen-nanohydroxyapatite cryogels for bone tissue regeneration. J Biomed Mater Res A. 2016, 104, 57-70. doi: 10.1002/jbm.a.35540

[71] Przekora, A. Current trends in fabrication of biomaterials for bone and cartilage regeneration: Materials modifications and biophysical stimulations. Int J Mol Sci. 2019, 20, 435. doi: 10.3390/ijms20020435

[72] Song, J. M.; Shin, S. H.; Kim, Y. D.; Lee, J. Y.; Baek, Y. J.; Yoon, S. Y.; Kim, H. S. Comparative study of chitosan/fibroin–hydroxyapatite and collagen membranes for guided bone regeneration in rat calvarial defects: micro-computed tomography analysis. Int J Oral Sci. 2014, 6, 87-93. doi: 10.1038/ijos.2014.16

[73] Zakaria, S. M.; Sharif Zein, S. H.; Othman, M. R.; Yang, F.; Jansen, J. A. Nanophase hydroxyapatite as a biomaterial in advanced hard tissue engineering: a review. Tissue Eng Part B Rev. 2013, 19, 431-441. doi: 10.1089/ten.TEB.2012.0624

[74] Sedghi, R.; Shaabani, A.; Sayyari, N. Electrospun triazole-based chitosan nanofibers as a novel scaffolds for bone tissue repair and regeneration. Carbohydr Polym. 2020, 230, 115707. doi: 10.1016/j.carbpol.2019.115707

[75] Ardean, C.; Davidescu, C. M.; Nemeş, N. S.; Negrea, A.; Ciopec, M.; Duteanu, N.; Negrea, P.; Duda-Seiman, D.; Musta, V. Factors influencing the antibacterial activity of chitosan and chitosan modified by functionalization. Int J Mol Sci. 2021, 22, 7449. doi: 10.3390/ijms22147449

[76] Verlee, A.; Mincke, S.; Stevens, C. V. Recent developments in antibacterial and antifungal chitosan and its derivatives. Carbohydr Polym. 2017, 164, 268-283. doi: 10.1016/j.carbpol.2017.02.001

[77] Jeong, J.; Kim, J. H.; Shim, J. H.; Hwang, N. S.; Heo, C. Y. Bioactive calcium phosphate materials and applications in bone regeneration. Biomater Res. 2019, 23, 1-11. doi: 10.1186/s40824-018-0149-3

[78] Pinto, R. V.; Gomes, P. S.; Fernandes, M. H.; Costa, M. E.; Almeida, M. M. Glutaraldehyde-crosslinking chitosan scaffolds reinforced with calcium phosphate spray-dried granules for bone tissue applications. Mater Sci Eng C Mater Biol Appl. 2020, 109, 110557. doi: 10.1016/j.msec.2019.110557

[79] Lai, G.-J.; Shalumon, K.; Chen, J.-P. Response of human mesenchymal stem cells to intrafibrillar nanohydroxyapatite content and extrafibrillar nanohydroxyapatite in biomimetic chitosan/silk fibroin/nanohydroxyapatite nanofibrous membrane scaffolds. Int J Nanomedicine. 2015, 10, 567. doi: 10.2147/IJN.S73780

[80] Barros, J.; Ferraz, M. P.; Azeredo, J.; Fernandes, M.; Gomes, P.; Monteiro, F. Alginate-nanohydroxyapatite hydrogel system: Optimizing the formulation for enhanced bone regeneration. Mater Sci Eng C Mater Biol Appl. 2019, 105, 109985. doi: 10.1016/j.msec.2019.109985

[81] Giannobile, W. V.; Kaigler, D.; Nevins, M. Preclinical Model Development for the Reconstruction of Oral, Periodontal, and Craniofacial Defects In Osteology guidelines for oral and maxillofacial regeneration: preclinical models for translational research, Giannobile, W. V.; Nevins, M., Eds.; Quintessence: 2011; Chapter 1, doi: -

[82] Han, J.; Menicanin, D.; Marino, V.; Ge, S.; Mrozik, K.; Gronthos, S.; Bartold, P. Assessment of the regenerative potential of allogeneic periodontal ligament stem cells in a rodent periodontal defect model. J Periodontal Res. 2013, 49, 333-345. doi: 10.1111/jre.12111

[83] B Kaczmarek, B.; Sionkowska, A.; Gołyńska, M.; Polkowska, I.; Szponder, T.; Nehrbass, D.; Osyczka, A. *In vivo* study on scaffolds based on chitosan, collagen, and hyaluronic acid with hydroxyapatite. Int J Biol Macromol. 2018, 118, 938-944. doi: 10.1016/j.ijbiomac.2018.06.175

[84] Kyriakides, T. Molecular events at tissue–biomaterial interface. In Host response to biomaterials: The impact of host response on biomaterial selection, Badylak, S., Eds.; Academic Press: Oxford, 2015; Chapter 5, 81-116. doi: 10.1016/B978-0-12-800196-7.00005-0

CHAPTER V

Bone Regeneration Driven by a Nano-Hydroxyapatite/Chitosan Composite Bioaerogel for Periodontal Regeneration

Bone Regeneration Driven by a Nano-Hydroxyapatite/Chitosan Composite Bioaerogel for Periodontal Regeneration

Souto-Lopes M [1,2,3,] Grenho L [4,5], Manrique Y [6,7], Dias MM [6,7], Lopes, JCB [6,7], Fernandes MH [4,5], Monteiro FJ [1,2,3,8], Salgado CL [1,2]

1 – i3S – Instituto de Investigação e Inovação em Saúde da Universidade do Porto

2 – INEB – Instituto de Engenharia Biomédica, Universidade do Porto

3 – Faculdade de Engenharia da Universidade do Porto

4 – Faculdade de Medicina Dentária da Universidade do Porto

5 – LAQV/REQUIMTE – Laboratório Associado para a Química Verde/ Rede de Química e Tecnologia

6 – LSRE-LCM – Laboratory of Separation and Reaction Engineering – Laboratory of Catalysis and Materials, Faculty of Engineering, University of Porto

7 – ALiCE – Associate Laboratory in Chemical Engineering, Faculty of Engineering, University of Porto

8 – Porto Comprehensive Cancer Center (P.CCC)

Frontiers in Bioengineering and Biotechnology, 2024, 12:1355950. doi: 10.3389/fbioe.2024.1355950

ABSTRACT

The most recent progress for reconstructive therapy for the management of periodontitits and peri-implantitis bone defects has relied on the development of highly porous biodegradable bioaerogels for guided bone regeneration. The objective of this work was to evaluate *in vitro* the osteoinduction of periodontal-originating cells (human dental follicle mesenchymal cells, DFMSCs) promoted by a nano-hydroxyapatite/chitosan (nHAp/CS) bioaerogel, which was purified and sterilized by a sustainable technique (supercritical CO_2). Moreover, the *in vivo* bone regeneration capacity of the nHAp/CS bioaerogel was preliminarily assessed as a proof-of-concept on a rat calvaria bone defect model. The quantification of DNA content of DFMSCs seeded upon nHAp/CS and CS scaffolds (control material) showed a significant increase from the 14^{th} to the 21^{st} day of culture. These results were corroborated through confocal laser scanning microscopy analysis (CLSM). Furthermore, the alkaline phosphatase (ALP) activity increased significantly at the 21^{st} day, similarly for both materials. Moreover, the presence of nHAp promoted a significantly higher expression of osteogenic genes after 21 days when compared to CS scaffolds and control. CLSM images of 21 days of culture also showed an increased deposition of OPN over the nHAp/CS surface. The *in vivo* bone formation was assessed by microCT and histological analysis. The *in vivo* evaluation showed a significant increase in bone volume in the nHAp/CS test group when compared to CS and the empty control, as well as higher new bone formation and calcium deposition within the nHAp/CS structure. Overall, the present study showed that the nHAp/CS bioaerogel could offer a potential solution for periodontal and peri-implant bone regeneration treatments since the *in vitro* results demonstrated that it provided favorable conditions for the DFMSC proliferation and osteogenic differentiation, while the *in vivo* outcomes confirmed that it promoted higher bone ingrowth.

KEYWORDS

Bioaerogel, Nano-hydroxyapatite/chitosan scaffold, Dental follicle mesenchymal cells, Osteogenic differentiation, Bone regeneration, Biomaterials.

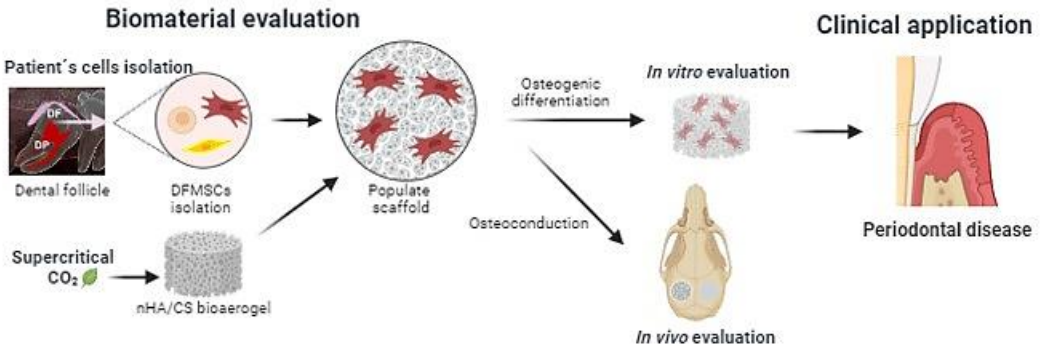

Graphical abstract

1. INTRODUCTION

Periodontology is a dental medicine field, which has been developing faster and gaining more worldwide emphasis in recent years, with increasing impact factor of the related scientific publications [1, 2]. This is due to the high prevalence of periodontal and peri-implant diseases, which lead to the degradation of the supporting tissues, namely alveolar bone, and, consequently, to tooth or dental implant loss, respectively [3]. Since periodontitis and peri-implantitis severely affect masticatory function, orofacial aesthetics and individual wellbeing [4], serious efforts have been made in the improvement of new surgical techniques and biomaterials to promote tissue regeneration around teeth and dental implants [5]. The regeneration of the functional tooth-bone interface requires adequate growth of the acellular cementum, periodontium ligament (PDL) and cryptal bone [6]. Dental follicle cells (DFCs), which are a type of mesenchymal cells (MSCs) found in periodontal tissues [7], are responsible for the building of the interface between bone and dental root during their development. These cells are key players in bone remodeling and periodontium tissue development [8]. Human dental follicle mesenchymal cells (DFMSCs) can differentiate into osteoblasts and contribute to alveolar tissue formation. Those MSCs have also shown immunomodulatory properties that are instrumental in protecting damaged tissues by releasing anti-inflammatory molecules, reducing fibrosis and promoting tissue regeneration [9]. A previous research compared different *in vitro* microenvironments (dynamic vs static and with vs without medium supplementation) for DFMSCs culture [10], and there is still some uncertainty about the conditions and materials that are more favorable for their proliferation rate and differentiation capacity, due to the scarcity of studies.

One of the major applications of bone regeneration biomaterials is in periodontal and peri-implant clinical cases. The commercially available treatments rely on autogenous grafts or on biomaterials that do not always show predictable results in long-term application. Bioaerogels are novel highly porous and biodegradable biomaterials developed using a polymeric matrix from either natural or synthetic origins. Bioaerogels produced with different natural polymers (e.g. polysaccharides and proteins) are safe, economical, and sustainable to be used as biomedical devices [11-13]. Polysaccharides being biocompatible, degradable, renewable, and highly available in nature have garnered great interest in tissue regenerative applications [14]. Bioaerogels are materials with a large specific surface area and high porosity that possess a high permeable and appropriate structure to retain large amounts of aqueous fluids [15]. Aerogels are solid materials that are obtained after drying, which removes the liquid phase of a gel (being replaced by air) with minimal contraction [16]. The outstanding properties of bioaerogels favor cell attachment along with a tunable network of interconnected pores that allows the nutrient and oxygen supply to the cells and the disposal of cellular metabolic by-products, making them suitable for application in regenerative medicine [17].

The development and production of large-scale biomaterials, in particular, requires decreased use of hazardous compounds and increased use of sustainable sources of materials in order to reduce the environmental impact [18]. Based on this, chitosan (CS) has garnered great

attention due to its availability (from the by-products of seafood industries) [19], and pro-regenerative properties such as healing effects, antimicrobial properties, biocompatibility and biodegradability [20]. Since its degradation produces a harmless amino sugar that could be absorbed by human tissues, CS has a low risk of bioproduct accumulation in important organs such as the liver and kidneys [21, 22]. Ruphuy *et al.* (2018) proposed that chitosan-based bioaerogels were produced with freeze drying, followed by exposure to supercritical CO_2 ($scCO_2$), which allowed obtaining a porous structure and extracting 80% of the CS solvent (acetic acid) from the scaffold [23]. Unlike other methods for production of chitosan-based scaffolds published in the literature ([19, 24-29]), the $scCO_2$ technique exempted the use of additional solvents and time-consuming washing and drying steps for acid neutralization, resulting in a more sustainable method for scaffold production. Moreover, the $scCO_2$ technique allowed us to simultaneously obtain a sterile and ready-to-use final product, as demonstrated in a previous work by a microbiologic assay [23]. However, CS also showed poor mechanical stability, and to overcome this limitation, a biocomposite was developed by combining this biopolymer with suitable inorganic nanomaterials (nano-hydroxyapatite, nHAp), which provided important characteristics such as higher stiffness and osteoconduction [23, 30]. One of the major advantages of the presence of nHAp in the composite's formulation is that it promotes bioactivity, which increases the cell response of forming a direct bond with the bone surrounding tissue [31, 32]. In a previous work, the production of the nHAp/CS (70/30 %) bioaerogel scaffold was optimized to a simple eco-friendly three-step method (including the $scCO_2$ solvent extraction and terminal sterilization) [23]. This 3D scaffold highly resembles the element compositions and structures of native bones [23, 30] and simultaneously mimics the structure and chemical properties of bone tissue, which is a composite of ~70 % mineral (mostly hydroxyapatite (HA) nanocrystals) and ~30 % organics (e.g., natural polymers and glycoproteins) [33]. In a subsequent study, this developed nHAp/CS bioaerogel showed *in vitro* cytocompatibility, appropriate mechanical behavior for low-load bearing sites, biodegradability, antimicrobial properties and *in vivo* biocompatibility in a subcutaneous implant (mouse model) [30].

To propose the nHAp/CS bioaerogel as an alternative to classic autograft and allograft treatments for bone regeneration of periodontal/peri-implant defects, the present study aimed at exploring, *in vitro*, the scaffold's osteoinductive and osteoconductive capacity to drive the osteogenic differentiation of DFMSCs, which are periodontal tissue precursor cells with multifunctional properties and excellent potential for regenerative medicine applications. Moreover, as a proof-of-concept, the nHAp/CS scaffold's capacity to promote bone regeneration *in vivo* was assessed using a simple critical-sized bone defect model before advancing to more complex *in vivo* alveolar bone defect models.

2. MATERIALS AND METHODS

2.1. Materials

CS (from granules from marine animals' exoskeleton solution, 90/200/A1, Biolog-Heppe, Landsberg, Germany, deacetylation degree 91.9 %), nHAp (nanoXIM-HAp102, rod-like nano-particles < 50 nm) aqueous paste (Fluidinova S.A., Maia, Portugal), bovine serum albumin (BSA), p-nitrophenol phosphate, p-nitrophenol, sodium hydroxide (NaOH), formaldehyde 4 %, Triton X-100, Alizarin Red S, and rabbit anti-human osteopontin were purchased from Merck (Darmstadt, Germany). Dulbecco's modified eagle medium (DMEM), fetal bovine serum (FBS), penicillin-streptomycin, and trypsin were purchased from Gibco (Thermo Fisher Scientific, Waltham, MA, United States). The Thermo Scientific™ Pierce™ BCA Protein Assay Kit, Alexa Fluor Phalloidin 488, Alexa Fluor 488 goat anti-rabbit IgG secondary antibody, and the Quant-iT™ Picogreen® DNA assay kit were purchased from Invitrogen (Thermo Fisher Scientific, Waltham, Massachussets, United States). PrimePCR™ SYBR® Green Assays (Human GAPDH, SP7 and BMP-2) were purchased from Bio-Rad Laboratories (Algés, Portugal). The NucleoSpin RNA kit was purchased from Macherey-Nagel (Dueren, Germany). The iScript™ cDNA Synthesis Kit, and the iTaqTM Universal SYBR® Green Supermix were purchased from Bio-Rad (Hercules, California, United States). Propidium iodide was purchased from BD Pharmingen ™ (BD Biosience, Franklin Lakes, New Jersey, United States). Fluoromont VECTASHIELD® Mounting Medium, hematoxylin and eosin, and Masson's Trichrome histological staining kits were purchased from Vector Laboratories (Newark, California, United States).

2.2. Preparation of nHAp/CS and CS scaffolds

nHAp/CS scaffolds were prepared using a previously described method [23]. In brief, a homogenous dispersion was prepared at a 70/30 w/w proportion of, respectively, an nHAp paste (15 % w/w, pH 9-10) and a CS solution at 3.0 % w/v in acetic acid. The dispersion was poured into 55 mm Petri plates (10 mL in each) and stored at -20 ºC overnight.

Phase separation was achieved through a standard freeze-drying procedure (VirTis BenchTop 6K, model nº6KBTEL) for 24 h. The residual solvent removal and sterilization were performed by $scCO_2$ (in-house built unit) in continuous batch cycles at 8.0 MPa (80 bar) and 75 ºC for 2 h. Finally, the individual samples were packed in sterile conditions in Nasco Whirl-Pak® standard bags (2 oz.) and stored at room temperature (RT). Control samples of CS were prepared following the same protocol, except for the addition of the nHAp paste. The scaffolds were cut into smaller samples (cuboid shape of 5 x 5 mm with 4 mm height for *in vitro* experiments;

cylindrical shape of 4 mm of diameter and 2 mm height for *in vivo* experiments) in sterile conditions.

2.3. *In Vitro* Biological Evaluation

2.3.1. Establishment of Stem Cell Cultures from Human Dental Follicle Mesenchymal Cells

Human dental tissue fragments were isolated from young healthy patients (approved by the Ethical Committee of the University of Porto – 50/CEUP/2018, Porto, Portugal) and fully characterized according to the clinical procedures and laboratorial methods described at the supplementary material of a previous work [10]. It was necessary to retrieve follicular sacs from different patients, followed by digestion, adhesion to plastic tissue culture substrates, flow cytometry and RT-PCR for regular identity assays based on phenotypic and genotypic analyses of the expression of specific MSC markers. After isolation, DFMSCs were selected from a single donor that better fulfilled the predefined criteria such as plastic adherence, phenotypic profile (the presence and absence of specific cell mesenchymal markers), and lineage differentiation [10, 34, 35], following the recommendations of the updated guidelines of the International Society for Stem Cell Research (ISSCR) [36]. Cells were cultured in Dulbecco's modified Eagle medium supplemented with 10 % FBS and 1 % penicillin/streptomycin (3×10^4 mol/L and 5×10^4 mol/L) and kept at 37 °C in a 5 % carbon dioxide (CO_2) atmosphere (CO_2 Incubator, Binder, Tuttlingen, Germany). After achieving cell confluence, cells (passage 6) were detached with trypsin solution (0.5 %) at 37 °C for 5 min and seeded on the scaffolds (0.3×10^6 cells/scaffold). After that, scaffolds were incubated for 7, 14, and 21 days (time points) in similar conditions.

2.3.2. Cellular Proliferation Assay

DNA content was measured using the Quant-iT™ PicoGreen® DNA Assay according to the manufacturer's instructions. After each time point, scaffolds were washed with PBS and then incubated with 0.5 mL of ultra-pure water at 37 °C and 5 %/CO_2 for 1 h. Subsequently, scaffolds were placed in a freezer at -20 ºC until the end of the experiment and then thawed at RT to lyse all the cell membranes. The supernatant with the lysed cells was collected and incubated with PicoGreen® solution. Finally, the fluorescence intensity was measured by using a microplate spectrofluorometer (SynergyMx, BioTek, Winooski, Vermont, United States) at 480 and 520 nm excitation and emission wavelengths, respectively. The results are expressed in nanograms of DNA per mL.

2.3.3. Cellular Differentiation Assay

The alkaline phosphatase (ALP) activity was measured using a quantitative analysis for early osteogenic characterization. The same supernatant with the lysed cells obtained as described above (Section 2.3.2) was used for assessment of the enzyme activity and total protein content. The ALP enzyme activity was assessed by monitoring substrate hydrolysis using p-nitrophenol phosphate in an alkaline buffer solution (pH = 10). After 1 h of incubation at 37 °C, the reaction was terminated by adding NaOH (0.02 M), and the p-nitrophenol was quantified by absorbance at 405 nm using a plate reader (Synergy MX, BioTek, Winooski, Vermont, United States). Finally, the ALP results were expressed in nanomoles (nmol) of p-nitrophenol produced per minute (min). The ALP activity results were normalized to the total DNA content (cell density) and expressed in nanomoles of p-nitrophenol produced per minute per µg of DNA.

Total protein content was measured by Lowry's method (Thermo Scientific™ Pierce™ BCA Protein Assay Kit) with bovine serum albumin used as the standard. Results were expressed in miligrams of protein concentration per mL.

The expression of relevant osteogenic genes was monitored throughout the 21-day culture and analyzed by real-time quantitative polymerase chain reaction (RT-qPCR) at the time points 14 and 21 days. In brief, total RNA was extracted using a NucleoSpin RNA Kit and reverse-transcribed into complementary DNA (cDNA) using the iScriptTM cDNA Synthesis Kit as per the manufacturers' instructions. The expression of the target genes was quantitatively determined on RT-PCR equipment (CFX384, Bio-Rad, Hercules, CA, United States) using the iTaq™ universal SYBR® Green Supermix. All genes were normalized to the reference gene glyceraldehyde 3-phosphate dehydrogenase (GAPDH) and are described in Table 1. Relative quantification of gene amplification by qPCR was performed using the cycle threshold (Ct) values, and relative expression levels were calculated using the $2^{-\Delta\Delta CT}$ method. DFMSCs cultured at time 0 were used as a normalizer, for the osteogenic gene expression (value 1). A 2D control (tissue culture plate) was used for 14 days and 21 days. For each qPCR, samples were analyzed in duplicate, and three independent experiments were performed.

Table 1. Gene name and respective primers for RT-qPCR

Gene	**Primers assay ID (Bio-Rad)**	
GAPDH	qHsaCED0038674	
SP7	qHsaCED0003759	
BMP-2	qHsaCID0015400	
	Primer Sequence (Forward)	**Primer Sequence (Reverse)**
OPN	5' – ACTCGAACGACTCTGATGATGT – 3'	5' – GTCAGGTCTGCGAAACTTCTTA – 3'
Col-1	5' – TCCGGCTCCTGCTCCTCTTA – 3'	5' – ACCAGCAGGACCAGCATCTC – 3'

2.3.4. Confocal Laser Scanning Microscopy

Samples from each time point were fixed with 4 % paraformaldehyde and incubated for 30 min at RT. Then, the materials were incubated with 0.1 % Triton X-100 solution and then in 1 % BSA solution to enhance sensitivity by reducing background interference. The cells cytoplasm (actin fibers) was stained with Alexa Fluor-conjugated Phalloidin 488 nm (dilution of 1:150) for 1 h, and nuclei were stained with propidium iodide (1 mg/mL) for 10 min at RT and under dark conditions. For human osteopontin immunostaining, an identical protocol was performed was employed for the cell membrane's permeabilization and to block nonspecific binding, as described above. Samples were then incubated with rabbit anti-human osteopontin (AB 1870, 1:500) overnight at 4°C. This procedure was followed by 1 h incubation with Alexa Fluor 488 goat anti-rabbit IgG secondary antibody (1:1000). All samples were covered by Fluoromount. Images were acquired with excitation lasers of 405 (CS autofluorescence), 488 nm and 594 nm and evaluated by confocal laser scanning microscopy (CLSM, Leica SP2 AOBS SE Camera, Leica, Wetzlar, Germany).

2.4 *In Vivo* Evaluation

2.4.1. Animal model

nHAp/CS and CS scaffolds were implanted into the calvarial bone of 10-week-old male Wistar rats (12 animals; i3S animal house, Portugal). Based on the results of other published reports, G*Power software was used to estimate the minimum number of animals needed for the study (n = 6 for each tested group (nHA/CS and CS) with an effect size of 2.12 for paired samples). All animal experiments were approved by the i3S animal Ethics Committee (EC) and by DGAV (Portugal). All tests followed EC guidelines for animal welfare. Researchers involved in animal handling were FELASA-accredited and DGAV-certified. Animals were anesthetized with 3 % – 5 % isoflurane for induction and 1 % – 2 % for surgical procedures that were performed under standard aseptic conditions. A midline incision was performed through the parietal midline skin, and two 4 mm (diameter) bone defect were created, one on the right side (control – empty defect) and another one on the left side (scaffolds) (Figure 1). An *in vivo* microCT scan was performed after 3 days (control) and 1, 2 and 3 months to follow the bone volumetric changes.

In brief, the animals were individually placed in an induction chamber, and anesthesia was induced at 3 % – 5 % and maintained with 1 % – 2 % isoflurane during *in vivo* assessment in the microCT device (Bruker SkyScan1276, Bruker Corporation, Billerica, Massachusetts, United States). Data were collected from a region of interest (ROI) shaped like of cylinder with a diameter of 4 mm and thickness of 1.5 mm, based on the size of created defect area. 3D images

of the defects were obtained, and the quantitative parameters calculated were the bone volume (BV – mm^3), bone volume *versus* tissue volume (BV/TV – %), and bone surface (BS – mm^2).

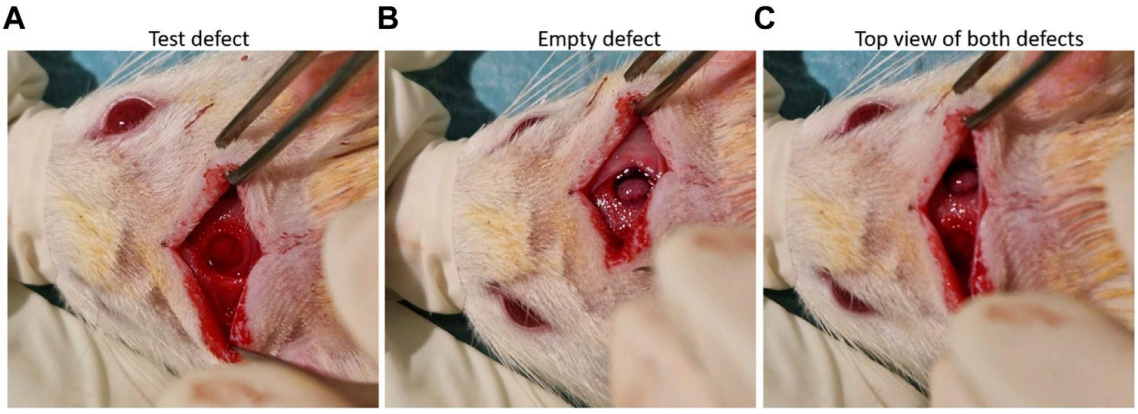

Figure 1. (A) nHA/CS scaffold implant, (B) view of the empty defect, and (C) both defects created in the rat calvaria.

After recovery, the rats were caged in pairs and allowed to move without restriction. They were fed with commercial rat chow and water for 3 months *ad libitum*. After the required period, the animals were euthanized with carbon dioxide asphyxiation.

2.4.2. Histology Analysis

All samples were explanted and fixed in 10 % neutral buffered formalin for 3 days and then processed for histology (Paraffin Tissue Processor Microm STP 120-1, Thermo Fisher Scientific, Waltham, MA, United States). Fixed samples were decalcified according to manufacturer's instructions (Shandon TBD-1™ Decalcifier, Thermo Fisher Scientific, Waltham, MA, United States), embedded in paraffin according to manufacturer's instructions (Modular Embedding System Microm, Thermo Fisher Scientific, Waltham, MA, United States), and sectioned transversally into 5 µm-thick slices (Paraffin Microtome Microm HM335E, Thermo Fisher Scientific, Waltham, MA, United States) and stained with hematoxylin and eosin, while the longitudinal sections were stained with Masson's Trichrome and Alizarin Red S (calcium deposition) for light microscopy examination.

2.5. Statistical Analysis

Data were presented as the mean and standard deviation and analyzed using the two-way ANOVA test for *in vitro* experiments and one-way ANOVA for *in vivo* experiments (GraphPAD

software, Insight Venture Partners, New York City, NY, United States). Differences between groups and time points were considered statistically significant when $p < 0.05$.

3. RESULTS

3.1. *In vitro* evaluation

DFMSCs were seeded into nHAp/CS and CS scaffolds and evaluated after 7, 14 and 21 days (Figure 2A). Few cells were observed in both materials after 7 and 14 days. However, on day 21, both scaffolds showed a statistically higher cell number (4-fold cellular increase). Protein content increased from day 7 to 14, being approximately stable afterward (Figure 2B). ALP activity increased throughout the culture time, and on day 21, values were significantly higher than those measured on days 7 and 14 (Figure 2C). The three parameters were similar in nHAp/CS and CS scaffolds thoughout the evaluation time.

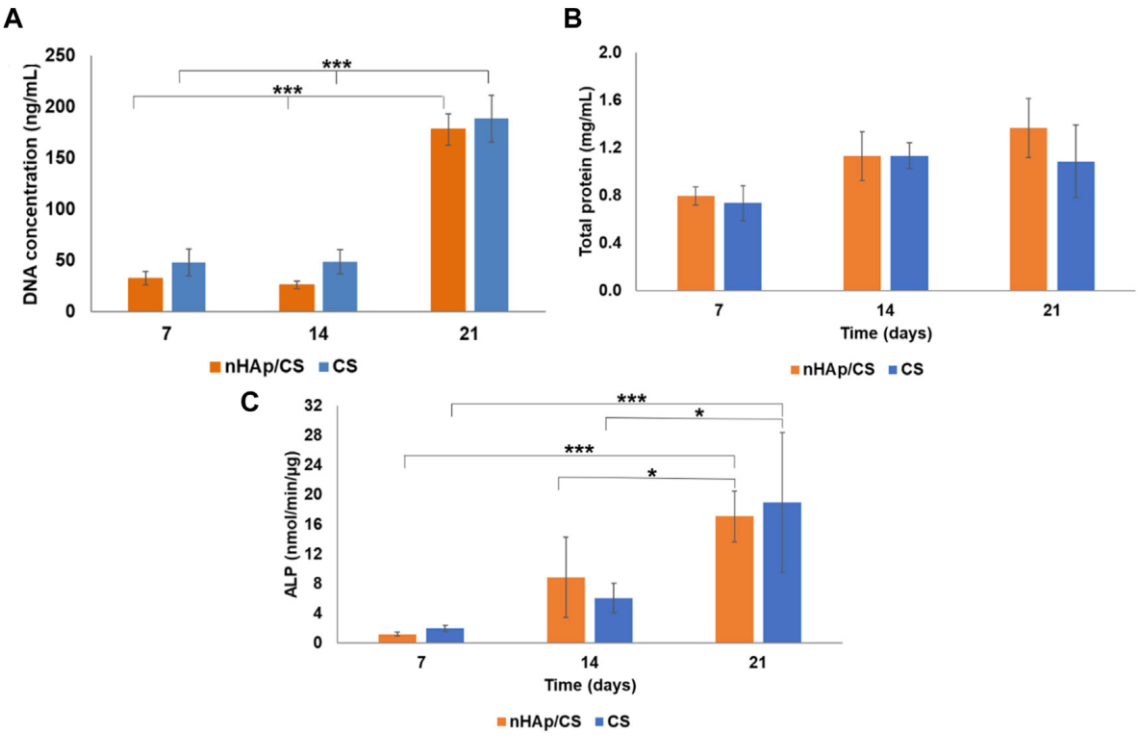

Figure 2. (A) Total DNA content, (B) total protein, and (C) ALP activity of DFMSCs cultured within nHAp/CS biocomposite and CS scaffolds for 7, 14, and 21 days. Statistical differences between samples from different time points. *$p < 0.05$ and ***$p < 0.001$.

The results obtained for the expression of the osteopontin (OPN), Osterix (SP7), bone morphogenetic protein 2 (BMP-2), and collagen 1 (Col-1) on days 14 and 21 of culture are shown in Figure 3. Cultures performed within the nHAp/CS scaffold presented a significantly higher

expression of SP7 (coding for Osterix) (Figure 3A) and OPN (Figure 3C) when compared to the gene expression of cells in the CS scaffold and the control. The gene expression increased approximately 4-fold for SP7 and 5-fold for OPN on day 14. At day 21, the high expression of these genes in nHAp/CS was maintained, i.e., 5-fold for SP7 and 7.5-fold for OPN. The expression of BMP-2 was similar to the undifferentiated DFMSCs' expression for all materials and control for both time-points. Col-1 expression was similar for both biomaterials after 14 days and decreased on day 21, but both scaffolds were statistically different from the control throughout the time (Figure 3B).

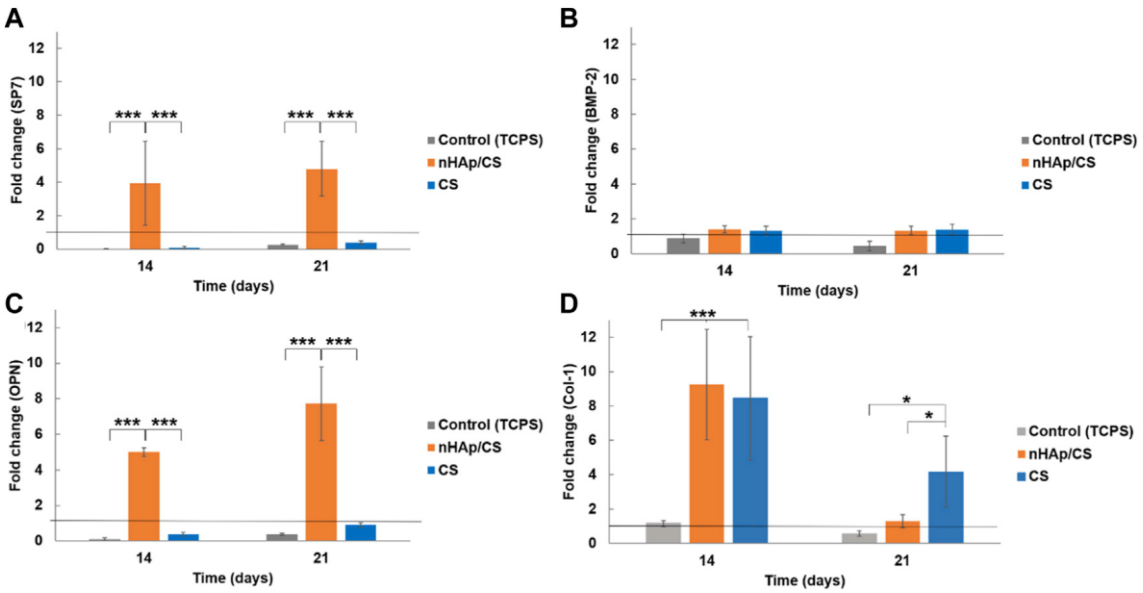

Figure 3. Quantitative real-time polymerase chain reaction (qPCR) for the osteogenic genes (Osterix gene, SP7 (A); bone morphogenetic protein 2, BMP-2 (B); osteopontin, OPN (C); and collagen 1, Col-1 (D) for DFMSCs cultured within the nHAp/CS or CS scaffolds for 14 and 21 days. Quantitative data were calculated by the ΔΔCt method using GAPDH gene expression as an endogenous reference. Sample results were normalized to the 2D (standard culture plate, black horizontal line) cultured cells (average results). These are represented as fold changes. Statistical analysis: *p < 0.05 and ***p < 0.001.

The cellular morphology and the human proteins secreted by DFMSCs were evaluated by the immunostaining of cytoplasmic actin and OPN after 14 and 21 days of culture within the scaffolds. Results are shown in Figure 4. Cultures stained for the actin cytoskeleton showed low cell colonization within both scaffolds at day 14, appearing mostly as cellular aggregates (Figures 4A and D). Images of the 21st day of culture showed a higher number of cells in the nHAp/CS scaffolds (Figure 4B) when compared to CS scaffold (Figure 4E). Furthermore, cells exhibited higher cell volume, a well-identified nucleus, and cytoplasm, and cell colonization was visible throughout the composite scaffold (Figure 4B), when compared to CS samples (Figure 4E).

The osteopontin deposition on the 21st day of culture showed a larger amount of this protein over the nHAp/CS scaffold surface than that over CS scaffolds (Figures 4C and F). These results corroborate the OPN gene expression showed in Figure 3.

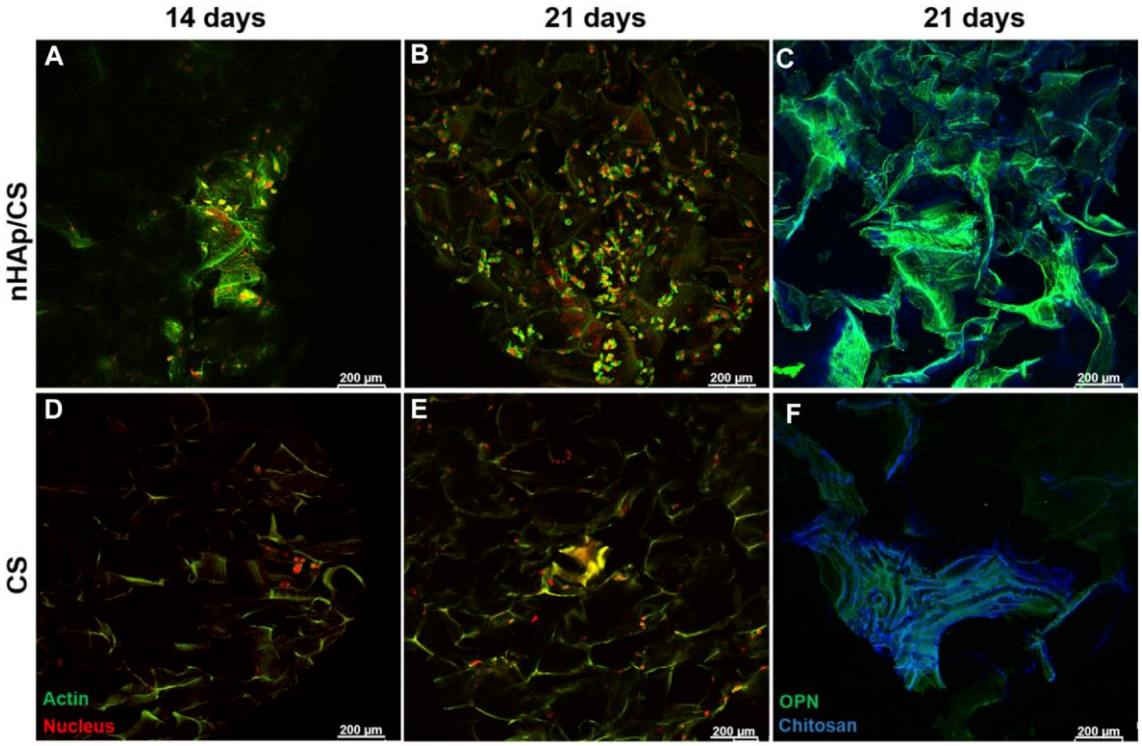

Figure 4. CLSM images showing the DFMSC morphology (staining for actin cytoskeleton and nucleus (A, B, D, E)) and human osteogenic ECM (staining for OPN; (C, F)) after 14 and 21 days of culture within the nHAp/CS or CS scaffold. Actin cytoskeleton, OPN (green), and nucleus (red); blue staining refers to chitosan autofluorescence. Scale bar: 200 µm.

3.2. *In vivo* evaluation

3.2.1. MicroCT quantitative analysis

nHAp/CS and CS scaffolds were implanted in a calvarial bone critical defect model, and *in vivo* microCT imaging was performed after 3 days and 1, 2, and 3 months (Figure 5A). Two animals died after surgery, and a total of ten animals underwent microCT scans. Quantitative analysis was further displayed, and the BV was significantly higher in the nHAp/CS group than in the CS group: 1.23 mm^3 (BV/TV: 6.69 %; BS: 40.3 mm^2) *versus* 0.19 mm^3 (BV/TV: 1.15 %; BS: 5.0 mm^2), 2.18 mm^3 (BV/TV: 11.88 %: BS: 42.6 mm^2) *versus* 0.41 mm^3 (BV/TV: 2.46 %; BS: 8.3 mm^2), and 1.81 mm^3 (BV/TV: 9.84 %; BS: 32.5 mm^2) *versus* 0.57 mm^3 (BV/TV: 3.41 %; BS: 9.7 mm^2), respectively, after 1, 2 and 3 months (Figures 5B, C and D).

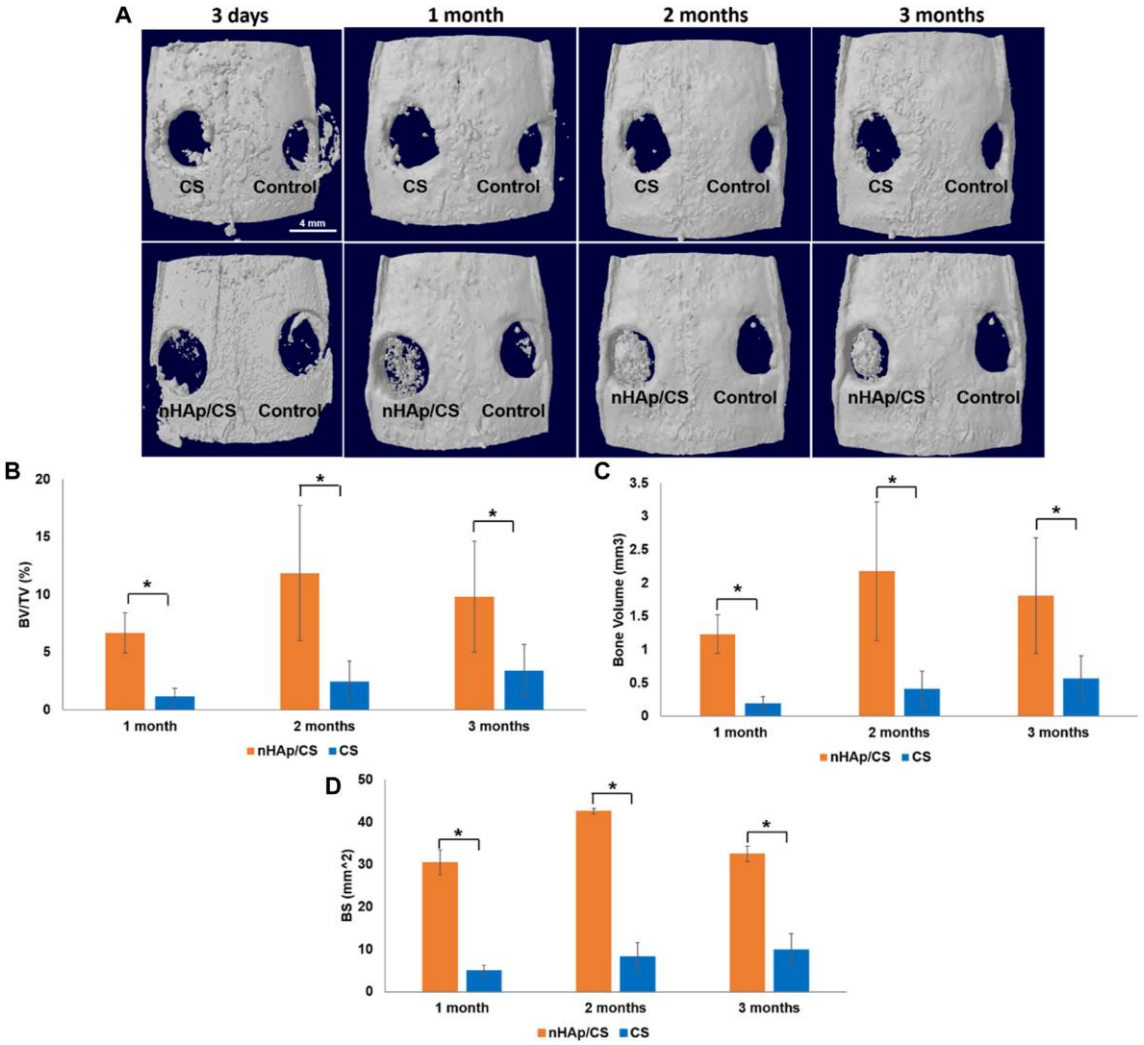

Figure 5. (A) Top defect views of 3D reconstructed microCT image analysis showing the degree of bone repair in empty defects (control), nHAp/CS and CS scaffolds implanted into the rat calvaria after 3 days and 1, 2, and 3 month post-surgery (scale bar 4 mm). (B) Quantitative microCT data analysis of the bone level/tissue level ratio (%). (C) Quantitative microCT data analysis of bone volume (mm^3). (D) Quantitative microCT data analysis of the bone surface (mm^2). Statistical analysis: $*p < 0.05$.

3.2.2. Histological analysis

Figure 6 shows one set of representative ground sections per group of the calvarial defect, corresponding to the median transversal slices (stained by H&E) of nHAp/CS (a), CS (b) and control (empty bone defect (c)), in terms of bone regeneration, that were in accordance with the microCT analysis. Higher bone formation was also observed inside the nHAp/CS scaffolds and in the surrounding tissue (defect borders) (Figure 6A). On the contrary, bone formation was observed only around the CS scaffolds after 3 months (Figure 6B). The empty bone defect in the control group was mainly filled by connective tissue (Figure 6C). The qualitative imaging analysis

revealed that in the central compartment of the defect, the bone formation area was significantly higher in the nHAp/CS group than in the CS group and control (empty defect) (Figure 6).

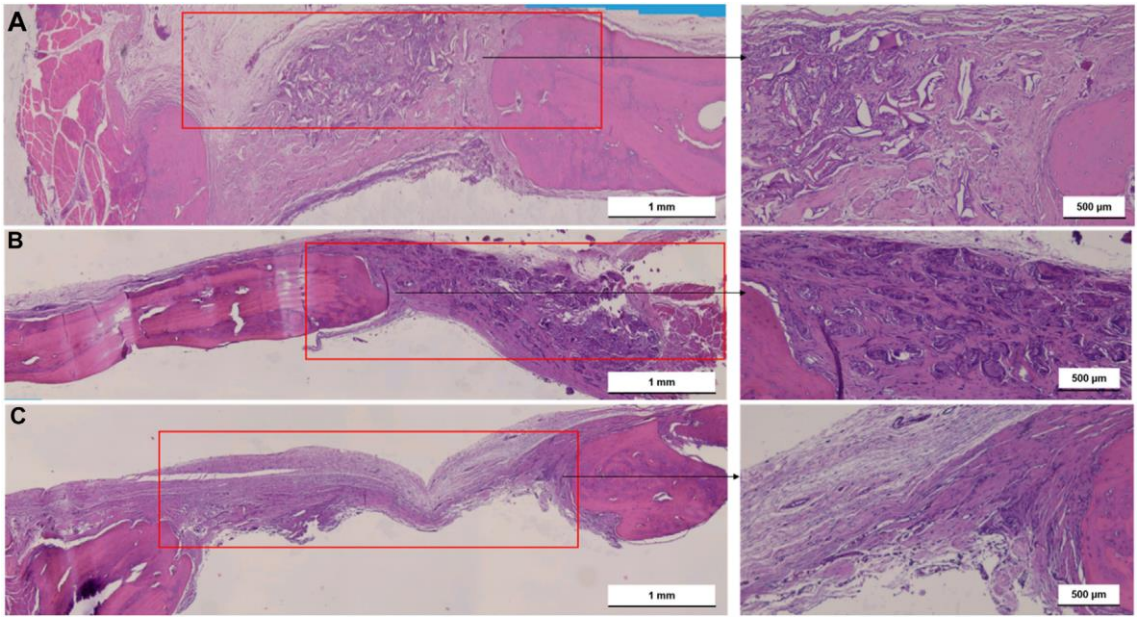

Figure 6. Light microscopy images of nHAp/CS (A), CS (B) scaffolds implanted for 3 months and empty bone defects as control (C). Transversal slides were stained by H&E. Scale: 500 µm and 1 mm. Red square, bone defect.

High bone formation inside the nHAp/CS was confirmed by the longitudinal section, (stained by Masson's Trichome, Figures 7A and B). The fibers of the original scaffold structure (dark pink) were either surrounded by the new bone or soft tissue. This new bone formed trabecular ridges with random orientation, and it was enclosed by thin layers of parallel-trabecular bone. On the contrary, fibrous tissue with random collagen orientation could be observed inside the CS scaffold (Figures 7C and D, dark blue color).

The longitudinal slides of the external parietal bone in Figure 8 (stained by Alizarin Red S) show that the deposition of calcium was only visible around the nHAp/CS biomaterial (Figure 8B) since no calcium deposition was observed in the CS scaffolds (Figure 8A).

4. DISCUSSION

The present work compared the osteogenic potential of nHAp/CS with that of CS bioaerogel scaffolds, as possible graft biomaterials to fill bone defects in low-load-bearing sites such as in periodontal and peri-implant regenerative treatments. The scaffolds' composition and surface properties are key factors in achieving bone tissue regeneration with adequate MSC osteogenic differentiation [37]. However, MSC isolation for *in vitro* testing usually requires an invasive surgical procedure. Furthermore, MSCs experience a progressive decline in

regenerative and differentiation capacities with aging [38]. To overcome these limitations, human dental MSCs, in particular follicle-derived MSCs, have received increased interest in the field of regenerative medicine since they can be isolated from unerupted and impacted teeth, which are usually discarded as a dental medical waste, with no extra surgery being required, providing economic value for waste-derived tissue [39]. Furthermore, these neural crest-originated cells have other advantages such as high viability and proliferation rate [40], active self-renewal capability, immunomodulatory properties, feasible cryopreservation, and absence of ethically related issues [8, 41]. DFMSCs also have a multipotent differentiation capacity with high pluripotency and plasticity, since they can differentiate into osteoblasts, chondrocytes, adipocytes, neuronal cells, and different dental cells such as periodontal ligament (PDL)-type lineages [42]. Therefore, DFMSCs have strong osteogenic capability to differentiate into the osteoblastic lineage [43]. Graziano *et al.* (2008) [44] confirmed that dental MSCs are a promising source for bone tissue regeneration regarding their high capacity to adhere to biomaterial surfaces.

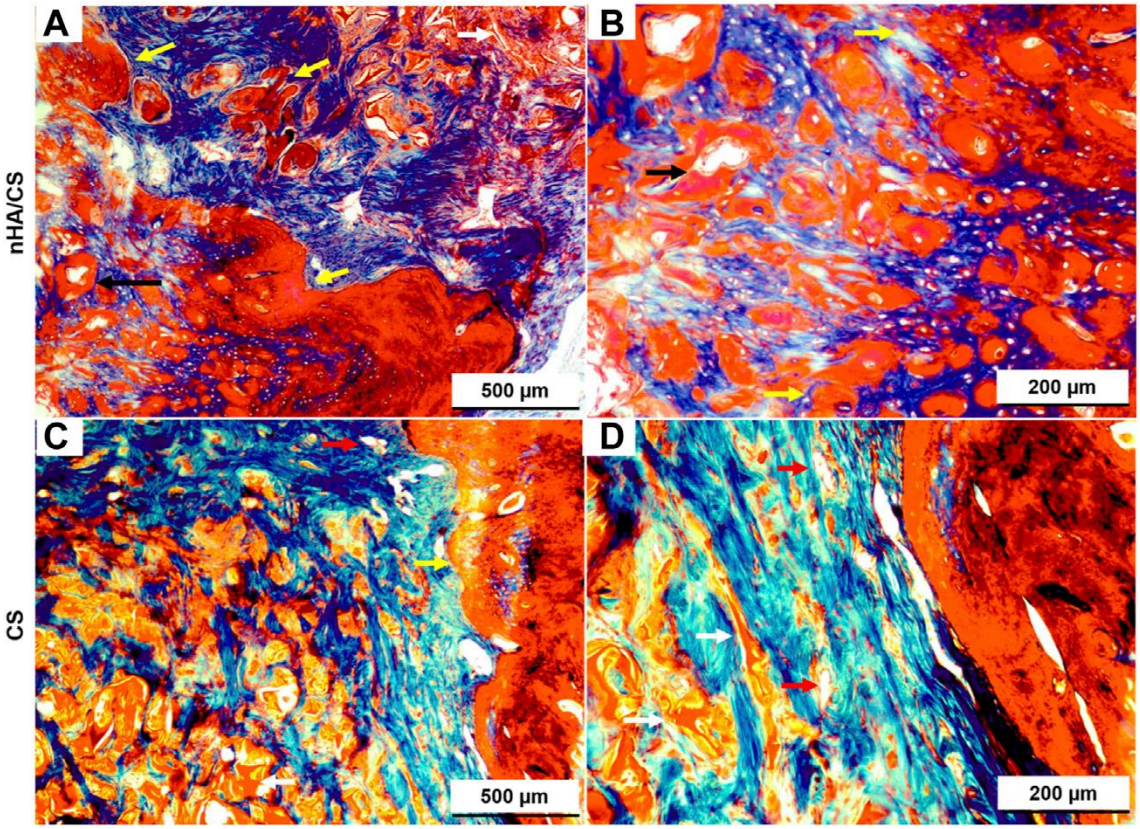

Figure 7. Light microscopy images of nHAp/CS (A, B) and CS (C, D) scaffolds implanted for 3 months. Longitudinal slides were stained using Masson's trichome. Scale: 500 and 200 µm. White arrows, scaffolds; black arrows, blood vessels; and yellow arrow, new bone tissue.

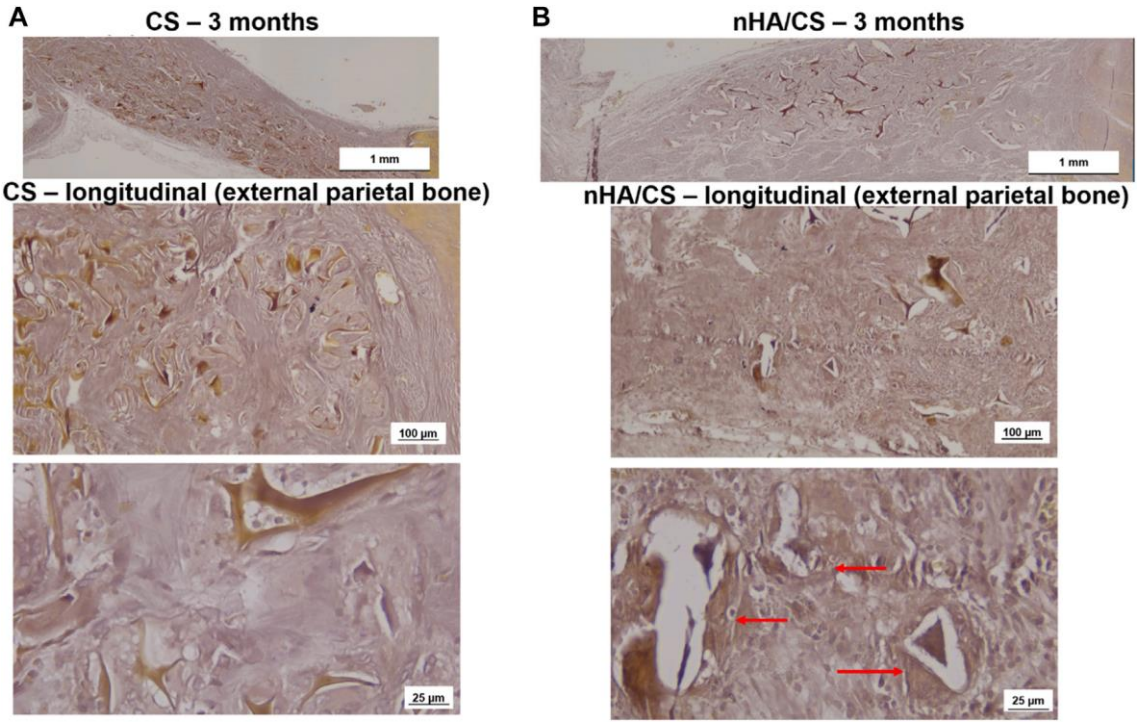

Figure 8. Light microscopy images of CS (A) and nHAp/CS (B) scaffolds implanted for 3 months. Longitudinal slides (external parietal bone) were stained using Alizarin Red S. Scale: 1mm, 100 µm, and 25 µm. Red arrows, calcium deposition circumventing the nHAp/CS biomaterial.

The DNA quantitative analysis is a simple and accurate *in vitro* test that quantifies the number of cells in a sample and gives a glimpse of the cellular proliferation rate. The higher the DNA concentration, the higher the cell number and, subsequently, the higher proliferation rate. The DFMSCs cultured into nHAp/CS or CS scaffolds displayed similar DNA concentration, which significantly increased during long culture times, i.e., on day 21, and appeared to be a consequence of the cell aggregation observed at the lower time points (on days 7 and 14), as confirmed by CLSM images. The initial lower proliferation rate (on days 7 and 14) could be explained by the CS surface characteristics. The positive surface charge arising from protonated amino groups in CS is known to predict cell adhesion. The lack of negatively charged groups on the CS surface for interactions with the positively charged amino groups of proteins could be the reason for the poor cell adhesion, on chitosan membranes, as reported previously by Reis and co-workers [45, 46] and other authors [47-49].

The presence of bioceramic nanoparticles in bone scaffolds has been shown to provide excellent bioactivity, which promotes bone tissue development [50]. During regeneration of mineralized tissues such as bone, the mineralization processes are triggered by the presence of other negatively charged groups, the phosphate groups. The importance of these groups has been recognized by the biomaterial research community for a long time, and calcium phosphate materials are commonly used in bone regenerative medicine. This was our hypothesis, although, the CS matrix covered the HAp nanoparticles and its low degradation rate would allow the release of the ceramic only after 14 days since the cell behavior changed after 14 days. This new

hypothesis is in accordance with the results of the ALP enzyme activity that increased only after the 14th day. ALP is highly expressed in the cells of mineralized tissues and, *in vitro*, its activity is higher in the initial phases of the osteoblastic differentiation process [51]. In the present work, the DFMSCs' ALP activity was similar in both materials, as was the expression of the BMP-2 gene. The activation of the BMP-2 signaling pathway shall control the ALP expression and lead to osteoblast differentiation and higher ALP activity [51]. The upregulation of BMP-2 could be induced by N-acetylglucosamine (the degradation product of CS), which promotes osteoblast activity and an increase in the expression of BMPs [52]. The total protein content was quantified to provide information on the ECM production, which also showed an increased tendency until day 21 (not statistically different) with the nHA/CS scaffold, demonstrating again the DFMSCs differentiation. Instead of the total protein content, another parameter that could influence cell differentiation is the increase in one of bone ECM's components, osteopontin, after 14 and 21 days. At those time-points, fluorescence microscopy observations showed DFMSC images showing spindle-like morphologies within the porous structure of the nHAp/CS scaffold, which shows that the surface's chemical composition, topography, and energy are more favorable for osteoconduction than the plain CS scaffold (Figure 4). Pitrolino *et al.* (2022) also achieved a higher number of cells attached to the nHAp/CS scaffold surface, while at the CS-only scaffold, the cells exhibited clusters with a more rounded morphology [19]. Bozorgi *et al.* (2022) reported that a favorable Saos-2 cell morphology (with extended filopodia) was observed after seeding those pre-osteoblast cells on a nHAp/CS/Gel scaffold for 3 days of analysis [24]. Zhang *et al.* (2019) also tested hDPMSCs seeded on their chitosan/poly (γ-glutamic acid)/hydroxyapatite (CPH) hydrogel (or without HAp) scaffolds. They found that besides an increase in the metabolic activity from 24 to 72 h, the cells showed a polygonal morphology and spread with multiple filopodia contacts during microscopy observation [42]. The presence of bioactive ceramics serves as topographical cues, promoting cellular interaction with the biomimetic surface of the scaffold and allowing focal cell adhesions, which not only enhance adhesion itself but also the formation of filopodia and cellular spreading and, consequently, osteointegration [31]. The results from previous work with the nHAp/CS scaffold showed that apatite crystals start to precipitate *in vitro* upon the surface after 7 days of incubation in SBF, evolving into needle-like crystals after 21 days [30], which also explains the delay in DFMSCs attachment and proliferation.

Our qPCR results are expressed as a function of the fold change (FC), which relates gene expression obtained for each scaffold and by the control (cells cultured in 2D conditions, i.e., the standard culture plate). Thus, an FC greater than 1 implies that gene expression is greater than in the control. Therefore, qPCR results also clearly showed that the nHAp/CS biocomposite triggered higher cellular differentiation, as evidenced by the observed osteoblastic gene expression profile and OPN immunostaining of the colonized scaffolds. Thus, DFMSCs cultured into the nHAp/CS composite displayed significantly higher expression of SP7 and OPN genes. The SP7 gene is associated with the osteoblastic phenotype, being the gene coding for the late osteogenic transcription factor Osterix. This factor regulates and induces the expression of a set of mature osteoblastic genes coding for the synthesis of late ECM proteins involved in terminal

osteoblastic differentiation, including OPN [53]. OPN is a major non-collagenous ECM structural protein, being part of the organic component of bone. Its expression mainly occurs in osteoblastic-lineage cells, and it is expected to be associated with the induction of osteogenic differentiation. A study showed that the presence of OPN in the material played a vital role in the recruitment of MSCs during tissue regeneration [54], as well as promoting cellular differentiation into the early pre-osteoblast phenotype [55]. Furthermore, CLSM images of the colonized nHAp/CS and CS samples clearly evidenced a significantly higher OPN deposition in the composite bioaerogel. It appears that OPN binds tightly to hydroxyapatite (HAp) and seems to form an integrated part of the mineralized matrix. In the bone repair process, hydroxyapatite plays a key role in the proliferation of osteoblasts [56]. In addition, CS contributes to osteoblast differentiation and bone healing [57]. Control cells, corresponding to DFMSCs at passage 6 seeded in a 24-well tissue culture plate, were harvested at day 0 for the RNA isolation and purification assays. In this passage, Costa *et al.* (2023) showed that the MSCs maintain the mesenchymal phenotype, and the $2^{-\Delta\Delta CT}$ method was used as a normalizer for osteogenic gene expression (value 1 in the graphs, Figure 3) [55]. Since DFMSCs in osteoinductive medium/biomaterials were able to start differentiation after 14 and 21 days (shown by the increased expression of those osteogenic genes), they showed the osteoblast phenotype. A 2D control was added to the qPCR analysis for 14 and 21 days to provide additional information about the difference in gene expressions of DFMSCs cultured at 2D or 3D, as also shown in a previous work (Figure 3 of supplementary results of Salgado and co-workers [10]). The control (2D) results were similar to or below 1 in Figure 3B or 3D, indicating that the cells were still expressing the mesenchymal phenotype and did not start to differentiate to the osteoblast phenotype.

The *in vivo* experiments of this research were performed in a well-established small animal model (the calvaria of Wistar rats), as a proof-of-concept of the osteogenic potential of the nHAp/CS bioaerogel before proceeding into more complex bone defects such as those found in the periodontal context. Creating that kind of critical-sized defects in small animal models such as the rat would be visually challenging and could result in iatrogenic lesions such as tooth necrosis, compromising the masticatory function and causing unnecessary morbidity to the animals [58, 59]. Therefore, it was possible to create two critical-size defects in each animal, allowing for a decrease in the number of animals used in a site (calvaria) subjected to relatively low loads. When considering the histologic section and microCT, some of the newly formed bone was located inside and outside the defect margin and within the space created by the scaffold into the defect area. Similar results were shown by Strauss and collaborators with collagen membrane implants [60]. The bone regeneration was significantly advanced in the nHAp/CS group compared to the CS and control groups (empty defect). Interestingly enough, CS had no impact on bone formation, but served just as a template for cell proliferation [61], but nHAp adsorbs proteins and other biomolecules, releasing calcium and phosphate ions, acting as an osteoconductive carrier [62]. This osteoconductive activity is supported by the regeneration pattern displayed in the microCT images, suggesting that the nHAp/CS scaffold is not a passive porous material, as it was observed with the CS scaffold. Another study using polymeric gel

showed in the histological examination that there was a tendency for new bone to be formed near the cranial dura matter side of the bone defect, above the site where new blood vessels were formed [63]. Similar bone tissue growth was observed with nHAp/CS implants by microCT images (inner bone formation, Figure 5A) and histology, where newly formed vessels surrounded by mineralized tissue (early angiogenesis, Figure 6A; Figure 7B) being promoted by the biocomposite would also contribute to bone regeneration. These observations, together with the histological analysis (Masson trichrome staining), suggested that the bone regeneration was not restricted to the area of the scaffold modified with nHAp, but it was also observed in the borders of the bone defect, and in the absence of the nanoparticles, the biomaterial is full filled with scar tissue (CS scaffold and empty defect control). Taken together, these findings show that nHAp presence in the scaffold composition plays an important role in the neo-formation of a mineralized ECM and induced bone formation in a rat calvarial critical defect model. Cao *et al.* (2022) also observed higher bone growth for their CS/nHAp scaffold after 3 months [25]. Chatzipetros *et al.* (2021) observed a significantly higher fraction of bone regeneration (FBR) from the second to the eight week for the HAp/CS 75/25 w/w scaffolds (19.96 % vs 42.13 %) than for empty controls (14.88 % vs 15.98 %), after histomorphometry evaluation of the bilateral 5 mm defects on rat calvaria [64]. The chitosan/poly (γ-glutamic acid) (CP) scaffolds, reinforced or not with hydroxyapatite (CPH) and enriched with platelet-rich fibrin (CPH-PRF), developed by Zhang *et al.* (2019) were first tested in 5 mm calvaria defects in rats, and by the eight week, all groups showed a large amount of newly formed bone, though the CPH−PRF group exhibited a significantly higher bone repair effect (mean integrated density of ~70 % of control, evaluated by microCT) [28].

It has been reported that the porous structure of the CS scaffold, particularly after lyophilization, provided lower mechanical stability, having a negative impact on bone regeneration [65]. Therefore, the combination of CS with nHAp resulted in a reinforced structure, increasing its potential to successfully promote bone cells and MSC proliferation and differentiation, allowing bone tissue growth within the bone defect site [66]. However, in a previous study, we observed that both the nHAp/CS and CS scaffolds implanted in subcutaneous pockets in mice showed stable structures after 5 weeks post-implantation, probably due to the high deacetylation degree of the CS used to produce the bioaerogels [30]. As can be observed in the histologic images (Figures. 6-8), even at 3 months post-surgery, the structures of both scaffold types are still visible.

Despite the advantages of the nHAp/CS scaffold demonstrated in the present work, there are still more specific experiments that would be necessary in order to achieve alveolar bone regeneration, such as additional studies on the bioaerogel antimicrobial effect against anaerobic oral bacteria species and periodontopathogens in particular. It would also be important to evaluate, *in vitro*, the nHAp/CS scaffold angiogenic potential and to create defects in the alveolar bone in *in vivo* experiments with larger animal models to study more reliably the clinical application of the nHAp/CS scaffolds in order to achieve a bone graft biomaterial suitable for clinical use in the field of periodontology.

5 CONCLUSION

This work showed encouraging *in vitro* and *in vivo* results obtained with the nHAp/CS scaffolds produced with a low environment impact and an eco-friendly process. The study supported that the nHAp/CS bioarogel increased the *in vitro* differentiation of DFMSCs into bone-like cells when compared to the CS-only bioaerogel. The nHAp/CS scaffold also showed *in vivo* bone tissue ingrowth over time, leading to higher critical defect fulfillment compared to empty and CS-filled defects, as reported by the longitudinal microCT analysis. Therefore, the bioaerogel showed that it could be an innovative biodegradable bone graft to be applied in low-load-bearing sites such as those found in periodontal and peri-implant bone defects. Future research efforts should focus on further exploring and developing the nHAp/CS scaffold as an alternative material for guiding alveolar bone tissue regeneration *in vivo* in periodontal and peri-implant bone defects since it was able to promote DFMSC osteogenic differentiation.

Data availability statement

The original contributions presented in the study are included in the article/Supplementary Material; further inquiries can be directed to the corresponding author.

Ethics statement

The studies involving humans were approved by the Ethical Committee of the University of Porto. The studies were conducted in accordance with the local legislation and institutional requirements. The participants provided their written informed consent to participate in this study. The animal study was approved by i3S Animal Ethics Committee (CEA–Comissão de Ética Animal) and licensed by the Direcção Geral de Alimentação e Veterinária (DGAV). The study was conducted in accordance with the local legislation and institutional requirements.

Author contributions

MS-L: data curation, formal analysis, investigation, validation, visualization, and writing–original draft. LG: methodology, validation, visualization, and writing–review and editing. YM: methodology and writing–review and editing. MD: funding acquisition, project administration, resources, validation, visualization, and writing–review and editing. JL: funding acquisition, project administration, resources, validation, visualization, and writing–review and editing. MF: funding acquisition, methodology, project administration, supervision, validation, visualization, and writing–review and editing. FM: funding acquisition, project administration, validation, visualization, and writing–review and editing. CS: conceptualization, funding acquisition, methodology, project administration, supervision, validation, visualization, and writing–review and editing.

Funding

The author(s) declare that financial support was received for the research, authorship, and/or publication of this article. This article was supported by UIDB/50020/2020 and UIDP/50020/2020 (LSRE-LCM), and by LA/P/0045/2020 (ALiCE), funded by national funds through FCT/MCTES (PIDDAC). The last author, CS, gratefully acknowledges FCT/MCTES (Fundação para a Ciência e a Tecnologia) for financial support (CEECINST/00091/2018/CP1500/CT0019).

Acknowledgments

The histology analysis was performed at the HEMS core facility at i3S, University of Porto, Portugal, with the assistance of Rossana Correia and Cláudia Machado. The authors acknowledge the i3S Scientific Platform Bioimaging and HEMS, both members of the national infrastructure PPBI—Portuguese Platform of Bioimaging (PPBI-POCI-01-0145-FEDER-022122), the support of the i3S Scientific Platform Cell Culture and Genotyping for the real-time qPCR, and the i3S Scientific Platform Animal Facility for *in vivo* experiments. The graphical abstract was created with BioRender.com (academic license).

Conflict of Interest

The authors declare that the research was conducted in the absence of any commercial or financial relationships that could be construed as a potential conflict of interest.

Publisher's note

All claims expressed in this article are solely those of the authors and do not necessarily represent those of their affiliated organizations, or those of the publisher, the editors, and the reviewers. Any product that may be evaluated in this article, or claim that may be made by its manufacturer, is not guaranteed or endorsed by the publisher.

V. References

[1] Fischer, R. G.; Gomes Filho, I. S.; Cruz, S. S. d.; Oliveira, V. B.; Lira-Junior, R.; Scannapieco, F. A.; Rego, R. O. What is the future of Periodontal Medicine? Braz Oral Res. 2021, 35, doi: 10.1590/1807-3107bor-2021.vol35.0102

[2] Nazir, M.; Al-Ansari, A.; Al-Khalifa, K.; Alhareky, M.; Gaffar, B.; Almas, K. Global prevalence of periodontal disease and lack of its surveillance. Sci World J. 2020, 2020, doi: 10.1155/2020/2146160

[3] Relvas, M.; López-Jarana, P.; Monteiro, L.; Pacheco, J. J.; Braga, A. C.; Salazar, F. Study of prevalence, severity and risk factors of periodontal disease in a Portuguese population. J Clin Med. 2022, 11, 3728. doi: 10.3390/jcm11133728

[4] Tonetti, M. S.; Jepsen, S.; Jin, L.; Otomo-Corgel, J. Impact of the global burden of periodontal diseases on health, nutrition and wellbeing of mankind: A call for global action. J Clin Periodontol. 2017, 44, 456-462. doi: 10.1111/jcpe.12732

[5] Woo, H. N.; Cho, Y. J.; Tarafder, S.; Lee, C. H. The recent advances in scaffolds for integrated periodontal regeneration. Bioact Mater. 2021, 6, 3328-3342. doi: 10.1016/j.bioactmat.2021.03.012

[6] Soares, M. P. C. M.; Soares, P. V.; Pereira, A. G.; Moura, C. C. G.; Soares, P. B. F.; Naves, L. Z.; de Magalhães, D. Biocompatibility of three bioabsorbable membranes assessed in FGH fibroblasts and human osteoblast like cells culture. Head Face Med. 2014, 10, 1-6. doi: 10.1186/1746-160X-10-29

[7] Liu, J.; Wang, L.; Liu, W.; Li, Q.; Jin, Z.; Jin, Y. Dental follicle cells rescue the regenerative capacity of periodontal ligament stem cells in an inflammatory microenvironment. PLoS One. 2014, 9, e108752. doi: 10.1371/journal.pone.0108752

[8] Bi, R.; Lyu, P.; Song, Y.; Li, P.; Song, D.; Cui, C.; Fan, Y. Function of dental follicle progenitor/stem cells and their potential in regenerative medicine: from mechanisms to applications. Biomolecules. 2021, 11, 997. doi: 10.3390/biom11070997

[9] da Silva Meirelles, L.; Fontes, A. M.; Covas, D. T.; Caplan, A. I. Mechanisms involved in the therapeutic properties of mesenchymal stem cells. Cytokine Growth Factor Rev. 2009, 20, 419-427. doi: 10.1016/j.cytogfr.2009.10.002

[10] Salgado, C. L.; Barrias, C. C.; Monteiro, F. J. Clarifying the tooth-derived stem cells behavior in a 3D biomimetic scaffold for bone tissue engineering applications. Front Bioeng Biotechnol. 2020, 8, 724. doi: 10.3389/fbioe.2020.00724

[11] Goimil, L.; Braga, M. E.; Dias, A. M.; Gomez-Amoza, J. L.; Concheiro, A.; Alvarez-Lorenzo, C.; de Sousa, H. C.; Garcia-Gonzalez, C. A. Supercritical processing of starch aerogels and aerogel-loaded poly (ε-caprolactone) scaffolds for sustained release of ketoprofen for bone regeneration. J CO2 Util. 2017, 18, 237-249. doi: 10.1016/j.jcou.2017.01.028

[12] Goimil, L.; Santos-Rosales, V.; Delgado, A.; Evora, C.; Reyes, R.; Lozano-Perez, A. A.; Aznar-Cervantes, S. D.; Cenis, J. L.; Gómez-Amoza, J. L.; Concheiro, A. scCO$_2$-foamed silk fibroin aerogel/poly (ε-caprolactone) scaffolds containing dexamethasone for bone regeneration. J CO2 Util. 2019, 31, 51-64. doi: 10.1016/j.jcou.2019.02.016

[13] Martins, M.; Barros, A. A.; Quraishi, S.; Gurikov, P.; Raman, S.; Smirnova, I.; Duarte, A. R. C.; Reis, R. L. Preparation of macroporous alginate-based aerogels for biomedical applications. J Supercrit Fluids. 2015, 106, 152-159. doi: 10.1016/j.supflu.2015.05.010

[14] Verma, A.; Thakur, S.; Goel, G.; Raj, J.; Gupta, V. K.; Roberts, D.; Thakur, V. K. Bio-based sustainable aerogels: New sensation in CO_2 capture. Curr Res Green Sustain Chem. 2020, 3, 100027. doi: 10.1016/j.crgsc.2020.100027

[15] Zheng, L.; Zhang, S.; Ying, Z.; Liu, J.; Zhou, Y.; Chen, F. Engineering of aerogel-based biomaterials for biomedical applications. Int J Nanomedicine. 2020, 15, 2363-2378. doi: 10.2147/IJN.S238005

[16] Vareda, J. P.; Lamy-Mendes, A.; Durães, L. A reconsideration on the definition of the term aerogel based on current drying trends. Microporous Mesoporous Mater. 2018, 258, 211-216. doi: 10.1016/j.micromeso.2017.09.016

[17] Sehaqui, H.; Zhou, Q.; Berglund, L. A. High-porosity aerogels of high specific surface area prepared from nanofibrillated cellulose (NFC). Compos Sci Technol. 2011, 71, 1593-1599. doi: 10.1016/j.compscitech.2011.07.003

[18] Khan, A.; Alamry, K. A. Recent advances of emerging green chitosan-based biomaterials with potential biomedical applications: A review. Carbohydr Res. 2021, 506, 108368. doi: 10.1016/j.carres.2021.108368

[19] Pitrolino, K. A.; Felfel, R. M.; Pellizzeri, L. M.; McLaren, J.; Popov, A. A.; Sottile, V.; Scotchford, C. A.; Scammell, B. E.; Roberts, G. A.; Grant, D. M. Development and *in vitro* assessment of a bi-layered chitosan-nano-hydroxyapatite osteochondral scaffold. Carbohydr Polym. 2022, 282, 119126. doi: 10.1016/j.carbpol.2022.119126

[20] Sencadas, V.; Correia, D. M.; Ribeiro, C.; Moreira, S.; Botelho, G.; Ribelles, J. G.; Lanceros-Méndez, S. Physical-chemical properties of cross-linked chitosan electrospun fiber mats. Polym Test. 2012, 31, 1062-1069. doi: 10.1016/j.polymertesting.2012.07.010

[21] Levengood, S. K. L.; Zhang, M. Chitosan-based scaffolds for bone tissue engineering. J Mater Chem B. 2014, 2, 3161-3184. doi: 10.1039/C4TB00027G

[22] Qasim, S. B.; Delaine-Smith, R. M.; Fey, T.; Rawlinson, A.; Rehman, I. U. Freeze gelated porous membranes for periodontal tissue regeneration. Acta Biomater. 2015, 23, 317-328. doi: 10.1016/j.actbio.2015.05.001

[23] Ruphuy, G.; Souto-Lopes, M.; Paiva, D.; Costa, P.; Rodrigues, A.; Monteiro, F.; Salgado, C.; Fernandes, M.; Lopes, J.; Dias, M. Supercritical CO_2 assisted process for the production of high-purity and sterile nano-hydroxyapatite/chitosan hybrid scaffolds. J Biomed Mater Res B Appl Biomater. 2018, 106, 965-975. doi: 10.1002/jbm.b.33903

[24] Bozorgi, A.; Mozafari, M.; Khazaei, M.; Soleimani, M.; Jamalpoor, Z. Fabrication, characterization, and optimization of a novel copper-incorporated chitosan/gelatin-based scaffold for bone tissue engineering applications. Bioimpacts. 2022, 12, 233. doi: 10.34172/bi.2021.23451

[25] Cao, S.; Li, Q.; Zhang, S.; Liu, K.; Yang, Y.; Chen, J. Oxidized bacterial cellulose reinforced nanocomposite scaffolds for bone repair. Colloids Surf B Biointerfaces. 2022, 211, 112316. doi: 10.1016/j.colsurfb.2021.112316

[26] Sadeghianmaryan, A.; Naghieh, S.; Yazdanpanah, Z.; Sardroud, H. A.; Sharma, N.; Wilson, L. D.; Chen, X. Fabrication of chitosan/alginate/hydroxyapatite hybrid scaffolds using 3D printing and impregnating techniques for potential cartilage regeneration. Int J Biol Macromol. 2022, 204, 62-75. doi: 10.1016/j.ijbiomac.2022.01.201

[27] Tsiourvas, D.; Sapalidis, A.; Papadopoulos, T. Hydroxyapatite/chitosan-based porous three-dimensional scaffolds with complex geometries. Mater. Today Commun. 2016, 7, 59-66. doi: 10.1016/j.mtcomm.2016.03.006

[28] Zhang, L.; Dong, Y.; Xue, Y.; Shi, J.; Zhang, X.; Liu, Y.; Midgley, A. C.; Wang, S. Multifunctional triple-layered composite scaffolds combining platelet-rich fibrin promote bone regeneration. ACS Biomater Sci Eng. 2019, 5, 6691-6702. doi: 10.1021/acsbiomaterials.9b01022

[29] Zia, I.; Jolly, R.; Mirza, S.; Umar, M. S.; Owais, M.; Shakir, M. Hydroxyapatite Nanoparticles Fortified Xanthan Gum–Chitosan Based Polyelectrolyte Complex Scaffolds for Supporting the Osteo-Friendly Environment. ACS Appl Bio Mater. 2020, 3, 7133-7146. doi: 10.1021/acsabm.0c00948

[30] Souto-Lopes, M.; Grenho, L.; Manrique, Y.; Dias, M. M.; Fernandes, M. H.; Monteiro, F. J.; Salgado, C. L. Full physicochemical and biocompatibility characterization of a supercritical CO_2 sterilized nano-hydroxyapatite/chitosan biodegradable scaffold for periodontal bone regeneration. Biomater Adv. 2023, 146, 213280. doi: 10.1016/j.bioadv.2023.213280

[31] Munir, M. U.; Salman, S.; Ihsan, A.; Elsaman, T. Synthesis, characterization, functionalization and bio-applications of hydroxyapatite nanomaterials: an overview. Int J Nanomedicine. 2022, 1903-1925. doi: 10.2147/IJN.S360670

[32] Zia, I.; Jolly, R.; Mirza, S.; Rehman, A.; Shakir, M. Nanocomposite Materials Developed from Nano-hydroxyapatite Impregnated Chitosan/κ-Carrageenan for Bone Tissue Engineering. ChemistrySelect. 2022, 7, e202103234. doi: 10.1002/slct.202103234

[33] Palmer, L. C.; Newcomb, C. J.; Kaltz, S. R.; Spoerke, E. D.; Stupp, S. I. Biomimetic systems for hydroxyapatite mineralization inspired by bone and enamel. Chem Rev. 2008, 108, 4754-4783. doi: 10.1021/cr8004422

[34] Bieback, K.; Kuçi, S.; Schäfer, R. Production and quality testing of multipotent mesenchymal stromal cell therapeutics for clinical use. Transfusion. 2019, 59, 2164-2173. doi: 10.1111/trf.15252

[35] Dominici, M.; Le Blanc, K.; Mueller, I.; Slaper-Cortenbach, I.; Marini, F.; Krause, D.; Deans, R.; Keating, A.; Prockop, D.; Horwitz, E. Minimal criteria for defining multipotent mesenchymal stromal cells. The

International Society for Cellular Therapy position statement. Cytotherapy. 2006, 8, 315-317. doi: 10.1080/14653240600855905

[36] Daley, G. Q.; Hyun, I.; Apperley, J. F.; Barker, R. A.; Benvenisty, N.; Bredenoord, A. L.; Breuer, C. K.; Caulfield, T.; Cedars, M. I.; Frey-Vasconcells, J. Setting global standards for stem cell research and clinical translation: the 2016 ISSCR guidelines. Stem cell reports. 2016, 6, 787-797. doi: 10.1016/j.stemcr.2016.05.001

[37] Granz, C. L.; Gorji, A. Dental stem cells: The role of biomaterials and scaffolds in developing novel therapeutic strategies. World J Stem Cells. 2020, 12, 897. doi: 10.4252/wjsc.v12.i9.897

[38] Oh, J.; Lee, Y. D.; Wagers, A. J. Stem cell aging: mechanisms, regulators and therapeutic opportunities. Nat Med. 2014, 20, 870-880. doi: 10.1038/nm.3651

[39] Rezai-Rad, M.; Bova, J. F.; Orooji, M.; Pepping, J.; Qureshi, A.; Del Piero, F.; Hayes, D.; Yao, S. Evaluation of bone regeneration potential of dental follicle stem cells for treatment of craniofacial defects. Cytotherapy. 2015, 17, 1572-1581. doi: 10.1016/j.jcyt.2015.07.013

[40] Patil, R.; Kumar, B. M.; Lee, W.-J.; Jeon, R.-H.; Jang, S.-J.; Lee, Y.-M.; Park, B.-W.; Byun, J.-H.; Ahn, C.-S.; Kim, J.-W. Multilineage potential and proteomic profiling of human dental stem cells derived from a single donor. Exp Cell Res. 2014, 320, 92-107. doi: 10.1016/j.yexcr.2013.10.005

[41] Mori, G.; Ballini, A.; Carbone, C.; Oranger, A.; Brunetti, G.; Di Benedetto, A.; Rapone, B.; Cantore, S.; Di Comite, M.; Colucci, S. Osteogenic differentiation of dental follicle stem cells. Int J Med Sci. 2012, 9, 480. doi: 10.7150/ijms.4583

[42] Zhang, J.; Ding, H.; Liu, X.; Sheng, Y.; Liu, X.; Jiang, C. Dental follicle stem cells: tissue engineering and immunomodulation. Stem Cells Dev. 2019, 28, 986-994. doi: 10.1089/scd.2019.0012

[43] Morsczeck, C. Mechanisms during osteogenic differentiation in human dental follicle cells. Int J Mol Sci. 2022, 23, 5945. doi: 10.3390/ijms23115945

[44] Graziano, A.; d'Aquino, R.; Papaccio, G.; Laino, G. Dental pulp stem cells: a promising tool for bone regeneration. Stem Cell Rev. 2008, 4, 21-26. doi: 10.1007/s12015-008-9013-5

[45] López-Pérez, P. M.; Marques, A. P.; da Silva, R. M.; Pashkuleva, I.; Reis, R. L. Effect of chitosan membrane surface modification via plasma induced polymerization on the adhesion of osteoblast-like cells. J Mater Chem. 2007, 17, 4064-4071. doi: 10.1039/B707326G

[46] Silva, S. S.; Luna, S. M.; Gomes, M. E.; Benesch, J.; Pashkuleva, I.; Mano, J. F.; Reis, R. L. Plasma surface modification of chitosan membranes: characterization and preliminary cell response studies. Macromol Biosci. 2008, 8, 568-576. doi: 10.1002/mabi.200700264.

[47] Chung, T.-W.; Lu, Y.-F.; Wang, S.-S.; Lin, Y.-S.; Chu, S.-H. Growth of human endothelial cells on photochemically grafted Gly–Arg–Gly–Asp (GRGD) chitosans. Biomaterials. 2002, 23, 4803-4809. doi: 10.1016/s0142-9612(02)00231-4

[48] Cuy, J. L.; Beckstead, B. L.; Brown, C. D.; Hoffman, A. S.; Giachelli, C. M. Adhesive protein interactions with chitosan: Consequences for valve endothelial cell growth on tissue-engineering materials. J Biomed Mater Res A. 2003, 67, 538-547. doi: 10.1002/jbm.a.10095

[49] Li, J.; Yun, H.; Gong, Y.; Zhao, N.; Zhang, X. Investigation of MC3T3-E1 cell behavior on the surface of GRGDS-coupled chitosan. Biomacromolecules. 2006, 7, 1112-1123. doi: 10.1021/bm050913r

[50] Lemos, R.; Maia, F. R.; Reis, R. L.; Oliveira, J. M. Engineering of Extracellular Matrix-Like Biomaterials at Nano-and Macroscale toward Fabrication of Hierarchical Scaffolds for Bone Tissue Engineering. Adv NanoBiomed Res. 2022, 2, 2100116. doi: 10.1002/anbr.202100116

[51] Vimalraj, S. Alkaline phosphatase: Structure, expression and its function in bone mineralization. Gene. 2020, 754, 144855. doi: 10.1016/j.gene.2020.144855

[52] Nagel, A. K.; Schilling, M.; Comte-Walters, S.; Berkaw, M. N.; Ball, L. E. Identification of O-linked N-acetylglucosamine (O-GlcNAc)-modified osteoblast proteins by electron transfer dissociation tandem mass spectrometry reveals proteins critical for bone formation. Mol Cell Proteomics. 2013, 12, 945-955. doi: 10.1074/mcp.M112.026633

[53] Liu, Q.; Li, M.; Wang, S.; Xiao, Z.; Xiong, Y.; Wang, G. Recent advances of osterix transcription factor in osteoblast differentiation and bone formation. Front Cell Dev Biol. 2020, 8, 601224. doi: 10.3389/fcell.2020.601224

[54] Wang, W.; Li, P.; Li, W.; Jiang, J.; Cui, Y.; Li, S.; Wang, Z. Osteopontin activates mesenchymal stem cells to repair skin wound. PLoS One. 2017, 12, e0185346. doi: 10.1371/journal.pone.0185346

[55] Costa, A. C.; Alves, P. M.; Monteiro, F. J.; Salgado, C. Interactions between Dental MSCs and Biomimetic Composite Scaffold during Bone Remodeling Followed by *In Vivo* Real-Time Bioimaging. Int J Mol Sci. 2023, 24, 1827. doi: 10.3390/ijms24031827

[56] Zastulka, A.; Clichici, S.; Tomoaia-Cotisel, M.; Mocanu, A.; Roman, C.; Olteanu, C.-D.; Culic, B.; Mocan, T. Recent Trends in Hydroxyapatite Supplementation for Osteoregenerative Purposes. Materials. 2023, 16, 1303. doi: 10.3390/ma16031303

[57] Tian, Y.; Wu, D.; Wu, D.; Cui, Y.; Ren, G.; Wang, Y.; Wang, J.; Peng, C. Chitosan-Based Biomaterial Scaffolds for the Repair of Infected Bone Defects. Front Bioeng Biotechnol. 2022, 10, doi: 10.3389/fbioe.2022.899760

[58] Giannobile, W. V.; Nevins, M., Eds. Osteology guidelines for oral and maxillofacial regeneration: preclinical models for translational research, 1st Ed.; Quintessence Publishing: London, 2011. doi: -

[59] Han, J.; Menicanin, D.; Marino, V.; Ge, S.; Mrozik, K.; Gronthos, S.; Bartold, P. Assessment of the regenerative potential of allogeneic periodontal ligament stem cells in a rodent periodontal defect model. J Periodontal Res. 2013, 49, 333-345. doi: 10.1111/jre.12111

[60] Strauss, F.-J.; Kuchler, U.; Kobatake, R.; Heimel, P.; Tangl, S.; Gruber, R. Acid bone lysates reduce bone regeneration in rat calvaria defects. J Biomed Mater Res A. 2021, 109, 659-665. doi: 10.1002/jbm.a.37050

[61] Pattnaik, S.; Nethala, S.; Tripathi, A.; Saravanan, S.; Moorthi, A.; Selvamurugan, N. Chitosan scaffolds containing silicon dioxide and zirconia nano particles for bone tissue engineering. Int J Biol Macromol. 2011, 49, 1167-72. doi: 10.1016/j.ijbiomac.2011.09.016

[62] Chesnutt, B. M.; Yuan, Y.; Buddington, K.; Haggard, W. O.; Bumgardner, J. D. Composite chitosan/nano-hydroxyapatite scaffolds induce osteocalcin production by osteoblasts *in vitro* and support bone formation *in vivo*. Tissue Eng Part A. 2009, 15, 2571-2579. doi: 10.1089/ten.tea.2008.0054

[63] Kurobane, T.; Shiwaku, Y.; Anada, T.; Hamai, R.; Tsuchiya, K.; Baba, K.; Iikubo, M.; Takahashi, T.; Suzuki, O. Angiogenesis involvement by octacalcium phosphate-gelatin composite-driven bone regeneration in rat calvaria critical-sized defect. Acta Biomater. 2019, 88, 514-526. doi: 10.1016/j.actbio.2019.02.021

[64] Chatzipetros, E.; Damaskos, S.; Tosios, K. I.; Christopoulos, P.; Donta, C.; Kalogirou, E.-M.; Yfanti, Z.; Tsiourvas, D.; Papavasiliou, A.; Tsiklakis, K. The effect of nano-hydroxyapatite/chitosan scaffolds on rat calvarial defects for bone regeneration. Int J Implant Dent. 2021, 7, 1-11. doi: 10.1186/s40729-021-00327-w

[65] Mohammadi, Z.; Mesgar, A. S.-M.; Rasouli-Disfani, F. Reinforcement of freeze-dried chitosan scaffolds with multiphasic calcium phosphate short fibers. J Mech Behav Biomed Mater. 2016, 61, 590-599. doi: 10.1016/j.jmbbm.2016.04.022

[66] Pighinelli, L.; Kucharska, M. Chitosan–hydroxyapatite composites. Carbohydr Polym. 2013, 93, 256-262. doi: 10.1016/j.carbpol.2012.06.004

CHAPTER VI

Discussion and Conclusions

A. DISCUSSION

In the literature from the last few decades, a wide variety of new generation 3D porous biodegradable multifunctional biomaterials made of natural/synthetic organic and/or inorganic raw materials have been studied for bone tissue regeneration [1], mainly in the field of orthopedics (trauma and infectious lesions) and bone cancer/metastasis [2, 3]. These alternative solutions have also been studied for clinical situations such as maxillo-facial surgery and periodontal (teeth and dental implants) bone regeneration [4]. Nevertheless, these surgical locations are challenging, namely the periodontal and peri-implant sites, since the oral cavity is naturally colonized by microorganisms, the chewing forces may disturb healing of the surgical wounds and destabilize the bone graft materials [5], as well as the pH and abrupt temperature fluctuations of the oral environment [6].

Recently, there has been an increasing global concern among the population and governments with sustainability and employing raw materials' sources and fabrication methods in industries in general that reduce environmental impacts [7]. Those principles also apply to health-related industries, such as those devoted to the development and manufacturing of bone graft materials [7]. In the current thesis, the nHAp/CS scaffold with aerogel distinct property was characterized for periodontal and peri-implant bone regeneration application. The nHAp/CS ratio was 70/30, which is similar to the chemical composition of natural bone ECM [8]. Compared to other CS and nHAp-based biomaterials with similar compositions [9, 10], the preparation method of the nHAp/CS scaffold is very simple in only three steps, and employs green chemicals (e.g. benign solvents like CO_2 in the supercritical state), making it easier for industrial large scale production and more cost-effective. Moreover, this aerogel biomaterial has the advantage of using CS, which has been gaining attention compared to other natural biopolymers like collagen, since it can be sustainably and economically obtained from by-products of seafood industries [9]. In the study by Ruphuy *et al.* (2018) it was demonstrated that the nHAp/CS scaffold was sterile after being submitted to the $scCO_2$ step, since no microbial growth was observed upon incubation in BHI suspension and culture in TSA plates [11]. This finding shows an increased value for the $scCO_2$ technique in the manufacturing of scaffolds for bone regeneration.

As presented in Chapter III, aerogel scaffolds present textural and porous structure that are interesting for bone regeneration, especially those which are prepared by freeze drying [12]. Porosity morphology promoted by this technique depends on both the water content of the dispersion, as well as the freezing temperature, thermal gradient and cooling rate [10, 13]. The nHAp/CS scaffold presents a fully interconnected high porosity (78 %), comparable to the ethyl(dimethylaminopropyl)carbodiimide/N-hydroxysuccinimide (EDC/NHS)-crosslinked CS/nHAp freeze dried scaffold (72.17 %) developed by Cao *et al.* study [14]. However, unlike

$scCO_2$ dried aerogels, which usually present pores in the nanometer scale [15-17] (as presented in Chapter III), the freeze drying processing of the nHAp/CS aerogel scaffold (after freezing at -20 ºC) allowed obtaining a wider range of pore sizes from less than 100 µm to more than 700 µm, with a mean pore diameter of *ca.* 200 µm, as determined by microCT analysis [18]. MicroCT analysis was the chosen method for the characterization of the scaffolds' morphology, since it is a non-destructive technique that allows gathering both quantitative and qualitative high-resolution information of the whole material volume [19]. On the contrary, SEM image analysis is limited to the scaffold's exposed surface area to measure the pore sizes and estimate their interconnectivity. Also, the manual sectioning required to expose the inner regions is destructive and may deform the microstructure, as well as by the 2D cross-section measurements that may not reliably reflect the 3D pore dimensions [19].

In a recent study, Pitrolino and co-authors (2022) developed a bilayered CS scaffold with a gradient of pore size for osteochondral regeneration, which had a bone-like layer with similar composition (70 % nHAp) to the nHAp/CS scaffold [9]. In their case, the CS matrix was cross-linked with genipin, and by the combination of freeze drying and porogen-leaching out methods they obtained a mean pore size of 275 µm (SEM) and a porosity of 71.79 % (microCT) in the nHAp-reinforced layer [9], which is very similar to the results that were obtained in this project. Tsiourvas *et al.* (2016) developed porous 3D scaffolds with a composition of HAp/CS 75/25 w/w, in which through freeze drying they managed to obtain highly interconnected scaffolds with pore size ranging from about 200 µm to 700 µm and a porosity around 90%, assessed by both optical microscopy and microCT [10]. Zia *et al.* (2020) also reported pore sizes between 100 and 500 µm (SEM) for their nHAp embedded xanthan gum−CS (XAN−CS/nHAp) nanocomposite prepared by freeze drying. Depending on the XAN−CS:nHAp ratios, the porosities varied between ~70 % (CS/nHAp without XAN polyelectrolyte complex) and ~95 % (XAN−CS/nHAp 50/50) [20].

The composite scaffolds that have been more recently studied have the advantage of being biodegradable, when compared to the commercially available products that are inorganic bone fillers (granules or blocks) from natural or synthetic sources, which usually present a very slow degradation profile [21, 22], with exception for β-TCP and BCP [4, 21]. However, it is essential that the scaffold's degradation is at the same rate as the bone tissue ingrowth, in order to provide the adequate support and volume maintenance, while bridging the production of ECM by osteogenic cells and the formation of a new osteoid tissue [20, 23, 24]. When compared to collagen, CS shows a slower degradation rate and it can be more easily tuned to provide tissue support during regeneration for longer periods of time [9]. In the present research, the nHAp/CS scaffold showed *in vitro* stable degradation profile for 4 weeks, even in the presence of lysozyme. The DD of the CS (91.9%) used in the present project is high, which contributes for a slower degradation and an increased resistance to hydrolyzation and enzymatic activity [9, 22]. The existence of HAp in the scaffold composition decisively contributed to the scaffold's stability (8.65 % of biodegradation in PBS; and 9.82 % in PBS with lysozyme), and these results are in accordance with other previous published studies [9, 20, 24, 25]. These results are comparable to Sadeghianmaryan and collaborators (2022) who obtained ~12 % degradation for the studied

CS/nHAp (10 % w/v) scaffold and 30 % for the CS scaffold after 28 days in PBS [25]. Cao *et al.* also showed a 14 % weight loss rate for their EDC/NHS-crosslinked CS/nHAp freeze dried scaffold after 28 days in PBS with lysozyme [23]. Pitrolino *et al.* reported 5 % mass loss after 21 days in PBS for their genipin-crosslinked nHAp-incorporated into CS scaffold [9]. Therefore, other factors like high interconnected porous structure, thinner pore-wall thickness, higher swelling ratio, lower crystallinity and no addition of cross-linkers or no polyelectrolyte complexation have been described as contributing to increase the materials' degradation rate [20]. Yet, the highest degradation rate (7 days in PBS with collagenase) was reported by Sun *et al.* (2022) for the studied glutaraldehyde-crosslinked gelatin/carboxymethyl CS/HCP (HCP corresponds to nHAp and β-TCP 3:2) scaffolds that showed 45.1 % for HCP 50 % and 56.9 % for HCP 10 % [4]. Also, the presence of gelatin in the nHAp/CS/Gel developed by the Bozorgi *et al.* (2022) study showed a higher degradation rate (38.94 % after 28 days in PBS) when compared to the results of this thesis [26]. Additionally, the longer degradation periods (until the 8th week in PBS with lysozyme) studied by Hu *et al.* (2022) showed a tendency to slight increase the degradation rate of the CS/Gel/nHAp multilayer scaffolds with time (from ~70 to ~85 %) [27]. The prolonged soaking detached the scaffold's surface from the inner structure, enabling the penetration of the solution and increasing the interaction of water and enzymes with CS [27].

In the clinical scenario, it is common practice to soak the graft biomaterials in fluids such as sterile saline, patient's blood or centrifuged blood plasma in order to facilitate the materials' manipulation and/or adsorb bioactive molecules before placing the fillers into the bone defects, which are wet environments as well [4, 20]. Therefore, in this research it was chosen to test the scaffolds' biomechanical properties in wet conditions in order to better mimic the clinical conditions in which the biomaterial will be implanted [24]. Moreover, as mentioned before, with time, the wet environment plays a critical role in the biodegradation and the biomechanical response may change, which is a material's behavior that must be taken into consideration [28]. It is essential for the regeneration of bone defects that the graft material is able to support the mechanical load, in order to avoid loss of new bone volume [4, 29]. It has been described in the literature [9, 20] that after swelling the composite biodegradable scaffolds become soft and elastic, which makes them more appropriate for low-load bearing applications like orofacial bone defects [4].

Zia *et al.* (2020) found that both the compressive strength and modulus of all of their XAN−CS/nHAp scaffolds were significantly reduced when tested after 24 hours in PBS (e.g. CS/nHAp was ~0.25 and ~2 MPa; XAN−CS/nHAp 50:50 was ~1.5 and ~7 MPa, respectively) when compared to their dry samples (e.g. CS/nHAp was ~0.75 and ~1.25 MPa; XAN−CS/nHAp 50:50 was ~2.0 and ~10.5 MPa, respectively) [20]. The plasticization effect of water was shown in the Pitrolino *et al.* (2022) study, where in dry conditions the compressive strength of the nHAp-incorporated scaffold was 100 kPa and the modulus was 1600 kPa, while after immersion in PBS for 1 hour, it decreased to 4 and 13 kPa, respectively [9]. Moreover, Pitrolino *et al.* also described that there was a significant increase in the compressive strength with the incorporation of nHAp (4.81 vs 2.33 kPa for CS-only scaffold), as well as for the compressive modulus (34.2 vs 18.6

kPa, respectively) [9], which is in accordance to the results obtained by the present study. This is a common finding in other studies [10, 25, 29], although the absolute values and mechanical parameters show variations according to the testing methods employed, as well as the raw materials, production methods and porous microstructure [9].

One of the major advantages of the presence of nHAp in the composite's formulation is promoting bioactivity, which increases the cell response to form a direct bond with the bone surrounding tissue [20, 23, 24]. The presence of bioactive ceramic plays as topographical cues, promoting cellular interaction with the biomimetic surface of the scaffold and allowing cells' focal adhesions, which, besides adhesion itself, promotes the formation of filopodia and cellular spreading and, consequently, osteointegration [1, 9, 16, 30]. The results of the present research showed that apatite crystals precipitate *in vitro* upon the nHAp/CS surface after 21 days of incubation in SBF. These results are comparable to Zia et al. (2020), who described the formation of a fiber-like apatite layer on their XAN−CS/nHAp nanocomposites after only 7 days in SBF, which process was increased until the 14th day by the higher hydrophilicity, along with the newly formed nHAp nucleation sites [20]. A similar result with chitosan/poly (γ-glutamic acid)/hydroxyapatite (CPH) hydrogels (or without HAp) was obtained after 2 months in SBF in a study done by Zhang *et al.* (2019) [24]. Cao *et al.* (2022) reported that their CS/nHAp scaffold reached an equilibrium mineralization rate after 14 days in SBF [23].

Considering that many bone defects are the result of infectious lesions and that the oral cavity is a naturally contaminated environment [21, 31, 32], it is of the utmost importance that the scaffold itself is able to inhibit the adhesion of microbial agents [20, 32]. Moreover, one of the major causes of post-operatory unsuccess on bone guided regeneration is the secondary infection of the graft [32]. Since CS is known for its antimicrobial effect [20], this polymer presence in the scaffold's composition becomes an advantage when compared to composites based on other biopolymers from natural sources, like collagen, or from synthetic origin, such as polyethylene glycol (PEG). Zia *et al.* (2020) reported that their XAN−CS/nHAp nanocomposites showed antibacterial activity (zone of inhibition) for *S. aureus* and *E. coli* culture, but a higher inhibition area was observed for the Gram-negative strain [20]. In addition, our results showed that the presence of nHAp might increase the antimicrobial effect of the scaffold, which was also observed by the work of Sadeghianmaryan and collaborators (2022). These authors reported more than 80 % reduction in the CFU counts (with no difference for *S. aureus* and *E. coli*) for their nHAp reinforced chitosan scaffold, when compared to the 70 % CFU reduction for the CS scaffold [25].

A key-factor in biomaterials' development to be applied as an implantable bone graft is the assessment of their cytotoxicity *in vitro*. Following the ISO 10993-5:2009 guidelines [33], it was showed that none of the leachable solutions from the tested scaffolds induced cytotoxicity to a human osteoblastic-like cell line. A similar result was obtained by Zhang *et al.* (2019) with 24 hours extracts of their CP and CPH hydrogels, which showed no cytotoxicity to 3T3 cells [24]. Cao *et al.* obtained ~100 % of MC3T3-E1 cells' viability after 1 day of incubation in CS/nHAp scaffold extracts, reaching up to almost 120 % of cell viability at the 7th day of culture [14]. Positive

results were also obtained by Bozorgi *et al.* (2022) with the nHAp/CS/Gel 24-hour extracts that showed 93.72 % of Saos-2 cells' viability at day 1 and increased to 159.3 % at day 7, which was also observed by the live/dead assay [26]. However, the present research demonstrated that it would be more favorable to soak nHAp/CS scaffolds for 1 hour before use to remove free unbonded nanoparticles that may induce pH changes at the cell culture medium. Nevertheless, this leaching procedure can be performed in the clinical practice while hydrating the scaffold and before materials' implantation into the bone defect.

Moreover, the lack of cytotoxicity was also confirmed by the adhesion and proliferation of the human pre-osteoblast cell line (MG63) and of the human dental follicle mesenchymal stem cells (hDFMSCs) to the nHAp containing scaffolds. Zia *et al.* (2020) reported a MG63 cells' viability > 80 % for CS/nHAp and > 90 % for XAN− CS/nHAp nanocomposites after seeding on the scaffolds for 24 hours [20]. Pitrolino *et al.* also achieved a significantly higher MSCs' metabolic activity and DNA content after 2 days of seeding cells on the CS-nHAp scaffold when compared to the CS scaffold [9]. In the present study, the use of MSCs derived from the DF is interesting for the purpose of the present research because besides being easily available (retrieved from the follicle of impacted teeth extracted from young individuals regarding orthodontic treatments), hDFMSCs are ectodermal mesenchymal stem cells, which are derived from neural crest cells that originate the periodontal tissue during the teeth development process [34-36]. Additionally, several recent studies have employed human dental pulp MSCs (hDPMSCs) [14, 24, 37, 38], as well as other teeth-derived MSCs types such as stem cells from human exfoliated deciduous teeth (SHEDs) [39], periodontal ligament stem cells (PDLSCs), stem cells from apical papilla (SCAPs) and gingival mesenchymal stem cells (GMSCs) [23].

Even after 21 days of culture, both cell types (MG63 and hDFMSCs) showed spindle-like morphologies within the porous structure of the nHAp/CS scaffold, which shows that the surface's chemical composition, topography and energy are more favorable for osteoconduction than the plain CS scaffold [9]. Additionally, SEM and fluorescence microscopy observations showed that the cells at the CS-nHAp scaffold were attached to the surface, while at the CS-only scaffold the cells exhibited clusters with a more rounded morphology [9]. A favorable Saos-2 cells' morphology (with extended filopodia) was also reported in the Bozorgi *et al.* (2022) work after seeding those pre-osteoblast cells on a nHAp/CS/Gel scaffold for 3 days [26]. Zhang *et al.* (2019) also tested hDPMSCs seeded on the CPH hydrogel (or without HAp) scaffolds, and besides their metabolic activity increased significantly from 24 to 72 hours, the cells showed polygonal morphology and spread with multiple filopodia contacts at SEM observation [24].

Moreover, while the ALP activity of MG63 cells was residual (low values and no significant changes with time), the hDFMSCs' ALP activity increased significantly with time, which demonstrates that the periodontal-related primary cells were positively stimulated towards osteogenic differentiation by both scaffold types. Comparatively, Pitrolino *et al.* (2022) showed in both scaffolds an increase in the ALP activity of MSCs in osteogenic medium from the 7th to the 14th day, but then a decrease in the enzyme activity to the 21st day [9]. A similar behavior was detected by Zia *et al.* (2020) in MG63 cells. It was shown that ALP activity increased from the 3rd

to the 7th day, but decreased at day 14 for XAN−CS/nHAp nanocomposites, while in the case of the CS/nHAp it increased until the 14th day [20]. Zhang *et al.* (2019) also obtained a significant decrease in hDPSCs' ALP activity from the 7th to the 10th day after seeding on CP and CPH scaffolds, suggesting that the cells achieved a more mature stage of the osteogenic differentiation [24].

In the present research, the presence of nHAp was important for an increased gene expression of RUNX2, col A1 and Sp7 by the MG63 cells and for an upregulation of Sp7 and OPN by the hDFMSCs after 21 days. RUNX2, collagen A1 (Col A1) and OPN are genes expressed earlier in the osteoblastic differentiation pathway, while Sp7 is expressed by more mature osteoblast cells [40]. Zia *et al.* (2020) reported enhanced expression of OPN and OCN (Western Blot analysis) in MG63 cells seeded on XAN−CS/nHAp scaffolds, which supported their osteogenic potential [20]. Zhang *et al.* reported an upregulation of the expression of ALP (~2-fold), Col A1 (~1.7-fold) and OPN (~1.3-fold) by hDPSCs at the 14th day when platelet-rich fibrin (PRF) was added to their CPH scaffold, due to the GFs present in PRF [24].

Despite the encouraging results obtained *in vitro*, it is essential to assess the *in vivo* biocompatibility of the scaffolds, since even 3D *in vitro* cultures do not cover yet the molecular, cellular and tissue complexity of the living organisms [41]. *In vivo* biocompatibility screening tests have been implemented to conduct an adequate evaluation of whether the biomaterials are safe and potentially effective [13, 41]. However, since pre-clinical *in vivo* studies are generally difficult and expensive, it is important to perform pre-clinical screening tests with small animal models, like mice and rats, which provide more reproducible and translational results [41]. The mid-term subcutaneous implantation of both nHAp/CS and CS scaffolds in mice did not increase the acute or chronic inflammatory responses, and the scaffolds gross observation and histological analysis showed that the materials were well integrated within the surrounding soft tissues. In agreement with the results of the present work, Forero *et al.* (2017) reported that their CS/Gel/nHAp/nCuZn scaffold showed higher cellular infiltration when compared to the CS/Gel scaffold after the 4-week of subcutaneous implantation in rabbits [13].

Moreover, the subcutaneous implantation of the scaffolds allowed the evaluation of their biodegradation analysis *in vivo*. In line with the *in vitro* biodegradation results, even after 5 weeks of implantation, the scaffolds exhibited structural stability, especially the nHAp/CS biomaterial, that was also observed by Forero *et al.* (2017) with the CS/Gel/nHAp/nCuZn scaffold [13]. These results are important, since the scaffold should provide enough support, maintain the biological space for the first month and favor the bone regenerative process [42]. Probably, the fact that the CS used in this research had high DD and crystallinity could have contributed to the lower degradation rate in physiological conditions [43]. He *et al.* (2015), who performed an intramuscular implantation in rats of the nHAp-CS scaffold, reported that the walls around the scaffolds' pores were breaking down at the 6th week and were visibly disrupted at the 12th week [42].

Since bone healing is influenced by many factors (biomechanics, cellular and vascular responses) that are best assessed *in vivo* [41, 44], the next step was the implantation of the scaffolds in critical size bone defects, which is the minimum defect dimension that does not

spontaneously heal entirely [41, 45]. In critical size defects, the bone regeneration begins from the defect limits and at their interface with the scaffold borders, advancing into the interior of the template, until the defect size is not critical anymore and it is able to full fill the whole scaffold volume [46]. There is some variation between studies in the dimensions of the calvaria full-thickness critical defects in rats (between 5 and 8 mm of diameter) [44, 47-53]. In the present research it was chosen to perform bilateral defects because it would allow the reduction of the number of control specimens used [44, 47], as well a better comparison between the empty controls and test defects within the same animal, reducing the individual variation of the regenerative process. Therefore, it was performed two 4 mm defects that better accommodated in the parietal bones of young rats, reducing the fragility and the risks of fracture of the surrounding skull. Indeed, after 3 months of experiment, the empty controls were not full filled with bone tissue showing the feasibility of the 4 mm as a critical defect.

MicroCT is considered the gold standard imaging technique for the evaluation of bone healing in small animal models [47], and it has been employed in many studies in this field in recent years [29, 44, 47, 48, 51-54]. In the present study, it allowed a precise quantification of the regenerated bone and real-time periodic evaluations (at 1 and 2 months) during the 3-month follow-up of the same animals, which reduced not only the number of animals used, but also decreased the error between time points. Other authors have employed other imaging techniques such as cone beam computed tomography (CBCT) [47] and planar digital radiography [30].

When compared to the CS scaffolds, the 3D images obtained by microCT of the bone defects showed that radiopaque new bone began to form inside the nHAp/CS aerogel scaffold even after the 1st month. Moreover, it was not only restricted to the borders of the scaffold, which was also observed by Cao *et al.* (2022) for their CS/nHAp scaffold after 3 months [14]. These results showed the importance of the presence of nHAp as an osteoinductive factor to boost the bone tissue regeneration. Moreover, even after 3 months, it was possible to observe the porous structures of both nHAp/CS and CS in the histologic analysis, indicating that the aerogels were still able to support and maintain the volume of the newly formed bone, which was also pointed out by Cao *et al.* (2022) in their study [14]. Chatzipetros *et al.* (2021) observed a significantly higher fraction of bone regeneration (FBR) from the 2nd to the 8th week for the HAp/CS 75/25 w/w scaffolds (19.96 % vs 42.13 %) when compared to the empty controls (14.88 % vs 15.98 %), after histomorphometry evaluation of the bilateral 5 mm defects on rat calvaria [45]. The CP, CPH and CPH-PRF scaffolds developed by Zhang and co-workers (2019) were firstly tested in 5 mm calvaria defects in rats, and by the 8th week all groups showed a large amount of newly formed bone, though the CPH−PRF group exhibited a significantly higher bone repair effect (mean integrated density of ~70 % of control, evaluated by microCT) [24]. A similar result (~70 % of control) was showed in a subsequent study, after 8 weeks of the scaffolds' implantation in alveolar bone defects with 5 mm of diameter in rabbits [38]. Histologically, in both experiments, no inflammatory response was observed around the implanted materials and, at after the 8th week, all groups showed the formation of mineralized osteoid tissue, but it was more prevalent in the CPH-PRF group [24, 38].

B. CONCLUSIONS

The research conducted within the scope of this thesis has demonstrated that the nHAp/CS scaffold has potential as a sustainable graft biomaterial for periodontal bone regeneration.

It has been shown that the nHAp/CS scaffold, prepared by freeze drying followed by $scCO_2$ extraction/sterilization, has aerogel features with a highly interconnected open porosity (78 %) and a mean pore diameter of 200 µm. This microstructure fulfills the requirements for a favorable cellular infiltration and the circulation of essential biomolecules.

The *in vitro* biodegradation experiment revealed that the nHAp/CS scaffold maintains a stable structure after 4 weeks in PBS (8.65 % of biodegradation) and in PBS with lysozyme (9.82 %), when compared to the plain CS scaffold. This feature is important for the maintenance of the mechanical strength in simulated adverse conditions like a wet environment for 4 weeks (storage modulus: 40 – 50 kPa). The mechanical experiments' results showed that the scaffold is appropriate for low-load bearing bone defects, such as those found in periodontal and maxillofacial lesions. These results also highlighted the importance of the presence of nHAp in the biomaterial's composition.

It was also shown that the nHAp/CS biomaterial is bioactive *in vitro*, promoting the formation of an apatite layer after 21 days, which is a favorable result for the induction of graft osteointegration *in vivo*.

Both scaffolds tested exhibited high antimicrobial activity against Gram-positive (*S. aureus*) and Gram-negative (*E. coli*) bacteria strains. This finding emphasizes the importance of CS in the scaffolds' composition, though this antimicrobial effect may also be enhanced by the presence of nHAp in the dispersed phase.

Besides, the scaffolds' extracts did not show cytotoxicity to an osteoblastic-like cell line (MG63), according to the ISO 10993-5:2009 standard parameters. Moreover, both MG63 and DFMSCs showed higher metabolic activity, adhesion and proliferation rate when seeded on the nHAp/CS scaffolds for 21 days. Furthermore, the higher ALP activity of DFMSCs and the expression of relevant osteogenic genes showed that the presence of nHAp induced the cells towards the osteogenic differentiation.

The subcutaneous implantation of the scaffolds *in vivo* in mice demonstrated that the biomaterials were biocompatible, stimulated angiogenesis and collagen deposition (specially the nHAp/CS scaffold). This experiment also showed that the scaffolds maintain their structure after 5 weeks post-implantation, which is essential to support bone tissue ingrowth. These scaffolds porous architecture was also observed after 3 months post-implantation at critical size bone

defects in rats. Significantly higher new bone formation was quantified inside the nHAp/CS implants when compared to the CS group and empty defects.

C. FUTURE PERSPECTIVES

Despite the advantages of the nHAp/CS scaffold demonstrated in the present research, there are still more specific experiments and improvements that could be performed, in order to achieve a bone graft biomaterial suitable for clinical use in the field of Periodontology.

Besides terminal sterilization, $scCO_2$ has become a very versatile method in the preparation of graft biomaterials, since it enables a great diversity of functions. For instance, $scCO_2$ has been efficiently used for tissue decellularization, leaving no traces of genetic material or toxic residues, no structural or mechanical changes, while performing simultaneous sterilization [55]. $ScCO_2$ foaming is another example of this solvent-free green technology to induce pore formation, during which $scCO_2$ aids with mixing the bioactive agents with the polymer at its rubbery state [46, 56]. Therefore, it is an advantageous method that should be even more explored in diverse stages of bone graft biomaterials development and production e.g. the incorporation of bioactive compounds (GFs, drugs) sensitive to extreme temperatures [46, 57].

Despite the high nHAp proportion that was possible to incorporate in the CS matrix, which provided enhanced biodegradation and biomechanical features to the nHAp/CS scaffold in relation to the plain CS biomaterial, it would be interesting to compare whether adding a cross-linking agent would improve the biomaterial even more. The addition of some non-cytotoxic options, such as genipin [9, 30] or the combination of other polymers to form polyelectrolyte complexes (intermolecular physical cross-linking) [20, 30, 58] could afterwards be tested in wet conditions. Most studies agree that there is still work to be done in terms of the mechanical strength of these biomaterials [4].

Another issue that should be additionally investigated is the *in vitro* antimicrobial effect of the nHAp/CS scaffolds against anaerobic oral bacteria species, and periodontopathogens in particular. Encouraging results were reported by Lazaveric *et al.* (2023), who tested the antimicrobial effect of commercial collagen membranes modified with CS and HAp nanoparticles (CS–HAp 1:1) against monomicrobial biofilms of oral bacteria species [37]. Their results showed that compared to the control collagen membranes, the CS–HAp modification contributed significantly to a decrease in the CFU values of the biofilm formed on the membranes (~6-fold reduction for *S. mitis*, ~4 log reduction for *P. gingivalis* and *F. nucleatum*) and of the medium of incubation of the membranes (~1.6-fold reduction for *S. mitis*, ~4 log reduction for *P. gingivalis* and ~5 log reduction for *F. nucleatum*) [37].

Besides, *in vitro* research should be conducted to evaluate the performance of other bone regeneration-related cell types seeded on the nHAp/CS scaffolds. The angiogenic potential of the biomaterial should be evaluated through the culture of human endothelial cells, as well as co-

cultures of endothelial and osteoblastic cells, by the characterization of the viability, proliferation and phenotypical and functional markers. The osteoclastic differentiation should also be explored using human osteoclastic precursor cells and co-cultures of osteoblastic/osteoclastic cells seeded on the scaffold. Osteoclast relevant intracellular signaling pathways (e.g. MEK, NFkB, PKC and JNK) should be addressed to understand the subjacent mechanisms underlying cell response to the scaffold. Other dental/periodontal-related cell types (e.g. hDPMSCs and PDLSCs) could also be investigated in relation to their response when seeded on the nHAp/CS scaffold.

Full regeneration of the periodontal apparatus is difficult, since it implies not only bone regeneration, but also of the cement and PDL with organized Sharpey's fibers [59]. Based on the nHAp/CS scaffold developed so far, it could be interesting to progress into the preparation of stratified scaffolds, with multilayered structures to mimic the complexity between bone and ligaments [59]. 3D printing could be a useful technology for this purpose, as well as for tailoring scaffolds that would perfectly fit the bone defects [60]. Moreover, the regulation of the mineralization of the different periodontal tissues is complex and there is the risk that the regenerated PDL might become mineralized by the influence of the surrounding hard tissues, resulting in tooth ankylosis [21]. The mechanisms that control the mineral homeostasis are not fully understood yet, and therefore the strategies to avoid that negative outcome are still being studied, namely the application of moderate mechanical stimulation to the PDL, and the use of molecules that contribute for the regulation of the mineralization, by stimulating the mineralization of hard tissues (bone and cement) and others that inhibit these processes in the soft tissues (PDL) [21]. *In vitro*, these stimuli could be simulated by the use of bioreactors that transduce the mechanical loads and shear stress forces, promoting the circulation of nutrients, oxygen and GFs [27]. This dynamic environment could reach cells in the inner layers of the scaffold, stimulating their differentiation and promoting the tissue regeneration [27].

In vivo experiments with larger animal models would be useful to perform periodontal lesions or other types of defects in the alveolar bone to study more reliably the clinical application of the nHAp/CS scaffolds. Alveolar defects could be performed in rabbits, similarly to the experiment of Zhang *et al.* (2023) [38], before advancing to e.g. periodontal and peri-implant lesions in larger animal models, which are more similar to humans in terms of oral and maxillo-facial regenerative treatments [41].

Nevertheless, nowadays bioengineering is developing towards tissue regeneration based on *in vitro* 3D tissue models (organ-on-a-chip), in order to substitute animal models in a near future. Therefore, the biomaterials development that is being pursued in projects similar to the present research will be a step forward in finding more sustainable and ethical paths for biomedical engineering research.

VI. References

[1] Pérez-Moreno, A.; Reyes-Peces, M. V.; Vilches-Pérez, J. I.; Fernández-Montesinos, R.; Pinaglia-Tobaruela, G.; Salido, M.; De la Rosa-Fox, N.; Piñero, M. Effect of washing treatment on the textural properties and bioactivity of silica/chitosan/TCP xerogels for bone regeneration. Int J Mol Sci. 2021, 22, 8321. doi: 10.3390/ijms22158321

[2] Campana, V.; Milano, G.; Pagano, E.; Barba, M.; Cicione, C.; Salonna, G.; Lattanzi, W.; Logroscino, G. Bone substitutes in orthopaedic surgery: from basic science to clinical practice. J Mater Sci Mater Med. 2014, 25, 2445-2461. doi: 10.1007/s10856-014-5240-2

[3] Zou, Z.; Wang, L.; Zhou, Z.; Sun, Q.; Liu, D.; Chen, Y.; Hu, H.; Cai, Y.; Lin, S.; Yu, Z. Simultaneous incorporation of PTH (1–34) and nano-hydroxyapatite into Chitosan/Alginate Hydrogels for efficient bone regeneration. Bioact Mater. 2021, 6, 1839-1851. doi: 10.1016/j.bioactmat.2020.11.021

[4] Sun, Q.; Yu, L.; Zhang, Z.; Qian, C.; Fang, H.; Wang, J.; Wu, P.; Zhu, X.; Zhang, J.; Zhong, L. A novel gelatin/carboxymethyl chitosan/nano-hydroxyapatite/β-tricalcium phosphate biomimetic nanocomposite scaffold for bone tissue engineering applications. Front Chem. 2022, 10, 958420. doi: 10.3389/fchem.2022.958420

[5] Gauthier, R.; Attik, N.; Chevalier, C.; Salles, V.; Grosgogeat, B.; Gritsch, K.; Trunfio-Sfarghiu, A.-M. 3D Electrospun Polycaprolactone Scaffolds to Assess Human Periodontal Ligament Cells Mechanobiological Behaviour. Biomimetics. 2023, 8, 108. doi: 10.3390/biomimetics8010108

[6] Cheng, D.; Ding, R.; Jin, X.; Lu, Y.; Bao, W.; Zhao, Y.; Chen, S.; Shen, C.; Yang, Q.; Wang, Y. Strontium Ion-Functionalized Nano-Hydroxyapatite/Chitosan Composite Microspheres Promote Osteogenesis and Angiogenesis for Bone Regeneration. ACS Appl Mater Interfaces. 2023, 15, 19951-19965. doi: 10.1021/acsami.3c00655

[7] García-González, C. A.; Budtova, T.; Durães, L.; Erkey, C.; Del Gaudio, P.; Gurikov, P.; Koebel, M.; Liebner, F.; Neagu, M.; Smirnova, I. An opinion paper on aerogels for biomedical and environmental applications. Molecules. 2019, 24, 1815. doi: 10.3390/molecules24091815

[8] Sugimoto, K.; Zhou, Y.; Galindo, T. G. P.; Kimura, R.; Tagaya, M. Investigation of Surface Layers on Biological and Synthetic Hydroxyapatites Based on Bone Mineralization Process. Biomimetics. 2023, 8, 184. doi: 10.3390/biomimetics8020184

[9] Pitrolino, K. A.; Felfel, R. M.; Pellizzeri, L. M.; McLaren, J.; Popov, A. A.; Sottile, V.; Scotchford, C. A.; Scammell, B. E.; Roberts, G. A.; Grant, D. M. Development and *in vitro* assessment of a bi-layered chitosan-nano-hydroxyapatite osteochondral scaffold. Carbohydr Polym. 2022, 282, 119126. doi: 10.1016/j.carbpol.2022.119126

[10] Tsiourvas, D.; Sapalidis, A.; Papadopoulos, T. Hydroxyapatite/chitosan-based porous three-dimensional scaffolds with complex geometries. Mater. Today Commun. 2016, 7, 59-66. doi: 10.1016/j.mtcomm.2016.03.006

[11] Ruphuy, G.; Souto-Lopes, M.; Paiva, D.; Costa, P.; Rodrigues, A.; Monteiro, F.; Salgado, C.; Fernandes, M.; Lopes, J.; Dias, M. Supercritical CO_2 assisted process for the production of high-purity and sterile nano-hydroxyapatite/chitosan hybrid scaffolds. J Biomed Mater Res B Appl Biomater. 2018, 106, 965-975. doi: 10.1002/jbm.b.33903

[12] Souto-Lopes, M.; Fernandes, M. H.; Monteiro, F. J.; Salgado, C. L. Bioengineering Composite Aerogel-Based Scaffolds That Influence Porous Microstructure, Mechanical Properties and *In Vivo* Regeneration for Bone Tissue Application. Materials. 2023, 16, 4483. doi: 10.3390/ma16124483.

[13] Forero, J. C.; Roa, E.; Reyes, J. G.; Acevedo, C.; Osses, N. Development of useful biomaterial for bone tissue engineering by incorporating nano-copper-zinc alloy (nCuZn) in chitosan/gelatin/nano-hydroxyapatite (Ch/G/nHAp) scaffold. Materials. 2017, 10, 1177. doi: 10.3390/ma10101177

[14] Cao, S.; Li, Q.; Zhang, S.; Liu, K.; Yang, Y.; Chen, J. Oxidized bacterial cellulose reinforced nanocomposite scaffolds for bone repair. Colloids Surf B Biointerfaces. 2022, 211, 112316. doi: 10.1016/j.colsurfb.2021.112316

[15] Pérez-Moreno, A.; Piñero, M.; Fernández-Montesinos, R.; Pinaglia-Tobaruela, G.; Reyes-Peces, M. V.; Mesa-Díaz, M. d. M.; Vilches-Pérez, J. I.; Esquivias, L.; de la Rosa-Fox, N.; Salido, M. Chitosan-Silica Hybrid Biomaterials for Bone Tissue Engineering: A Comparative Study of Xerogels and Aerogels. Gels. 2023, 9, 383. doi: 10.3390/gels9050383

[16] Perez-Moreno, A.; Reyes-Peces, M. d. l. V.; de Los Santos, D. M.; Pinaglia-Tobaruela, G.; de la Orden, E.; Vilches-Pérez, J. I.; Salido, M.; Piñero, M.; de la Rosa-Fox, N. Hydroxyl groups induce bioactivity in silica/chitosan aerogels designed for bone tissue engineering. *In vitro* model for the assessment of osteoblasts behavior. Polymers (Basel). 2020, 12, 2802. doi: 10.3390/polym12122802

[17] Reyes-Peces, M. V.; Fernández-Montesinos, R.; Mesa-Díaz, M. d. M.; Vilches-Pérez, J. I.; Cárdenas-Leal, J. L.; de la Rosa-Fox, N.; Salido, M.; Piñero, M. Structure-Related Mechanical Properties and Bioactivity of Silica–Gelatin Hybrid Aerogels for Bone Regeneration. Gels. 2023, 9, 67. doi: 10.3390/gels9010067

[18] Souto-Lopes, M.; Grenho, L.; Manrique, Y.; Dias, M. M.; Fernandes, M. H.; Monteiro, F. J.; Salgado, C. L. Full physicochemical and biocompatibility characterization of a supercritical CO_2 sterilized nano-hydroxyapatite/chitosan biodegradable scaffold for periodontal bone regeneration. Biomater Adv. 2023, 146, 213280. doi: 10.1016/j.bioadv.2023.213280

[19] Santos-Rosales, V.; Gallo, M.; Jaeger, P.; Alvarez-Lorenzo, C.; Gómez-Amoza, J. L.; García-González, C. A. New insights in the morphological characterization and modelling of poly (ε-caprolactone) bone scaffolds obtained by supercritical CO_2 foaming. J Supercrit Fluids. 2020, 166, 105012. doi: 10.1016/j.supflu.2020.105012

[20] Zia, I.; Jolly, R.; Mirza, S.; Umar, M. S.; Owais, M.; Shakir, M. Hydroxyapatite Nanoparticles Fortified Xanthan Gum–Chitosan Based Polyelectrolyte Complex Scaffolds for Supporting the Osteo-Friendly Environment. ACS Appl Bio Mater. 2020, 3, 7133-7146. doi: 10.1021/acsabm.0c00948

[21] Liang, Y.; Luan, X.; Liu, X. Recent advances in periodontal regeneration: A biomaterial perspective. Bioact Mater. 2020, 5, 297-308. doi: 10.1016/j.bioactmat.2020.02.012

[22] Said, H. A.; Mabroum, H.; Lahcini, M.; Oudadesse, H.; Barroug, A.; Youcef, H. B.; Noukrati, H. Manufacturing methods, properties, and potential applications in bone tissue regeneration of hydroxyapatite-chitosan biocomposites: A review. Int J Biol Macromol. 2023, 125150. doi: 10.1016/j.ijbiomac.2023.125150

[23] Cao, L.; Su, H.; Si, M.; Xu, J.; Chang, X.; Lv, J.; Zhai, Y. Tissue engineering in stomatology: a review of potential approaches for oral disease treatments. Front Bioeng Biotechnol. 2021, 9, 662418. doi: 10.3389/fbioe.2021.662418

[24] Zhang, L.; Dong, Y.; Xue, Y.; Shi, J.; Zhang, X.; Liu, Y.; Midgley, A. C.; Wang, S. Multifunctional triple-layered composite scaffolds combining platelet-rich fibrin promote bone regeneration. ACS Biomater Sci Eng. 2019, 5, 6691-6702. doi: 10.1021/acsbiomaterials.9b01022

[25] Sadeghianmaryan, A.; Naghieh, S.; Yazdanpanah, Z.; Sardroud, H. A.; Sharma, N.; Wilson, L. D.; Chen, X. Fabrication of chitosan/alginate/hydroxyapatite hybrid scaffolds using 3D printing and impregnating techniques for potential cartilage regeneration. Int J Biol Macromol. 2022, 204, 62-75. doi: 10.1016/j.ijbiomac.2022.01.201

[26] Bozorgi, A.; Mozafari, M.; Khazaei, M.; Soleimani, M.; Jamalpoor, Z. Fabrication, characterization, and optimization of a novel copper-incorporated chitosan/gelatin-based scaffold for bone tissue engineering applications. Bioimpacts. 2022, 12, 233. doi: 10.34172/bi.2021.23451

[27] Hu, X.; Zheng, S.; Zhang, R.; Wang, Y.; Jiao, Z.; Li, W.; Nie, Y.; Liu, T.; Song, K. Dynamic process enhancement on chitosan/gelatin/nano-hydroxyapatite-bone derived multilayer scaffold for osteochondral tissue repair. Biomater Adv. 2022, 133, 112662. doi: 10.1016/j.msec.2022.112662

[28] Tyshkunova, I. V.; Poshina, D. N.; Skorik, Y. A. Cellulose cryogels as promising materials for biomedical applications. Int J Mol Sci. 2022, 23, 2037. doi: 10.3390/ijms23042037

[29] Liu, X.-L.; Zhang, C.-J.; Shi, J.-J.; Ke, Q.-F.; Ge, Y.-W.; Zhu, Z.-A.; Guo, Y.-P. Nacre-mimetic cerium-doped nano-hydroxyapatite/chitosan layered composite scaffolds regulate bone regeneration via OPG/RANKL signaling pathway. J Nanobiotechnology. 2023, 21, 259. doi: 10.1186/s12951-023-01988-y

[30] Makar, L. E.; Nady, N.; Shawky, N.; Kandil, S. H. Genipin versus Ferric Chloride cross-linked unmodified Gum Arabic/Chitosan/nano-Hydroxyapatite nanocomposite hydrogels as potential scaffolds for bone regeneration. Sci Rep. 2023, 13, 14402. doi: 10.1038/s41598-023-41413-w

[31] Basyuni, S.; Ferro, A.; Santhanam, V.; Birch, M.; McCaskie, A. Systematic scoping review of mandibular bone tissue engineering. Br J Oral Maxillofac Surg. 2020, 58, 632-642. doi: 10.1016/j.bjoms.2020.03.016

[32] Tamburaci, S.; Tihminlioglu, F. Development of Si doped nano hydroxyapatite reinforced bilayer chitosan nanocomposite barrier membranes for guided bone regeneration. Mater Sci Eng C Mater Biol Appl. 2021, 128, 112298. doi: 10.1016/j.msec.2021.112298

[33] International Organization for Standardization. ISO 10993-5:2009(E). Biological evaluation of medical devices — Part 5: Tests for *in vitro* cytotoxicity. Switzerland. 2009.

[34] Morsczeck, C. Mechanisms during osteogenic differentiation in human dental follicle cells. Int J Mol Sci. 2022, 23, 5945. doi: 10.3390/ijms23115945

[35] Nagata, M.; English, J. D.; Ono, N.; Ono, W. Diverse stem cells for periodontal tissue formation and regeneration. Genesis. 2022, 60, e23495. doi: 10.1002/dvg.23495

[36] Pieles, O.; Höring, M.; Adel, S.; Reichert, T. E.; Liebisch, G.; Morsczeck, C. Energy metabolism and Lipidome are highly regulated during osteogenic differentiation of dental follicle cells. Stem Cells Int. 2022, 2022, 3674931. doi: 10.1155/2022/3674931

[37] Lazarevic, M.; Petrovic, S.; Pierfelice, T. V.; Ignjatovic, N.; Piattelli, A.; Vlajic Tovilovic, T.; Radunovic, M. Antimicrobial and Osteogenic Effects of Collagen Membrane Decorated with Chitosan–Nano-Hydroxyapatite. Biomolecules. 2023, 13, 579. doi: 10.3390/biom13040579

[38] Zhang, L.; Dong, Y.; Liu, Y.; Liu, X.; Wang, Z.; Wan, J.; Yu, X.; Wang, S. Multifunctional hydrogel/platelet-rich fibrin/nanofibers scaffolds with cell barrier and osteogenesis for guided tissue regeneration/guided bone regeneration applications. Int J Biol Macromol. 2023, 253, 126960. doi: 10.1016/j.ijbiomac.2023.126960

[39] Yuan, Z.; Ren, Y.; Shafiq, M.; Chen, Y.; Tang, H.; Li, B.; EL-Newehy, M.; EL-Hamshary, H.; Morsi, Y.; Zheng, H. Converging 3D printing and electrospinning: effect of poly (L-lactide)/gelatin based short nanofibers aerogels on tracheal regeneration. Macromol Biosci. 2022, 22, 2100342. doi: 10.1002/mabi.202100342

[40] Lang, N. P.; Berglundh, T.; Giannobile, W. V.; Sanz, M., Eds. Lindhe's Clinical Periodontology and Implant Dentistry, 7th Ed.; Wiley-Blackwell: Oxford, 2021. doi: -

[41] Giannobile, W. V.; Nevins, M., Eds. Osteology guidelines for oral and maxillofacial regeneration: preclinical models for translational research, 1st Ed.; Quintessence Publishing: London, 2011. doi: -

[42] He, Y.; Dong, Y.; Cui, F.; Chen, X.; Lin, R. Ectopic osteogenesis and scaffold biodegradation of nano-hydroxyapatite-chitosan in a rat model. PLoS One. 2015, 10, e0135366. doi: 10.1371/journal.pone.0135366

[43] Lauritano, D.; Limongelli, L.; Moreo, G.; Favia, G.; Carinci, F. Nanomaterials for periodontal tissue engineering: chitosan-based scaffolds. A systematic review. Nanomaterials. 2020, 10, 605. doi: 10.3390/nano10040605

[44] Chatzipetros, E.; Christopoulos, P.; Donta, C.; Tosios, K. I.; Tsiambas, E.; Tsiourvas, D.; Kalogirou, E.-M.; Tsiklakis, K. Application of nano-hydroxyapatite/chitosan scaffolds on rat calvarial critical-sized defects: A pilot study. Med Oral Patol Oral Cir Bucal. 2018, 23, e625. doi: 10.4317/medoral.22455

[45] Chatzipetros, E.; Damaskos, S.; Tosios, K. I.; Christopoulos, P.; Donta, C.; Kalogirou, E.-M.; Yfanti, Z.; Tsiourvas, D.; Papavasiliou, A.; Tsiklakis, K. The effect of nano-hydroxyapatite/chitosan scaffolds on rat calvarial defects for bone regeneration. Int J Implant Dent. 2021, 7, 1-11. doi: 10.1186/s40729-021-00327-w

[46] Goimil, L.; Santos-Rosales, V.; Delgado, A.; Evora, C.; Reyes, R.; Lozano-Perez, A. A.; Aznar-Cervantes, S. D.; Cenis, J. L.; Gómez-Amoza, J. L.; Concheiro, A. scCO$_2$-foamed silk fibroin aerogel/poly

(ε-caprolactone) scaffolds containing dexamethasone for bone regeneration. J CO2 Util. 2019, 31, 51-64. doi: 10.1016/j.jcou.2019.02.016

[47] Chatzipetros, E.; Yfanti, Z.; Christopoulos, P.; Donta, C.; Damaskos, S.; Tsiambas, E.; Tsiourvas, D.; Kalogirou, E.-M.; Tosios, K. I.; Tsiklakis, K. Imaging of nano-hydroxyapatite/chitosan scaffolds using a cone beam computed tomography device on rat calvarial defects with histological verification. Clin Oral Investig. 2020, 24, 437-446. doi: 10.1007/s00784-019-02939-4

[48] Li, Y.; Wang, J.; Qian, D.; Chen, L.; Mo, X.; Wang, L.; Wang, Y.; Cui, W. Electrospun fibrous sponge via short fiber for mimicking 3D ECM. J Nanobiotechnology. 2021, 19, 131. doi: 10.1186/s12951-021-00878-5

[49] Liu, M.; Shafiq, M.; Sun, B.; Wu, J.; Wang, W.; EL-Newehy, M.; EL-Hamshary, H.; Morsi, Y.; Ali, O.; Khan, A. u. R. Composite superelastic aerogel scaffolds containing flexible SiO_2 nanofibers promote bone regeneration. Adv Healthc Mater. 2022, 11, 2200499. doi: 10.1002/adhm.202200499

[50] Liu, S.; Li, D.; Chen, X.; Jiang, L. Biomimetic cuttlebone polyvinyl alcohol/carbon nanotubes/hydroxyapatite aerogel scaffolds enhanced bone regeneration. Colloids Surf B Biointerfaces. 2022, 210, 112221. doi: 10.1016/j.colsurfb.2021.112221

[51] Liu, S.; Zhou, C.; Mou, S.; Li, J.; Zhou, M.; Zeng, Y.; Luo, C.; Sun, J.; Wang, Z.; Xu, W. Biocompatible graphene oxide–collagen composite aerogel for enhanced stiffness and *in situ* bone regeneration. Mater Sci Eng C Mater Biol Appl. 2019, 105, 110137. doi: 10.1016/j.msec.2019.110137

[52] Weng, L.; Boda, S. K.; Wang, H.; Teusink, M. J.; Shuler, F. D.; Xie, J. Novel 3D hybrid nanofiber aerogels coupled with BMP-2 peptides for cranial bone regeneration. Adv Healthc Mater. 2018, 7, 1701415. doi: 10.1002/adhm.201701415

[53] Ye, K.; Liu, D.; Kuang, H.; Cai, J.; Chen, W.; Sun, B.; Xia, L.; Fang, B.; Morsi, Y.; Mo, X. Three-dimensional electrospun nanofibrous scaffolds displaying bone morphogenetic protein-2-derived peptides for the promotion of osteogenic differentiation of stem cells and bone regeneration. J Colloid Interface Sci. 2019, 534, 625-636. doi: 10.1016/j.jcis.2018.09.071

[54] Liu, X.; Zhang, G.; Hou, C.; Wang, H.; Yang, Y.; Guan, G.; Dong, W.; Gao, H.; Feng, Q. Vascularized bone tissue formation induced by fiber-reinforced scaffolds cultured with osteoblasts and endothelial cells. Biomed Res Int. 2013, 2013, doi: 10.1155/2013/854917

[55] Amirazad, H.; Dadashpour, M.; Zarghami, N. Application of decellularized bone matrix as a bioscaffold in bone tissue engineering. J Biol Eng. 2022, 16, 1-18. doi: 10.1186/s13036-021-00282-5

[56] Goimil, L.; Braga, M. E.; Dias, A. M.; Gomez-Amoza, J. L.; Concheiro, A.; Alvarez-Lorenzo, C.; de Sousa, H. C.; Garcia-Gonzalez, C. A. Supercritical processing of starch aerogels and aerogel-loaded poly (ε-caprolactone) scaffolds for sustained release of ketoprofen for bone regeneration. J CO2 Util. 2017, 18, 237-249. doi: 10.1016/j.jcou.2017.01.028

[57] Santos-Rosales, V.; Iglesias-Mejuto, A.; García-González, C. A. Solvent-free approaches for the processing of scaffolds in regenerative medicine. Polymers (Basel). 2020, 12, 533. doi: 10.3390/polym12030533

[58] Tang, S.; Jiang, L.; Jiang, Z.; Ma, Y.; Zhang, Y.; Su, S. Preparation and Characterization of a Novel Tragacanth Gum/Chitosan/Sr-Nano-Hydroxyapatite Composite Membrane. Polymers. 2023, 15, 2942. doi: 10.3390/polym15132942

[59] Golafshan, N.; Castilho, M.; Daghrery, A.; Alehosseini, M.; van de Kemp, T.; Krikonis, K.; de Ruijter, M.; Dal-Fabbro, R.; Dolatshahi-Pirouz, A.; Bhaduri, S. B.; Bottino, M. C.; Malda, J. Composite Graded Melt Electrowritten Scaffolds for Regeneration of the Periodontal Ligament-to-Bone Interface. ACS Appl Mater Interfaces. 2023, 15, 12735-12749. doi: 10.1021/acsami.2c21256

[60] Larsson, L.; Decker, A.; Nibali, L.; Pilipchuk, S.; Berglundh, T.; Giannobile, W. Regenerative medicine for periodontal and peri-implant diseases. J Dent Res. 2016, 95, 255-266. doi: 10.1177/0022034515618887

CHAPTER VII

Supplementary Material

Table 1S. Morphology of periodontal bone defects [1, 2]

Suprabony lesions	Horizontal bone defects (the base of the pocket is coronal to the bone crest)			
Infrabony lesions	Angular/vertical defects (the base of the pocket is apical to the bone crest)	Intrabony defects	Three-walled	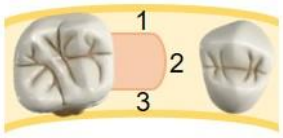
			Two-walled	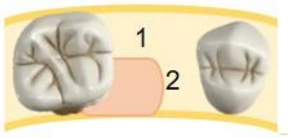
			One-walled	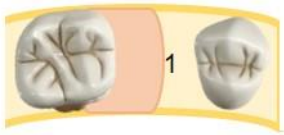
			Combination defects	
		Interdental crater defect		
Interradicular/ furcation defects		Class I		
		Class II		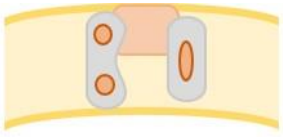
		Class III		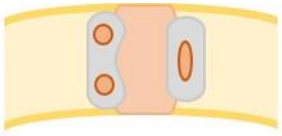

VII. References

[1] Lang, N. P.; Berglundh, T.; Giannobile, W. V.; Sanz, M., Eds. Lindhe's Clinical Periodontology and Implant Dentistry, 7th Ed.; Wiley-Blackwell: Oxford, 2021. doi: -

[2] Nibali, L.; Sultan, D.; Arena, C.; Pelekos, G.; Lin, G. H.; Tonetti, M. Periodontal infrabony defects: Systematic review of healing by defect morphology following regenerative surgery. J Clin Periodontol. 2021, 48, 101-114. doi: 10.1111/jcpe.13381

Supercritical CO_2 Assisted Process for the Production of High-Purity and Sterile Nano-Hydroxyapatite/Chitosan Hybrid Scaffolds

G. Ruphuy[1,2], M. Souto-Lopes[3,4,5], D. Paiva[6], P. Costa[1], A. E. Rodrigues[1], F. J. Monteiro[3,4,5], C. L. Salgado[3,4,5], M. H. Fernandes[7,8], J. C. Lopes[1], M. M. Dias[1], M. F. Barreiro[2]

1 – Laboratory of Separation and Reaction Engineering – Laboratory of Catalysis and Materials LSRE-LCM, Faculty of Engineering, University of Porto, Portugal

2 – Laboratory of Separation and Reaction Engineering – Laboratory of Catalysis and Materials LSRE-LCM, Bragança Polytechnic Institute, Bragança, Portugal

3 – INEB – Institute of Biomedical Engineering, University of Porto, Portugal

4 – Department of Metallurgical and Materials Engineering, Faculty of Engineering of the University of Porto, Portugal

5 – i3S – Instituto de Investigação e Inovação em Saúde, University of Porto, Portugal

6 – Laboratory of Process Engineering, Environment, Biotechnology and Energy LEPABE, Faculty of Engineering, University of Porto, Portugal

7 – Laboratory for Bone Metabolism and Regeneration, Faculty of Dental Medicine of the University of Porto FMDUP, Portugal

8 – REQUIMTE/LAQV, University of Porto, Portugal

J Biomed Mater Res Part B, 2018, 106, 965-975. doi: 10.1002/jbm.b.33903

ABSTRACT

Hybrid scaffolds composed of hydroxyapatite (HAp), in particular in its nanometric form (nHAp), and chitosan (CS) are promising materials for non-load-bearing bone graft applications. The main constraints of their production concern the successful implementation of the final purification/neutralization and sterilization steps. Often, the used purification strategies can compromise scaffold structural features, and conventional sterilization techniques can result in material's thermal degradation and/or contamination with toxic residues. In this context, this work presents a process to produce nHAp/CS scaffolds mimicking bone composition and structure, where an innovative single step based on supercritical CO_2 extraction was used for both purification and sterilization. A removal of 80 % of the residual acetic acid was obtained (T = 75 ºC, *p* = 8.0 MPa, 2 extraction cycles of 2 h) giving rise to scaffolds exhibiting adequate interconnected porous structure, fast swelling and storage modulus compatible with non-load-bearing applications. Moreover, the obtained scaffolds showed cytocompatibility and osteoconductivity without further need of disinfection/sterilization procedures. Among the main advantages, the proposed process comprises only three steps (nHAp/CS dispersion preparation; freeze drying; and supercritical CO_2 extraction), and the supercritical CO_2 extraction show clear advantages over currently used procedures based on neutralization steps.

KEYWORDS

Bone tissue engineering, nHAp/CS scaffolds, Supercritical CO_2, Sterilization

INTRODUCTION

The production of bone grafts based on hydroxyapatite ($Ca_{10}(PO_4)_6(OH)_2$, HAp) and chitosan (CS) has been widely studied and proven to be a suitable combination for bone tissue engineering applications [1]. HAp by itself is highly brittle and CS on its own does not induce the deposition of bone minerals even though it does promote osteogenic cells attachment and proliferation. However, by combining both components, HAp provides the required bioactivity while CS adds elasticity to the final material, resulting in a great candidate for non-load-bearing bone graft applications [1,2]. Properties can be improved if nano-hydroxyapatite (nHAp) is used since it presents clear advantages over its micrometric form in terms of adhesion promotion, cellular differentiation and proliferation, osseointegration and surface mineralization [3].

In bone self-regeneration the scaffold has to act as a 3D template, which once implanted in the defect, allows cell migration, adhesion, proliferation, and formation of new bone tissue. Hence, critical features comprise microstructure that should be highly porous with interconnected pores allowing cells mobility, diffusion of nutrients, and vascularization. In addition, availability of off-the-shelf grafts is desirable for such applications. These aspects are highly dependent of the manufacturing process that should be reproducible and easily scalable as well [4].

Typically, production of HAp/CS scaffolds starts with the preparation of a HAp/CS aqueous dispersion. This is a key step that can be done in a number of ways, and the most common is the so-called simple mixing method that consists in physically mixing HAp particles, micrometer or nanometer sized, into a CS solution [1,5]. In a second step, the scaffolds are prepared by freeze drying [1,6]. Many authors following this procedure reported materials with the desirable high porosity and pore interconnectivity [7–10], but in most cases residual acetic acid remains at levels able to cause scaffold disruption in aqueous medium and/or hinder cell growth and proliferation [6,11]. Purification/neutralization is then carried out by immersing the scaffold in an alkaline solution, washing (ultrapure water), and drying (usually through another freeze drying step) [8–10]. This process is time consuming leading to materials with low purity (residual salts) and compromised structural integrity, as reported in studies performing neutralization with NaOH solutions [12,13].

An alternative technique that recently has proven to be viable for the purification of CS scaffolds is based on supercritical fluid extraction. This technique is advantageous since it is appropriate for processing thermosensitive materials and preserves the structural features of the scaffold. Baldino *et al.* (2014) [14] produced CS scaffolds exhibiting multilevel structure (macro-, micro- and nano-) suitable for tissue engineering applications by a Supercritical Freeze Extraction Process. CS solutions (in diluted acetic acid) were poured in steel molds, frozen, and subjected to solvent exchange by immersion in an acetone bath at -20 ºC; the acetone was then removed using supercritical CO_2 ($scCO_2$) extraction (200 bar and 35 ºC). The produced scaffolds presented different morphologies depending on the concentration of the CS solution. In a more recent study, Baldino *et al.* (2015) [15] evaluated the viability of $scCO_2$ extraction for the production and purification of CS scaffolds crosslinked with glutaraldehyde. In this case, CS solutions were

crosslinked with glutaraldehyde, washed with water and subjected to solvent exchange by immersion in ethanol. The samples were then subjected to $scCO_2$ extraction (200 bar and 35 ºC). The authors have shown that the $scCO_2$ and ethanol mixture was successful to satisfactorily remove glutaraldehyde residues entrapped within the CS matrix. A different approach was used by Duarte *et al.* (2009) [16] with a $scCO_2$ assisted process for the preparation of dexamethasone-loaded CS scaffolds; however, in this case, the scaffolds were produced by freeze drying and purified by the common neutralization method by immersion in alkaline solution, and $scCO_2$ (8.0 MPa and 35 ºC) was used (and proved suitable) for the impregnation of the scaffold with dexamethasone.

Finally, when designing HAp/CS scaffolds, another important step to consider is sterilization. Common sterilization techniques (dry heat and steam) can induce thermal degradation of CS (a thermosensitive material), ethylene oxide risks the deposition of toxic residues on the material's surface and gamma irradiation can cause material degradation as well [17]. In this context, $scCO_2$ extraction is emerging as an innovative sterilization technique, capable to surpass these constraints [18–20]. However, no works were found regarding the use of the $scCO_2$ extraction to simultaneously purify and sterilize the scaffolds.

In this work, a 3-step process to produce nHAp/CS scaffolds mimicking bone composition and structure, where an innovative step based on $scCO_2$ extraction is introduced for simultaneous purification and sterilization, is presented and compared with currently used procedures based on neutralization steps. The most promising solutions, in terms of structural and mechanical features and compatible residual acetic acid levels, were tested in what concerns sterility and cell growth.

MATERIALS AND METHODS

Materials

HAp aqueous paste *nanoXIM-HAp102* from Fluidinova S.A. (composed of 15.0 ± 1.0 % wt. of HAp rod-like nanoparticles (particle size < 50 nm) suspended in pure water), and CS brand 90/200/A1 from Biotechnologie GmbH (deacetylation degree and dynamic viscosity of 91.9 % and 128 mPa s (1 % at 20 ºC in 1 % acetic acid solution)) were used. Glacial acetic acid and sodium acetate trihydrate, were both of analytical grade, 8 M sodium hydroxide solution brand Fluka, trypsin, EDTA, resazurin sodium salt, and PBS, all acquired from Sigma Aldrich. Brain heart infusion (BHI) was acquired from LiofilchemVR s.r.l. Eagle minimum essential medium (MEM), alpha modification (α-MEM), fetal bovine serum, penicillin, streptomycin, and amphotericin B brand GibcoTM were from Thermo Fisher Scientific.

Dispersions preparation

HAp nanoparticles (nHAp) were incorporated in the CS solution by simple mixing, with rigorous mixing and pH control, as described elsewhere [21]. Briefly, the nHAp paste was pumped at 240 rpm (32 mL/min) and dispersed into the CS solution using an ultraturrax device Miccra D-9 at its minimum speed rate (11,000 rpm) in a set-up designed to achieve mixing times below 100 ms. The nHAp/CS dispersions were prepared at nHAp concentration of 20 g/L, final pH of 5.5 (room temperature), and nHAp/CS weight ratio of 70/30 (typical bone composition).

Scaffolds preparation and purification/neutralization procedures

A schematic representation of the three used procedures is shown in Figure 1. In all procedures, scaffolds were prepared from samples of 10 mL of the nHAp/CS dispersions poured in 55 mm diameter polystyrene petri dishes, firstly by freezing at -20 ºC overnight, and then freeze-dried for 24 h using a VirTis BenchTop 6 K Freeze Dryer (model n86KBTEL). The samples that were not subjected to purification/neutralization are referred as *nHApCS-5.5-untreated*.

Two conventional purification methodologies based on acetic acid neutralization (Figure 1, 5-step Procedure I and 5-step Procedure II), and a third innovative approach based on supercritical CO_2 extraction (Figure 1, 3-step Procedure III) were tested. In Procedure I neutralizing was performed directly on the nHApCS-5.5 dispersion, previously to scaffold preparation, by dropwise addition of NaOH (1 M) until pH 7.0 (room temperature). After freeze drying, the scaffolds were washed thrice with ultrapure water and freeze dried again. These samples are referred as *nHApCS-7.0*. In Procedure II, neutralization was performed on the obtained scaffolds, by immersion in a NaOH/ethanol solution, according to the procedure described by He *et al.* (2011) [22]. The neutralized scaffolds were washed thrice with ultrapure water and freeze dried. These samples are referred as *nHApCS-NaOHEtOH*. In Procedure III, acetic acid was removed by $scCO_2$ extraction using the in-house built unit described by Gomes *et al.* (2007) [23]. Concisely, samples (5 per experiment) were placed equally distributed inside the 1 L extraction cell; CO_2 was cooled down, pumped into the cell, and compressed until the desired pressure (8.0 MPa). To find the best conditions to remove acetic acid from the produced nHAp/CS scaffolds, and achieve viable materials to support cell attachment and proliferation, different experimental conditions were tested (Table I). For the first experiment (A), mild conditions right above critical conditions (T = 40 ºC, p = 8.0 MPa) were chosen. For experiments B and C, sterilization conditions (namely T = 75 ºC) based on Spilimbergo *et al.* (2003) [19] who reported total inactivation of Bacillus subtilis spores using $scCO_2$ treatment at 75 ºC for 2 hours, were selected. In this case, samples were subjected to 1 (B) and 2 (C) extraction cycles. Subsequently to each cycle, two depressurization steps were carried out (4 and 0.2 MPa, sequentially). Samples were recovered under sterile environment and stored in sterile bags.

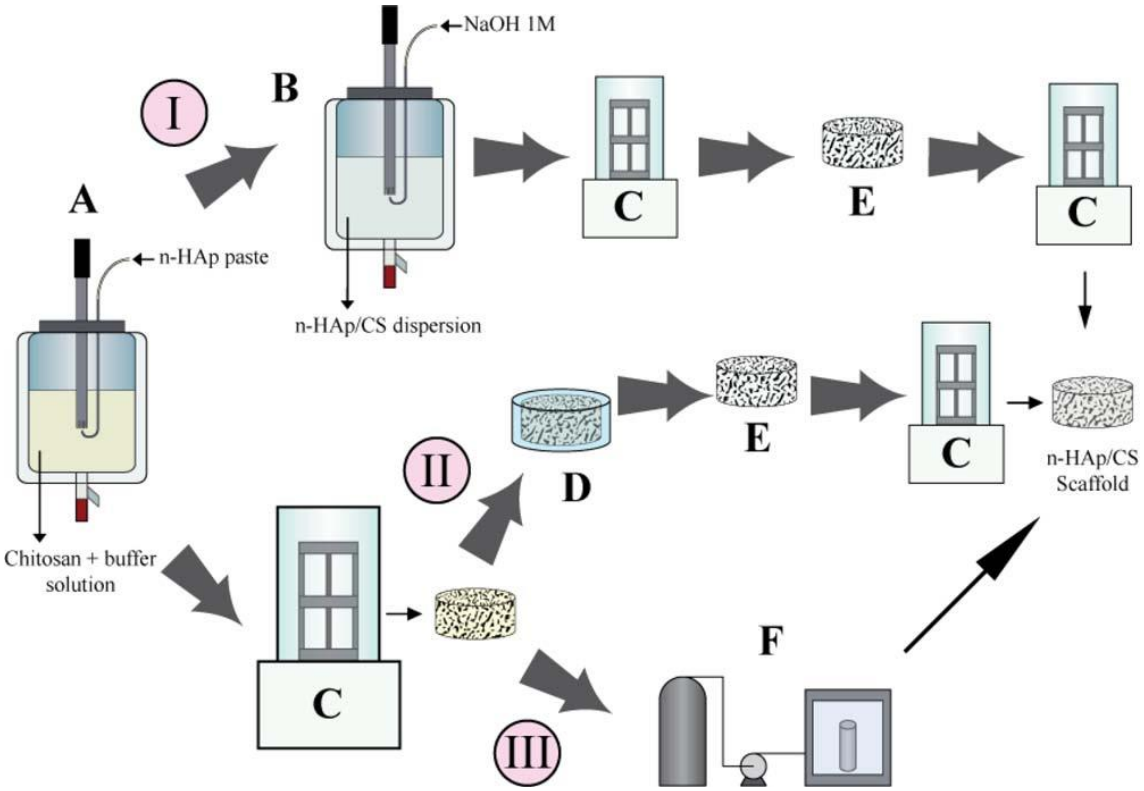

Figure 1. Schematic representation of the three studied procedures (I, II, and III) for the production of nHAp/CS scaffolds, that comprise the following steps: (a) Dispersion preparation; (b) Neutralization of acetic acid by dropwise addition of NaOH 1 M; (c) Freeze drying; (d) Neutralization by immersion in NaOH/ethanol solution; (e) Washing with ultrapure water; (f) Acetic acid extraction with $scCO_2$.

Table I. Experimental Conditions Tested for the $scCO_2$ Extraction Process and Estimated Mass of CO_2 per Mass of Scaffold for Each Experiment

		Temperature (ºC)		
Sample	**Number of Cycles**	**Cycle 1**	**Cycle 2**	**Mass of CO_2/Mass of Scaffold**
(A) nHApCS-$scCO_2$-40	1	40	_	179.0
(B) nHApCS-$scCO_2$–75	1	75	_	107.3
(C) nHApCS-$scCO_2$–75/75	2	75	75	214.6 (107.3 + 107.3)

Scaffolds characterization

Thermogravimetric analysis and extraction yield

Thermogravimetric analysis was performed using a TG 209 F3 TarsusVR under nitrogen atmosphere, temperature range of 30 – 700 ºC and heating rate of 10 ºC/min. The peak attributed to acetic acid degradation was used to quantify the residual acetic acid (wt %, scaffold weight-basis). The extraction yield was calculated relative to the acetic acid content of the *nHApCS-untreated* sample.

Morphological characterization and elemental analysis

Scanning electron microscopy (SEM) coupled with Energy dispersive X-ray spectroscopy (EDS) using a Phenom Pro microscope from Phenom World was used. Mean pore size and pore size distributions were obtained by image analysis using the public domain software ImageJ developed by Wayne Rasband at the National Institute of Health (NIH). A minimum of 200 pores were analyzed per each sample. Elemental analysis was used to inspect the Ca/P ratio and the presence of impurities (for example, salts derived from the applied neutralization procedures).

Porosity determination

The total porosity of the nHAp/ CS scaffolds was estimated as:

$$\phi = 1 - \frac{\rho_{apparent}}{\rho_{real}}$$

where $\rho_{apparent}$ and ρ_{real} are the apparent and real densities, respectively. $\rho_{apparent}$ was determined experimentally based on three specimens per sample measured in triplicate (height and diameter with a vernier caliper, and weight with analytical balance). ρ_{real} was determined experimentally using a gas pycnometer (in-house made equipment) by carrying out measurements in triplicate.

Swelling tests

Samples (20 x 4 mm) were weighted dried (W_d) and after swollen in a PBS solution (pH 7.4, room temperature; W_s). Measurements were carried out in triplicate at immersion times ranging from 0 to 60 min. Swelling capacity was calculated as a mass-swelling ratio [24,25]:

$$C_w = \frac{W_s - W_d}{W_d}$$

Mechanical properties

The mechanical behavior was characterized using a DMA 242 E Artemis (NETZSCH-Gerätebau GmbH) in wet state under dynamic compression solicitation at 20 ºC, according to Rodrigues *et al.* (2013) [24]. The samples (cylinders of 9 mm diameter and 4 mm height) were firstly immersed in a PBS solution (pH 7.4, room temperature) for 60 min, followed by measurements, in triplicate, carried out in compression mode with cycles of increasing frequency (0.1 – 10 Hz).

In vitro cell culture

To infer the viability for *in vitro* cell culture, a preliminary test comprises pH evaluation of the culture medium upon contact with the scaffold. Samples of 5 x 5 x 5 mm (~5.29 x 10^{-3} g), were placed in 48-well plates under sterile conditions, and then added with 0.5 mL of the culture medium with phenol red. A change in color indicates pH deviation from the optimal range (7.2 – 7.4). Only samples passing this test were tested for sterility (microbiological assay) and subjected to the cell culture assays. For *in vitro* cell culture, osteoblast-like cells (MG63 cell line, ATCC number CRL-1427TM) were seeded in Eagle MEM, alpha modification (α-MEM) supplemented with 10 % fetal bovine serum, 100 IU/mL penicillin, 2.5 mg/mL streptomycin, and 2.5 mg/mL amphotericin B, and incubated in a humidified atmosphere of 5 % CO_2 at 37 ºC. The culture medium was replaced 2 – 3 times a week. At 70 – 80 % confluence, cells were removed from the culture plates by enzymatic digestion, using 1 mL of 0.05 % trypsin in 0.25 % EDTA for 10 min in standard culture conditions, and the cell suspension was used in the experiments. The cell culture was subcultured at least for 2 passages before the experiments.

Without further traditional disinfection or sterilization methods, samples (5 x 5 x 5 mm) were cut in sterile conditions and incubated 15 min at 37 ºC in fresh supplemented α-MEM for swelling. The wet samples were placed in 48-well plates and seeded with MG63 cells (1.25 x 10^5

cells/cm^2) in standard conditions. Seeded scaffolds were cultured for up to 21 days, and characterized for cell viability/proliferation, at time-points 1, 3, 7, 10, 14, 17, and 21 days, by the Alamar blue assay and SEM observation. Cultures performed without scaffold samples were used as control. In addition, a parallel experiment with culture medium alone was run as a blank.

Microbiological assay

Samples (5 x 5 x 5 mm) were cut in sterile conditions, placed in individual sterile eppendorfs, then added with 1 mL of BHI broth, sealed and incubated at 37 ºC. Samples from the three different batches were tested in triplicate. Two extra eppendorfs, prepared in the same conditions without scaffold samples, were used as negative controls. The presence/absence of turbidity was verified after 24, 48, and 120 h of incubation. After 120 h, each eppendorf was vortexed, and 20 mL of the BHI suspension, per duplicate, were plated into a nonselective trypticase soy agar (TSA) culture medium. Bacterial growth was assessed after 24 h of incubation at 37 ºC, by colony forming units counting in the TSA plates.

RESULTS AND DISCUSSION

Thermogravimetric analysis and extraction yield

Figure 2 shows the TG plots obtained for the nHAp/CS-untreated sample together with the samples exposed to $scCO_2$ extraction under the different tested conditions. In Figure 3, the samples subjected to different purification/neutralization procedures, including the one subjected to $scCO_2$ extraction under the best-achieved conditions (nHApCS-$scCO_2$-75/75), are analyzed against the nHAp/CS-untreated sample. Water and acetic acid evaporation were detected as mass losses in the range 30 – 100 ºC and 100 – 190 ºC, respectively. CS starts to degrade at 200 ºC and the achieved residual mass, between 65 and 70 wt %, can be mainly attributed to the nHAp used in the formulation.

In what concerns the nHApCS-untreated sample, the achieved residual acid content was 4.1 % (wt %, scaffold weight-basis), indicating that the freeze drying process itself promotes a reduction of 63 % (a residual acetic content of 11 % was expected based on the used formulation). Analyzing the results of Figure 2, the extraction yield attributed to the $scCO_2$ treatment was 44, 46, and 80 %, for the samples nHApCS-$scCO_2$-40 (179.0 $g_{CO2}/g_{scaffold}$), nHApCS$scCO_2$-75 (107.3 $g_{CO2}/g_{scaffold}$) and nHApCS-$scCO_2$-75/75 [214.6 $g_{CO2}/g_{scaffold}$ ratio (107.3 + 107.3)], respectively. In fact, the temperature increment from 40 to 75 ºC, even partially supported by the lower CO_2/scaffold weight ratio, has a negligible effect on the achieved extraction yield, but the use of

two cycles at 75 ºC was very effective resulting in a scaffold with a final residual acid content of 0.8 %. Additionally, only this sample was viable for cell growth.

Relative to the different purification/neutralization procedures, the corresponding extraction yield were 80, 70, and 80 % for nHApCS-5.5-NaOHEtOH, nHApCS-7.0, and nHApCS-scCO$_2$-75/75 samples, respectively. Based on these results the neutralization procedure used with the sample nHApCS-5.5-NaOHEtOH resulted in a residual acid content of 0.8 %, similarly to the one achieved with sample nHApCS-scCO$_2$-75/75. Nevertheless, based on the described preliminary test, the sample nHApCS-5.5-NaOHEtOH was not viable for *in vitro* cell culture.

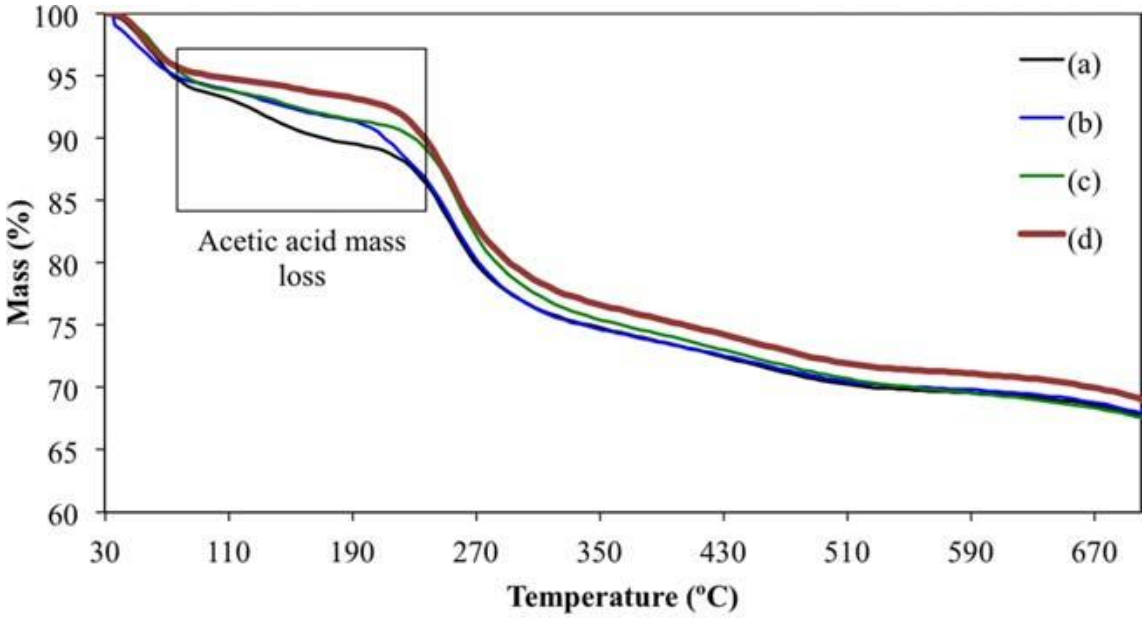

Sample	Acetic acid content (wt.%)	Extraction yield (%)
(a) n-HApCS-untreated	4.1	-
(b) n-HApCS-scCO$_2$-40	2.4	44%
(c) n-HApCS-scCO$_2$-75	2.2	46%
(d) n-HApCS-scCO$_2$-75/75	0.8	80%

Figure 2. Thermograms of: (a) nHApCS-5.5-untreated; (b) nHApCSscCO$_2$-40; (c) nHApCS-scCO$_2$-75; and (d) nHApCS-scCO$_2$-75/75 (From 30 to 700 ºC at 10 ºC/min; N$_2$ atmosphere).

Morphological characterization and elemental analysis

Differences resulting from the applied purification/neutralization procedures were perceptible even at a macroscale level (Figure 4): the nHApCS-5.5-untreated sample [Figure 4(a)] generated homogeneous, porous and elastic 3D structures, characteristics maintained after $scCO_2$ extraction (nHApCS-5.5-$scCO_2$-75/75 sample) [Figure 4(b)]; the nHApCS-NaOHEtOH sample showed a porous and elastic-like structure but with visible deterioration [Figure 4(c)]; and the nHApCS-7.0 sample [Figure 4(d)], even though its integrity in terms of shape was preserved, became highly brittle, and was not used in further characterizations.

Microstructure, a key factor for bone regeneration, was evaluated by SEM (Figure 4). In fact, a combination of adequate pore sizes and interconnectivity is needed to enable cells motion and diffusion of nutrients and metabolites for cells survival and proliferation [4]. Studies in literature showed that pores larger than 100 µm allow angiogenesis and contribute to nutrient and waste transport, whereas pores smaller than 50 µm improve osteointegration and generate cell anchoring sites [26,27]. SEM micrographs (Figure 5) and pore size distribution plots, deriving from image analysis (Figure 6), were obtained for the produced scaffolds samples. The nHApCS-untreated sample [Figure 5(a)] exhibits the desired interconnected porous structure, with a mean pore size of 86 ± 40 µm [Figure 6(a)]. These features were generally maintained for the nHApCS-$scCO_2$-75/75 sample [Figure 5(b)], that is, the desired interconnected structure and pore size of 72 ± 35 µm [Figure 6(b)], showing the adequacy of the $scCO_2$ treatment. In what concerns the nHApCS-5.5-NaOHEtOH sample, a lower mean pore size of 63 ± 27 µm was observed [Figure 6(c)] and modifications in scaffold's morphology were observed [Figure 5(c)]. All these three samples present pore sizes in the range of adequate dimensions, that is, pores with sizes larger than 100 µm and smaller than 50 µm, however in different proportions. The nHApCS-NaOHEtOH sample presented the lower amount of pores with sizes > 100 µm (14 %), and the nHApCS-untreated sample the larger one (42 %). The nHApCS-scCO2-75/75 sample presented a similar proportion (about 30 %) of both pore size categories.

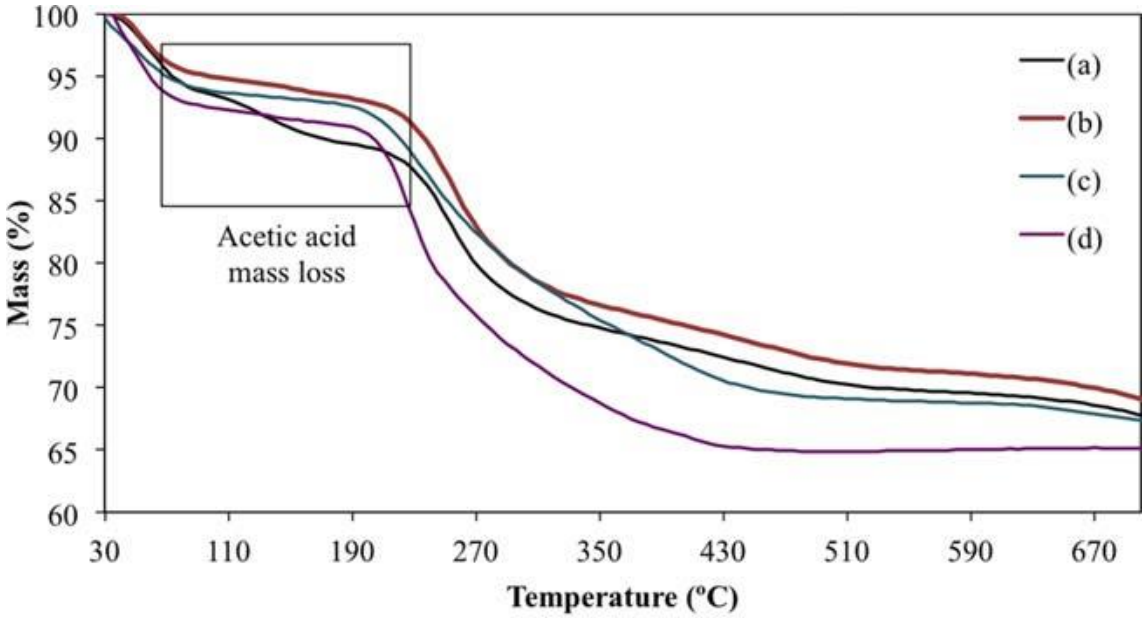

Sample	Acetic acid content (wt.%)	Extraction yield (%)
(a) n-HApCS-untreated	4.1	-
(b) n-HApCS-scCO$_2$-75/75	0.8	80%
(c) n-HApCS-NaOHEtOH	0.8	80%
(d) n-HApCS-7.0	1.2	70%

Figure 3. Thermograms of: (a) nHApCS-5.5-untreated; (b) nHApCSscCO$_2$-75/75; (c) nHApCS-5.5-NaOHEtOH and; (d) nHApCS-7.0 (From 30 to 700 ºC at 10 ºC/min; N_2 atmosphere).

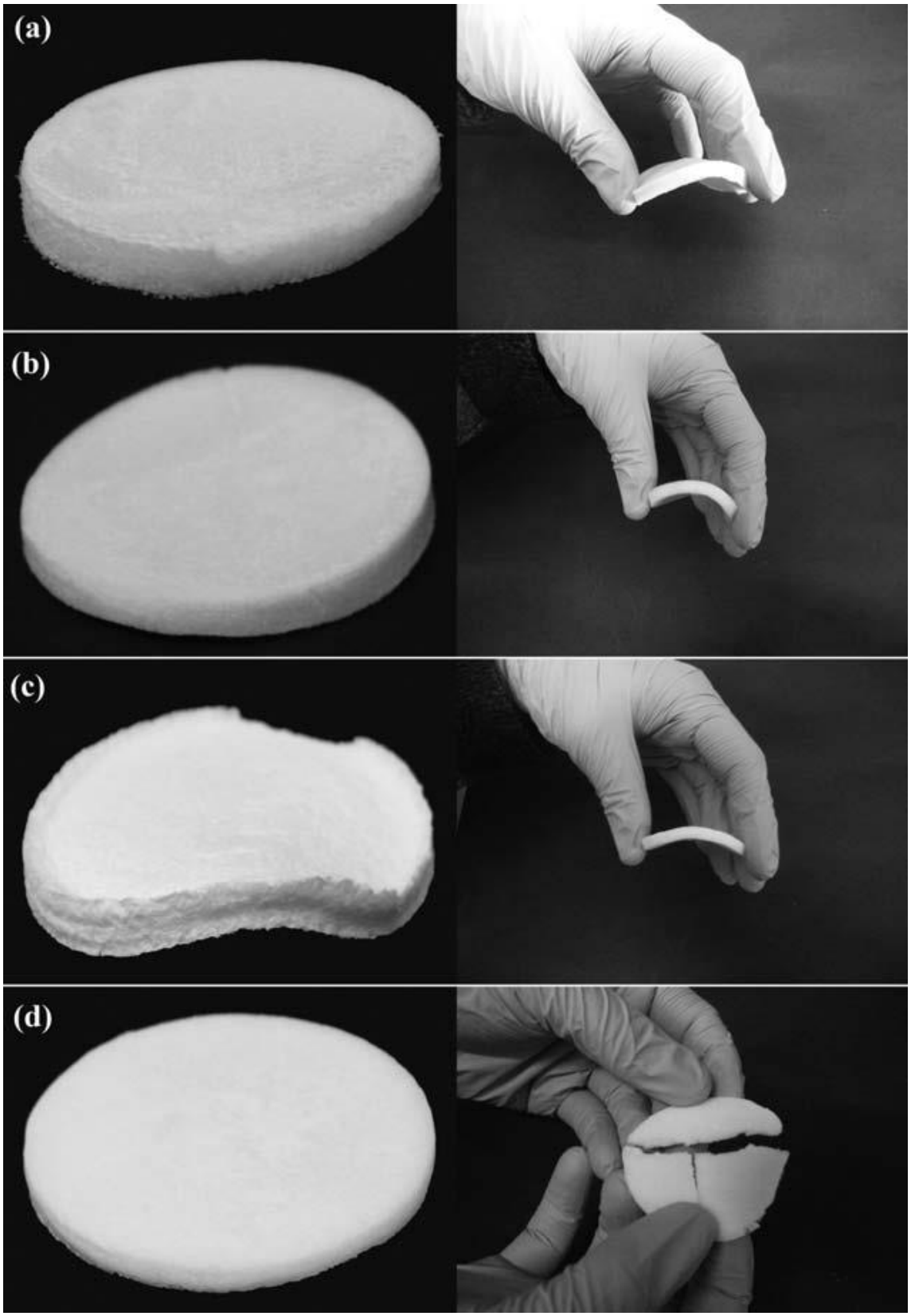

Figure 4. Images of the produced scaffolds: (a) nHApCS-5.5-untreated; (b) nHApCS-5.5-scCO$_2$; (c) nHApCS-5.5-NaOH/EtOH; (d) nHApCS-7.0.

In addition to the morphological study, elemental analysis was also performed (Figure 7). Results show that, despite the repeated washing steps, sodium salts derived from the used alkaline treatment were detected in the nHApCSNaOHEtOH sample [Figure 7(c), cross symbol 1]. These impurities were not observed in the SEM images of both nHApCS-untreated [Figure 7(a)] and nHApCS-scCO_2-75/75 [Figure 7(b)] samples. Elemental analysis was also used to estimate the Ca/P ratios of the produced samples (Table II). Ca/P ratios of 1.70 and 1.68 were obtained for nHApCS-untreated and nHApCS-scCO_2-75/75 scaffolds, respectively, values very close to the HAp Ca/P stoichiometric ratio (1.67). However, non-stoichiometric Ca/P ratio was obtained for nHApCS-5.5-NaOHEtOH (2.0 ± 0.18), corroborating that the neutralization procedure with alkaline solution compromises nHAp purity.

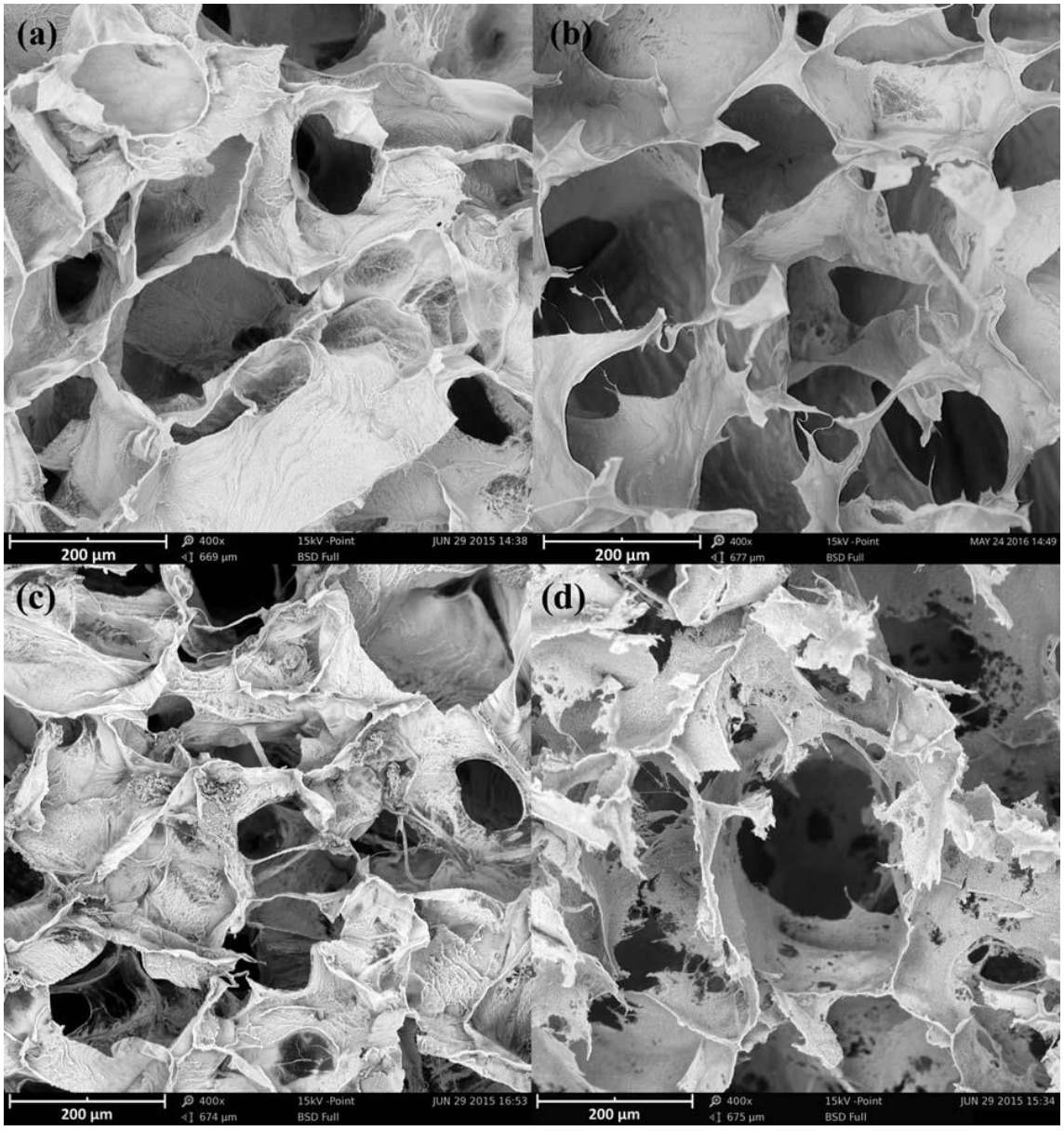

Figure 5. SEM micrographs (400x) of a cross-section of: (a) nHApCS-5.5-untreated; (b) nHApCS-5.5-scCO_2-75/75; (c) nHApCS-5.5-NaOHEtOH; (d) nHApCS-7.0.

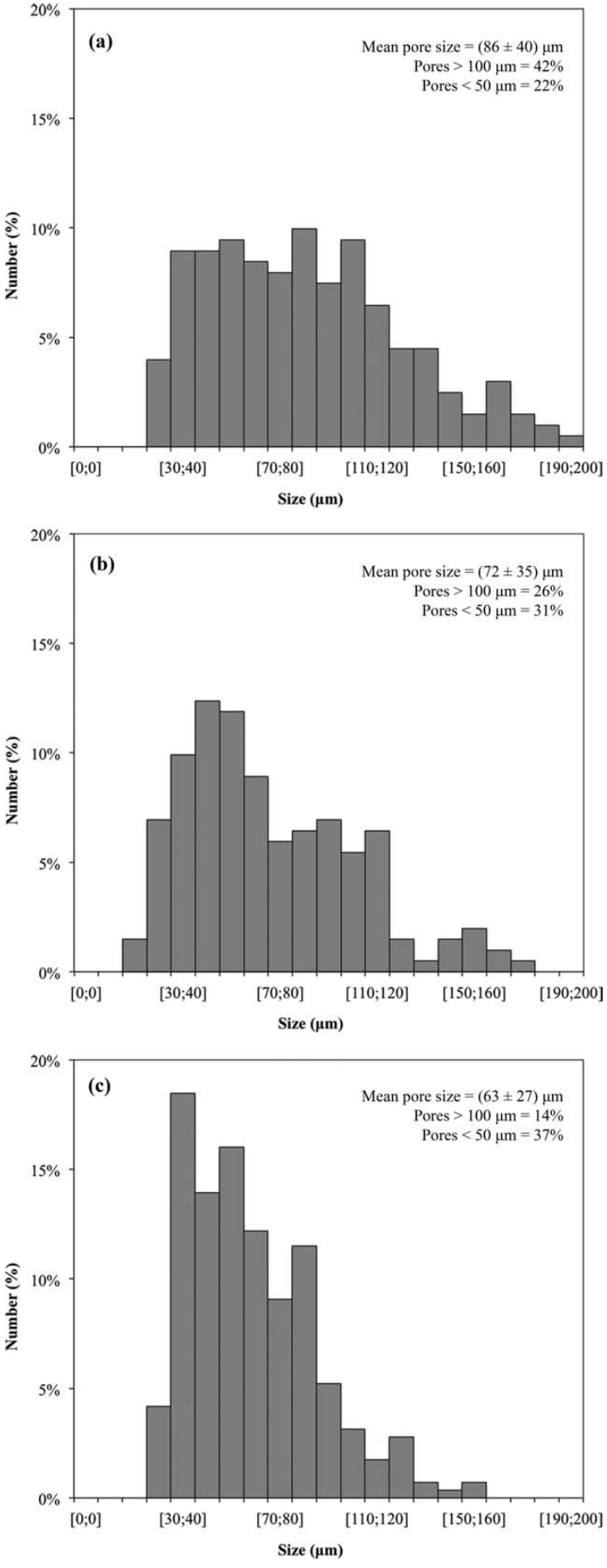

Figure 6. Particle size distributions of: (a) nHApCS-untreated; (b) nHApCS-$scCO_2$-75/75; (c) nHApCS-NaOHEtOH.

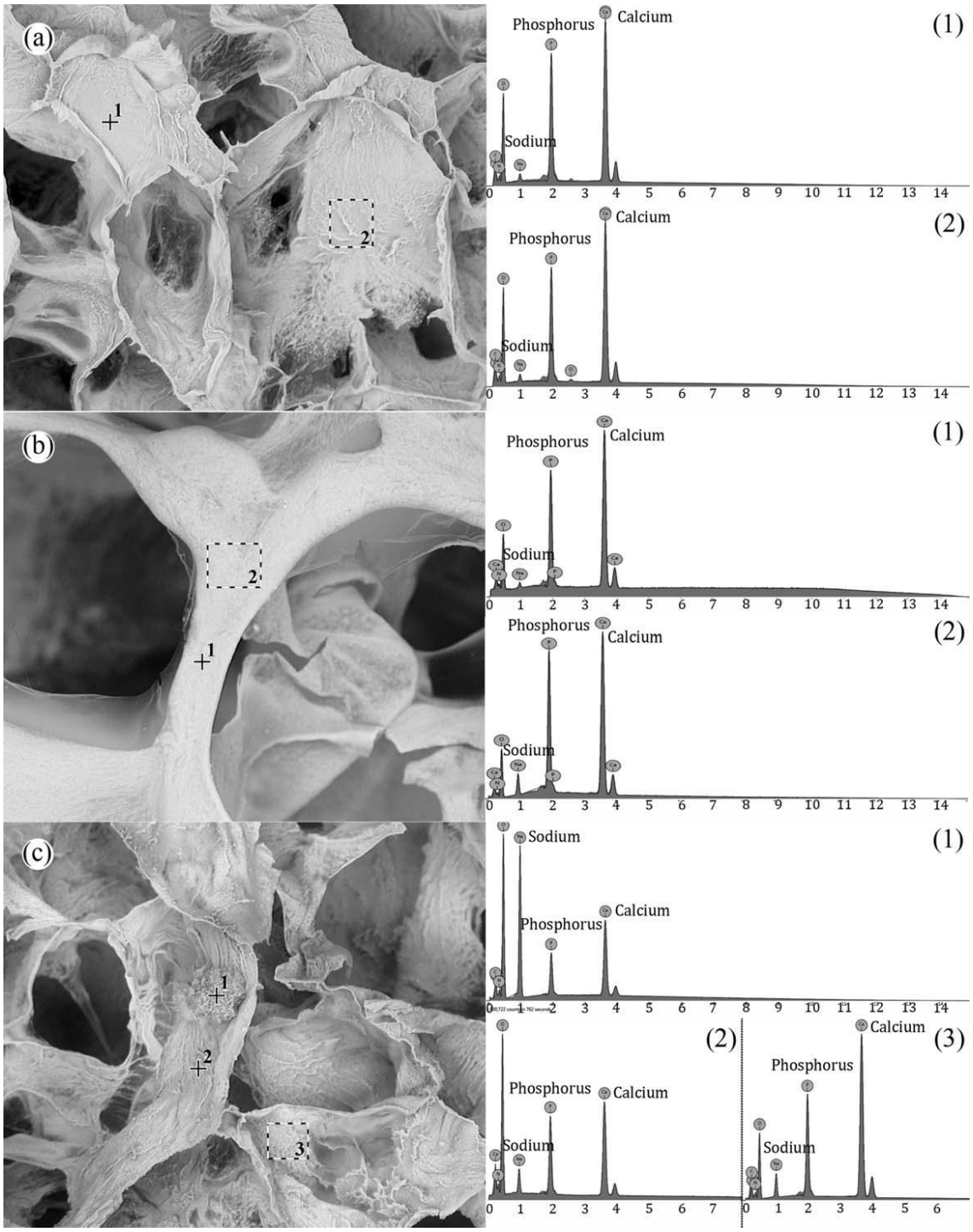

Figure 7. SEM micrographs and EDS analysis spectra of: (a) nHApCS-untreated; (b) nHApCS-scCO$_2$-75/75; (c) n-HApCS-NaOHEtOH. The cross symbol and the square in the images represent the areas analyzed by EDS.

Table II. Atomic Concentrations of Ca and P Obtained by EDS			
	Atomic concentration (%)		
Sample	**Ca**	**P**	**Ca/P**
Stoichiometric HAp	10	6	1.67
(a) nHApCS-5.5-untreated	14.4	8.45	1.70 ± 0.06
(b) nHApCS-5.5-scCO$_2$–75/75	17.7	10.6	1.68 ± 0.08
(c) nHApCS-5.5-NaOHEtOH	10.6	5.20	2.00 ± 0.18

Scaffold overall porosity

Depending on the surgical requirements, bone grafts can be either cortical, cancellous, or a combination of both [28]. Cancellous bone lacks mechanical strength due to its high porosity (30 – 90 % porosity) but induces osteogenesis [1,6,29], being frequently used for small defects such as nonunion fractures, maxillofacial and dental defects, and spinal fusion [28]. In what concerns bone grafts, it has been reported that the ideal overall porosity ranges from 60 to 99 % [30] Accordingly, all of the produced scaffolds exhibit the desirable high porosity (> 60 %). No substantial difference was observed in the determined theoretical porosity between the nHApCS-5.5-untreated (83 %) and nHApCS-scCO$_2$-75/75 (81 %) samples, showing that the purification with scCO$_2$ extraction does not compromise the overall porosity. However, an increase of ~10 % was observed for the nHApCS-5.5-NaOHEtOH sample (93 %), probably associated with the microstructural changes occurring during the second freeze drying step.

Swelling behavior

When implanted *in vivo*, scaffolds are introduced in an aqueous environment, influencing their overall properties; therefore, it is of primordial importance to evaluate their swelling behavior. In this study, the structural integrity of the scaffolds during swelling was firstly assessed by immersing the samples in PBS during 60 min (Figure 8). Fast swelling was observed for all samples, which is typical of highly hydrophilic materials and/or microstructures with a large range of pore interconnectivity, allowing a fast circulation of nutrients throughout the scaffold [24]. After 60 min immersion, the nHApCS-untreated sample exhibited the major swelling, and structure disruption was detected [Figure 8(a)]. In the case of nHApCS-scCO$_2$-75/75 and nHApCS-NaOHEtOH samples, both presented similar swelling behavior. However, while nHApCS-scCO$_2$-75/75 preserved its structural integrity [Figure 8(b)], the nHApCSNaOHEtOH sample suffered structure disruption after 60 min immersion [Figure 8(c)]. According to Berger *et al.* (2004) [31],

for CS-containing scaffolds, swelling is highly influenced by ionic interactions being favoured by the protonation and repulsion of CS free amino groups. The high content of residual acetic acid present in the nHApCS-untreated sample (4.1 %) induces the protonation of free amino groups favouring swelling; however, at the same time it promotes dissolution causing material's disruption. In the case of the nHApCS-NaOHEtOH sample, that presents the same residual acetic acid content of the nHApCS-scCO_2-75/75 sample (0.4 %), disruption can be associated with structure damage deriving from the applied purification/neutralization step, as discussed in the previous section. Due to the difficulties inherent to sample's disruption the swelling capacity was only determined for the nHApCS-scCO_2-75/75 sample. For this sample, swelling equilibrium was reached at 10 min and the swelling capacity was estimated as 24 ± 2.7 g g^{-1}. Based on these results, scCO_2 extraction appears as a favourable process that promotes an effective acetic acid extraction without affecting microstructure, thus promoting swelling without inducing dissolution/disruption.

Mechanical properties

To mimic *in vivo* conditions, the mechanical performance of the produced scaffolds was evaluated by DMA in wet state and within the physiological frequency range in load-bearing applications (1 to 10 Hz) [32] (Figure 9). Figure 9(a) shows data obtained for the storage modulus (E'), where a tendency to increase with frequency was observed for all samples. The nHApCS-untreated sample exhibits the lowest E' values, which can be mainly attributed to its high swelling and tendency to disrupt in aqueous medium, as observed during the swelling tests. After applying the purification/neutralization procedures, the scaffolds display an increase in E', but with differences depending on the used procedure, that is, the nHApCS-scCO_2-75/75 sample exhibited higher E' than the nHApCS-NaOHEtOH. This is in agreement with the observed microstructural changes of the nHApCS-NaOHEtOH sample, which suffered an increase of 10 % in its overall porosity. In fact, it has been reported that an increase of 10 to 20 % in the overall porosity decreases mechanical strength up to a factor four [33]. When using scCO_2 extraction the microstructural properties were preserved.

Relative to the loss factor (tan δ) [Figure 9(b)], an increase with frequency was observed for all cases, indicating that the samples tend to lose elasticity while their viscous properties become more relevant. The loss of elasticity is more evident for the nHApCS-5.5-untreated scaffold. No substantial differences were observed between the other two samples.

Taking as reference frequency of 1 Hz, E' values, reported as mean ± SD, were 6.75 ± 0.72, 13.3 ± 1.5, and 20.5 ± 2.9 kPa, for nHApCS-untreated, nHApCS-NaOHEtOH, and nHApCS-scCO_2-75/75 samples respectively. Considering that the compression modulus of natural cancellous bone ranges from 50 to 500 MPa, scaffolds exhibiting compression modulus below 25 MPa can be only suitable for non-load-bearing applications [30]. The low compression modulus

values are attributed to the high porosity of the scaffolds, generally > 80 %, which is essential for bone ingrowth [30].

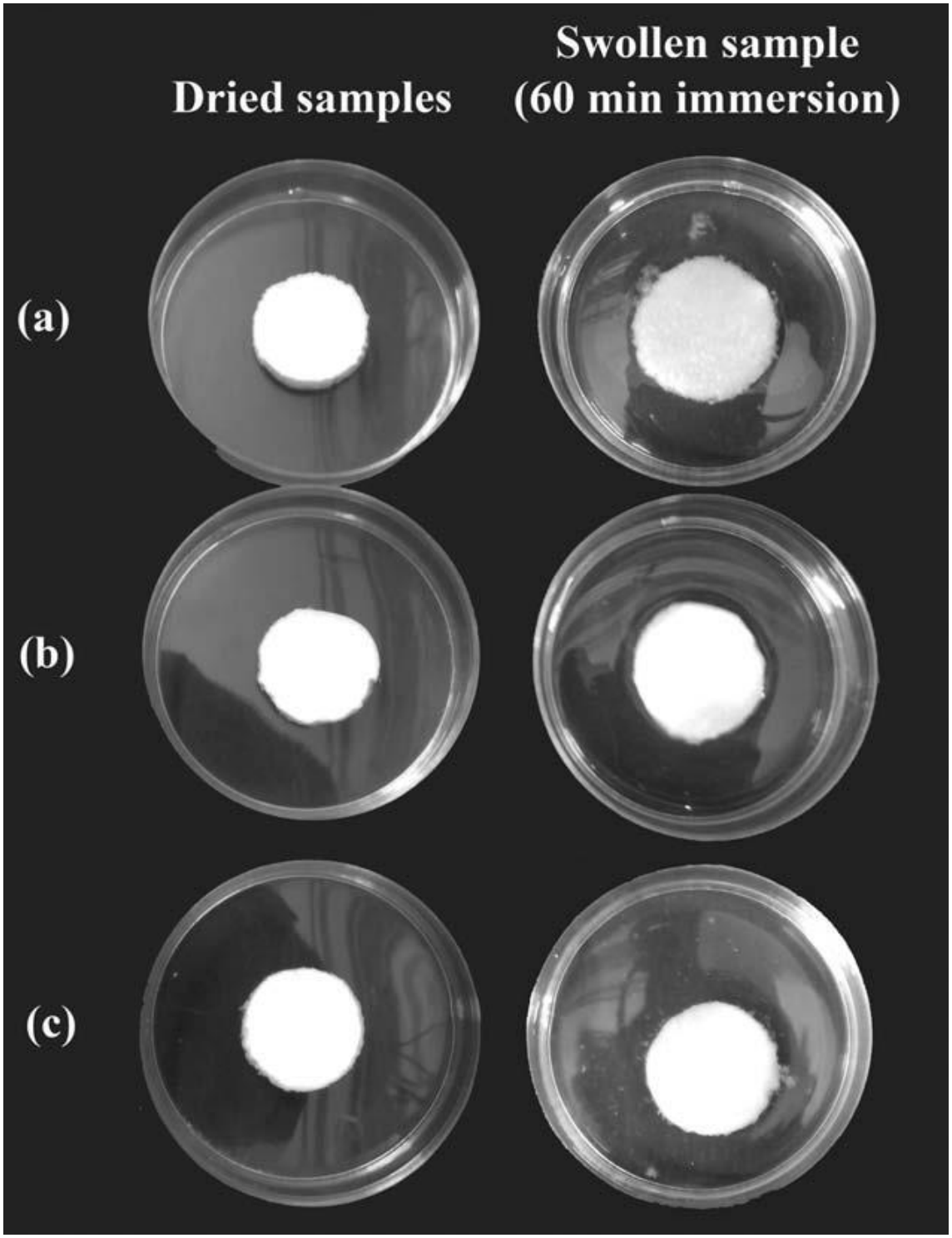

Figure 8. Dried and swollen samples, after 60 min of immersion in PBS, of: (a) nHApCS-untreated; (b) nHApCS-scCO_2-75/75; (c) nHApCS-NaOHEtOH.

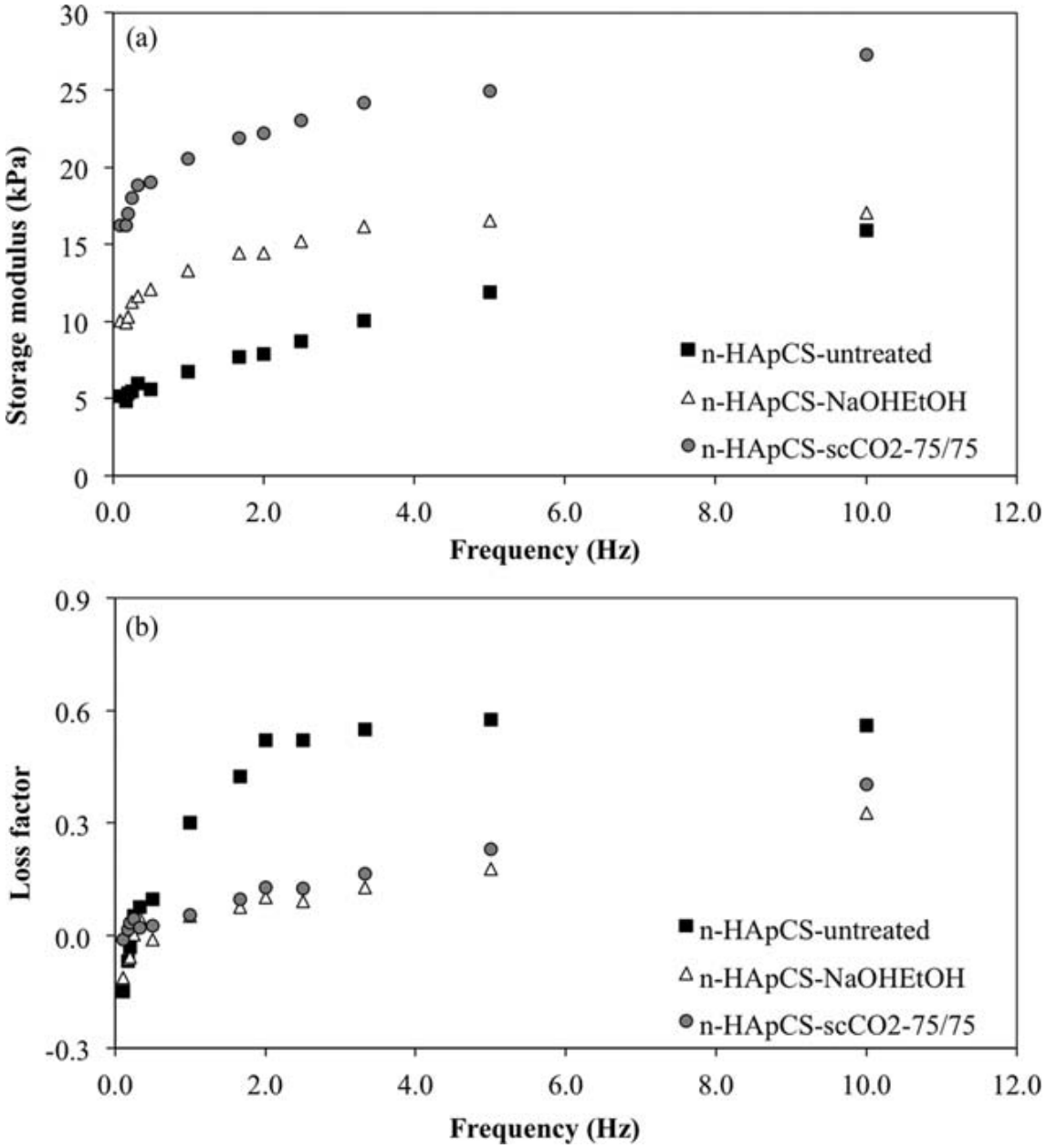

Figure 9. Storage modulus (a) and loss factor (b) under dynamic compression solicitation as a function of frequency, increasing from 0.1 to 10 Hz

In vitro biological studies

The cell viability test was carried out with the nHApCSscCO$_2$-75/75 scaffolds without any further disinfection or sterilization treatment after scCO$_2$ extraction. Following the antimicrobial test, after 24, 48, and 120 h of incubation in BHI suspension, the culture medium in contact with the sample was clean and comparable to the negative controls. Furthermore, no UFCs were counted after culturing the medium in TSA medium, evidencing that the nHApCSscCO$_2$-75/75

scaffolds were sterile. The sterility of the nHApCS-scCO$_2$-75/75 samples was also corroborated through the observation of the attachment and proliferation of cells to the scaffolds.

Figure 10 shows the SEM micrographs of osteoblast-like MG63 cells cultured on nHApCS-scCO$_2$-75/75 samples after 1, 7, 14, and 21 days. It can be observed cells changing from a roundish morphology (day 1) to a spindle-like shape (day 7). At day 14, flattening of the cells is evident. Moreover, cells presented good adherence to the scaffold, as well as filopodial-like growth along the assayed 21 days period. At day 7, the cells already started forming continuous cell layers, and by days 14 and 21 the scaffold was almost completely covered, with cells spreading in its surface and inside the pores.

According to the resazurin assay, cells exhibited good viability and proliferation, with a gradual increase in fluorescence intensity, proportional to resorufin content. Moreover, a 5-fold increase in the cell proliferation was registered from day 3 to day 21, which is a quite promising result. Thus, the nHApCS-scCO$_2$-75/75 scaffolds appear to be cytocompatible, osteoconductive, and allow the adhesion of osteoblast-like cells to its surface.

Although some recent studies have shown that nHAp/CS based materials are cytocompatible, osteoconductive and allow osteoblast-like cells adhesion to the biomaterial's surface, the performed work was based on samples disinfected by immersion in ethanol solution prior the cytotoxicity test [34,35]. In this work, rezasurin assay was carried out with the nHApCS-scCO$_2$-75/75 sample without any disinfection or sterilization treatment, confirming its sterility, which is a clear advantage.

CONCLUSIONS

In this work, a simple 3-step process to produce HAp/CS hybrid scaffolds was developed, including a single step, based on scCO$_2$ extraction, for both purification and sterilization. The best achieved conditions, giving rise to an acetic acid extraction yield of 80 %, were two 2 h cycles in static mode at T = 75 ºC and p = 8.0 MPa. The produced scaffolds mimicking bone composition, and containing highly pure nanocrystalline HAp, presented a storage modulus of 20.5 ± 2.9 kPa at 1 Hz frequency (compatible with non-load bearing applications) and elastic properties, exhibited adequate porosity, interconnected porous structure, and fast swelling, highly desirable features for bone regeneration. Moreover, from the microbiological assay, no microbial growth was observed, evidencing that the produced nHApCS-scCO$_2$-75/75 scaffolds were sterile, enabling the adhesion and proliferation of osteoblastic cells, which increased gradually along the tested 21-days period, without any disinfection or sterilization treatment, which is a quite promising result.

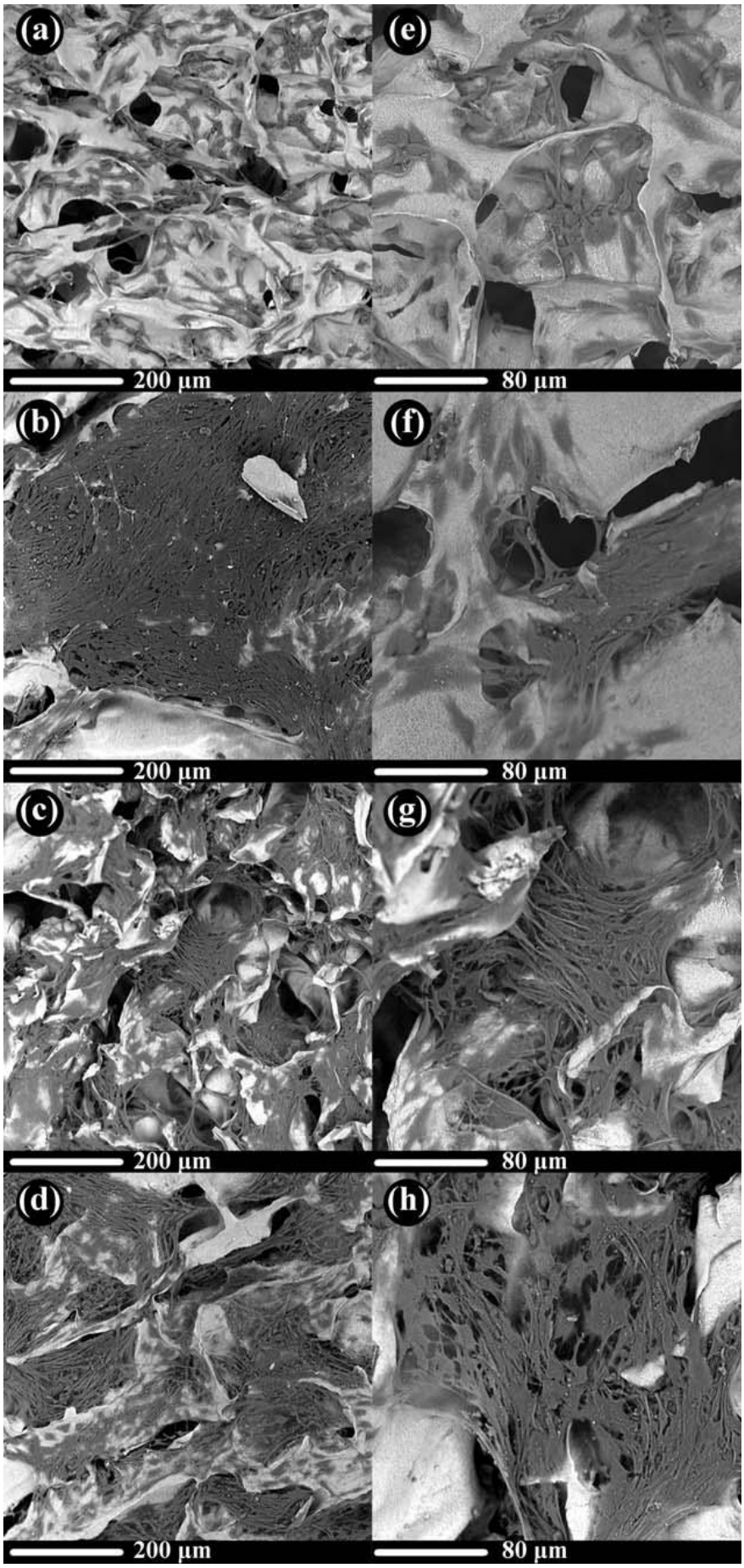

Figure 10. SEM micrographs of osteoblast-like MG63 cells cultured on nHApCS-scCO$_2$-75/75 samples after 1 day (a, e); 7 days (b, f); 14 days (c, g); 21 days (d, h). Magnification: 410x (a – d); 1000x (e – h)

Although acetic acid extraction yield can be further optimized by evaluating other parameters of the supercritical fluid process, for example, higher pressures and longer extraction times, this study has shown that $scCO_2$ extraction configures a very promising technique to achieve simultaneous purification and sterilization of the scaffolds. Contrasting to other currently used purification/neutralization procedures, the $scCO_2$-assisted process here proposed presented clear advantages, simplifying the overall productive process, from a 5-step (including neutralization with alkaline solution and washing steps) to a 3-step process.

Acknowledgments

Authors thank Fluidinova S.A. for providing the *nanoXIMHAp102*.

Contract grant sponsor: Associated Laboratory LSRE-LCM funded by FEDER funds through COMPETE2020 – Programa Operacional Competitividade e Internacionalizaçãoo (POCI) and FCT – Fundação para a Ciência e a Tecnologia (POCI-01-0145-FEDER-006984)

Contract grant sponsor: QREN, ON2, FCT and FEDER (Project NORTE-07–0162-FEDER-000050)

Contract grant sponsor: Universidad de Costa Rica and Ministerio de Ciencia, Tecnologıa y Telecomunicaciones de Costa Rica (MICIT) / Consejo Nacional para Investigaciones Científicas y Tecnologicas de Costa Rica (CONICIT) (G. Ruphuy research grant)

Contract grant sponsor: FCT (SFRH/BPD/93108/2013, P. Costa research grant)

Contract grant sponsor: European Union (FEDER funds POCI/01/0145/FEDER/007265) Contract grant sponsor: National Funds (FCT/MEC, Fundação para a Ciência e Tecnologia and Ministério da Educação e Ciência) under the Partnership Agreement PT2020 (UID/QUI/50006/2013)

VII. References

[1] Levengood, S. K. L.; Zhang, M. Chitosan-based scaffolds for bone tissue engineering. J Mater Chem B. 2014, 2, 3161-3184. doi: 10.1039/C4TB00027G

[2] Dorozhkin, S. V. Biocomposites and hybrid biomaterials based on calcium orthophosphates. Biomatter. 2011, 1, 3-56. doi: 10.4161/biom.1.1.16782

[3] Dorozhkin SV. Nanosized and nanocrystalline calcium orthophosphates. Acta Biomater. 2010, 6, 715–734. doi: 10.1016/j.actbio.2009.10.031

[4] O'Brien FJ. Biomaterials & scaffolds for tissue engineering. Mater. Today. 2011, 14, 88–95. doi: 10.1016/S1369-7021(11)70058-X

[5] Peniche C, Solís Y, Davidenko N, García R. Chitosan/hydroxyapatite-based composites. Biotecnología Aplicada. 2010, 27, 202–210. doi: -

[6] Costa-Pinto AR, Reis RL, Neves NM. Scaffolds based bone tissue engineering: the role of chitosan. Tissue Eng Part B Rev. 2011, 17, 331-347. doi: 10.1089/ten.teb.2010.0704

[7] Jiang L, Li Y, Wang X, Zhang L, Wen J, Gong M. Preparation and properties of nano-hydroxyapatite/chitosan/carboxymethyl cellulose composite scaffold. Carbohydr Polym. 2008, 74, 680–684. doi: 10.1016/j.carbpol.2008.04.035

[8] Kong L, Gao Y, Cao W, Gong Y, Zhao N, Zhang X. Preparation and characterization of nano-hydroxyapatite/chitosan composite scaffolds. J Biomed Mater Res A. 2005, 75A, 275–282. doi: 10.1002/jbm.a.30414

[9] Oliveira JM, Rodrigues MT, Silva SS, Malafaya PB, Gomes ME, Viegas CA, Dias IR, Azevedo JT, Mano JF, Reis RL. Novel hydroxyapatite/chitosan bilayered scaffold for osteochondral tissue-engineering applications: Scaffold design and its performance when seeded with goat bone marrow stromal cells. Biomaterials. 2006, 27, 6123–6137 doi: 10.1016/j.biomaterials.2006.07.034.

[10] Thein-Han WW, Misra RDK. Biomimetic chitosan–nanohydroxyapatite composite scaffolds for bone tissue engineering. Acta Biomater. 2009, 5, 1182–1197. doi: 10.1016/j.actbio.2008.11.025

[11] Barile FA. Principles of Toxicology Testing, 2nd Ed.; CRC Press: Boca Raton, FL, USA, 2013.

[12] Madihally SV, Matthew HWT. Porous chitosan scaffolds for tissue engineering. Biomaterials. 1999, 20, 1133–1142. doi: 10.1016/s0142-9612(99)00011-3

[13] Seda Tığlı R, Karakeçili A, Gümüşderelioğlu M. *In vitro* characterization of chitosan scaffolds: influence of composition and deacetylation degree. J Mater Sci Mater Med. 2007, 18, 1665–1674. 10.1007/s10856-007-3066-x

[14] Baldino L, Cardea S, De Marco I, Reverchon E. Chitosan scaffolds formation by a supercritical freeze extraction process. J Supercrit Fluids. 2014, 90, 27–34. doi: 10.1016/j.supflu.2014.03.002

[15] Baldino L, Concilio S, Cardea S, De Marco I, Reverchon E. Complete glutaraldehyde elimination during chitosan hydrogel drying by SC-CO_2 processing. J Supercrit Fluids. 2015, 103, 70–76. doi: 10.1016/j.supflu.2015.04.020

[16] Duarte ARC, Mano J, Reis R. Supercritical fluids in biomedical and tissue engineering applications: a review. Int Mater Rev. 2009, 54, 214–222. doi: 10.1179/174328009X411181

[17] Checinska A, Fruth IA, Green TL, Crawford RL, Paszczynski AJ. Sterilization of biological pathogens using supercritical fluid carbon dioxide containing water and hydrogen peroxide. J Microbiol Methods. 2011, 87, 70–75. doi: 10.1016/j.mimet.2011.07.008

[18] Hemmer JD, Drews MJ, LaBerge M, Matthews MA. Sterilization of bacterial spores by using supercritical carbon dioxide and hydrogen peroxide. J Biomed Mater Res B Appl Biomater. 2007, 80B, 511–518. doi: 10.1002/jbm.b.30625

[19] Spilimbergo S, Bertucco A, Lauro FM, Bertoloni G. Inactivation of Bacillus subtilis spores by supercritical CO_2 treatment. Innov Food Sci Emerg Technol. 2003, 4, 161–165. doi: 10.1016/S1466-8564(02)00089-9

[20] Zhang J, Burrows S, Gleason C, Matthews MA, Drews MJ, LaBerge M, An YH. Sterilizing Bacillus pumilus spores using supercritical carbon dioxide. J Microbiol Methods. 2006, 66, 479–485. doi: 10.1016/j.mimet.2006.01.012

[21] Ruphuy G, Saralegi A, Lopes JC, Dias MM, Barreiro MF. Spray drying as a viable process to produce nano-hydroxyapatite/chitosan (n-HAp/CS) hybrid microparticles mimicking bone composition. Adv Powder Technol. 2016, 27, 575–583. doi: 10.1016/j.apt.2016.02.010

[22] He Q, Ao Q, Gong Y, Zhang X. Preparation of chitosan films using different neutralizing solutions to improve endothelial cell compatibility. J Mater Sci Mater Med. 2011, 22, 2791–2802. doi: 10.1007/s10856-011-4444-y

[23] Gomes PB, Mata VG, Rodrigues AE. Production of rose geranium oil using supercritical fluid extraction. J Supercrit Fluids. 2007, 41, 50–60. doi: 10.1016/j.supflu.2006.08.018

[24] Rodrigues SC, Salgado CL, Sahu A, Garcia MP, Fernandes MH, Monteiro FJ. Preparation and characterization of collagen-nanohydroxyapatite biocomposite scaffolds by cryogelation method for bone tissue engineering applications. J Biomed Mater Res A. 2013, 101A, 1080–1094. doi: 10.1002/jbm.a.34394

[25] Zhu J, Marchant RE. Design properties of hydrogel tissue engineering scaffolds. Expert Rev Med Devices. 2011, 8, 607–626. doi: 10.1586/erd.11.27

[26] Klenke FM, Liu Y, Yuan H, Hunziker EB, Siebenrock KA, Hofstetter W. Impact of pore size on the vascularization and osseointegration of ceramic bone substitutes *in vivo*. J Biomed Mater Res A. 2008, 85A, 777–786. doi: 10.1002/jbm.a.31559

[27] Polak SJ, Levengood SKL, Wheeler MB, Maki AJ, Clark SG, Johnson AJW. Analysis of the roles of microporosity and BMP-2 on multiple measures of bone regeneration and healing in calcium phosphate scaffolds. Acta Biomater. 2011, 7, 1760–1771. doi: 10.1016/j.actbio.2010.12.030

[28] Oryan A, Alidadi S, Moshiri A, Maffulli N. Bone regenerative medicine: Classic options, novel strategies, and future directions. J Orthop Surg Res, 2014, 9, 1–27. doi: 10.1186/1749-799X-9-18

[29] Bose S, Roy M, Bandyopadhyay A. Recent advances in bone tissue engineering scaffolds. Trends Biotechnol. 2012, 30, 546–554. doi: 10.1016/j.tibtech.2012.07.005

[30] Pilia M, Guda T, Appleford M. Development of Composite Scaffolds for Load-Bearing Segmental Bone Defects. BioMed Res Int. 2013, 2013, 15. doi: 10.1155/2013/458253

[31] Berger J, Reist M, Mayer JM, Felt O, Peppas NA, Gurny R. Structure and interactions in covalently and ionically crosslinked chitosan hydrogels for biomedical applications. Eur J Pharm Biopharm 2004, 57, 19–34. doi: 10.1016/s0939-6411(03)00161-9

[32] Malafaya PB, Santos TC, van Griensven M, Reis RL. Morphology, mechanical characterization and *in vivo* neo-vascularization of chitosan particle aggregated scaffolds architectures. Biomaterials. 2008, 29, 3914–3926. doi: 10.1016/j.biomaterials.2008.06.023

[33] Hannink G, Arts JJC. Bioresorbability, porosity and mechanical strength of bone substitutes: What is optimal for bone regeneration? Injury. 2011, 42, Supplement 2, S22–S25. doi: 10.1016/j.injury.2011.06.008

[34] Qasim SB, Delaine-Smith RM, Fey T, Rawlinson A, Rehman IU. Freeze gelated porous membranes for periodontal tissue regeneration. Acta Biomater. 2015, 23, 317–328. doi: 10.1016/j.actbio.2015.05.001

[35] Lai G-J, Shalumon KT, Chen J-P. Response of human mesenchymal stem cells to intrafibrillar nanohydroxyapatite content and extrafibrillar nanohydroxyapatite in biomimetic chitosan/silk fibroin/nanohydroxyapatite nanofibrous membrane scaffolds. Int J Nanomedicine. 2015, 10, 567–584. doi: 10.2147/IJN.S73780

CHARACTERIZATION OF A NANO-HYDROXYAPATITE/ CHITOSAN SCAFFOLD FOR BONE REGENERATION

Mariana do Souto Fontes Antunes Lopes

FACULDADE DE ENGENHARIA